Laser-driven beams of fast ions, relativistic electrons and coherent x-ray photons

Lundh, Olle

2008

Laser-driven beams of fast ions, relativistic electrons and coherent x-ray photons

Olle Lundh

Doctoral Thesis
2008

Lund University

Laser-driven beams of fast ions, relativistic electrons and coherent x-ray photons

Printed in Sweden by Media-Tryck, Lund, 2008

Division of Atomic Physics
Department of Physics
Faculty of Engineering, LTH
Lund University
P.O. Box 118
SE–221 00 Lund
Sweden

http://www.atom.fysik.lth.se

ISSN 0281-2762
Lund Reports on Atomic Physics, LRAP-391

ISBN: 978-91-628-7482-7

Abstract

This thesis presents experimental results on the development and optimization of novel and highly compact sources of beams of fast ions, relativistic electrons and coherent x-rays, driven by intense laser-plasma interactions.

The rapid development of high-power, short-pulse laser systems have made available peak powers reaching the petawatt regime and focused intensities reaching 10^{21} W/cm^2. When interacting with matter, the extreme energy density (>GJ/cm^3) associated with the focused laser pulses can create exceptionally high quasi-stationary electric fields, beyond several teravolt-per-meter (TV/m). By careful selection of the interaction conditions, electrons, protons or heavy ions can be accelerated to the multi-MeV kinetic energy level in distances ranging from a only a few micrometers up to several centimeters.

The thesis addresses three important topics and summarizes results obtained using the multi-terawatt laser at the Lund Laser Centre in Sweden and the Vulcan Petawatt laser at the Rutherford-Appleton Laboratory in the United Kingdom.

The thesis discusses laser-plasma acceleration of protons and heavy ions from thin foil metallic targets. The ion energy scalings with laser pulse and target parameters are investigated, and protons have been accelerated up to 55 MeV. Ultrathin targets, with thicknesses below 100 nm, and ultrahigh contrast laser pulses are shown to substantially enhance the proton maximum energy and laser-to-particle beam conversion efficiency. Shock waves, launched by the intrinsic laser prepulse, are shown to significantly influence the acceleration mechanisms. Novel schemes, involving multiple laser pulses, for active control of the spatial energy distribution of the accelerated ion beams are also presented.

Results regarding the generation and optimization of quasi-monoenergetic electron beams are presented. Acceleration occurs in a plasma wave that is excited in the wake of an intense laser pulse in a tenuous plasma. Electrons are accelerated up to 200 MeV in less than 2 mm acceleration length. It is shown that, in the quasi-monoenergetic regime, electrons originate from the first plasma wave period. Current challenges such as electron beam stability are also specifically addressed.

The thesis also reports the implementation of a laser in the soft x-ray regime. By using a grazing incidence pumping scheme, picosecond x-ray laser pulses with energies up to 3 μJ at a wavelength of 18.9 nm are produced at 10 Hz repetition rate, using Ni-like molybdenum ions as amplifying medium.

Populärvetenskaplig sammanfattning

I avhandlingen beskrivs hur intensiva strålar av snabba joner, relativistiska elektroner och koherenta fotoner i röntgenområdet kan genereras under laserplasma växelverkan vid mycket höga laserintensiteter. Forskningen syftar till att utveckla nya typer av mycket kompakta strålkällor.

Toppeffekten som kan levereras i form av extremt korta laserpulser kan vid moderna laserfaciliteter idag vara uppemot en petawatt (10^{15} W). Denna effekt är många gånger högre än hela världens effektförbrukning, men varar endast under en mycket kort tidsrymd, mindre än en pikosekund (10^{-12} s). När en sådan puls fokuseras till en mikrometerstor fläck, uppstår intensitieter som överstiger 10^{19} W/cm^2. Energidensiteten i den fokuserade laserpulsen kan vara flera GJ/cm^3. När dessa hårt fokuserade laserpulser träffar ett strålmål uppstår tryck motsvarande flera miljarder atmosfärer. Atomer som kommer i laserstrålens väg joniseras omedelbart så huvuddelen av laserpulsen växelverkar därför med ett plasma, bestående av fria negativt laddade elektroner och positivt laddade joner. I detta plasma drivs elektroner till relativistiska hastigheter och temperaturer på mer än tio miljarder grader uppstår vilket är tusen gånger högre än temperaturen i solens centrum. De lättare elektronerna trycks snabbt iväg av laserpulsen, medan de mycket tyngre jonerna ligger stilla under den korta tid laserpulsen varar. Detta resulterar i en laddningsseparation vilken i sin tur ger upphov till några av de starkaste elektriska och magnetiska fält som går att framkalla i laboratorier idag. Möjligheten att använda dessa extremt höga elektriska fält för att accelerera partiklar till betydande energier på en mycket kort accelerationssträcka motiverar mycket av det arbete som presenteras i avhandlingen.

Partikelacceleratorer har under lång tid varit ett mycket viktigt redskap inom många olika grenar av naturvetenskaperna. I konventionella acceleratorer begränsas den elektriska fältstyrka som kan användas av risken för överslag i vakuumkammaren. Det leder till stora och kostsamma anläggningar eftersom man då får accelerera över långa sträckor. I ett plasma finns inte motsvarande begränsing, och med intensiva laserpulser kan fältstyrkor som är flera tiopotenser högre uppnås vilket medför att accelerationssträckan kan skalas ned med motsvarande faktor. En annan fördel med laserdriven acceleration är att ingen farlig strålning genereras förrän ljuset fokuseras på ett strålmål, vilket gör att mängden strålskydd kan minskas avsevärt.

I det experimentella arbete som ligger till grund för avhandlingen har både multi-terawatt-lasern vid högeffektslaserlaboratoriet vid Lunds Universitet och petawatt-lasern vid Central Laser Facility, Rutherford-Appleton Laboratory, i Storbritannien använts.

I avhandlingen presenteras experiment som undersöker hur protoner och tunga joner kan accelereras. Dessa partiklar är för tunga för att påverkas direkt av lasern, så en indirekt metod används. Man skjuter då på en mikrometertjock folie, varvid elektroner i det plasma som bildas effektivt tar upp laserenergin. Elektronerna strömmar genom folien till baksidan, där ett mycket starkt elektrostatiskt fält bildas genom laddningsseparation. I detta fält joniseras atomer på ytan, varefter de accelereras till höga energier över ett fåtal mikrometer.

Arbetet har varit inriktat på att undersöka hur jonernas kinetiska energi och rumsliga fördelning skalar med olika experimentella parametrar. Protoner med energier upp till 55 megaelektronvolt (MeV) har uppmätts och mycket tunna folier, ner till 20 nm (motsvarande 100 atomlager), har använts för mycket effektiv generering av protonstrålar. Vi har även undersökt hur lasergenererade chockvågor kan användas för att deformera folien strax innan jonerna accelereras och därigenom kontrollera deras riktning. Vi har också visat att strålkvaliteten kan höjas avsevärt genom att kombinera olika laserpulser.

En kompakt källa av energirika protoner kan få ett flertal tillämpningar. Ett medicinskt exempel är att alstra de kortlivade radioaktiva isotoper som används för PET-tomografi. Ett annat exempel är att utnyttja att protoner som bromsas ner i materia lämnar största delen av sin energi på ett väldefinierat djup där de stoppas helt. Det gör att djupt liggande cancertumörer kan behandlas utan att omgivande vävnad tar allt för mycket skada. Dessa tillämpningar ligger dock längre fram i tiden och nuvarande experiment är av grundforskningskaraktär.

Genom att istället fokusera lasern genom i gas, så genereras en plasmakanal i vilken en elektrostatisk våg färdas tillsammans med laserpulsen. Genom att surfa på vågen kan elektroner accelereras upp till 200 MeV på mindre än två millimeters accelerationssträcka. I avhandlingen visas att, om plasmavågens och laserpulsens egenskaper matchas till varandra, kan elektronerna koncentreras till en mycket kort puls med liten energispridning.

En mycket viktig tillämpning av energirika elektronstrålar är att producera kortvågiga ljuspulser i mjukröntgenområdet. I avhandlingen beskrivs en alternativ, laserbaserad, metod för generering av röntgenlaserpulser. Två infraröda laserpulser användes för att driva en röntgenlaser i en geometri som ger en mycket hög konversionseffektivitet. Detta möjliggjorde en studie av röntgenlaserns egenskaper vid en relativt hög pulsrepetitionsfrekvens på 10 Hz.

List of publications

This thesis is based on the following papers, which will be referred to by their Roman numerals in the text.

I **Laser-accelerated protons with energy-dependent beam direction**
F. Lindau, O. Lundh, A. Persson, P. McKenna, K. Osvay, D. Batani and C.-G. Wahlström.
Physical Review Letters **95**, 175002 (2005).

II **High-intensity laser-driven proton acceleration: influence of pulse contrast**
P. McKenna, F. Lindau, O. Lundh, D. Neely, A. Persson and C.-G. Wahlström.
Philosophical Transactions of the Royal Society A **364**, 711 (2006).

III **Influence of shockwaves on laser-driven proton acceleration**
O. Lundh, F. Lindau, A. Persson, P. McKenna, D. Batani and C.-G. Wahlström.
Physical Review E **76**, 026404 (2007).

IV **Active steering of laser-accelerated ion beams**
O. Lundh, Y. Glinec, C. Homann, F. Lindau, A. Persson, C.-G. Wahlström, P. McKenna and D. C. Carroll.
Applied Physics Letters **92**, 011504 (2008).

V **Enhanced proton beams from ultrathin targets driven by high contrast laser pulses**
D. Neely, P. Foster, A. Robinson, F. Lindau, O. Lundh, A. Persson, C.-G. Wahlström and P. McKenna.
Applied Physics Letters **89**, 021502 (2006).

VI **Active manipulation of the spatial energy distribution of laser-accelerated proton beams**
D. C. Carroll, P. McKenna, O. Lundh, F. Lindau, C.-G. Wahlström, S. Bandyopadhyay, D. Pepler, D. Neely, S. Kar, P. T. Simpson, K. Markey, M. Zepf, C. Bellei, R. G. Evans, R. Redaelli, D. Batani, M. H. Xu and Y. T. Li.
Physical Review E **76**, 065401(R) (2007).

VII **Scaling of proton acceleration driven by petawatt-laser–plasma interactions**
L. Robson, P. T. Simpson, P. McKenna, K. W. D. Ledingham, R. J. Clarke, T. McCanny, D. Neely, O. Lundh, F. Lindau, C.-G. Wahlström and M. Zepf.
Nature Physics **3**, 58 (2007).

VIII **Detection of short lived radioisotopes as a fast diagnostic for intense laser–solid interactions**
R. J. Clarke, K. W. D Ledingham, P. McKenna, L. Robson, T. McCanny, D. Neely, F. Lindau, O. Lundh, C.-G. Wahlström, P. T. Simpson and M. Zepf.
Applied Physics Letters **89**, 141117 (2006).

IX **Low- and medium-mass ion acceleration driven by petawatt laser plasma interactions**
P. McKenna, F. Lindau, O. Lundh, D. C. Carroll, R. J. Clarke, K. W. D. Ledingham, T. McCanny, D. Neely, A. P. L. Robson, P. T. Simpson, C.-G. Wahlström and M. Zepf.
Plasma Physics and Controlled Fusion **49**, B223 (2007).

X **Lateral electron transport in high-intensity laser-irradiated foils diagnosed by ion emission**
P. McKenna, D. C. Carroll, R. J. Clarke, R. G. Evans, K. W. D. Ledingham, F. Lindau, O. Lundh, T. McCanny, D. Neely, A. P. L. Robinson, L. Robson, P. T. Simpson, C.-G. Wahlström and M. Zepf.
Physical Review Letters **98**, 145001 (2007).

XI **Laser-wakefield acceleration of monoenergetic electron beams in the first plasma-wave period**
S. P. D. Mangles, A. G. R. Thomas, M. C. Kaluza, O. Lundh, F. Lindau, F. S. Tsung, Z. Najmudin, W. B. Mori, C.-G. Wahlström and K. Krushelnick.
Physical Review Letters **96**, 215001 (2006).

XII **On the stability of laser wakefield electron accelerators in the monoenergetic regime**
S. P. D. Mangles, A. G. R. Thomas, O. Lundh, F. Lindau, M. C. Kaluza, A. Persson, C.-G. Wahlström, K. Krushelnick and Z. Najmudin.
Physics of Plasmas **14**, 056702 (2007).

XIII **Effect of laser contrast ratio on electron beam stability in laser wakefield acceleration experiments**
S. P. D. Mangles, A. G. R. Thomas, M. C. Kaluza, O. Lundh, F. Lindau, A. Persson, Z. Najmudin, C.-G. Wahlström, C. D. Murphy, C. Kamperidis, K. L. Lancaster, E. Divall and K. Krushelnick.
Plasma Physics and Controlled Fusion **48**, B83 (2006).

XIV **Optimization toward a high-average-brightness soft-x-ray laser pumped at grazing incidence**
K. Cassou, S. Kazamias, D. Ros, F. Plé, G. Jamelot, A. Klisnick, O. Lundh, F. Lindau, A. Persson, C.-G. Wahlström, S. de Rossi, D. Joyeux, B. Zielbauer, D. Ursescu and T. Kühl.
Optics Letters **32**, 139 (2007).

XV **Characterization of a transient collisional Ni-like molybdenum soft x-ray laser pumped in grazing incidence**
S. Kazamias, K. Cassou, D. Ros, F. Plé, G. Jamelot, A. Klisnick, O. Lundh, F. Lindau, A. Persson, C.-G. Wahlström, S. de Rossi, D. Joyeux, B. Zielbauer, D. Ursescu and T. Kühl.
Physical Review A **77**, 033812 (2008).

XVI **Quantitative study of 10 Hz operation of a soft x-ray laser – energy stability and target considerations**
F. Lindau, O. Lundh, A. Persson, K. Cassou, S. Kazamias, D. Ros, F. Plé, G. Jamelot, A. Klisnick, S. de Rossi, D. Joyeux, B. Zielbauer, D. Ursescu, T. Kühl and C.-G. Wahlström.
Optics Express **15**, 9486 (2007).

Contents

Papers

Chapter 1

Introduction

The peak power of ultrashort laser pulses generated at state-of-the-art high-power laser facilities, has reached the petawatt (10^{15} W) regime. When these pulses, with sub-picosecond durations, are focused, intensities up to 10^{21} W/cm^2 are generated in a focal spot with a diameter of only a few micrometers. Moreover, the energy density associated with the focused laser pulse is several GJ/cm^{-3} and the photon pressure, exerted during absorption of the laser beam, is several hundred Gbar. When such a laser pulse strikes upon matter, ionization occurs almost instantaneously and the main part of the laser pulse interacts with ionized matter, a plasma. The laser pulse swiftly thrusts plasma electrons out from regions of high energy density while the much heavier plasma ions remain almost immobile on the timescale of the duration of the laser pulse and, during the intense interactions, quasi-stationary electric fields of the order of teravolt-per-meter (TV/m) and magnetic fields of more than 10 000 tesla can be generated in the plasma.

The physics of high-intensity laser-plasma interactions is truly an exciting discipline where extreme physical quantities are part of everyday laboratory work. Currently, the field is attracting interest from many parts of society since recent experiments have demonstrated the prospects of constructing very compact high-quality sources of beams of energetic particles and short wavelength radiation, based on the physics of intense laser-plasma interactions.

Particle accelerators

The acceleration of particles has historically been a very important area of research within the physical sciences, and it will without doubt continue to be so in the future. Beams of energetic *electrons*, with kinetic energies by far exceeding the electron rest

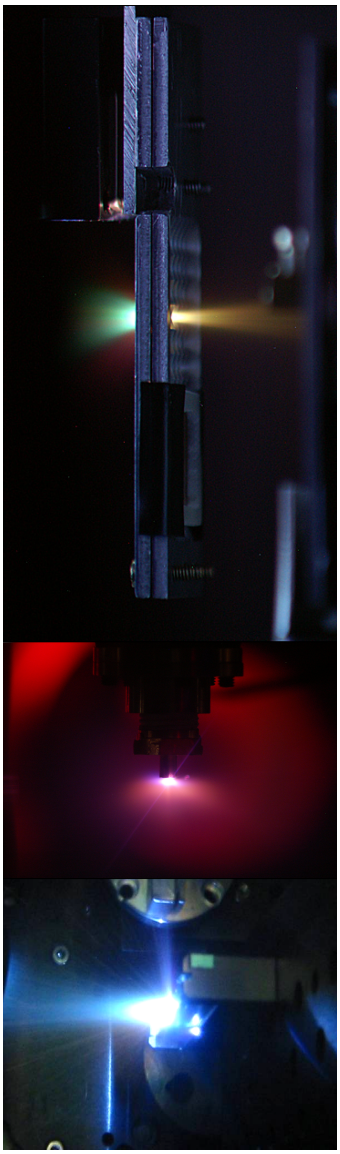

Figure 1.1. *Photographs of intense laser-plasma interactions, taken during experiments reported on in this thesis. Top, laser-driven ion acceleration from a thin foil target. The laser is incident from the left, and the proton beam emerges to the right. Middle, laser-driven electron acceleration in a gas-jet from a nozzle. Bottom, soft x-ray laser generation. Two laser beams are incident on the slab target, from the left, and from the top.*

mass, are used in widely different areas such as in high energy particle physics in the search for the inner constituents of matter, materials science to probe the structure of novel materials, and to study radiation damage to biological tissue. Beams of fast *ions* are used in medicine for radiation treatment of deep seated cancer tumors and in spallation related research for producing intense bursts of neutrons for studies of, for instance, nuclear phenomena and radiation damage of new materials for future fusion reactors.

The size, and consequently also the cost of particle accelerators scale with the desired particle kinetic energy. Accelerators with output energies on the GeV level are typically several hundred meters long. To shrink the size of these machines, one needs to increase the accelerating fields. State-of-the-art superconducting radio-frequency technology currently facilitates accelerating electric fields up to 50 MV/m, but is limited due to ionization of the inner walls of the accelerator structure. As already mentioned, and as will be shown in Chapter 3 and 4, extremely large electric fields can be generated in laser-produced plasma, and in a plasma accelerator particles can be accelerated to interesting energies in lengths that are measured in terms of millimeters, or even micrometers.

Laser-plasma particle accelerators

Two different types of plasma accelerators are studied in this thesis. The first kind is described in Chapter 3 and is used for acceleration of protons and heavy ions. In the experiments described there, a high power laser pulse is tightly focused on the surface of a thin metallic foil. The intense laser-plasma interaction that follows generates a cloud of hot electrons that surrounds the foil and sets up strong quasi-static electric fields at its surfaces. These fields prevail long after the laser pulse has passed and initiate a rapid plasma expansion in which ions are accelerated to multi-MeV energies over a distance of only a few micrometers. This extremely compact source of energetic ions has a number of unique characteristics that distinguish it from conventional sources, such as an ultrashort bunch duration and an exceptionally low emittance[1] [1]. Typically, laser-accelerated ions have a continuous energy distribution that range from almost zero up to a cut-off maximum energy. These ions are emitted in a well defined beam which is directed along the normal direction of the target foil and has an energy dependent divergence angle that decreases with increasing ion energy. Laser-accelerated protons

[1]Beam emittance is an important measure of the quality of a particle beam. It is the area occupied by the beam particles in momentum phase-space. Loosely one could say it is a measure of the focusability of the beam. As such, it is a particle beam analogue to the M^2 measure of the quality of a laser beam in optics.

have already been used to probe transient electric and magnetic fields in dense, laser-produced plasmas [2]. Many other applications of this potentially very compact source of fast ions include ion radiotherapy for cancer treatment [3] and isotope production for medical imaging techniques [4]. A very interesting proposal is to make use of the very high ion densities during the initial stages of the acceleration, and focus the ion beam into the core of a highly compressed deuterium-tritium plasma to ignite a fusion reaction, according to the fast ignition approach to laser-driven inertial confinement fusion [5]. Moreover, the low emittance of the laser-accelerated ion beams makes it an interesting prospect to investigate laser-driven injectors for large conventional ion accelerators [6].

Experimental studies of another important laser-acceleration technique, namely laser-wakefield acceleration, is described in Chapter 4. In these experiments, beams of energetic electrons are generated by focusing intense laser pulses into a gas target. As an intense laser pulse propagates through the tenuous plasma and expels electrons from regions of high intensity, it excites a plasma wave oscillation in its wake. In this plasma wave, strong electric fields are generated and background plasma electrons can be accelerated to several hundred mega-electronvolts in only a few millimeters. An important difference to the ion acceleration mechanism described in Chapter 3, is that the electrons acquire kinetic energies comparable to their rest mass energy during an early stage of the acceleration. Hence, they propagate at velocities close to the speed of the laser pulse in the plasma and can therefore be accelerated over relatively long distances. Recently, a new regime of laser-wakefield acceleration has been identified (the so-called 'bubble' regime) that results in high quality ultrashort electron bunches with narrow energy spread and low divergence. The experimental verification of this novel type acceleration has spurred significant interest worldwide. There are many envisioned applications of laser-accelerated electron beams. One example is short pulse and low emittance, laser-driven injectors for large conventional accelerators. Another important application is to use the electron beams to produce electromagnetic radiation with frequencies ranging from the terahertz regime [7] to x- and γ-rays [8].

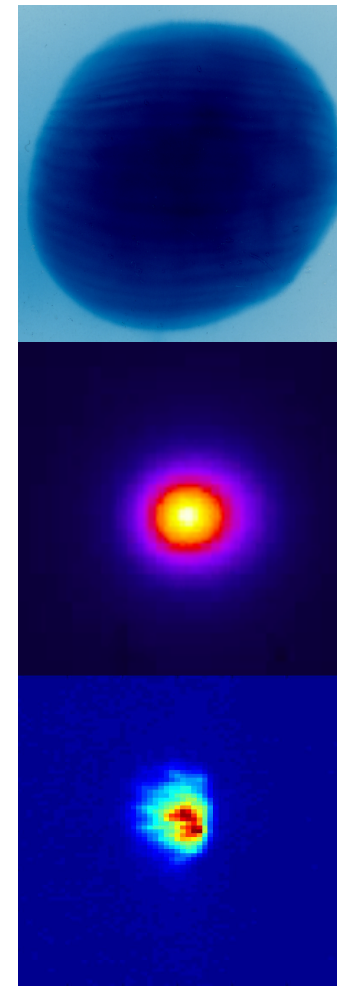

Figure 1.2. *Unprocessed raw data showing laser-driven beams of, from top to bottom, protons, electrons and coherent x-rays.*

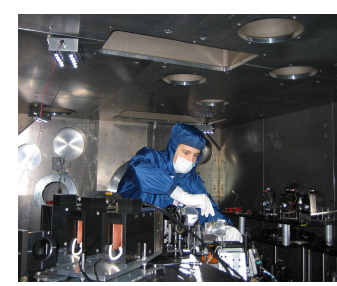

Figure 1.3. *Photograph, showing the author inside the Vulcan Petawatt interaction chamber during work on the experiments reported on in Papers **VII**–**X**.*

Short wavelength radiation generation

An important application of energetic electron beams is to generate short wavelength radiation. X-rays, produced by electrons interacting with bulk matter are used in hospitals for radiography and for cancer treatment. Short wavelength radiation, ranging from the deep ultraviolet to the x-ray regime, are produced in undulators and bending magnets at synchrotron radiation facil-

ities, and is used in many different applications, for example in crystallography to develop new curing drugs.

Laser-driven sources of *coherent* radiation in the extreme ultraviolet (XUV) region have been developed since the mid-eighties and several different approaches exist. In particular, Chapter 5 describes experimental investigations of a novel design for plasma based soft x-ray lasers, the so-called grazing incidence pumping scheme. In this scheme, two intense laser pulses are focused on a solid slab target. The first laser pulse ionizes the target and initiates a plasma expansion while the second pulse, arriving only a short time later, heats the plasma and establishes population inversion between low lying levels in highly charged ions. Lasing starts from spontaneous emission and is amplified in a single pass through the plasma. Presently, soft x-ray lasers are developing rapidly since this novel scheme facilitates studies using high-repetition rate university scale laser systems.

Organization of the thesis

The aim of the efforts over the past four years, the results of which have now been condensed to this thesis, have primarily been the investigation of laser-driven acceleration of ions and electrons. This part of the work was distributed over many experimental campaigns of different lengths, ranging from a few weeks to several months and using different laser systems. In addition, in one very important experiment, a soft x-ray laser at 10 Hz repetition rate was demonstrated.

This thesis is based on sixteen published papers, ten of which reports on experiments on laser-driven ion acceleration (Papers **I**-**X**), three on laser-driven electron acceleration (Papers **XI**-**XIII**) and three reporting on the soft x-ray laser experiment (**XIV**-**XVI**).

A short description of the high-power laser systems that have been used for the experiments is given in Chapter 2. Chapter 3 constitutes a large fraction of the thesis in which many aspects of laser-acceleration of protons and heavy ions are discussed, such as the scaling with laser pulse and target parameters, influence of prepulses and possibilities for gaining active optical control of the acceleration. Chapter 4 describes important and topical experimental findings regarding the acceleration of quasi-monoenergetic electron beams. Chapter 5 presents results from the x-ray laser experiment. Finally, in Chapter 6, the work within the thesis is put in perspective to the current progress of the field.

Chapter 2

High-power lasers

Two different laser systems were used in most of the experiments presented in Papers **I** to **XVI**, the Lund multi-terawatt laser, placed at Lund University in Sweden, and the Vulcan Petawatt laser, placed at the Rutherford-Appleton Laboratory in the United Kingdom. Both systems are based on the chirped pulse amplification (CPA) technique [9] but are otherwise very different. The Lund multi-terawatt laser produces very short pulses at high repetition rate while the Vulcan Petawatt laser, currently the most powerful laser in the world, delivers extremely energetic pulses but with longer durations and at significantly lower repetition rates as compared to the Lund system. A comparison of important characteristics of the two systems is presented in Table 2.1. Overview descriptions of the laser systems are given in Secs. 2.1 and 2.2. An important fact to consider when discussing experiments using this class of high power lasers is that, due to the very large gain and *amplified spontaneous emission* (ASE) in the laser amplifiers, the main high-power ultrashort laser pulse sits on top of a low-power nanosecond pulse. When focused, this ASE *pedestal* can become so intense that it ionizes the irradiated target and significantly changes the interaction conditions prior to the arrival of the main pulse. Several experiments discussed in this thesis aimed at investigating the effects of ASE. The results from these studies are presented in Papers **I**, **II**, **III** and **XIII**. Moreover, the experiments presented in Papers **IV**, **V** and **VI** were profoundly dependent on techniques to reduce the influence of ASE. Section 2.3 gives brief descriptions of the methods used to limit and control the ASE pedestal.

	Lund TW	Vulcan PW
Peak power	35 TW	1 PW
Energy	1 J	400 J
Pulse duration	30 fs	400 fs
Repetition rate	10 Hz	1 shot/20 min
Average power	10 W	0.3 W
Wavelength	800 nm	1053 nm
Bandwidth	30 nm	5 nm
Beam diameter	50 mm	600 mm
Focused intensity	$> 10^{19}$ W/cm^2	up to 10^{21} W/cm^2
Intensity contrast ratio	10^9	10^7
Used in Papers	**I**–**V**, **XI**–**XVI**	**VI**–**X**

Table 2.1. *Comparison of the output characteristics of the Lund multi-terawatt and the Vulcan Petawatt laser systems. Both systems were used in the experiments described in this thesis.*

2.1 The Lund multi-terawatt laser

Most of the experiments described in this thesis (Papers **I**–**V** and **XI**–**XVI**) were performed using the multi-terawatt laser at the Lund High Power Laser Facility in Sweden. This laser system operates at 10 Hz, has a central wavelength of 800 nm and is capable of delivering pulses with durations down to 30 fs and energies of more than 1 J to the experiment. It is a standard CPA system [10], based on titanium doped sapphire (Ti:Sapphire) as amplifying medium. Ti:Sapphire is well suited for the generation and amplification of ultrashort pulses since the material supports a large spectral bandwidth. The laser system is to a large extent operated by doctorate students and a significant fraction of the work during this thesis has been devoted to the operation, maintenance and various upgrades of this laser system.

A schematic view of the system is shown in Fig. 2.1. The front end is a Kerr-lens modelocked oscillator [11] which produces a train of 5 nJ pulses. These pulses are amplified in a multipass configuration and cleaned with a saturable absorber, as described in Sec. 2.3, before they are stretched to ∼300 ps in a grating stretcher. A pulse picker selects one pulse from the train which is amplified in three steps: first in a regenerative amplifier and then in two consecutive multipass amplifiers. Finally, the laser beam is expanded to a diameter of 50 mm and the pulses compressed in a grating compressor under vacuum (not shown in Fig. 2.1). These amplifiers are pumped by frequency doubled, Q-switched Nd:YAG lasers, and a total energy of ∼7 J at a wavelength of 532 nm is used to pump the three amplifiers. Before the final pass in the last amplifier, a polarizing beamsplitter extracts a fraction of the main beam that is sent via a separate path to the experiment. The relative energies in the two pulses are controlled by rotating

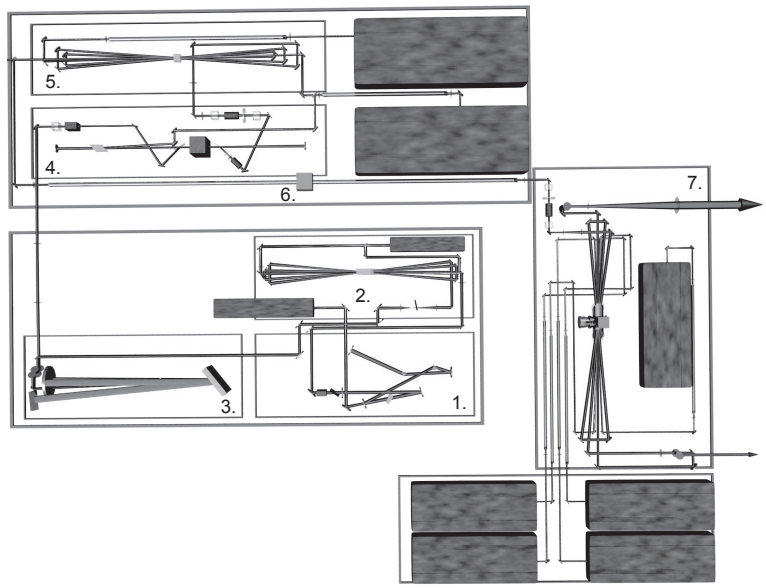

Figure 2.1. *Schematic view of the Lund multi-terawatt laser system. 1. Oscillator. 2. Preamplifier and saturable absorber for contrast enhancement. 3. Stretcher. 4. Regenerative amplifier and two Pockels cell and polarizer assemblies for temporal cleaning from the ASE pedestal. 5. Multipass amplifier. 6. Vacuum spatial filter. 7. Cleaning Pockels cell and cryogenically cooled multipass amplifier. Before the final pass through the amplifier, an adjustable fraction of the laser pulse is extracted using a polarizing beamsplitter. The two beams are sent to separate compressors and the experimental chamber (not shown).*

a half-wave plate in front of the polarizer.

This secondary beam has been used in a variety of ways. In the experiments described in Papers **XIV**, **XV** and **XVI**, the laser pulse remained uncompressed and was used to create a highly ionized, expanding plasma prior to the arrival of the compressed laser pulse. To facilitate the plasma wave measurements described in Sec. 4.3.7, the pulse was compressed in a separate compressor (not shown in Fig. 2.1) and frequency doubled before it was sent to the interaction chamber. A slightly different configuration was used in the experiment described in Paper **IV**, when a fraction of the energy from one of the pump lasers was redirected along this beam path and used to drive a shock wave through a thin target foil.

2.2 The Vulcan Petawatt laser

The Vulcan Petawatt laser is built at the Central Laser Facility, Rutherford-Appleton Laboratory, in the United Kingdom. The laser system, and the facilities that are used for experimentation, are managed as a national scale user facility and are very different from the less powerful, but more configurable laser system in Lund. The Vulcan laser has two short-pulse arms with separate interaction facilities. One arm delivers pulses with peak powers up to 100 TW (100 J, 1 ps) and was used for the experiment described in Paper **VI**. The Vulcan Petawatt arm (400 J, 400 fs) is briefly described here and was used for the experiments described in Papers **VII**−**X** and in Sec. 3.4.4. When the 600 mm diameter beam is focused by a 1.8 m focal length, $f/3$ off-axis parabolic mirror, intensities up to 10^{21} W/cm^2 are generated. Detailed descriptions of the Vulcan Petawatt laser are given in [12, 13].

The front end of the laser system is a Kerr lens modelocked Ti:Sapphire oscillator, which is tuned to operate at a central wavelength of 1.053 μm. A pulse picker selects a single pulse for amplification which is stretched in a grating stretcher to a duration of ∼2.5 ns. The first amplifier in the system is based on optical parametric chirped pulse amplification (OPCPA) in BBO. OPCPA can provide uniform gain over a much larger spectral bandwidth than ordinary Nd:glass amplifiers and gain narrowing is thereby mitigated during this early stage amplification [14–16].

To prevent gain narrowing in the subsequent amplification stages, two types of Nd:glass, with slightly different gain profiles, are used as amplifying medium. The laser beam diameter is gradually increased as the laser pulse energy increases during amplification in several different stages. Starting with rod amplifiers with diameters 9 mm, 16 mm, 25 mm, and 45 mm, the pulse is then amplified in several disc amplifiers with diameters 108 mm and 208 mm, before it is spatially cleaned in a vacuum spatial filter and expanded to its final diameter of 600 mm. The laser pulse is compressed in a grating compressor, placed inside a vacuum chamber, with a grating separation of 13 m, and pulses with energies up to 400 J and pulse durations down to 400 fs are delivered to the experiment in the interaction chamber.

The Petawatt target area was recently upgraded to facilitate the experiment that is described in Sec. 3.4.4. This experiment required a nanosecond laser pulse with an energy up to 100 J to irradiate the target prior to the short pulse interaction. For this purpose, one of the six Vulcan nanosecond long pulse beams, with a diameter of 200 mm, was redirected into the Petawatt target area and used for this experiment.

2.3 Amplified spontaneous emission

The amplifier chains in high power laser systems, such as the ones described in Sec. 2.1 and 2.2, typically have a total gain between 10^9 and 10^{11}. However, once population inversion has been established, the amplifier crystals emit a small amount of light through spontaneous emission before the seed laser pulse extracts the stored energy. Spontaneous emission occurring in the early stages of the amplification chain can be amplified to significant energies in the subsequent stages and, normally, the high intensity femtosecond laser pulse sits on top of a low intensity nanosecond pulse. Once focused, it can reach intensities significantly above the ionization threshold of the irradiated target material. Therefore, the intensity *contrast ratio*, between the high intensity main laser pulse and the Amplified Spontaneous Emission[1] (ASE) is a very important characteristic of all high power lasers.

During the work presented in this thesis, considerable efforts were made to develop alignment and optimization techniques to minimize, but also control, the amounts of ASE emanating from the Lund multi-terawatt laser system. These are briefly described below.

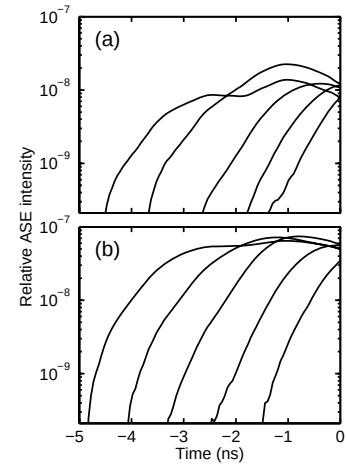

Figure 2.2. *ASE pulse preceding the main laser pulse, measured using a fast photodiode, for different timings of the gating Pockels cells and for two different seed energies to the regenerative amplifier. In (a) the seed energy was 63 pJ, and in (b) it was 10 pJ. Each diode measurement has been normalized to corresponding third-order autocorrelator measurements of the pulse contrast, 100 ps before the main pulse.*

ASE duration and intensity

On the nanosecond timescale, the ASE pedestal is diagnosed by a fast photodiode and a high bandwidth oscilloscope. Three synchronized Pockels cells, with risetimes of 1.0 ns and installed at positions shown in Fig. 2.1, are used together with polarizers to gate the main laser pulse and suppress the ASE pedestal. By changing the timings of these optical gates, the duration of the ASE pedestal is controlled, as shown in Fig. 2.2.

On a picosecond time scale, the temporal pulse shape is diagnosed by a high dynamic range, third-order scanning autocorrelator. An example of a temporal profile is shown in Fig. 2.3, measured under conditions described in Sec. 2.3. On this timescale, the laser intensity is reasonably constant, until it starts rising 20 ps before the main pulse. In all Papers, the intensity contrast ratio of the Lund laser is stated 100 ps before the main pulse. As shown in Fig. 2.2 and in the inset in Fig. 2.3, the intensity contrast ratio is highly dependent on the energy that seeds the regenerative amplifier. Positioned at the oscillator output, the system incorporates an acousto-optic programmable dispersive filter (Dazzler [17]). Normally, it is used to precompensate for high-order dispersion and gain narrowing in the amplifier chain, but it can also be used as a programmable attenuator, to control the contrast ratio of the laser system, as shown in Fig. 2.3(a).

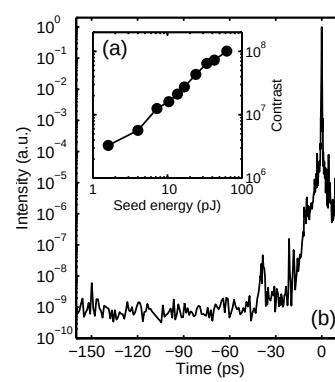

Figure 2.3. *(a) By controlling the seed energy to the regenerative amplifier, it is possible to control the amplified pulse contrast. (b) Third-order autocorrelation measurement of the laser pulse shape. By using the preamplifier and saturable absorber, a contrast of* 10^9 *is achieved.*

[1] ASE is a result of spontaneous decay of excited states in the amplifier crystal. In an optical parametric amplifier there are no excited states. The equivalent of ASE in an OPCPA system is called *parametric flourescence*.

These techniques for controlling the duration and intensity of the ASE pedestal were used for parametric investigations of the influence of the ASE, the results of which are discussed in Papers **I**, **II**, **III** and **XIII**.

Saturable absorber for pulse cleaning

The measurements presented in Fig. 2.3(a) suggest that, increasing the seed energy beyond 100 pJ would result in a contrast of more than 10^8. For this reason, a multipass amplifier with a gain of more than 10^3 was installed between the oscillator and the stretcher. To remove any ASE that is generated in this amplifier, the amplified pulses are sent through a saturable absorber (RG850), which has a saturated transmission of ∼10%, before they are sent to the stretcher. The purpose of the RG850 filter is to absorb the low intensity ASE in front of the pulse, but to transmit the intense main pulse. With this setup, the contrast is increased to 10^9, as shown in Fig. 2.3, which is exceptional for this class of laser systems. This technique for improving the contrast, was essential for the experiment described in Paper **IV**.

Plasma mirrors

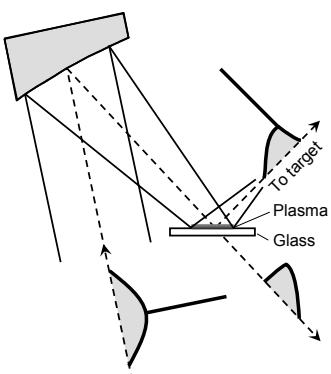

Figure 2.4. *Working principle of plasma mirrors for contrast enhancement. A low-contrast laser pulse is loosely focused on a glass substrate. The low intensity ASE pedestal is transmitted while the intense main pulse ionizes a thin layer at the surface of the substrate which switches the reflectivity. The plasma mirror reflects the high intensity part of the pulse which now has a significantly improved contrast ratio.*

A plasma mirror can be used to improve the pulse contrast beyond 10^9, but at the expense of a large fraction of the laser energy. The schematic illustration in Fig. 2.4 shows the design that was used in the experiments presented in Sec. 3.4.4 and in Papers **V** and **VI**. A converging laser beam is intercepted by an optically flat glass substrate, which is tilted for p-polarized irradiation close to the Brewster angle and reflects the laser beam to the target. The area of the beam on the substrate is adjusted so that the intensity of the ASE pedestal is well below the plasma formation threshold of the glass and is transmitted. When the intensity of the rising edge of the main pulse exceeds the ionization threshold (∼10^{14} W/cm^2 [18]), it quickly ionizes the atoms at the surface of the glass. This forms a thin layer of overdense plasma on the surface of the mirror, which efficiently reflects the high intensity part of the main pulse [19] (Sec. 3.1.3). It is important that ionization occurs only a few picoseconds before the peak of the pulse so that the plasma has no time to expand and develop instabilities that imprints phase errors on the reflected laser beam [20]. The contrast enhancement is given by the ratio between the reflectivity of the overdense plasma (∼50%) and the Fresnel reflectivity of the unperturbed substrate (∼0.5%). A higher contrast enhancement is therefore obtained if the glass substrate is antireflection coated. In the experiment described in Paper **V**, we estimated the reflected pulse contrast to an exceptional ∼10^{10}.

Chapter 3

Proton and heavy ion acceleration

Ion acceleration, driven by intense laser-plasma interactions, has been studied for more than two decades. In early experiments (for a review, see [21]), protons and carbon ions were accelerated to energies of the order of tens of keV in the isotropic plasma expansion following the irradiation of solid slab targets by long pulse (nanosecond) lasers at focused intensities of approximately 10^{16} W/cm^2.

In the year 2000, laboratories in the USA and the UK, reported observations of laminar *beams* of protons and highly charged ions, with energies up to many tens of MeV, emerging from the interactions of sub-picosecond ultraintense laser pulses with thin foil targets at intensities exceeding 10^{19} W/cm^2 [22–25]. These *unexpected* observations sparked significant international interest and several, sometimes conflicting, theories describing the mechanisms involved appeared in scientific journals. Since then, the field has matured through significant experimental and theoretical activities, to which the work on this thesis attempts to contribute. It is by now widely accepted that, as described in Sec. 3.2, the acceleration is driven by exceptionally high electrostatic fields that are generated at the surfaces of the thin foil [26, 27], which ionizes and accelerates a thin layer of atoms on its surfaces, forming a beam of multi-MeV ions.

This chapter discusses the generation and characterization of laser-accelerated beams of protons and highly charged ions. Section 3.1 gives an overview of relativistic laser-plasma interactions. Section 3.2 describes a very important mechanism, the target normal sheath acceleration. Many of the techniques that we have used for laser-plasma, and ion beam characterization are described in Sec. 3.3. Section 3.4 summarizes the main results from Papers

I to **X**. The sections and papers (within parenthesis) have been ordered according to the following logic. Sections 3.4.1 to 3.4.4 (**I** to **VIII**) treat the acceleration of protons while Secs. 3.4.6 and 3.4.7 (**IX** and **X**) concern heavy ion acceleration. The experiments in Secs. 3.4.1 to 3.4.3 (**I** to **V**) were done using the Lund multi-terawatt laser and the experiments described in Secs. 3.4.4 to 3.4.7 (**VI** to **X**) were done using the Vulcan Petawatt laser.

3.1 Relativistic laser-plasma interactions

Note that, *throughout this thesis, only linearly polarized laser pulses have been used, and all discussions, derivations and formulas etc. relating to intense laser-plasma interactions concern linear polarization.*

This section considers ultra-intense ($> 10^{19}$ W/cm^2) laser-plasma interactions that are relevant to ion acceleration. Section 3.1.1 starts with a relatively simple description of the motion of a single electron subjected to an infinite plane wave. It is found that, for typical intensities, the quiver (or ponderomotive) energy of the electron in the laser field can easily exceed its rest mass energy and therefore its motion is dominated by relativistic effects. In Sec. 3.1.2 it is demonstrated that, for a tightly focused laser pulse, the intensity variations, and the corresponding variations of the electron quiver energy lead to a strong time-averaged force (the ponderomotive force) acting on the particle and that this force can accelerate electrons to considerable kinetic energies. Next, in Sec. 3.1.3, the collective response of a plasma containing a large number of electrons is considered. It is found that the electron number density has a major influence on the laser propagation through the plasma and, in particular, two regimes of propagation are identified, separated by a critical density. In the experiments described in this chapter, a laser pulse is focused onto a thin solid foil target which, when ionized, has an overcritical electron number density. An important aspect of the interaction is that, at an intensity of the order of 10^{19} W/cm^2, a large fraction of the laser pulse energy can be converted into a beam of relativistic electrons that is directed into the bulk of the target foil. Section 3.1.4 gives an overview of the most important mechanisms for the generation of this hot electron beam and Sec. 3.1.5 discusses electron transport through the target. When the electrons exit the rear side of the thin foil, the induced charge separation results in a large electrostatic field that is capable of accelerating ions to the multi-MeV range in only a few μm. This is the Target Normal Sheath Acceleration (TNSA) mechanism, discussed in Sec. 3.2. A numerical model of the acceleration mechanism is discussed extensively in Sec. 3.2.1. Other mechanisms than TNSA may also lead to ion acceleration, but for the laser intensities and target configurations in Papers **I** to **X**, TNSA is likely to be the dominant mechanism. For an overview of alternative acceleration mechanisms, see for example [28].

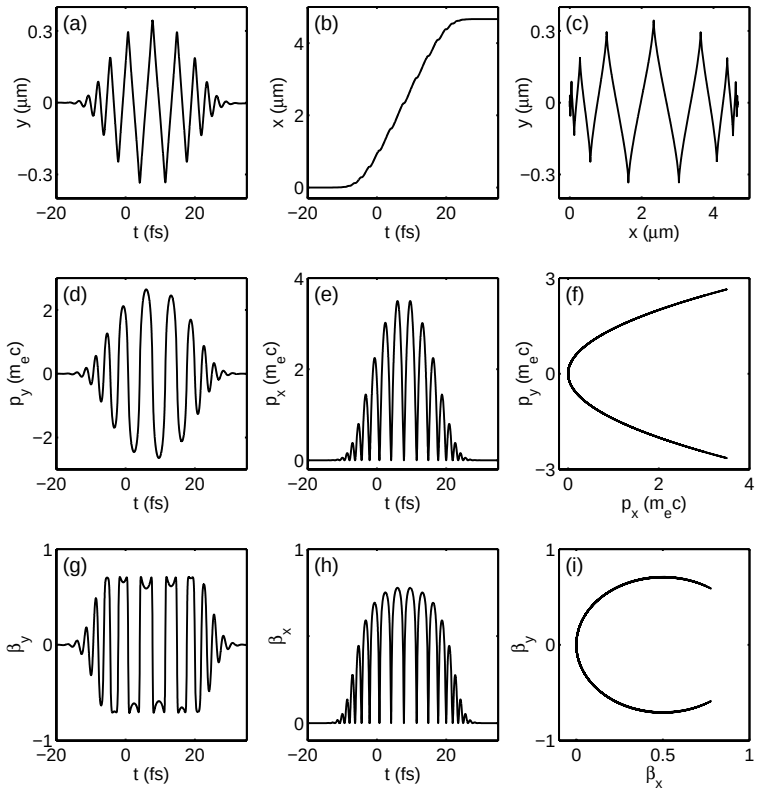

Figure 3.1. *Trajectory of an electron, driven by an ultra-short, linearly polarized laser pulse with a peak intensity of* 1.5×10^{19} *W/cm*^{2}*. (a)-(c) Transverse (y) and longitudinal (x) electron position. (d)-(f) Transverse* (p_y) *and longitudinal* (p_x) *electron momentum. (g)-(i) Transverse* (β_y) *and longitudinal* (β_x) *velocity, normalized to the speed of light.*

3.1.1 Motion of a single electron in the laser field

The motion of a free electron with charge $-e$ and mass m in the external electric and magnetic fields, $\mathbf{E}$ and $\mathbf{B}$, of the light wave, is described by the Lorentz force equation,

$$\frac{d\mathbf{p}}{dt} = -e\left(\mathbf{E} + \mathbf{v} \times \mathbf{B}\right) , \tag{3.1}$$

where $\mathbf{p} = \gamma m \mathbf{v}$ is the electron momentum, and $\gamma = \sqrt{1 + (|\mathbf{p}|/mc)^2} = 1/\sqrt{1-\beta^2}$ is the relativistic factor and $\beta = v/c$ is the electron velocity in terms of the speed of light. The electron trajectory depends on the polarization state of the laser pulse [29], but only linearly polarized laser pulses are considered here. For a plane wave in vacuum, $|\mathbf{B}| = \frac{1}{c}|\mathbf{E}|$ and two regimes of interaction can be directly identified from Eq. 3.1. In the non-relativistic case ($v \ll c$) the dominant force acting on the electron is the electric field component of the wave and the electron os-

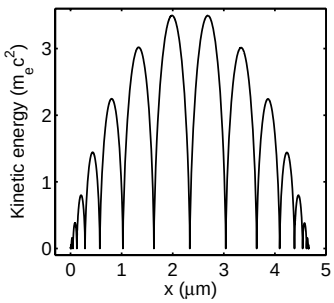

Figure 3.2. *Kinetic energy of the electron in the simulation in Fig. 3.1, in terms of its rest mass energy and as a function of its longitudinal position.*

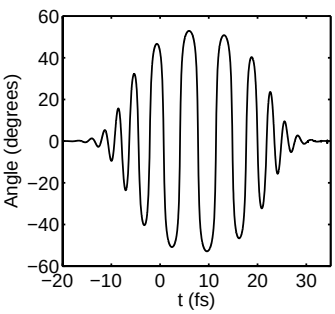

Figure 3.3. *Angle of the electron velocity vector, with respect to the laser polarization axis.*

cillates only along the polarization direction. However, for very strong fields, the speed of the oscillating electron approaches c and the magnetic component of the Lorentz force may become very important. The main effect of the $v \times B$ force is to push the particle forward, along the Poynting vector of the wave.

Figure 3.1 shows the results from a numerical integration of Eq. 3.1 where the electron, initially at rest, is subjected to a linearly polarized laser pulse with a peak intensity of 1.5×10^{19} W/cm^2 and wavelength of 800 nm. For clarity, the pulse duration is only 8 fs (FWHM). The laser propagates along $\hat{\mathbf{x}}$ and has a linear polarization along $\hat{\mathbf{y}}$. The transverse momentum p_y oscillates with the frequency of the laser field whereas the forward directed momentum p_x oscillates with twice this frequency. During each oscillation the electron is pushed forward, but remains at rest after the laser pulse has passed. The net effect is therefore just a forward translation and the electron does not gain energy from the laser field. Fortunately, in most experimental situations, the laser field is not an infinite plane wave, but a tightly focused laser pulse. Under such conditions, as will be shown in the next section, the electron can gain a significant amount of energy. In the simulation in Fig. 3.1, the peak of the laser pulse passes the initial position of the electron at $t = 0$. Since the electron moves in the forward direction, together with the laser pulse, the peak of the laser pulse passes the electron at a later time. This effect actually induces a Doppler down-shift of the frequency of the field that is perceived by the moving electron. Although the kinetic energy of the electron at the peak of the interaction exceeds the rest mass of the electron several times; see Fig. 3.2, the transverse and the longitudinal velocities each never exceed $0.7c$. The reason is that the $\mathbf{v} \times \mathbf{B}$ component of the Lorentz force shifts the velocity vector of the electron away from the polarization axis, as shown in Fig. 3.3.

In the non-relativistic limit ($v \ll c$) and for a linearly polarized laser pulse, $\mathbf{E}(x,t) = \hat{\mathbf{y}} E_0 \cos(\omega t - kx)$, we can ignore the $\mathbf{v} \times \mathbf{B}$ component and integrate Eq. 3.1 to obtain the momentum of the electron, $p = -(eE_0/\omega)\sin(\omega t - kx)$. We recall that the kinetic energy of the electron is $p^2/2m$ and that, in vacuum, the intensity and wavelength of the laser light wave are $I = c\epsilon_0 E^2/2$ and $\lambda = 2\pi c/\omega$, respectively. The average electron kinetic energy, or the *ponderomotive* energy, during one laser cycle can then be written

$$U_p = \frac{e^2 I_0 \lambda^2}{8\pi^2 \epsilon_0 m c^3}\,, \tag{3.2}$$

where I_0 is the intensity of the laser field. A more rigorous derivation gives the ponderomotive energy in the relativistic case [30],

$$U_p = mc^2 \left(\sqrt{1 + \frac{e^2 I_0 \lambda^2}{4\pi^2 \epsilon_0 m^2 c^5}} - 1 \right)\,. \tag{3.3}$$

For a laser wavelength of 800 nm, the ponderomotive energy becomes equal to the electron rest mass (511 keV) at an intensity of 1.3×10^{19} W/cm^2. At the highest intensity that was used for experiments in this thesis, 6×10^{20} W/cm^2 at 1.053 μm (Paper **VII**), the quiver energy of the electron in the laser field is 15 times higher than the rest mass. Note that, even at this intensity, representing the state-of-the-art of present day laser technology, the ponderomotive energy of a proton is only 0.004% of its rest mass energy. For this reason, ions are often regarded as stationary on the time scale of a single laser oscillation. However, the collective displacement of a large number of electrons interacting with the laser pulse may give rise to strong electric and magnetic fields that vary on the time scale of the pulse duration. On these longer time scales, also ions can be accelerated to multi-MeV energies, as discussed in Sec. 3.2.

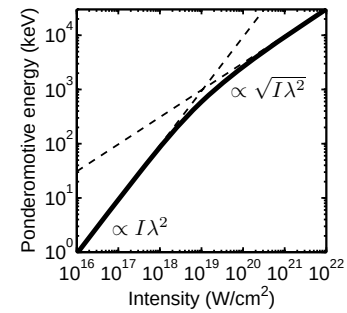

Figure 3.4. *Ponderomotive energy as function of laser intensity at a wavelength of 1 μm. At intensities below 10^{18} W/cm^2, U_p scales as $I\lambda^2$ while at intensities above 10^{20} W/cm^2, it scales as $\sqrt{I\lambda^2}$.*

3.1.2 The ponderomotive force

In a homogeneous field, no net momentum can be gained by a free electron. In a tight laser focus, the intensity distribution is far from homogeneous and the electron experiences a weaker restoring force at the outer endpoint of the oscillation. Therefore it does not return back to its initial position and is expelled from regions of high intensity. The ejection of electrons from a tight laser focus is illustrated in Fig. 3.5, showing the results from a numerical integration of Eq. 3.1. The electrons are initially at rest but at different starting positions relative to the central axis of the laser pulse. The electron starting exactly on the laser axis returns to rest after the laser pulse has passed while all other electrons are ejected from the laser focus at some angle. Note, that these simulations show the interactions of single particles and Coulomb interactions between the electrons are not included.

The ejection angle, with respect to the laser propagation axis, is determined by the ratio between the transverse and longitudinal momentum of the electron and can be derived from Eq. 3.1 [31, 32],

$$\theta = \arctan\left(\frac{p_y}{p_x}\right) = \arctan\sqrt{\frac{2}{\gamma - 1}}\,. \tag{3.4}$$

Figure 3.6 shows the resulting angular distribution from the simulation in Fig. 3.5 (symbols) which is in perfect agreement with Eq. 3.4 (solid lines).

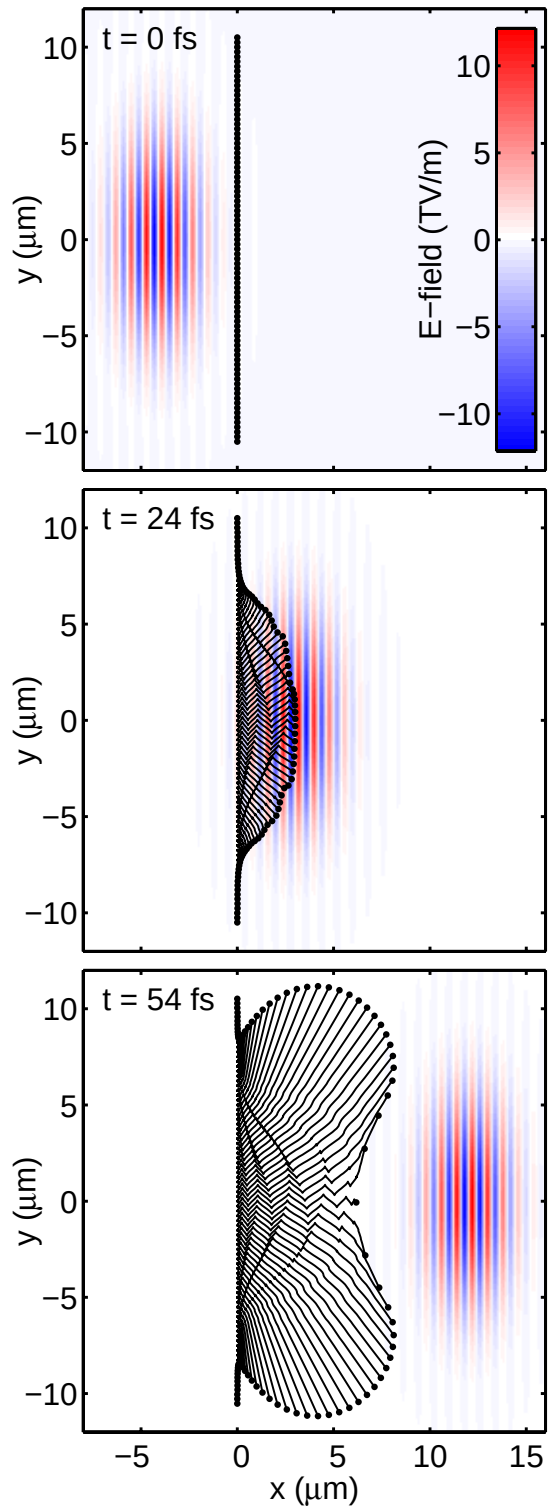

Figure 3.5. *Electron trajectories for a focused laser pulse. The laser field is polarized along the vertical axis, has a wavelength of 800 nm, a pulse duration of 8 fs (FWHM), is focused to a 6 μm (FWHM) spot and has a peak intensity of* 2×10^{19} *W/cm*^{2}*. The electric field strength of the laser pulse is indicated by the color scale while the solid lines show the time history of the position of the electrons (indicated at each time by solid circles).*

As the electrons oscillate in the laser field, there is a time averaged gradient force, the *ponderomotive force*, pushing the particles out from regions of high intensity. Derivations of the ponderomotive force can be found in text books on laser-plasma interactions, for instance in [33]. Under a slowly varying envelope approximation of the laser intensity distribution, I, and for weak fields ($\gamma \approx 1$), the ponderomotive force on a single particle with charge q and mass m can be written:

$$\mathbf{F}_{pond} = -\frac{q^2}{8\pi^2\epsilon_0 m c^3}\nabla(I\lambda^2)\,. \tag{3.5}$$

Three main conclusions can be drawn from Eq. 3.5. These are that the ponderomotive force (1) has no polarization dependence, (2) has no dependence on the sign of charge and (3) always expels particles from regions of high intensity.

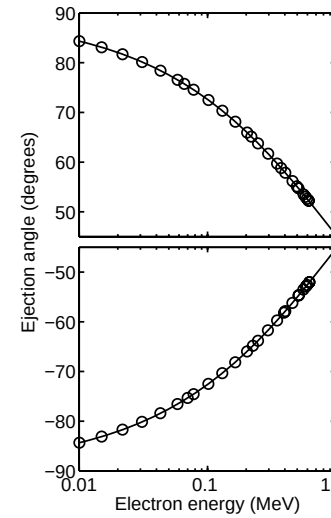

Figure 3.6. *Electron ejection angle with respect to the laser propagation axis as a function of scattered electron energy. The results from the simulation in Fig. 3.5 (circles) are in perfect agreement with the predictions of Eq. 3.4 (solid lines).*

3.1.3 Light propagation in a plasma

In a plasma, the collective motion of a large number of electrons leads to self-generated electric and magnetic fields that influence the dynamics over long distances. If the plasma electrons are displaced relative to the ion background by a perturbation, such as for example the ponderomotive force, a restoring electrostatic force builds up due to the induced charge separation. When the perturbation is over, the electrons recoil and oscillate around their equilibrium positions. The force acting on the electrons is $m_e\ddot{\mathbf{r}} = -e\mathbf{E}$. Assuming a small density perturbation and a harmonic plane wave, we write the electric field as $\mathbf{E} = E_0\cos(kx - \omega t)\hat{\mathbf{x}}$. The current density is $\mathbf{J} \equiv -en_e\dot{\mathbf{r}}$ giving,

$$\frac{\partial^2\mathbf{E}}{\partial t^2} = -\omega^2\mathbf{E}, \quad \nabla^2\mathbf{E} = -k^2\mathbf{E}, \quad \frac{\partial\mathbf{J}}{\partial t} = en_e\left(\frac{e\mathbf{E}}{m_e}\right)\,. \tag{3.6}$$

For a small density perturbations, the wave equation, derived from the Maxwell equations [34], becomes

$$\nabla^2\mathbf{E} - \frac{1}{c^2}\frac{\partial^2\mathbf{E}}{\partial t^2} = \mu_0\frac{\partial\mathbf{J}}{\partial t}\,. \tag{3.7}$$

Inserting 3.6 into 3.7 gives the plasma wave dispersion relation

$$\omega^2 - \omega_p^2 = k^2c^2\,, \tag{3.8}$$

where

$$\omega_p = \sqrt{\frac{e^2n_e}{\epsilon_0 m_e}} \tag{3.9}$$

is the *plasma frequency*. The plasma frequency is the natural oscillation frequency of the plasma. The plasma electrons are able

to follow an external perturbation that varies with a frequency lower than this. Hence, an electromagnetic wave with a frequency $\omega < \omega_p$ cannot propagate in the plasma since the plasma electrons are able to shield the laser field. When $\omega > \omega_p$, the plasma is transparent to the laser field since the collective response of the plasma electrons is slower than the variations of the electromagnetic wave. If the laser pulse propagates on a gradient of continuously increasing electron density, it is stopped and reflected at a density where the plasma frequency equals the laser frequency. This is the *critical density*,

$$n_c = \frac{\epsilon_0 m_e \omega^2}{e^2}\,. \tag{3.10}$$

Numerical example. *The critical density for a laser wavelength of 800 nm is* 1.7×10^{21} cm^{-3}. *The corresponding value for 1.053* μm *is* 1.0×10^{21} cm^{-3}.

The critical density divides plasma in two categories, *underdense* plasmas, where $n_e < n_c$ and the laser can propagate, and *overdense* plasmas, where $n_e > n_c$ and the plasma is opaque to the laser beam. For relativistic intensities, the relativistic electron mass shift increases the critical density by a factor γ.

From the dispersion relation in Eq. 3.8 it is straightforward to deduce the phase velocity

$$v_{ph} \equiv \frac{\omega}{k} = \frac{c}{\eta} \tag{3.11}$$

and the group velocity

$$v_{gr} \equiv \frac{\partial \omega}{\partial k} = c\eta \tag{3.12}$$

of a wave in the plasma. Here, η is the refractive index

$$\eta = \sqrt{1 - \left(\frac{\omega_p}{\omega}\right)^2}\,. \tag{3.13}$$

The refractive index of a plasma is always smaller than 1. As a result, the phase velocity is larger than c, while the group velocity is smaller than c. Plasma waves and laser propagation in underdense plasmas are discussed at length in Chapter 4. In the remainder of this chapter we will concentrate on the interaction between an intense laser pulse and a thin foil solid density target that forms an overdense plasma upon ionization.

3.1.4 Electron heating at relativistic intensities

Laser plasma interactions at solid density are usually intricate to analyze. A large variety of non-linear effects associated with collective electron dynamics results in a complex picture of the interaction. However, it turns out that several tens of percent of the laser energy can be efficiently converted into a *beam* of MeV electrons going into the target. This is in contrast to collisional

plasma heating which is important at lower laser intensity and results in an almost *isotropic* electron velocity distribution. Collisional absorption is crucial for the realization of the soft x-ray laser described in Chapter 5. At relativistic intensities, there are several processes that can lead to the generation of directed beams of hot electrons. As these different processes potentially influence each other, a complete description of the interaction can only be accessed through complex numerical simulations.

Depending on the experimental conditions, different processes become dominant. Frequently, the ASE pedestal that precedes the main laser pulse is intense enough to ionize the target and form a plasma on the target front side. When it expands into vacuum the initially steep vacuum-solid interface is modified into a smooth density profile where the electron density drops from solid density ($\sim 10^{24}$ cm^{-3}, see Table 3.1) to zero over a characteristic length. Usually this *scale length* is defined as the length after which the density has dropped by a factor $1/e$. Different interactions occur at different parts of this gradient and their relative importance varies with the shape of the gradient and the intensity, duration, polarization and angle of incidence of the laser pulse.

	Z	n_e (cm^{-3})
Al	13	0.8×10^{24}
Ti	22	1.3
Fe	25	2.1
Cu	29	2.5
Pd	46	3.1
Sn	50	1.8
Au	79	4.7

Table 3.1. *Electron densities in different solid metals used during the present thesis work.*

Ponderomotive ($\mathbf{v} \times \mathbf{B}$) acceleration

When the main laser pulse is incident on the plasma gradient, it propagates through the underdense region until it reaches the critical surface ($\sim 10^{21}$ cm^{-3}) where it is reflected. While the critical surface is initially parallel to the target, at an oblique incidence angle, it is deformed during the interaction as the ponderomotive force of the laser pulse (see Sec. 3.1.2) pushes electrons forward and sideways. Due to this effect, sometimes referred to as laser *hole boring* [35], the direction of electron acceleration is no longer only perpendicular to the target surface, but occurs in a direction between the target normal and the laser directions [36, 37]. The mean energy, or the temperature, of electrons accelerated in this way is determined by the ponderomotive energy in Eq. 3.3, repeated here in convenient units

$$T_e = 0.511 \text{ MeV} \cdot \left(\sqrt{1 + \frac{I_L \lambda_L^2}{2.74 \times 10^{18} \text{ W/cm}^2 \mu\text{m}^2}} - 1 \right). \quad (3.14)$$

The conversion efficiency from laser energy into hot electrons increases with increasing intensity and can be very high. Typically, at the intensities considered here, more than 30% of the laser energy can be converted to hot electron kinetic energy [38, 39].

Numerical example. *Assuming a conversion efficiency of 30%, a laser pulse containing 1 J of energy and focused to an intensity of 3×10^{19} W/cm^2 at a wavelength of 800 nm, generates a thermal distribution of 2×10^{12} electrons with a mean energy of 0.9 MeV.*

Note that, *following the conventions of plasma physics, throughout this thesis, temperatures are given in eV.*

Resonance absorption

Numerical example. *At a laser intensity of 9×10^{18} W/cm^2 and a wavelength of 800 nm, both resonance absorption and ponderomotive acceleration result in electron populations with temperatures of 400 keV.*

Another important process that occurs at the critical surface is resonance absorption [33]. An obliquely incident, p-polarized laser pulse is continuously refracted in a density gradient in front of a solid target. Close to the critical surface, at the point of closest approach, the laser electric field is directed along the target normal. Since $\omega_L = \omega_p$ at the critical surface, the laser resonantly drives a plasma wave to high amplitudes in this region. Eventually, the wave energy is transferred to the particles through collisions (low laser intensity) or Landau damping (high laser intensity). The result is a hot electron population propagating into the target, along the target normal and with an opening angle of approximately 30° [36]. The temperature scales as [40]

$$T_e = 100 \text{ keV} \cdot \left(\frac{I_L \lambda_L^2}{1 \times 10^{17} \text{ W/cm}^2 \mu\text{m}^2} \right)^{1/3} . \tag{3.15}$$

Note that, at normal incidence, this mechanism does not contribute to the heating.

Brunel heating

When a p-polarized laser pulse is obliquely incident on an overdense plasma with a very short scale length, of the order of the laser wavelength or even shorter, a process called Brunel heating [41] (sometimes also referred to as vacuum heating) becomes important. In vacuum, electrons would oscillate symmetrically around the laser axis, but in regions close to the critical surface of the solid, the electrons only experience the electric field of the laser during part of an oscillation cycle. During the first half cycle, the electrons are accelerated toward the vacuum, turned around and driven into the solid. Inside the solid they do not feel a restoring force anymore as the laser field cannot penetrate into the overdense regions. For the effect to be significant, there has to be a large difference between the forces acting on the electrons during the two half cycles. This means that it only works at a steep density gradient. The transverse excursion of the electron in the simulation in Fig. 3.1 is 300 nm, indicating that the scale-length of the plasma must be of the order of, or shorter than this value.

Wakefield acceleration

For very long plasma scale-lengths, the laser pulse propagates over a long distance in the plasma before it reaches the critical surface. The ponderomotive force of the laser pulse pushes electrons out from regions of high intensity while the heavier plasma ions are

stationary on the femtosecond timescale. The induced charge separation pulls the electrons back behind the laser pulse and sets up a plasma wave oscillation in its wake. This plasma wave travels behind the laser pulse with a phase velocity that equals the group velocity of the laser pulse. The electric field in the plasma wave can be very strong and, if the wave is driven to sufficiently high amplitudes, it can break accelerate electrons to very high energies (>100 MeV). Laser-wakefield acceleration is treated extensively in Chapter 4 where the experimental results from Papers **XI** to **XIII** are summarized. For wakefield acceleration to be efficient, the laser pulse needs to propagate over a sufficient distance in the plasma. It is therefore only important for very long scale-length plasmas (>100 μm).

3.1.5 Hot electron transport

As described in the previous section, there are many mechanisms that can lead to the generation of a large quantity ($\sim 10^{12}$) of relativistic (MeV) electrons. Since acceleration occurs only during the laser pulse (< 1 ps), the current that enters the target is of the order of mega-amperes. For a current of this magnitude, in vacuum, self-generated magnetic fields pinch the electron beam to the point where it actually turns around, effectively preventing the beam from propagating. The fundamental physical limit to the maximum current that can propagate through vacuum was given by Alfvén in 1939 [42],

Numerical example. 2×10^{12} *electrons with a kinetic energy of 0.9 MeV, produced by a 30 fs pulse, form a current of 10 MA. The Alfvén limit is 44 kA.*

$$I_{limit} = \beta\gamma \cdot 17 \text{ kA} \tag{3.16}$$

Nevertheless, as the electron beam is driven into the solid density plasma, self-generated electric and magnetic fields act to generate a counter-propagating cold return current. This return current is of the same magnitude as the fast-electron beam, but is carried by a larger number of slow electrons. These counter-propagating beams are prone to develop propagation instabilities, such as the Weibel instability [43], that tend to cause filamentation of the hot electron beam. In addition, the target material must be able to supply electrons for the return current. In an insulator, free electrons are only available after the material has been ionized (through field- or collisional ionization). So, depending on the propagation length, the electron beam might become unstable and break into filaments. In a conductor, free electrons are readily available so the electron beam propagation is likely to be much more stable. This is the main reason why metallic foil targets were used in all the ion acceleration experiments presented in this thesis.

3.2 Target normal sheath acceleration

Many different mechanisms can lead to the generation of fast ion beams in the interaction between ultra-intense and ultra-short laser pulses and solid targets. A review of different acceleration mechanisms can be found in [28] and [44]. The main mechanism of importance for the experimental work described in this thesis is sheath acceleration at the surfaces of the target foil. This mechanism can generate high quality beams of multi-MeV protons and heavy ions and will be discussed shortly. Other mechanisms will become important in the future as laser technology develops and the intensity of the driving laser pulse increases significantly. At the target front, the ponderomotive potential of the laser pulse is balanced by an electrostatic potential (due to the induced charge separation) that accelerates ions into the target [45]. This leads to ions with energies of the order of the ponderomotive potential going into the target foil. The photon pressure associated with the laser pulse, $p = 2I/c$, can be very high (several gigabar at 10^{19} W/cm^2) and at high intensities it causes a rapid recession of the target front that launches an ion acoustic wave into the target. This wave can evolve into an electrostatic shock that traps and accelerates ions [46]. Shock accelerated ions can have higher energies than sheath accelerated ions for intensities above 10^{21} W/cm^2 and thick targets. At even higher intensities, $\sim 10^{23}$ W/cm^2, that will become available in the future, the radiation pressure will dominate the interaction and will be directly and efficiently converted into ion energy via the space charge force related to the displacement of the electrons [47].

Under the experimental conditions described in Papers **I** to **X**, the most energetic ions are likely to be generated by large quasi-static electric fields, set up by laser-accelerated electrons at the surfaces of the target. This is the Target Normal Sheath Acceleration (TNSA) mechanism [48], which is schematically illustrated in Fig. 3.7. The electron beam that is generated in the laser focus, traverses the thin target foil and emerges at the rear surface. As the electron beam leaves the target, the return current is going into the bulk of the target. This leaves behind a positive charge at the surface and leads to a large electro-static field. The field lines are directed outwards from the target in a direction that is perpendicular to the target surface (hence the term target normal acceleration). This field is large enough (typically teravolt-per-meter, TV/m) to turn around most of the electrons and to pull them back into the target. It is also strong enough to field-ionize atoms on the surface and drive a rapid plasma expansion in which the ions are accelerated to the MeV level over a few μm. The expansion is driven by a layer of charge separation, a *sheath*, at the ion front.

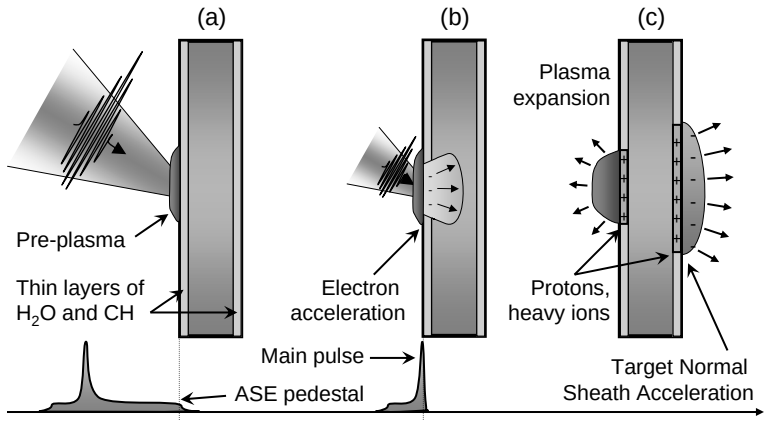

Figure 3.7. *Sequential illustration of TNSA. (a) The ASE-pedestal, arriving on the target surface prior to the peak of the laser pulse, creates a plasma. (b) The peak of the laser pulse interacts with the preformed plasma and drives a beam of MeV electrons into the target. (c) The accelerated electrons emerge at the target rear surface and forms a sheath with μm scale Debye length. The resulting quasi-static electric field, of the order of TV/m, field-ionizes atoms and accelerates the resulting ions to multi-MeV energies in the target normal direction.*

The formation of the sheath is in fact a fundamental characteristic of a plasma [49]. The charges quickly redistribute themselves around an externally applied potential and shields it over a characteristic length, the *Debye* length,

$$\lambda_D = \sqrt{\frac{\epsilon_0 T_e}{n_e e^2}}\,. \tag{3.17}$$

Typically, for the hot electron beams in the experiments presented in this thesis, it is of the order of 0.1 to 1 μm.

3.2.1 Isothermal electrostatic plasma expansion

A full description of TNSA requires three-dimensional (3D) numerical simulations of the laser-plasma interaction at the front of the target, electron transport and the subsequent plasma expansion. However, a relatively simple one-dimensional (1D) isothermal plasma expansion model is still conceptually useful. The expansion of plasma into vacuum was studied already in the 70s for electron temperatures of the order of keV [50–53] driven by nanosecond laser pulses. Here we consider the expansion driven by MeV electrons, heated by intense sub-picosecond laser pulses. This problem was recently analyzed by P. Mora [54, 55] and the main points of the model are discussed in this section.

A pure proton-electron plasma is considered. The electron distribution $n_e(x,t)$ is assumed to have a constant Boltzmann temperature, T_e, and to be in thermal equilibrium with the po-

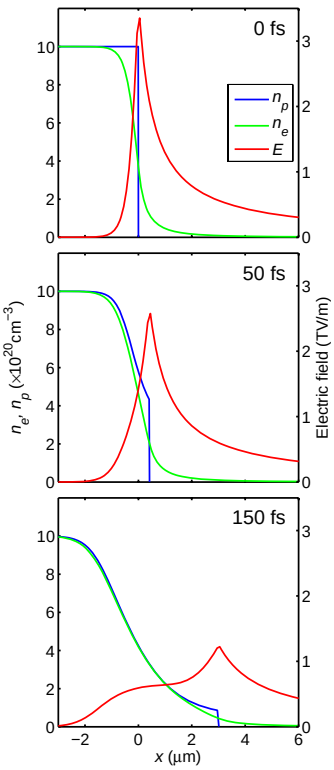

Figure 3.8. *Isothermal plasma expansion into vacuum for an electron temperature of 1 MeV and an initial ion density of* 1×10^{21} *cm*$^{-3}$.

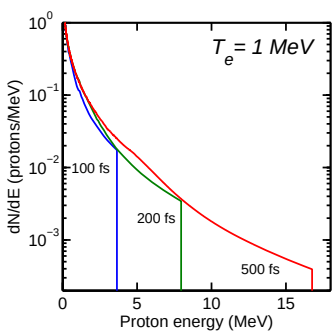

Figure 3.9. *Evolution of the proton energy spectrum for different times during the expansion. The electron temperature and initial ion density are the same as in Fig. 3.8.*

tential, $\Phi(x,t)$. For a particular background proton distribution $n_p(x,t)$, the potential is obtained by solving Poisson's differential equation,

$$\epsilon_0 \frac{\partial^2 \Phi}{\partial x^2} = e\left(n_0 \exp\left(e\Phi/T_e\right) - n_p(x,t)\right) . \tag{3.18}$$

At the start of the expansion, the proton distribution is

$$n_p(x,0) = \begin{cases} n_0, & (x \le 0) \\ 0, & (x > 0) \end{cases} . \tag{3.19}$$

The initial electric field, $\mathcal{E} = -\partial\Phi/\partial x$, is obtained by solving Eq. 3.18 numerically. In this section we use the notation $\mathcal{E}$ for the electric field to distinguish it from the proton energy E. Figure 3.8(a) shows the resulting electron, ion and electric field distributions for $T_e = 1$ MeV and $n_0 = 10^{21}$ cm^{-3}. This density is lower than the values in Table 3.1 but, as discussed in Sec. 3.4.5, corresponds to the density of hot electrons at the rear surface of the foil target. The electrons form a sheath at the sharp ion density discontinuity. The electric field peaks at the discontinuity and reaches a magnitude of 3.4 TV/m. Starting from these initial conditions, the plasma expands into vacuum, driven by the electric field at the ion front. The expansion is described by the equation of motion and the equation of continuity of the protons;

$$\frac{\partial v_p}{\partial t} + v_p \frac{\partial v_p}{\partial x} = \frac{e}{m_p}\mathcal{E}(x,t) , \tag{3.20}$$

$$\frac{\partial n_p}{\partial t} + \frac{\partial}{\partial x}\left(n_p v_p\right) = 0 . \tag{3.21}$$

A Lagrangian code was implemented in Matlab to solve Eqs. 3.18, 3.20 and 3.21 for various initial conditions. The resulting expansion is shown in Fig. 3.8(b) and (c). The evolution of the proton energy spectrum is shown in Fig. 3.9. The proton number density is monotonically decreasing with increasing energy and has a well defined maximum cut-off energy. The evolution of the maximum proton energy and the maximum electric field are shown Fig. 3.10. The protons are accelerated to several MeV in a few 100 fs while the peak electric field falls toward zero. The data from these simulations agree perfectly with the analytical model by Mora [54] which states that the spectral shape can be approximated by a self-similar analytical expansion model,

$$\frac{dN}{dE} = \frac{n_0 t}{\sqrt{m_p E}} \exp\left(-\sqrt{\frac{2E}{T_e}}\right) \tag{3.22}$$

for which the cut-off maximum energy is given by

$$E_{max} = 2T_e\left[\ln(\tau + \sqrt{1+\tau^2})\right]^2 , \tag{3.23}$$

where $\tau = \omega_{pi} t/\sqrt{2e_E}$, $\omega_{pi} = \sqrt{n_0 e^2/\epsilon_0 m_p}$ the ion plasma frequency, t is time and $e_E = 2.7183...$ is the natural logarithmic constant. This relation predicts that the maximum proton energy should scale linearly with the electron temperature. Therefore the maximum proton energy is expected to scale as $E_{max} \propto \sqrt{I_L}$ (see Eq. 3.14). This scaling law has been confirmed in experiments at many different laboratories at moderate laser intensities. In Paper **VII** we extended it, for the first time, to intensities above 10^{20} W/cm^2.

A characteristic feature that can be observed in the simulations is that, behind the ion front where the acceleration occurs, the ion beam is quasi-neutral. Another important fact is that the acceleration is very quick. In addition, for a fully three-dimensional expansion, the ions are initially cold and have no transverse momentum. These three facts taken together are important factors in explaining the highly laminar flow and extremely low emittance of the ion beams emerging from the expansion and that have been observed in experiments [1, 56].

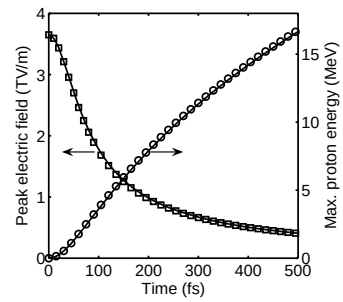

Figure 3.10. *Maximum proton energy (circles) and peak electric field (squares) as function of time during the expansion in Fig. 3.8. The simulations are in good agreement with the analytical formulas in given by P. Mora [54] (solid lines).*

Influence of the electron temperature

Figure 3.11 shows the magnitude of the peak electric field as function of the electron temperature. The output from the numerical simulation is in perfect agreement with the exact solution to the problem in Eq. 3.18 [54],

$$\mathcal{E}_{max} = \sqrt{\frac{2T_e n_0}{e_E \epsilon_0}}\,. \tag{3.24}$$

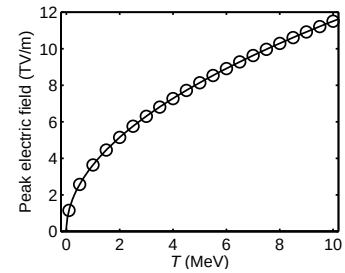

Figure 3.11. *Peak electric field at $t = 0$ as function of electron temperature. The symbols are output from the simulations, the solid line is the exact solution in Eq. 3.24.*

Influence of a density gradient

The extremely high accelerating fields in Fig. 3.11 are possible due to the sharp interface between the ion distribution and vacuum. However, as discussed in Papers **I** to **III**, amplified spontaneous emission (ASE) that precedes the main pulse can heat the bulk and the rear surface of the target by x-ray generation and/or by launching an intense shock wave into the target. By heating the ions, the ASE initiates a slow expansion into the vacuum prior to the arrival of the high intensity pulse, thereby creating a smooth density profile. Early experimental investigations showed that long density gradients significantly reduce the efficiency of the acceleration [57]. To investigate the influence of a density gradient, the initial proton density profile is modeled with the sigmoid function

$$n_p(x, 0) = n_0/(1 + \exp(4x/L))\,. \tag{3.25}$$

The parameter L here defines the length over which the density falls from $0.9n_0$ to $0.1n_0$. As shown in Fig. 3.12 the resulting maximum electric field is indeed much lower when the gradient is very

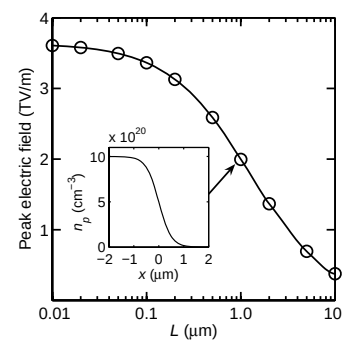

Figure 3.12. *Peak electric field at $t = 0$ as function of the initial scale-length, L. The inset shows an example of the density profile that was used in the simulation.*

long. However, when it is shorter than the Debye length (∼0.2 μm), the effect is relatively small, indicating that efficient acceleration is possible in reasonably short gradients. This was shown in a recent experiment in which a secondary laser was focused on the rear surface of the foil, thereby initiating a slow expansion before the main pulse arrived and accelerated the ions [58]. The influence of an initial density gradient has also been studied in simulations [59]. An interesting result is that the fast expansion, driven by the hot electrons, can overtake the initial slow expansion, with the result that the ion expansion wave breaks. This process could perhaps be used to generate proton beams with quasi-monoenergetic spectral features [60], as opposed to the exponentially decaying spectra more regularly reported in Papers **I** to **X**. There is, however, one exception, see Fig. 3.43.

Improvements to the model

In the isothermal model the acceleration would go on indefinitely. An improved model has been developed by P. Mora, that includes adiabatic cooling of the electrons as their energy is transferred to the ions, and the effects of a dual electron temperature [55]. Both the isothermal and the adiabatic models are compared to experimental data in Paper **VII**. The conclusion drawn in that paper is that, in addition to the already discussed improvements, agreement with the experimental data is possible only if also effects of the three-dimensional expansion is included in the model.

3.3 Experimental methods

Many different techniques were used in the experiments leading to Papers **I** to **X**, both to diagnose the laser-plasma interaction itself and the ion beams emerging from it. In Sec. 3.3.1, a short description of the relevant ion detectors is given. Please note that other detector technologies exist (but have not been used), such as micro channel plates, scintillators and Faraday cups, that can provide instantaneous detector readout. Section 3.3.2 describes four relevant ion beam characterization techniques. Again, there are other techniques which are not discussed, for example time-of-flight measurements. Section 3.3.3 describes an optical interferometric technique for characterization of the electron density profile in plasmas, which is relevant for the modeling of the ion acceleration process.

3.3.1 Ion detection

When an ultra-intense laser pulse interacts with the plasma, a large number of electrons are accelerated to MeV energies. When these electrons interact with the solid density plasma, part of their

	CR39	RCF	Activation
Readout time	hours	minutes	hours
$E_{min}(p^+)$	100 keV	1 MeV	10 MeV
Absolute charge	yes	no	yes
Sensitivity	high	moderate	high
Protons	yes	yes	yes
Heavy ions	yes	no	no
Electrons	no	yes	no
X-rays	no	yes	no
Used in Papers	**I-V**, **IX-X**	**VI**	**VII**, **VIII**

Table 3.2. *Strengths and weaknesses of various ion detectors.*

energy is converted into protons and heavy ions, but also into x-rays and γ-rays. Different detectors have different sensitivity to different types of ionizing radiation, and the choice of ion detection system is highly influenced by the relative amount of ions, electrons, x-rays and γ-rays that emerge from the interaction.

In the experiments described in Papers **I** to **X**, three different technologies have been used. These are plastic nuclear track detectors (CR39), radiochromic film (RCF), and nuclear activation (of Cu and Al). A qualitative comparison of the strengths and weaknesses of the different detectors is shown in Table 3.2. CR39 has a quantum efficiency of 1 for protons and heavy ions within certain energy limits, and is insensitive to electrons and photons. Therefore, CR39 has been the most used detector, despite the time consuming but necessary etching and microscope analysis (as explained below). RCF has a lower sensitivity, but a very high spatial resolution, so it is excellent for diagnosing the spatial distribution. Unfortunately, it is sensitive also to electrons and γ-rays which complicates the analysis. The main advantage of nuclear activation is that it is very sensitive to protons and suitable for detection of very energetic protons. In addition, it is insensitive to background radiation. The main drawbacks are the relatively high detection threshold and the long readout time. In Paper **VIII**, we describe a technique to significantly shorten the time required for readout.

CR39 plastic nuclear track detector

CR39 is a durable plastic that has found many applications in society [61]. In many of the experiments described in this thesis, CR39 in the form of plates of $50 \times 50 \times 1$ mm^3 (Track Analysis Systems [62]) were used as proton- and heavy ion detectors. As an ion strikes the material, polymer chains are destroyed along the path of the particle if its energy is above a certain threshold (~ 100 keV for protons). When etched in a solution of 20% NaOH and 80% water, heated to 80°C, the damaged tracks become visible pits

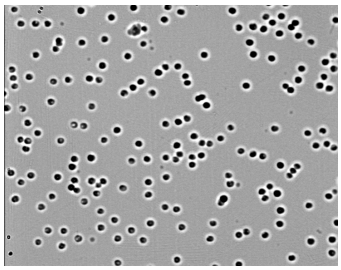

Figure 3.13. *Magnified image showing the proton impact craters that appear on the exposed CR39 detector after etching. In this example, individual pits are well separated and can easily be recognized by an automatic scanning system. The width of the image corresponds to approximately 100 μm on the detector.*

after around 30 minutes. In principle, under well controlled etching conditions, analysis of the pit size and shape can be used for ion identification and energy spectrometry [63], but this method has limited accuracy and has not been used. Instead, the particles are dispersed according to their charge-to-mass ratio and energy by magnetic and electric fields as discussed in Sec. 3.3.2. The particle density distribution behind the spectrometer can be determined by pit counting using a microscope.

Manual counting is clearly impractical. Instead, automatic scanning and pattern recognition systems were used to locate and count the tracks. In Lund I designed and programmed a system using LabVIEW, while at the Central Laser Facility in the UK, a commercial system is used. Some of the data in Papers **II**, **III**, **V**, **IX** and **X** were obtained using these automatic systems.

The sensitivity of CR39 drops with increasing energy. When ions are stopped in the plastic, they deposit most of their energy near the end of their trajectory. Consequently, the etched pit size is smaller for higher ion energies, and for protons CR39 is only practical up to ∼7 MeV. Protons with higher energies can be detected if a filter is placed in front of the CR39 that slows down the protons before they strike the CR39, or if a stack of several CR39 plates is used. Both these techniques are described in the next section.

Apart from the long etching time, the main disadvantage of CR39 is its limited dynamic range. When the particle flux is too high, overlapping pits makes accurate counting impossible. There is also a risk of overexposure, as areas of high particle density can be misinterpreted as regions of low flux [64]. For the analysis of the proton beams discussed in Paper **V**, we developed a technique to control the proton flux level on the CR39, that increased the dynamic range of the spectral measurement by more than one order of magnitude (see Sec. 3.4.3).

Radiochromic film

Initially developed for medical dosimetry applications [65], radiochromic film (RCF) is also a common diagnostic in laser plasma experiments. The film exists in a variety of forms with different sensitivities and dynamic ranges. In the experiments described in Paper **VI**, two different types with different sensitivity were used (MD-55 and HD-810). The initially transparent sensitive layers contain a compound that, when exposed to ionizing radiation, gradually turns blue. The absorbed dose is obtained by measuring the optical density of the exposed film.

A great advantage of RCF is its incredible spatial resolution (up to 1000 lines/mm) which makes it an ideal diagnostic of the proton beam profile. Another advantage is that the film requires no development so the data can be recovered immediately. How-

ever, the main drawback of RCF is probably that it is also sensitive to electrons and x-rays which sometimes complicates the interpretation of the data.

Nuclear activation

When an ion strikes a material, there is a possibility (cross section) for nuclear reactions to occur. By measuring the decay of residual radioactive nuclei, conclusions can be drawn regarding the incident particle beam. In laser-plasma experiments, proton activation of copper is a common diagnostic [67–70]. The lower energy threshold is in this case 4 MeV, as determined by the threshold of the

$$\mathrm{p} + {}^{63}\mathrm{Cu} \longrightarrow {}^{63}\mathrm{Zn} + \mathrm{n} \tag{3.26}$$

nuclear reaction. Usually, as in Paper **VII**, plates of copper with varying thickness are used in a stacked configuration as described in Sec. 3.3.2. The upper energy threshold is determined by the thickness of the stack and the stopping range of protons in copper. In Paper **VII**, this is 80 MeV. The ^{63}Zn isotope decays with a characteristic half-life of 38.1 minutes, predominantly through β^+-decay. The 511 keV gamma-ray signature of positron annihilation is detected using two NaI photomultiplier tube counters operated in coincidence. The measured activity of each copper plate is proportional to the total number of ^{63}Zn nuclei. The incident proton spectrum is calculated from these measurements using data for the energy dependent cross-section for the reaction and tabulated functions of the proton stopping power of copper [71].

Usually (p, n) reactions have a much higher cross-section than (γ, n) reactions so this diagnostic is primarily sensitive to protons. It is also very sensitive and has a high dynamic range since single decay events can be detected. Another advantage is that a single measurement of the induced activity gives an integrated measurement of the dose deposited by the full beam, as compared to other diagnostic techniques, such as Thomson spectrometers (Sec. 3.3.2), that are limited to sampling a small solid angle. The main disadvantage is the long readout time, since the activity must be measured during a time which is comparable to the life-time of the radioactive nuclei. In Paper **VIII**, we investigate the possibility of using short-lived radioisotopes as a fast detector. In particular, the reaction

$$\mathrm{p} + {}^{27}\mathrm{Al} \longrightarrow {}^{27}\mathrm{Si} + \mathrm{n} \tag{3.27}$$

with a life-time of only 4.2 seconds was used to measure the induced activity only seconds after the laser shot.

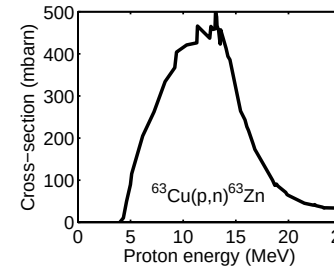

Figure 3.14. *Energy dependent cross-section data for the ^{63}Cu(p,n)^{63}Zn reaction. Data from [66].*

	Magnet	Thomson	Filter array	Stack
Energy resol. p^+	high	high	low	medium
Energy resol. Z^+	no	high	no	no
Divergence	no	no	yes	yes
Full angular dose	no	no	no	yes
Used in Papers	**II**, **III**, **V**	**IX**, **X**	**I-V**	**VI-VII**

Table 3.3. *Qualitative comparison of various ion beam characterization techniques.*

3.3.2 Ion beam diagnostics

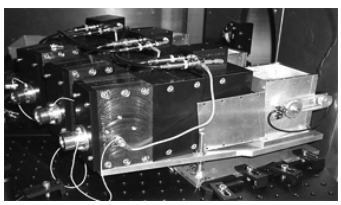

Figure 3.15. *Three Thomson ion spectrometers, positioned along the target normal direction (0°) and at ±10°, facing the laser irradiated side of the target. Three additional spectrometers were positioned on the rear side of the target. These, in total six, spectrometers were used as the main diagnostics for the experiment reported on in Papers **IX** and **X**.*

Several different techniques to characterize the ion beam were used in the experiments described in this thesis. The choice of method is based on the ion energy and the beam property of interest (see Table 3.3). To measure the proton energy spectrum, a simple magnetic deflection spectrometer may be used. To identify and measure the energy spectra of various heavy ions and different charge states, a Thomson mass spectrometer is used. An array of stopping filters gives a limited energy resolution and simultaneously information on the energy dependent beam divergence. If the proton numbers and energies are high enough, a full beam characterization of the energy dependent spatial distribution is possible by arranging several RCF films in a detector stack.

Magnetic deflection spectrometers

For a pure proton beam, a simple arrangement of a slit or pinhole and a dipolar magnetic field can be used to deflect and spatially separate protons according to their energy. However, the beams that are produced in these experiments are typically a mixture of protons and differently charged heavy ions. If the main interest is the proton distribution, a simple stopping filter can be placed in front of the detector, behind the magnet, so that heavy ions are stopped while protons above a certain threshold are transmitted. This technique was used in Papers **II**, **III** and **V**. Whereas it facilitates highly resolved measurements of the energy distribution, it is limited to sampling a small solid angle of the ion beam. This is true also for the Thomson spectrometer.

Thomson ion mass spectrometers

A Thomson spectrometer [72] is based on electric and magnetic fields, parallel to each other but perpendicular to the ion velocity vector. Ions enter the spectrometer through a pinhole collimator, are separated according to their charge-to-mass ratio and dispersed according to their energy along parabolic trajectories in the detector plane. In the following analysis we ignore the effects of fringe fields and assume small deflections inside the fields of the spectrometer. The time the particle spends in the force-field,

$t = L/v$, depends on its velocity v and the length L of the field. During this time, it is accelerated along the electric field vector by $a_x = qE/m_i$, where q/m_i is the ion charge-to-mass ratio, and along the perpendicular direction by $a_y = qvB/m_i$. The deflection is

$$\Delta X = \frac{qEL^2}{2m_i v^2} \quad \text{and} \quad \Delta Y = \frac{qBL^2}{2m_i v}\,. \tag{3.28}$$

Combining these relations shows that the deflection is parabolic.

$$\Delta X = \Delta Y^2 \frac{q}{m_i}\frac{E}{B^2}\frac{2}{L^2}\,. \tag{3.29}$$

Ions with different q/m_i are deflected along different parabolas, as shown by the example in Fig. 3.54. Many different ion species can be discerned and identified by comparing the shape of the parabolas to a numerical particle tracking code. Figure 3.15 shows a photograph of three of the total six Thomson spectrometers that were used as the main diagnostic in the experiment discussed in Secs. 3.4.6 and 3.4.7 and in Papers **IX** and **X**.

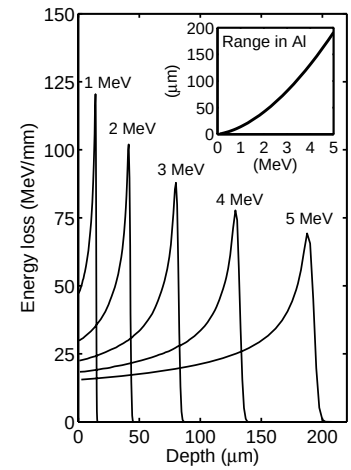

Figure 3.16. *Energy loss of protons with different incident energies in aluminium, obtained using the* SRIM *simulation package [73]. The protons deposit the majority of their energy toward the end of their path. Therefore protons (and heavier ions), have a well defined, energy dependent maximum range in matter, as shown by the inset.*

Filter arrays

A very simple, but effective way to diagnose the spatial distribution of the proton beam is to use an array of striped stopping filters. This method is used when the proton energies are too low to use the stacked detector arrangement described below. As shown in Fig. 3.16, protons have a well defined range in matter and only protons with energies above a certain threshold are transmitted through a filter of a particular thickness. By arranging several filters with different thickness in a striped array, as shown in Fig. 3.17, it is therefore possible to measure both the beam divergence and pointing above chosen threshold energies. This method was used extensively in the experiments reported on in Papers **I** to **V**.

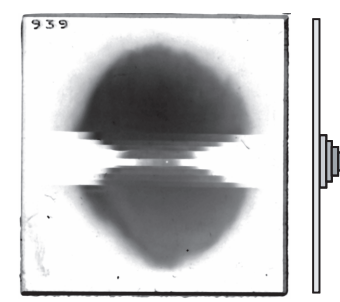

Figure 3.17. *Raw data, showing the proton beam imprint on a CR39 detector behind an array of stopping filters. To the right is a side-view sketch of the filter arrangement. The thinnest and thickest filters stop protons up to 0.9 and 2.8 MeV, respectively. The Lund multi-terawatt laser was used to accelerate the protons from a 6 μm Al foil target. The experimental conditions are given in Sec. 3.4.1. The size of the detector is* 50×50 *mm*^{2} *and it is placed 45 mm from the target.*

Stacked detectors

A stacked detector configuration may be used when the stopping range of the most energetic protons exceeds the thickness of at least one detector in the stack (usually RCF or copper plates). Typically stacked detectors are used when the maximum proton energy exceeds 10 MeV. The well defined stopping range of protons in matter allows detector plates at the front of the stack to act as energy high-pass filters for detectors at the back. The energy resolution depends on the thickness of the detector plates. In the experiment described in Paper **VII**, nuclear activation of a stack of Cu plates is the main diagnostic of the proton spectrum. In the experiment described in Paper **VI**, a stack of RCF facilitates energy-dependent characterization of the proton beam profile, as exemplified in Fig. 3.18.

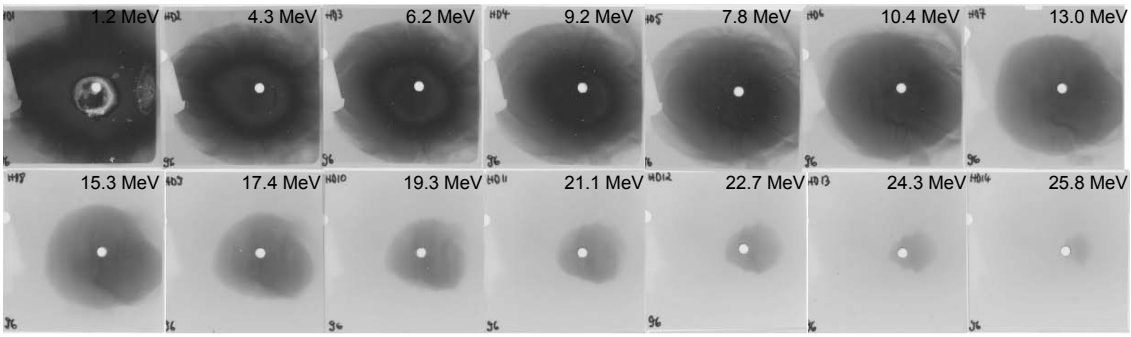

Figure 3.18. *Energy dependent proton beam profile, obtained on a single laser shot and measured by a stack of alternating layers of copper plates and RCF detectors. Each RCF detector integrates the dose of protons within a narrow energy range in the incoming beam. The Vulcan Petawatt laser was used to accelerate the protons at an intensity of* 4×10^{20} *W/cm*^{2} *from a 25* μ*m thick Cu foil. The experimental conditions are described in Sec. 3.4.4.*

3.3.3 Interferometry for plasma characterization

In the previous sections, we have discussed methods to diagnose the accelerated ions. In this section we focus on characterization of the plasma. Detailed knowledge on plasma densities, gradients and evolution is essential in order to model the ion acceleration process.

A common diagnostic in laser-plasma experiments is to use a probing laser pulse, synchronized to the main pulse, to backlight the interaction area either before- or after the main interaction. By changing the delay between the two pulses, the plasma evolution can be studied in a sequence of shots. For absolute synchronization on the fs time-scale, the probe beam is split off from the main beam either before or after compression. Since shorter wavelengths can propagate in denser plasmas, the probe is usually frequency doubled. This also facilitates straightforward discrimination of scattered light from the main laser pulse using interference filters. Two different beam geometries have been used in this thesis work for probing. As described in Sec. 4.3.7, spectral modulations of a co-linear probe pulse can be used as a diagnostic of periodic plasma density variations. This section describes transverse interferometry for plasma expansion characterization. This particular setup was used in an experiment at the Vulcan Petawatt laser, discussed in Sec. 3.4.4.

Polarized light interferometer

The principle for this type of interferometer is described by Benattar *et al.* [74] and is schematically illustrated in Fig. 3.19. A parallel probe beam illuminates the interaction region which is imaged by a high resolution lens system (L) onto a CCD detector. Between the lens and the detector, a Wollaston prism (W)

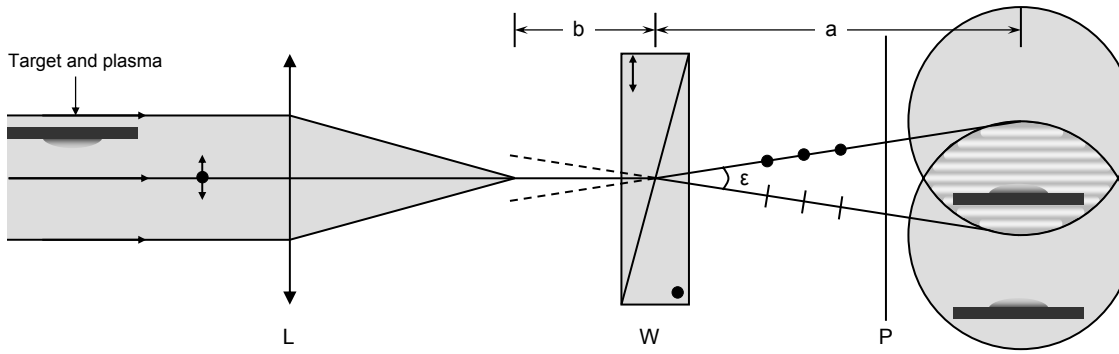

Figure 3.19. *Schematic representation of the principle for the interferometer. The polarization of the incoming probe beam is tilted by 45° to the plane of the figure and passes the target interaction area and an imaging lens. The Wollaston prism angularly separates the two components of the incoming beam with different polarization. A polarizer, again rotated 45° to the plane of the figure, allows interference. In the overlapping region, the upper part of the incoming beam that has passed the plasma on the target front surface, overlaps with the lower part, that did not propagate through the plasma. The image plane is flipped by 90° for better illustration.*

creates two displaced images, separated by an angle ϵ, in orthogonally polarized light. A Wollaston prism is a polarizing beam splitter [75], consisting of two birefringent wedges (usually calcite or quartz) put together to form a parallel plate. When the polarization of the incoming beam is at 45° to the optic axis of the Wollaston prism, the two beams have the same intensity but, since they have orthogonal polarization, they can not interfere. Interference is achieved by placing a polarizer (P) in front of the detector. Inserting the prism into the expanding beam, creates two virtual sources that are responsible for the interference. Using the notations in Fig. 3.19, the distance between interference fringes in the image plane is,

$$i \approx \frac{\lambda_L}{\epsilon}\frac{a}{b}\,. \tag{3.30}$$

Phase retrieval

Figure 3.20(a) shows a typical interferogram of an expanding plasma. In this particular example the target is a 25 μm Au foil. The plasma expansion is driven by a nanosecond laser pulse that is focused to a 470 μm diameter circular top-hat intensity distribution with a peak intensity of 5.0 TW/cm^2. The probe has a duration of 0.5 ps and takes a snapshot of the plasma evolution after 500 ps. The bending interference fringes are due to the change in refractive index as the plasma expands into the vacuum. The dark region outlining the expansion profile is due to refraction of the probe pulse in the plasma gradient. The experimental details of this study is given in Sec. 3.4.4.

The phase shift is retrieved by shifting the carrier frequency of

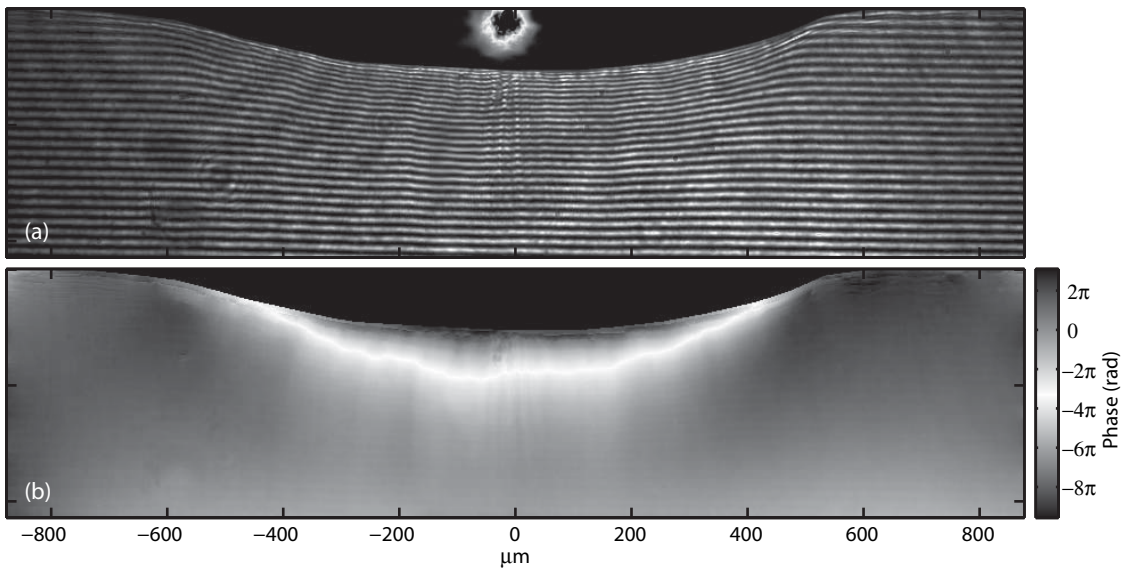

Figure 3.20. *(a) Interferogram of an expanding plasma in front of a thin foil target. (b) Retrieved phase map. The details of the laser and target conditions are given in the text. Vertical and horizontal scales are identical in both images.*

the interference pattern to zero using a two-dimensional (2D) Fast Fourier Transform algorithm, implemented in the interferogram analysis software IDEA [76]. The result is shown in Fig. 3.20(b).

Abel inversion and electron density retrieval

Assuming that the shift caused by refraction is small, the phase map in Fig. 3.20 is a plane projection of the 3D structure of the expanding plasma. In this particular example, cylindrical symmetry may be assumed and the accumulated phase shift, relative to the vacuum reference wave can be written

$$\Phi(y) = \frac{2\pi}{\lambda_L}\int_{x_1}^{x_2}[1-\eta(x)]dx \approx \frac{2\pi}{n_c\lambda_L}\int_{y}^{\infty}\frac{n_e(r)rdr}{\sqrt{r^2-y^2}} \qquad (3.31)$$

where $\eta = \sqrt{1-n_e/n_c} \approx 1 - n_e/2n_c$ is the refractive index and x, y and r are the transverse, longitudinal and radial positions, respectively. An Abel inversion of this equation gives

$$n_e(r) = -\frac{n_c\lambda_L}{\pi^2}\int_{r}^{\infty}\frac{d\Phi}{dy}\frac{dy}{\sqrt{y^2-r^2}} \qquad (3.32)$$

The inversion can be calculated for each coordinate along the expansion direction (y). Figure 3.21 shows the transverse electron density profile at several different positions relative to the initial target surface.

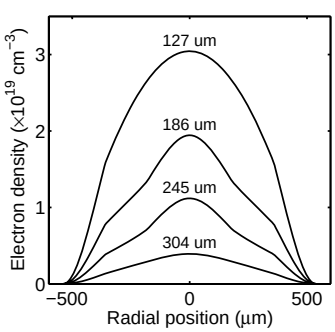

Figure 3.21. *Transverse electron density profiles, at different positions from the initial target surface.*

3.4 Results and discussion

As described in Sec. 3.2.1, ion acceleration is primarily driven by quasi-static electric fields at the surfaces of the foil target. The magnitude of these fields depends on the electron temperature and on the density (see Eq. 3.23), so to increase the maximum ion energy, at least one of these parameters must be increased. One obvious way to increase the electron temperature is by increasing the laser intensity (see Eq. 3.14). This is taken all the way to the limits of present day laser technology in Paper **VII** where protons are accelerated up to 55 MeV by focusing the Vulcan Petawatt laser to an intensity of 6×10^{20} W/cm^2. For a given laser pulse, the electron density at the rear surface can be increased by decreasing the target thickness. This minimizes the geometrical spreading of the electron beam during the passage through the target and consequently, the highest proton energies and the highest conversion efficiencies are reached by using very thin foils. In Paper **V**, also this scaling is taken to its limits by using ultra-thin targets down to a thickness of only 20 nm ($\sim$ 100 atom layers!). However, there are limits as to how thin foils can be used to optimize the proton beam. The most important limiting factor in most experiments is amplified spontaneous emission (ASE) preceding the main pulse. When focused, it can become so intense that it destroys or significantly changes the properties of the target prior to the main pulse arrival. The influence of ASE is studied in detail in Papers **I** to **III** and, in particular, it is found that under certain conditions, it can induce an energy dependent proton emission direction. These findings are further developed in Paper **IV**, where a controlled secondary laser pulse is used to optically control the proton beam direction. As described in Paper **VI**, a controlled prepulse can also significantly enhance the proton beam, both in terms of maximum energy and beam quality. Finally, heating the target to more than 1000°C prior to the laser pulse, removes surface contaminants containing hydrogen and facilitates efficient acceleration of heavy ions. During one such experiment, performed using the Vulcan PW laser and described in Papers **IX** and **X**, it was found that hot electrons can be transported over a significant distance laterally across the target and accelerate ions several mm away from the laser focal spot.

This section gives a summary of some of the most important results reported on in Papers **I**-**X**. The experiments described in Secs. 3.4.1-3.4.3 were performed using the Lund multi-terawatt laser. Sections 3.4.4-3.4.7 review experiments performed using the PW arm of the Vulcan laser. All sections focus on proton acceleration, except 3.4.6 and 3.4.7 which highlight heavy ion acceleration.

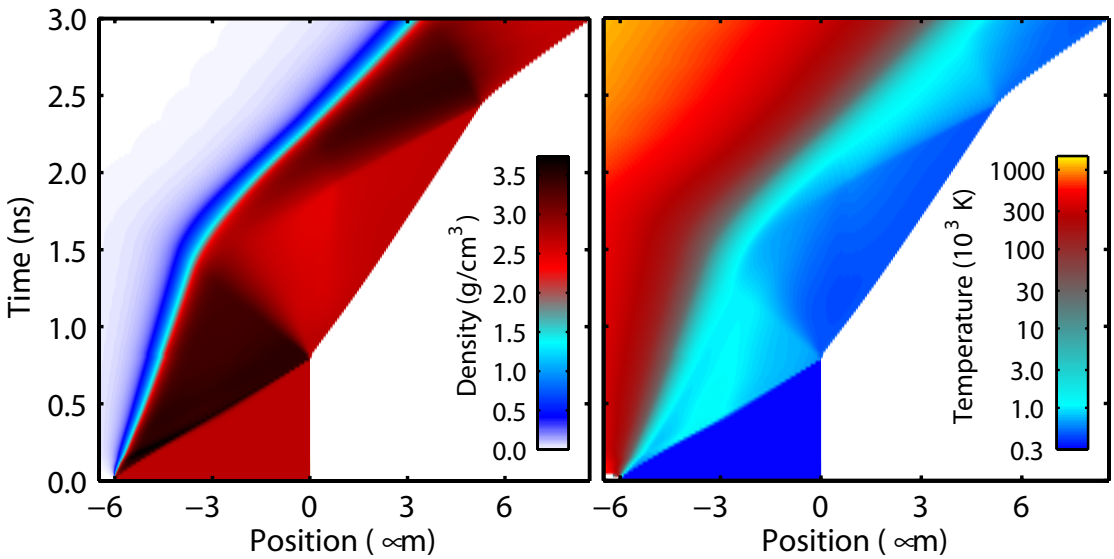

Figure 3.22. *Time evolution of the density (left panel) and temperature (right panel) of a 6 μm Al target, subjected to a laser pulse with an intensity of 1×10^{12} W/cm^2. The laser pulse enters the simulation box from the left and laser ablation at the target front launches a shock that propagates through the target with a constant speed. When the shock front strikes the rear surface, it starts to expand into vacuum while a rarefaction wave is backscattered into the target. The rear surface temperature never exceeds even the melting point of Al, and a steep rear surface density gradient is preserved so that efficient ion acceleration is facilitated.*

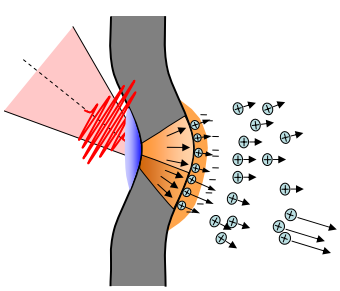

Figure 3.23. *Proton acceleration in a target that has been deformed by the ASE pedestal. The largest accelerating field is generated in a region where the target normal direction is shifted toward the laser axis.*

3.4.1 Influence of shock waves

The effects induced by the ASE pedestal varies with its intensity and, as we will see shortly, its duration. Even at a relatively low intensity of 10^{10} W/cm^2, material at the target front surface is ionized and heated through collisions prior to the main pulse arrival. As this pre-plasma expands into vacuum, the initially sharp target density profile is smoothed on the front of the foil. At medium ASE intensities ($\sim 10^{12}$ W/cm^2) not only the front, but also the bulk of the target is significantly influenced. The pre-plasma has in this case such a high temperature that the front side plasma expansion launches a compressional shock wave into the target. Given enough time, it will reach the rear surface of the foil and significantly influence the properties of the proton emitting region. At even higher ASE intensities ($> 10^{13}$ W/cm^2), the shock is strong enough to induce phase transitions and even evaporate the target material. In addition, phase transitions can be induced through heating by x-rays generated at the target front. These effects might create a long ion density scale length at the rear surface, thereby terminating efficient proton acceleration. To avoid this and other rear surface effects, most experimenters choose the foil thickness so that the shock front is still inside

the target when the main pulse arrives. In contrast, Papers **I** to **III** report experiments where the ASE is strong enough to significantly change the acceleration conditions, but yet not strong enough to terminate the proton emission. The influence of the ASE pedestal on the proton spectrum was investigated by Kaluza *et al.* [77] using a Thomson spectrometer, sampling a small solid angle in the target normal direction. Here, we investigate the influence of the ASE pedestal on the spatial distribution of the emitted proton beam.

Shock generation and propagation

Figure 3.22 shows the result of a 1D hydrodynamic simulation, obtained using the code MULTI [78], of the interaction between a 3 ns long ASE pedestal of medium intensity (1×10^{12} W/cm^2) and a 6 μm thick Al foil target. The laser hits the target (from the left side in the figure) at time zero and heats the plasma formed on the front side of the foil. The heated plasma expands out into the vacuum and in doing so it exerts a very high pressure, exceeding 30 GPa (0.3 Mbar), on the remaining target. Because of the abrupt change in pressure, a compressional shock is launched into the target. The shock wave moves with a constant pressure dependent velocity until it reaches the rear surface where shock breakout occurs. The rear surface then starts to expand while a rarefaction wave is backscattered into the target. The laser-driven ablation pressure continues to push on the front side so the net effect is that, after shock breakout, the target is moving with a speed of typically a few μm/ns. An interesting observation from these simulations is that, for this ASE intensity, the rear surface remains relatively cold even after the breakout. Therefore the steep rear surface gradient is maintained and efficient proton acceleration is possible, as discussed in Sec. 3.2.1.

Acceleration from shocked targets

Since the ASE intensity varies across the focal region, the highest shock pressure and, consequently, the largest rear surface deformation occurs behind the center of the focus. This means that, after shock breakout, the target foil takes on a locally convex profile as shown schematically in Fig. 3.23. The main, p-polarized, laser pulse is incident at an oblique angle and accelerates electrons according to a number of different mechanisms as described in Sec. 3.1.4. The shock is driven by a significant plasma expansion at the target front so, under these conditions, the electron beam is shifted toward the laser direction [36, 37]. When the electrons reach the rear surface, they are asymmetrically distributed across the deformation and the strongest accelerating field appears in a region where the local target normal points away from the global

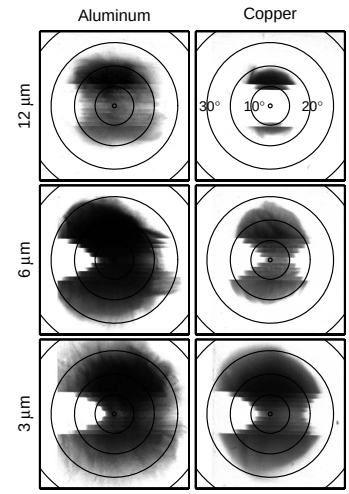

Figure 3.24. *Proton beam profiles obtained for Cu and Al target foils with different thickness under conditions when the ASE-driven shock wave strongly influences the proton emission angle. The scale shows angles relative to the target normal direction and the laser axis is at 45° to the right.*

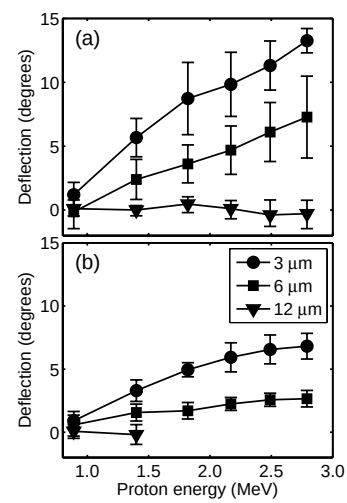

Figure 3.25. *Energy dependent proton beam emission direction for (a) Al and (b) Cu foils with different thickness.*

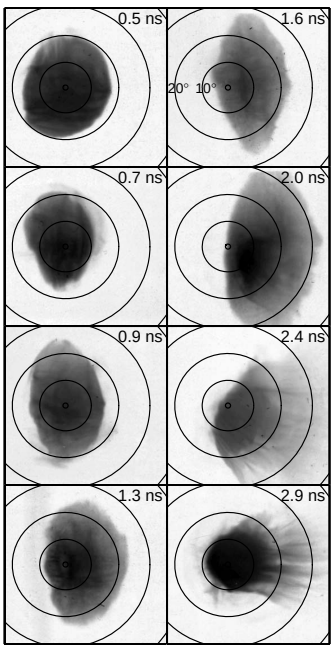

Figure 3.26. *Proton beam profiles, obtained for a constant ASE intensity of 2×10^{11} W/cm^2 and 6 μm Al targets for different durations of the ASE pedestal. In these images, the target normal direction is at 0° and the laser direction is at 45° to the right.*

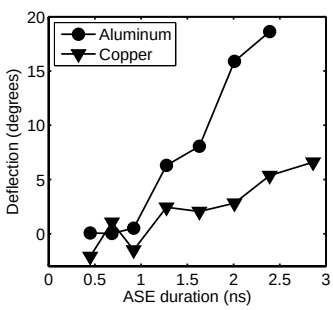

Figure 3.27. *Proton beam deflection toward the laser axis as function of the ASE duration. Beams emitted from Al foils are deflected to larger angles than beams emitted from Cu foils.*

target normal. Hence the direction of the most energetic protons is shifted toward the laser axis. Low energy protons are emitted from a much larger area [1], so for these, the deformation has a defocusing rather than a steering effect. This generates an energy dependent shift of the emission direction, as shown by the examples in Fig. 3.24. To observe this effect experimentally, a striped array of stopping filters (see Sec. 3.3.2) was used in front of the CR39 detectors.

Influence of the target properties

The onset of an energy dependent proton emission direction depends on the relation between the target thickness, the shock velocity, and the ASE pedestal duration. For given ASE conditions, a thinner target is more deformed and induces a larger shift than a thicker target due to the difference in shock transit time. This is illustrated in Fig. 3.24 for constant ASE intensity of 2×10^{12} W/cm^2 and duration of 1 ns. Note that for the 12 μm targets, the shock has not yet reached the rear surface when the main pulse arrives and therefore the proton beam is centered on the target normal. For a given thickness and ASE intensity, the density and stiffness of the target material determines the speed of the shock wave and the speed of the expansion. Therefore, as shown in Fig. 3.25, Al ($\rho = 2.7$ g/cm^3) produces a larger shift than Cu ($\rho = 8.9$ g/cm^3).

Influence of the ASE duration

For a given target foil, an increased proton beam deflection results from either increasing the ASE pedestal duration or the intensity. Using a single stopping filter in front of the CR39 detector plate, Fig. 3.26 shows the beam profile above 2.5 MeV as function of the ASE duration, obtained using a constant ASE intensity of 2×10^{11} W/cm^2 and a 6 μm Al target foil. The beam is emitted along the target normal, until the shock breaks through the rear surface after around 1 ns. After this point, the beam is steered toward the laser axis with an angle that increases with increasing pedestal duration. The time dependent deflection angle is shown in Fig. 3.27 together with data obtained using 6 μm Cu targets. As expected, the shock breaks out at a later time in Cu and the deflection angle increases at a slower rate as compared to the Al target. These observations are consistent with slower shock and expansion velocities in Cu as compared to Al.

Influence on the measurement of the energy spectrum

In many proton or ion acceleration experiments, the main diagnostic is a Thomson parabola, positioned along the target normal axis. Whereas this technique supports measurement of the continuous energy distribution of ions, it is limited to sampling a small solid angle. Figure 3.28 shows spectra, recorded in the target normal direction and at 14° away from the target normal, toward the laser axis. Under conditions when the ASE influences the curvature of the rear surface, the maximum proton energy decreases on-axis while it increases at 14°. Clearly, under such circumstances, the positioning of the ion spectrometer influences the recorded energy distribution.

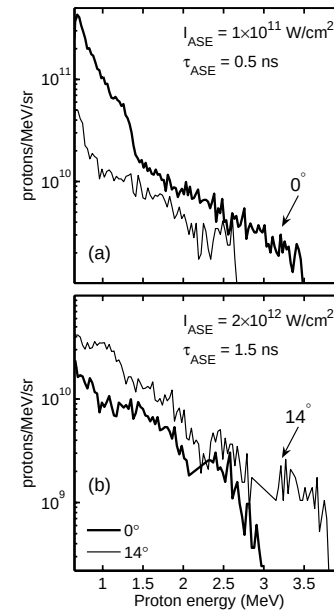

Figure 3.28. *Proton energy distribution, measured along target normal (0°) and at 14° toward the laser laser axis, under different ASE conditions.*

3.4.2 Active ion beam control

In the previous section it was shown that the target foil can be significantly deformed by a shock wave, launched by the ASE pedestal prior to the main pulse arrival, and that this deformation can, under oblique laser irradiation, significantly shift the proton beam emission direction. By controlling the intensity and the duration of the ASE, limited control over the proton emission direction can be gained. However, this method is limited to steering the proton beam toward the laser axis since the position and the spatial intensity distribution of the ASE are impossible to control independently of the main pulse. In the experiment which is schematically illustrated in Fig. 3.29, a separate nanosecond laser pulse, the long pulse (LP), is used to drive a shock and locally shape the target foil prior to the short pulse (SP) interaction. This work resulted in Paper **IV**.

Experimental arrangement

The LP is provided by a Q-switched Nd:YAG laser, electronically synchronized to the SP. The LP has a duration of 11 ns (FWHM) and is focused to a horizontal line focus with an intensity up to 40 GW/cm^2. As confirmed in the experiment, the proton emitting region is much smaller than the length of the line focus and, in this geometry, steering is expected only in the vertical plane. The SP is focused by an $f/3$ off-axis parabolic mirror to an intensity of 4×10^{19} W/cm^2 onto 3 μm Al foil targets. To minimize the influence of ASE, the preamplifier and saturable absorber setup for temporal pulse cleaning (Sec. 2.3) is used. This facilitates an exceptional main pulse to ASE intensity contrast ratio greater than 10^{10} at 1 ns and 10^9 at 100 ps before the main pulse. A vertical array of stopping filters (Sec. 3.3.2) is positioned in front of the CR39 detectors to facilitate simultaneous recording of the spatial distribution above several threshold energies, up to 2.8 MeV.

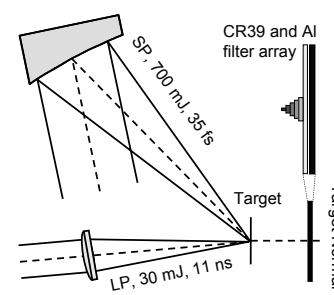

Figure 3.29. *Schematic view from above, of the setup used for proton steering. The LP line focus is oriented parallel to, and the stopping filter array is orthogonal to the plane of the drawing.*

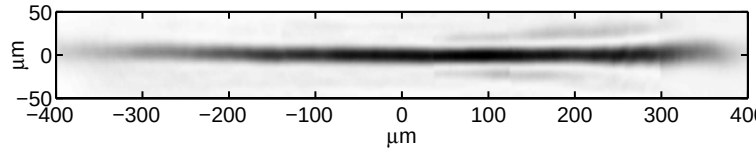

Figure 3.30. *Intensity distribution of the LP horizontal line focus, used for proton steering.*

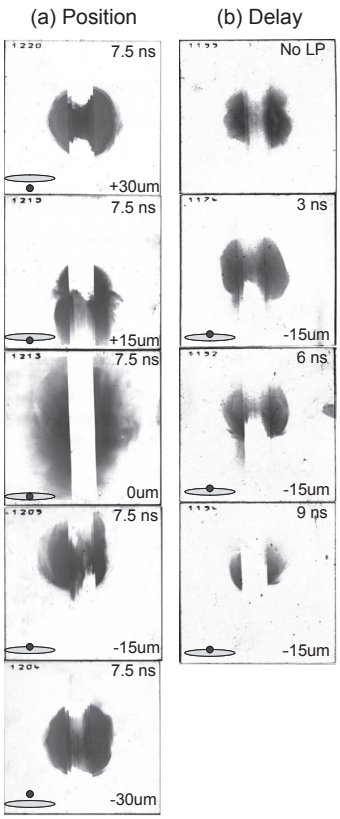

Figure 3.31. *Proton beam profiles, obtained by changing (a), the position the LP steering beam and (b), the delay between the LP and SP. The relative positions of the SP (circle) and the LP (oval) are indicated. The LP intensity is 25 GW/cm^2.*

Influence of the LP position, intensity and duration

The LP arrives on the target prior to the SP and locally deforms the target foil (as described in Sec. 3.4.1). The magnitude of the deformation depends on the LP intensity and on the time available for the target expansion following shock breakout. By changing the intensity, delay, or position of the LP relative to the proton driving SP, the ion emitting surface is locally manipulated and the proton emission direction is thereby controlled.

Figure 3.31(a) shows proton beams for various vertical positions of the LP horizontal line focus. As expected, the beam is steered downward when the LP is above the SP and vice versa. When the two pulses overlap on the target, the divergence is significantly increased in the vertical direction. This is due to the cylindrically convex shape of the emitting rear surface [79]. When the separation is large, ± 30 μm, there is no effect on the proton beam implying, as discussed below, that the proton emitting region is smaller than this value. For a fixed separation of 15 μm, the proton beam deflection increases as the delay between the LP and SP is increased, as shown in Fig. 3.31(b).

Modeling the deflection angle

In Papers **III** and **IV**, a simple model is developed to assess the shape of the target foil for arbitrary LP and target conditions. The different steps are summarized here to give a clear description.

The magnitude of the deformation depends on the time available for the laser-driven shock to transit the target and for the expansion following shock breakout. As described in Paper **III**, both the shock- and expansion velocities (u_s and u_e, respectively) depend on the equation of state of the target material and increase with the ablation pressure P,

$$u_s = (c_0/2)\sqrt{1+\chi}\,, \tag{3.33}$$

$$u_e = (c_0/\alpha)\sqrt{1-\chi}\,, \tag{3.34}$$

where $\chi = (4\alpha/\rho_0 c_0^2)P$ and ρ_0 is the density, c_0 the sound speed and α a dimensionless parameter of the order of unity. Typical values for these parameters are given in Table 3.4 for materials

common in ion acceleration experiments. To estimate the deformation of the rear surface, the induced pressure distribution is assumed to follow the transverse laser intensity distribution according to the scaling given by Lindl [80]:

$$P(y)[GPa] = 40(I_{12}(y)/\lambda_\mu)^{2/3}\,, \tag{3.35}$$

where I_{12} is the laser intensity in TW/cm^2, λ_μ is the wavelength in μm and y is a transverse coordinate. Neglecting transverse shock spreading, the shock propagates through the target with thickness L at a velocity $u_s(y)$ and breaks through the rear surface at a time $t_b(y) = L/u_s(y)$, depending on the pressure distribution $P(y)$. At a given time t, the shape of the rear surface is

$$x(y,t) = \begin{cases} 0, & (t \le t_b(y)) \\ (t - t_b(y))u_e(y), & (t > t_b(y)) \end{cases}\,. \tag{3.36}$$

Figure 3.32 shows the calculated deformation of a 3 μm Al foil for an intensity of 25 GW/cm^2 at times corresponding to the data in Fig. 3.31(b).

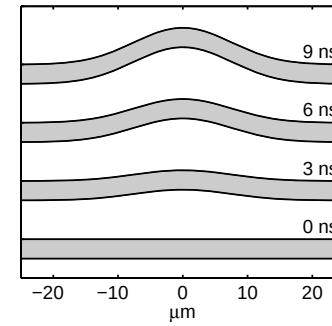

Figure 3.32. *Calculated profiles of the target foil, vertically offset for clarity, for an intensity of 25 GW/cm^2 and times corresponding to the delays in Fig. 3.31(b). Horizontal and vertical scales are identical.*

Influence on the maximum proton energy

When the SP is incident at the center of the LP line focus, the divergence of the proton beam increases in the vertical direction, as shown in Fig. 3.31(a). At same time, the maximum proton energy decreases. Figure 3.33 shows the maximum proton energy as function of the LP intensity, when the LP and SP positions overlap. It is clear that, when the LP intensity is increased, the maximum proton energy decreases. At these relatively low intensities, the steep gradient at the rear surface of the target is preserved after shock breakout, so the inferior proton energies are probably due to front side effects.

Due to the relatively long delay between the two pulses, a long scale length plasma is present in front of the target when the SP arrives. This could have several effects. A long plasma gradient can significantly affect the propagation of the laser pulse and reduce the intensity at the critical surface through filamentation instabilities or ionization defocusing (see Sec. 4.1.5). The plasma expansion also moves the critical surface which results in an effectively thicker target, which in turn results in lower proton energies due to the increased geometrical spreading of the electron beam passing through the target (see Sec. 3.4.3). Also the generation and propagation of the energetic electron beam is affected by the front side plasma gradient. For example, holeboring [35] results in an electron beam with increased divergence going into the target. In addition, the reflection efficiency of refluxing electrons (see Sec. 3.4.3 and 3.4.7) decreases in the presence of the plasma gradient. These effects reduce the electron density at the rear surface, and hence the magnitude of the accelerating field.

	ρ_0 (g/cm^3)	c_0 (μm/ns)	α
Al	2.70	5.24	1.40
Ti	4.53	4.91	1.02
Fe	7.86	3.77	1.65
Cu	8.93	3.94	1.49
Pd	11.99	4.01	1.55
Sn	7.29	2.59	1.49
Au	19.30	3.08	1.56
CH	0.92	2.76	1.59

Table 3.4. *Values of ρ_0, c_0 and α, for target materials that have been used in experiments [81] .*

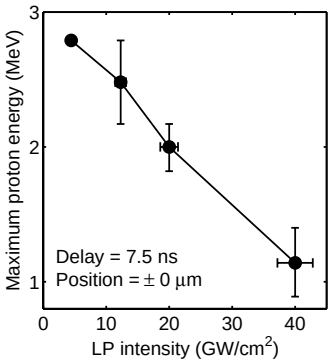

Figure 3.33. *Maximum proton energy as function of the LP intensity, when the LP and SP overlap on the target surface.*

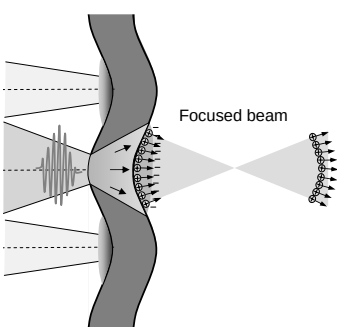

Figure 3.34. *Cross-sectional illustration of the proposed method for optically controlled ion beam focusing in which the LP is focused to a ring-shaped intensity distribution.*

Estimation of the source size

The dependencies of the size of the proton emitting region on various experimental parameters is a subject which has not been very well covered in the literature. However, in most experiments a source diameter of several hundreds of μm [1, 82] has been measured. An unexpected outcome of our steering experiment is that, when scanning the relative position of the two beams, we found that the source of protons above the detection threshold (0.9 MeV) must be smaller than 30 μm. The analytical model allows us to reduce this estimate to 20 μm, as given by the half-width of the region in which the proton beam is steered. These estimates are much smaller than previous measurements by other groups. The reasons are likely to be the thinner targets, shorter pulses and higher pulse contrast used in this experiment. Assuming that electrons, injected at an angle θ, recirculate inside the target during the laser pulse and are ballistically reflected at the surfaces (see Sec. 3.4.3 for a discussion on recirculation), we obtain a very rough estimate of the sheath radius at the rear; $r + (c\tau + L)\tan\theta$, where r is the focal spot radius, θ is the half opening angle of the injected electron distribution and τ is the pulse duration. For a full opening angle of 30° and our experimental parameters, the estimated sheath diameter is 14 μm. This value is consistent with our experimentally determined upper limit of 20 μm. This is much smaller than what is expected in the experiments performed using the Vulcan Petawatt laser, described in Secs. 3.4.4–3.4.7. There the laser pulse duration is approximately 1 ps and 25 μm target foils are commonly used. Under such conditions, the expected sheath diameter, using this very crude estimate, is more than 180 μm. Indeed, as discussed in Sec. 3.4.7, the lateral transport of electrons is very important and does not only contribute to a larger source diameter, but can also lead to ion emission several millimeters from the focal spot (see Paper **X**).

Controlled ion beam focusing

In conclusion, a method that facilitates optical control of the spatial distribution has been demonstrated. A line focus was used for the first-order application, beam steering. It is likely that using other, tailored, intensity distributions, other aspects of the spatial distribution could be controlled. For example, a ring-shaped beam might facilitate control of the ion beam divergence through a dynamic change of the target curvature (schematically illustrated in Fig. 3.34). This could bring the proton beam to focus at an adjustable distance from the foil. This would indeed be interesting for several applications such as for example ignition of fusion plasmas [5] or injection into large accelerators since, by controlling the divergence directly at the source, a higher charge could be delivered into the limited acceptance angle of the injection optics.

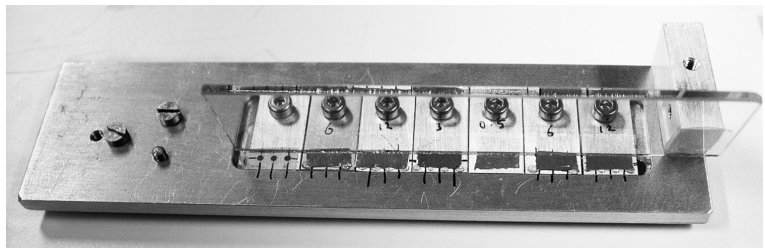

Figure 3.36. *Assembly of the uncoated glass plasma mirror and the holder for the ultrathin targets. The foils are mounted on cartridges, each of which has three individual shot positions, separated by 1 mm.*

3.4.3 Acceleration from ultrathin targets using ultrahigh contrast pulses

The maximum proton energy is determined by the electron temperature, and the electron density in the accelerating sheath at the rear surface of the target (Eq. 3.23). The temperature can be increased by using a larger (and probably more expensive) laser system, providing a higher intensity in the laser pulse driving the acceleration. That option is explored in Sec. 3.4.5 while this section explores a method by which the maximum proton energy can be maximized for given laser pulse energy.

If the target thickness is decreased, the transverse spreading of the electron beam during passage through the target is reduced, resulting in a higher electron density in the sheath at the rear surface. This results in a higher accelerating field and higher proton energies. But there is a limit to how thin foils can be used for efficient acceleration [77]. In particular, as discussed in Sec. 3.4.1, the ASE pedestal interactions can significantly change the properties of the foil prior to the main pulse interaction. In this experiment, which resulted in Paper **V**, the intensity contrast ratio was increased to $\sim 10^{10}$ by using plasma mirrors (see Sec. 2.3). This facilitated efficient acceleration using ultrathin foils with thickness down to 20 nm.

Experimental arrangement

In this experiment, the Lund multi-terawatt laser was used. A schematic view of the experiment is shown in Fig. 3.35. A close-up view of the uncoated glass plasma mirror and target holder assembly is shown in Fig. 3.36. The glass substrate is positioned 3 mm from the laser focus, leading to a main pulse intensity of 10^{15} W/cm^2 on the mirror surface. At a contrast of more than 10^8, the ASE intensity is well below the ionization threshold of the glass and only the Fresnel reflection of the ASE pedestal reach the target. The main pulse is much more efficiently reflected during plasma formation, leading to an on-target contrast ratio of 10^{10}.

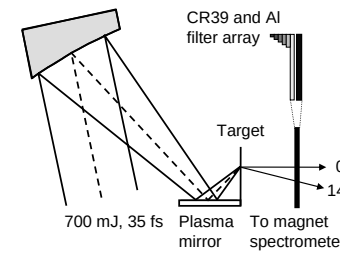

Figure 3.35. *Schematic illustration of the setup used for contrast enhancement and proton acceleration from ultrathin targets. The measured reflectivity of the plasma mirror leads to an on-target laser energy of 300 mJ and a pulse contrast of* 10^{10}.

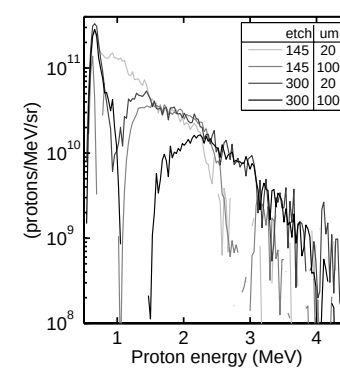

Figure 3.37. *To improve the dynamic range of the spectral measurements, a dual slit with two different widths was used in front of the magnet. In addition, the CR39 was periodically removed from the etch bath and scanned. The final spectrum is obtained by merging spectra from several etch times and the two slits.*

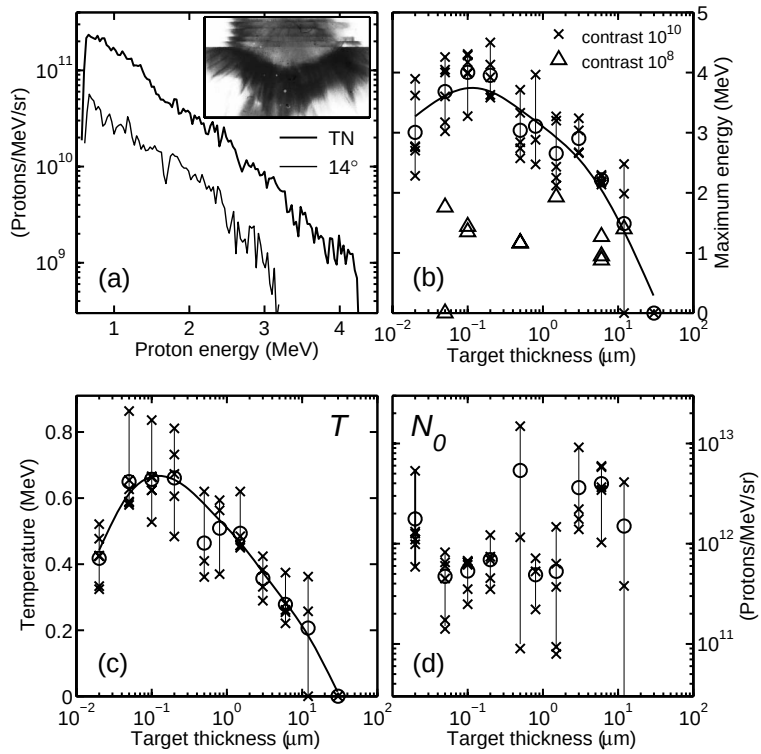

Figure 3.38. *(a) Data obtained for each laser shot. Two energy spectra, collected at different angles, and divergence data from the beam profile monitor are used to characterize the proton beam. This particular example is from a 50 nm Al foil. (b) Maximum proton energy at high, and ultra-high laser pulse contrast. (c) Effective temperature, measured along the target normal direction. (d) Effective proton number N_0. Individual data points are shown by crosses and open circles are average values for each thickness.*

The main diagnostics of the proton beam are two magnetic spectrometers and a beam profile monitor, which samples the lower half of the beam and is covered by an array of stopping filters.

Improvement of the detection system

Two techniques for improving the dynamic range of the spectral measurement were developed during this experiment. The main limitation is saturation of the CR39 detector since, during etching, the size of the pits increases and eventually they overlap. Normally, the number density is higher in the low energy range and, in addition, pits induced by low energy protons grow quicker during etching. Because of these two effects, the detector will saturate in the low energy range after a certain time in the etch bath. On the other hand, pits in the high energy range will only become visible after a longer etching time. Therefore, to

improve the dynamic range, two slits with different widths were placed side-by-side in front of each magnet yielding two parallel exposures with different intensity on each shot. In addition, each CR39 was periodically removed from the etch bath and scanned by the automatic pit counting system described in Sec. 3.3.1. The final spectra were obtained by merging data from different slit widths and etching times as illustrated in Fig. 3.37. These improvements have increased the dynamic range of the spectral measurements by approximately one order of magnitude.

Enhanced acceleration

Data from Al foils with different thickness in a range covering three orders of magnitude, from 30 μm down to 20 nm, were obtained. Typical proton spectra, registered by the on- and off-axis spectrometers, are shown in Fig. 3.38(a). These show an almost single temperature, Maxwellian-like distribution and for each shot, the number of protons/MeV/sr, $N(E)$, is fitted by a simple distribution of the form $N(E) = N_0 \exp(-E/T)$. The fitted temperature and the maximum detectable proton energy are shown as functions of the target thickness in Fig. 3.38(b) and (c). Both these quantities reach their maximum for a thickness around 100 nm and then decrease slightly for the 20 nm targets. On the contrary, the parameter N_0 shows no particular trend with target thickness, as shown in (d). For comparison, Fig. 3.38(b) also shows the maximum proton energy when the plasma mirror is not used. It is clear that enhanced acceleration for ultrathin targets is only obtained with ultrahigh contrast pulses.

Proton beam reconstruction

To estimate the laser-to-particle beam conversion efficiency, data from all three diagnostics, exemplified in Fig. 3.38(a), are used to reconstruct the proton beam profile. Assuming the beam to be circularly symmetric, the number of protons/MeV/sr is a surface of the form $N(E, \theta)$ where θ is the emission angle. The two spectrometers give two lines on this surface, $N(E, 0°)$ and $N(E, 14°)$. The beam profile data gives the energy dependent divergence which is a line where $N(E, \theta) = 0$. The reconstructed surface is obtained by spline interpolation between the three lines. Figure 3.39 shows an example of a reconstructed proton beam together with measured data. The total beam energy is calculated by integration, over all angles and from the lower cut-off energy of the beam profile measurement (0.9 MeV). The total beam energy and the total number of protons, above 0.9 MeV, are shown as function of target thickness in Fig. 3.40. By integrating $N(E, \theta)$ over energy only, the radial energy distribution is obtained, as exemplified in Fig. 3.41.

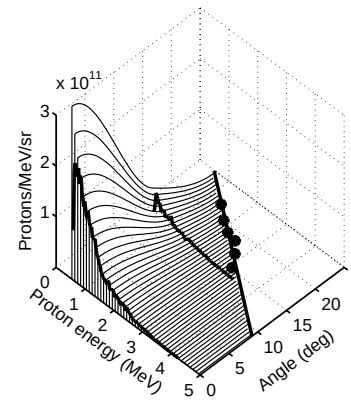

Figure 3.39. *3D interpolated surface illustrating the method for calculating of the conversion efficiency. The spectra and divergence data are the same as in Fig. 3.38(a).*

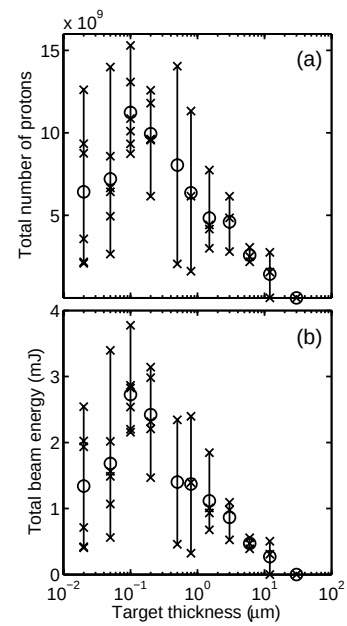

Figure 3.40. *For protons above the detection threshold of the beam profile measurement (0.9 MeV): (a) Total integrated proton numbers. (b) Total integrated proton beam energy.*

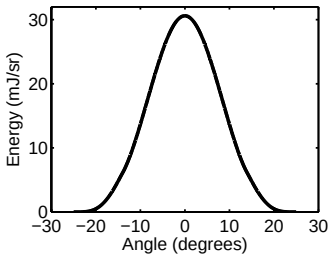

Figure 3.41. *Radial energy distribution, corresponding to the data in Fig. 3.38(a), and obtained by integration of the surface in Fig. 3.39.*

Regimes of enhanced acceleration

While decreasing the target thickness, we identify two regimes of enhanced acceleration. When the target thickness is much larger than the focal spot, the enhancement is mainly a geometrical effect due to the reduced spreading of the electron beam during passage through the target. When the thickness is much smaller than the focal spot (< 3 μm), the enhancement is likely to be due to enhanced heating of the electrons. One such mechanism is recirculation [45, 83]. Electrons leaving the front with energies lower than the potential energy of the sheath at the rear surface are trapped inside the foil and reflected back and forth between the the target surfaces. Upon each reflection at the front surface, energy can be gained from the laser field as long as the laser pulse is present. Recirculation effects become important when the pulse duration is longer than the roundtrip time of the electrons, $\tau_L > 2L/c$ where L is the target thickness. The hypothesis that the observed enhancement is due to more efficient electron heating is strengthened by the fact that, as shown in Fig. 3.38, approximately the same number of protons are accelerated for different thicknesses while the proton beam temperature exhibits a clear optimum for ultrathin foils.

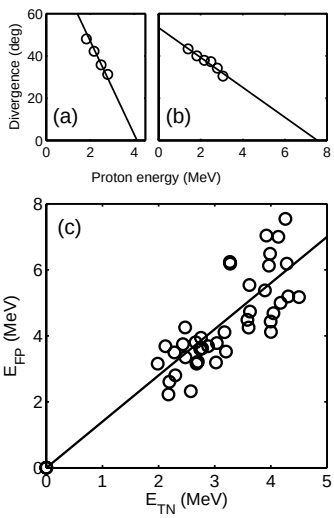

Figure 3.42. *(a) and (b) Energy dependent proton beam divergence for two typical beam profiles, obtained using 50 nm Al foils. (c) Correlation between the maximum energy measured by the target normal spectrometer (E_{TN}) and by extrapolating the linear fit to the divergence data (E_{FP}).*

Beam divergence and maximum energy

The following discussion concerns the possibility to use the divergence data to assess the maximum proton energy. The filter array in front of the CR39 enables measurement of the spatial distribution above chosen threshold energies. On most shots, as for the two examples in Fig. 3.42(a) and (b), the beam divergence angle shows an approximately linear dependence on the proton energy. The divergence data is characterized by a fit of the form $\theta = b - a \cdot E$. The maximum energy can then be estimated by extrapolation to zero divergence, $E_{max} = b/a$. As shown in Fig. 3.42, there is a clear correlation between of the maximum energy measured by the target normal spectrometer, E_{TN}, and the "footprint monitor", E_{FP}. The divergence measurement consistently gives a value which is 40% higher than the spectrometer measurement. The relative error is 18%, measured by the standard deviation of $1.4E_{TN}/E_{FP}$.

Observation of mono-energetic features

Normally, protons accelerated by the TNSA mechanism exhibit a continuous thermal energy spectrum. Several schemes have been suggested for the production of mono-energetic protons. Esirkepov *et al.* [84] proposed using a transversely limited proton source layer at the rear surface, with a diameter much smaller than the sheath. This scheme was later adopted by Schwoerer *et al.* [85] to

produce a quasi-monoenergetic proton beam. Another scheme, based on using a thin source layer of carbon was adopted by Hegelich *et al.* [86] to generate a quasi-monoenergetic carbon ion beam.

None of these schemes were used in our experiment and on the vast majority of shots, thermal spectra, such as the examples in Fig. 3.38, were registered by both spectrometers. However, on some occasional shots, the off-axis spectrometer registered clearly non-thermal spectra. An example is shown in Fig. 3.43, obtained for a 3 μm Al foil. At this point it is not yet clear what generates these anomalous beams. There is no systematics with target thickness, but anomalous beams were only observed at ultrahigh laser pulse contrast (i.e. when the plasma mirror was used). The observed effect could be due to a change in the shape of the sheath on the rear surface. The generation of magnetic fields at the target front can significantly affect the propagation of hot electrons and it would therefore be interesting to study the structure of such fields at high- and low pulse contrast conditions and at the same time monitor the proton beam.

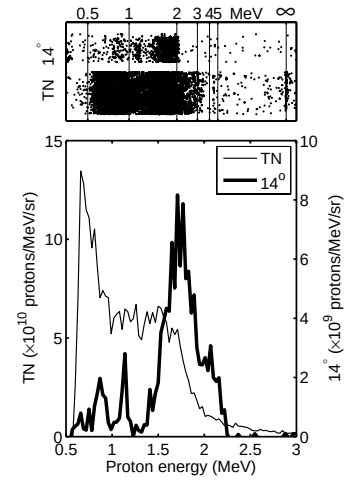

Figure 3.43. *Quasi-monoenergetic features in the off-axis spectrum. (a) Raw data, showing the coordinates of the pits on the CR39 detector behind the magnet spectrometers. (b) Extracted on- and off-axis spectra.*

3.4.4 Enhancement of the proton beam quality

In Sec. 3.4.1, we saw that a plasma expansion at the target front can drive a shock through the target that can significantly influence the acceleration dynamics. In this section, we concentrate on the effects of a long plasma density scale length at the target front. Our preliminary findings are reported in Paper **VI**. In that experiment, which used the 100 TW arm of the Vulcan laser, a separate low energy nanosecond laser pulse was incident on the target, driving a plasma expansion prior to the short pulse (SP) arrival. The key observation was that focusing the long pulse (LP) to an annular intensity profile, resulted in a significant enhancement of the quality of the spatial distribution of the proton beam as well as in an increase of the maximum proton energy.

We have recently completed a follow-up experiment, this time using the higher intensity and shorter pulses available at the Vulcan Petawatt laser. This experiment confirmed our findings in Paper **VI**, but this time we also obtained valuable additional data on the pre-plasma expansion by using an interferometric probe (Sec. 3.3.3). We have confirmed that the plasma expansion at the front indeed is the source of the enhancement and that focusing the LP to a top-hat intensity profile also yields enhanced proton beams. The following discussion refers to this follow-up experiment.

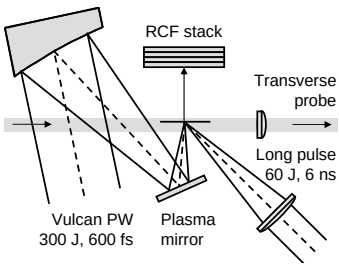

Figure 3.44. *Schematic view of the experiment described in Sec. 3.4.4.*

Experimental arrangement

The experiment is performed using the Petawatt arm of the Vulcan laser. A short pulse (SP) with an energy of 300 J and a duration 600 fs is used to drive the proton acceleration. A plasma mirror is positioned in the focusing beam to suppress ASE. With a measured reflectivity of 55%, the estimated on-target intensity is 4×10^{20} W/cm^2. At focus, 25 μm thick Cu foils are positioned at 5° angle of incidence. The arrangement is schematically illustrated in Fig. 3.44. A secondary, 6 ns long pulse (LP) with an approximately flat-top temporal profile, is focused using an $f/10$ lens to either an annular, or a top-hat intensity profile. The leading edge of the pulse can be adjusted to arrive at a given time relative to the SP, but is always chosen to guarantee that the shock front is well inside the target and has not broken through the rear surface when the SP arrives on the target. The intensity of the LP is varied in the range 3×10^{11} to 1×10^{13} W/cm^2. Both beams have a wavelength of 1053 nm. The spatial distribution of the accelerated protons is measured simultaneously for different proton energies using a stack of radiochromic film (RCF) with a hole machined in it to provide a line of sight to a Thomson ion spectrometer. The plasma expansion is diagnosed by interferometry using a transverse probe with a wavelength of 527 nm, arriving at the target 5 ps after the main pulse interaction.

Pre-plasma expansion

In the experiment described in Paper **VI**, the plasma expansion was driven by focusing the LP into an annular ring, but at that time we were not able to characterize the plasma evolution. During the follow-up experiment, we recreated similar conditions and studied the temporal evolution of the pre-plasma. The LP is focused into an annular ring with a peak intensity of 2×10^{12} W/cm^2 and the relative delay between the SP and LP is varied. The results, illustrated in Fig. 3.45, show interesting dynamics. The annular plasma expands out from the target, longitudinally, but also laterally. At 0.5 ns delay, we see a smooth plasma expansion. A channel, created in the pre-plasma by the SP during its propagation toward the target is clearly visible. The bright spot in the shadow of the expanding target is self-emission from the plasma following the SP interaction close to the critical surface. After 2.3 ns, the transverse plasma expansion has resulted in a collision in the center of the ring and a plasma jet is ejected from the target at high velocity. The center of the jet coincides with the SP propagation axis and at 3.6 ns delay, the same as in Paper **VI**, something unexpected happens. Strong emission appears in the center of the jet, far from the critical surface. The reproducibility of this anomalous plasma emission was confirmed several days

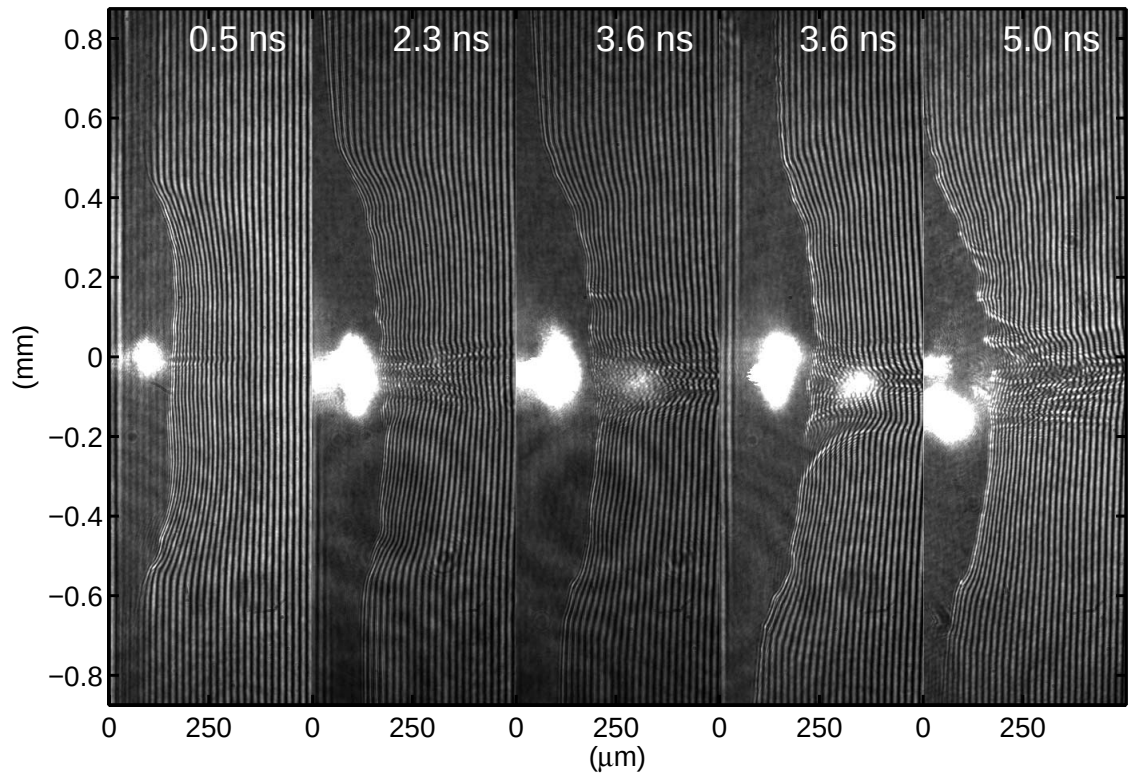

Figure 3.45. *Interferograms, obtained using a frequency doubled probe pulse, showing plasma expansion following LP irradiation. The target is a 25 μm Cu foil and the LP is focused to a 470 μm diameter ring and to a peak intensity of* 2×10^{12} *W/cm*^{2}*. The laser pulse has a flat-top temporal profile and the delay between the leading edge of the LP and the SP is varied. The experimental conditions of Paper* ***VI*** *are reproduced at a delay of 3.6 ns.*

later, also shown in Fig. 3.45. At longer times (5.0 ns) the secondary emission is no longer visible and plasma instabilities (e.g. Rayleigh-Taylor) are strongly affecting the plasma expansion.

It is not yet clear what is causing the secondary emission, but it is likely to be associated with electron acceleration. Recently, it has been shown that the breaking of a plasma wave and the swift acceleration of electrons can generate a broadband emission [87]. There is a possibility that, in the underdense plasma jet, the SP excites a plasma wave that is driven to the point of breaking and that the observed emission is wavebreaking radiation. However, spectral measurements would be necessary to confirm the broadband spectral signature of such radiation.

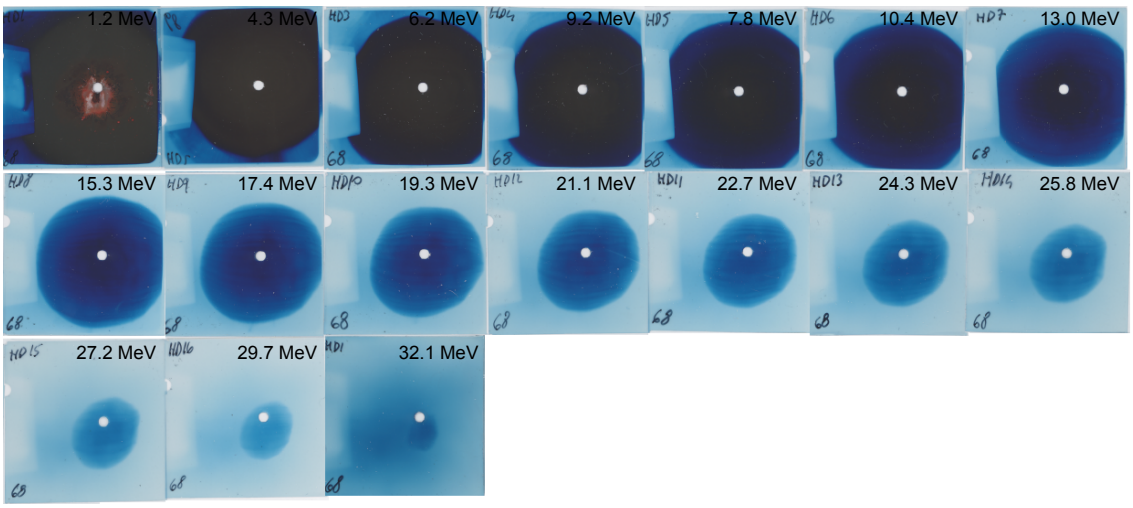

Figure 3.47. *When using the LP, proton beams with enhanced dose distribution uniformity and maximum energy are obtained. In this example, the LP-SP delay is 3.6 ns and the LP is focused to a 470 μm diameter, top-hat circular intensity profile, with a peak intensity of* 2×10^{12} *W/cm*^{2}*. The intensity of the SP is* 4×10^{20} *W/cm*^{2} *and the target is a 25 μm Cu foil. This data should be compared to the reference shot in Fig. 3.18, for which no LP was present on the target.*

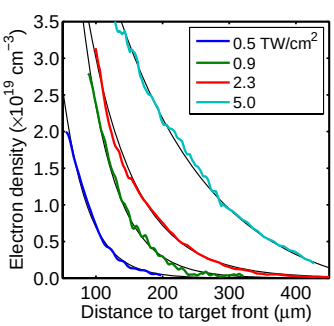

Figure 3.46. *Electron density profile in front of the target for a LP-SP delay of 0.5 ns. The scale-length increases when the plasma is heated at higher intensities.*

Influence of a long pre-plasma gradient

In contrast to the structured expansion resulting from the annular LP illumination in Fig 3.45, focusing the LP to a top-hat intensity profile produces a smooth and stable plasma expansion. Figure 3.46 shows the retrieved on-axis electron densities of the expanding plasma for a LP-SP delay of 0.5 ns and for a LP intensity between 0.5 and 5.0 TW/cm^2. As expected, when the plasma is heated at higher intensities, the plasma expands faster which creates a longer plasma scale length.

In the absence of the LP, proton beams with a broad energy distribution are detected from the rear of the target. The representative example of the spatial distribution in Fig. 3.18, shows typical modulations in the proton dose. Such modulations may arise due to the roughness of the target surface, modulations in the high intensity drive beam, and/or instabilities during electron transport through the foil. With the addition of the LP, focused to a top-hat intensity distribution, we observe a significant improvement in the spatial distribution of the accelerated proton beam. As shown in Fig. 3.47, the enhancement is primarily a significantly improved proton dose smoothness and a higher degree of beam circularity. We also consistently observe an increase of the maximum proton energy. As shown in Fig. 3.48, we find that the proton energy increases when the LP intensity is low and induces a relatively small plasma expansion, but decreases again as the LP intensity is increased further. The measured front side

electron density profiles corresponding to these spectra are shown in Fig. 3.46. A similar trend is found when the LP-SP delay is varied, with a clear optimum in the maximum proton energy at 0.5 ns as shown in Fig. 3.49. While the proton energy decreases for long delays or high intensities, the beam profile uniformity is constantly improving when these parameters are increased. It therefore seems possible that, by careful selection of the intensity and delay of the LP, the proton beam generation could be optimized for both high spatial quality and high maximum energy.

The increase of the maximum proton energy is likely to be due to an increased absorption in the pre-plasma, leading to a higher laser-to-hot-electron conversion efficiency. The processes behind the enhanced smoothness and circularity of the proton beam are at this moment not completely understood, but numerical simulations are being performed to elucidate the complex dynamics. It is expected that during propagation through the underdense plasma, the ultra-high intensity laser pulse is highly subjected to self-focusing and filamentation. The pre-plasma gradient could also affect the divergence of the generated electron beam due to holeboring effects [88].

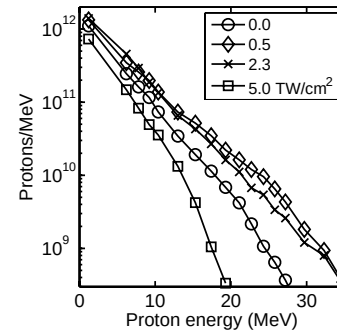

Figure 3.48. *Proton energy spectra as function of LP intensity for a LP-SP delay of 0.5 ns.*

3.4.5 Scaling with intensity and pulse duration

As discussed in the preamble of this chapter, there are many potential applications of laser-accelerated proton beams. Some of these, such as proton oncology of deep-seated tumors, require proton energies of about 200 MeV, which is more than the highest reported laser-accelerated proton energy of 60 MeV [22]. To investigate the feasibility of using high-power lasers as drivers of proton acceleration for such high energy applications, many research groups have investigated the scaling of laser-accelerated proton energies and efficiencies as function of laser parameters such as intensity, energy and pulse duration. This work has been experimental [24, 89, 90] as well as theoretical [91–93]. Of particular interest is a study reported by Fuchs *et al.* [94] in which scaling using pulses with durations in the range 0.15-10 ps and intensities from 10^{18} to 6×10^{19} W/cm^2 is investigated. An isothermal expansion model [54], similar to the one described in Sec. 3.2.1, is used to predict that a proton energy of 200 MeV could be achieved at an intensity of 5×10^{20} W/cm^2 and a laser pulse duration of 1 ps. Other groups have used PIC simulations to predict energies of 170 MeV at 1×10^{21} [85] and 380 MeV at 2×10^{21} [95].

In the experimental study, reported in Paper **VII**, we use the Vulcan Petawatt laser to extend the laser energy and intensity parametric range over which proton scaling is investigated to 400 J and 6×10^{20} W/cm^2, respectively. Using Al targets with thicknesses of 10 and 25 μm, the maximum proton energy is measured as function of laser intensity using nuclear activation of stacks of Cu plates. In the parameter scan shown in Fig. 3.50(a), the pulse

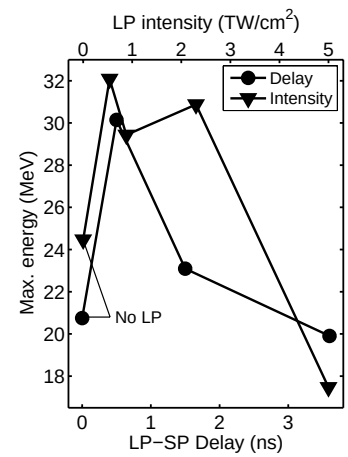

Figure 3.49. *Maximum energy as function of LP intensity, for a constant LP-SP delay of 0.5 ns and as function of the LP-SP delay, for a constant intensity of 1.2 TW/cm^2.*

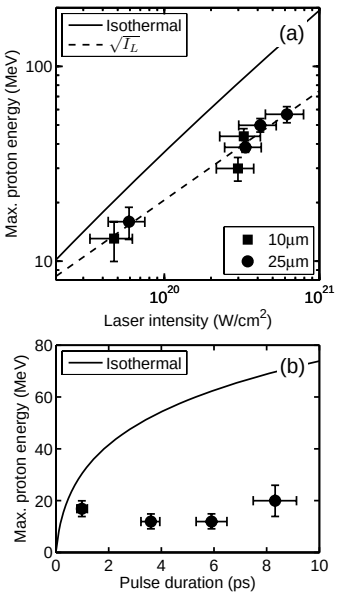

Figure 3.50. *Maximum proton energy as function of: (a) laser intensity at constant $\tau_L = 1$ ps and (b) pulse duration at constant $I_L = 8 \times 10^{19}$ W/cm^2. Solid lines show the results from the isothermal expansion model, described in the text.*

duration is held constant at 1 ps, while the laser energy is varied. At the highest intensity, 6×10^{20} W/cm^2, protons with energies up to 55 MeV are measured. In this higher intensity range, the maximum proton energy is found to scale as $\sqrt{I_L}$, as shown by the dashed line in Fig. 3.50(a). This confirms and extends the intensity scaling found at lower intensities [24].

Next, the laser intensity is held constant at 8×10^{19} W/cm^2 while the pulse duration is varied between 1 and 8 ps with a corresponding variation of the laser energy, up to a maximum of 400 J. The variation of the pulse duration is accomplished by adjusting the distance between the gratings in the stretcher. As shown in Fig. 3.50(b), the maximum proton energy shows no particular dependence on the pulse duration and stays approximately constant at an average value of ∼15 MeV.

Following the work by Fuchs *et al.* we attempted to use the isothermal model in Sec. 3.2.1 to fit our experimental data by using the method proposed by Kaluza *et al.* [77][1]. The results from these calculations are shown by the solid lines in Fig. 3.50. Although this simple 1D model has been widely used to fit experimental data at moderate laser intensities [77, 94], it greatly overestimates the maximum proton energy in this ultra-high intensity regime. The reason is that, at lower intensities and for shorter pulses, the plasma expansion is quasi-one-dimensional during the laser pulse. A proton with a kinetic energy of 5 MeV moves only 1 μm during 35 fs, while the transverse diameter of the sheath is often of the order of several several tens of μm. At higher intensities and for longer pulses, multi-dimensional effects are increasingly more important because the length of the expansion becomes of the order of the transverse size during the laser pulse. Taking an example from Fig. 3.50(b), a proton with a kinetic energy of 20 MeV moves 500 μm during 8 ps. During this type of long longitudinal expansion, the radial expansion significantly reduces the electron density at the ion front. In addition, as the electrons transfer their energy to the ions, their temperature is reduced. Both effects lead to a reduced accelerating field and a reduced maximum proton energy. A refined expansion model that takes both transverse effects and adiabatic energy transfer into account, was developed by P. Mora as part of the analysis of the data presented in Paper **VII**. As shown in this paper, the improved model gives better, albeit still not perfect agreement with the experimental results.

[1] The following method was used: The maximum proton energy is given by Eq. 3.23 and the acceleration is terminated after the laser pulse duration, τ_L. The hot electron temperature, T_e, is determined by the laser ponderomotive potential (Eq. 3.14). The total number of hot electrons is $N_e = \eta E_L / T_e$ where E_L is the laser energy and η here is the conversion efficiency ($\sim 30\%$). The hot electron density at the rear surface is $n_e = N_e / A / c\tau_L$, where τ_L is the laser pulse duration and A is the area of the electron beam at the rear surface. For a target thickness L and a laser spot diameter d, $A = \pi(d + 2L\tan\theta)^2/4$ where θ is the half opening angle of the electron beam.

3.4.6 Heavy ion acceleration

In all the previously discussed experiments, protons are provided for acceleration by a thin layer of water and hydrocarbons on the target surface that is formed under typical vacuum conditions (10^{-5} mbar). Protons have the largest charge-to-mass ratio (q/m) and are therefore accelerated faster than other, heavier ions. The protons at the leading edge of the ion front screen the heavier ions from the accelerating field. By removing the contamination layer, efficient acceleration of also heavier ions is facilitated [96–98]. In the experiment described in Paper **IX**, contaminations at both surfaces were removed by heating the target immediately prior to and during the laser shot.

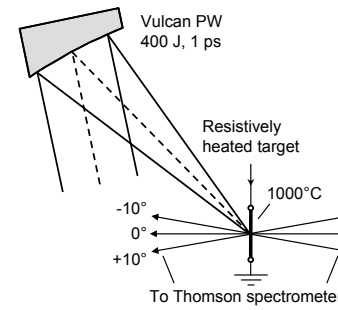

Figure 3.51. *Experimental arrangement for the experiment in Paper **IX**. Hydrogen containing contaminants are removed by resistively heating the target. Six Thomson parabolas register the heavy ion spectra in different directions.*

Experimental arrangement

The Vulcan Petawatt laser is used to drive the acceleration and is focused at 45° angle of incidence onto 25 μm thin Pd foil targets. The targets are mounted in a special conductive holder that allows a current of $\sim$1 A to be sent through the thin foils and resistively heat the foil to 1000°C. As in Paper **VII**, the laser intensity is varied between 8×10^{19} and 7×10^{20} W/cm^2 by adjusting either the pulse energy or pulse duration. Six identical Thomson spectrometers are positioned on both sides of the target, along the target normal and at $\pm 10°$ from this axis in the plane of incidence. The arrangement is schematically shown in Fig. 3.51.

Scaling with ion charge

With this setup, on average 60 different ion energy spectra are recorded in different directions, for every shot. Typically, large numbers of Pd and O ions are registered, while carbon and proton traces are weak. At the highest intensity (7×10^{20} W/cm^2), Pd ions with charge states up to 18+ are recorded with the rear side spectrometers while charge states up to 30+ are observed from the front. Assuming that field ionization by barrier suppression is the dominant ionization mechanism, field strengths of 2 TV/m and 17 TV/m are needed to produce the observed ionization states at the target rear and front, respectively [99]. The higher charge states at the target front are likely to be due to the intense fields of the laser pulse itself.

Figure 3.52(a) shows example spectra for selected charge states of Pd, emitted from the target front for a laser intensity of 2×10^{20} W/cm^2 and a pulse duration of 1 ps. In agreement with previously reported studies [24, 82, 97], the energy distribution shifts to higher energies with increasing charge. The energy spectra of the lower charge state ions are typically broad, Maxwellian-like, distributions while the higher charges exhibit plateau-like distributions.

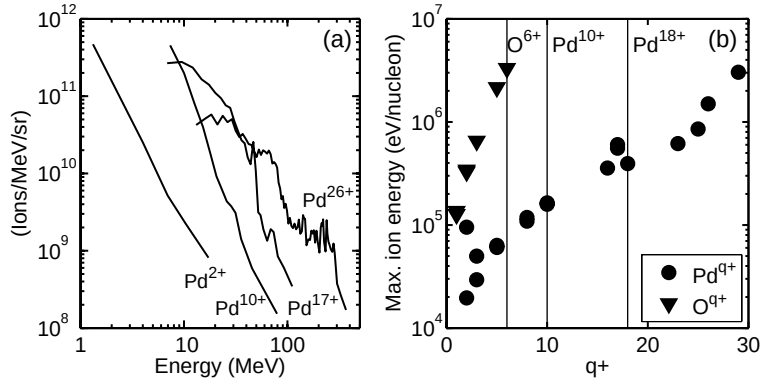

Figure 3.52. *(a) Pd ion spectra for various charge states, measured along the TN from the front surface for a laser intensity of* 2×10^{20} *W/cm*^{2}*. (b) Maximum energy of Pd and O ions. Vertical lines indicate closed shell configurations.*

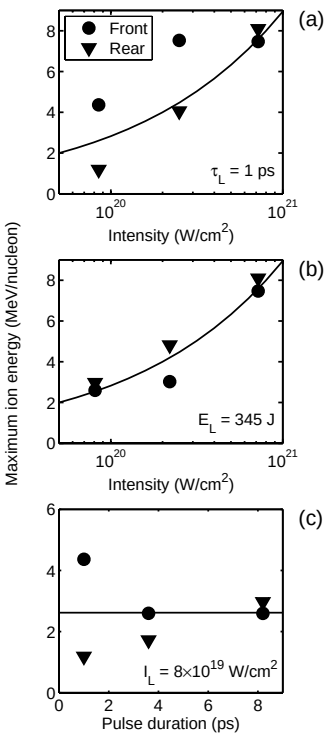

Figure 3.53. *Comparison of ion emission from the front- and back surfaces of the target. The diagrams show the maximum ion energy for (a) constant pulse duration, (b) constant energy, (c) constant intensity. Solid lines are a power fit of the form* $E_{max} = a\sqrt{I_L}$ *where a is identical for all diagrams.*

When comparing different ions and ionization states, it is informative to divide the kinetic energy with the number of nucleons in the ion species since this quantity (MeV/nucleon) is proportional to the square of the ion velocity (in the non-relativistic regime). A comparison of the maximum energy per nucleon of Pd and O ions as function of ion charge state is shown in Fig. 3.52(b). The laser intensity is 2×10^{20} W/cm^2 and the ions originate from the front surface. The highest charge states, Pd^{29+} and O^{6+}, have similar final maximum velocities ($\sim 2.5 \times 10^7$ m/s) and are leading the expansion at the ion front, while the lower charge states trail behind. Lower charge states are shielded and experience a lower accelerating field as shown in Fig. 2(c) in Paper **IX**. The vertical lines in Fig. 3.52(b) indicate closed shell configurations for Pd and O. The absence of ion traces immediately above these stable charge states is probably due to electron capture during the flight toward the spectrometer. Recombination of electrons and ions in the expanding plasma is a topic which is not very well covered in the literature but it could potentially have an influence on the ion yield from laser-driven ion accelerators. Normally, the beam of fast atoms mark the zero deflection axis of the Thomson spectrometer, but perhaps the in-flight recombination could also be harnessed to generate an intense beam of fast atoms.

Scaling with laser parameters

Similar to the study in Sec. 3.4.5 we vary the laser energy and pulse duration to investigate the scaling of ion acceleration. Figure 3.53 shows a comparison of the maximum energy per nucleon of all different ion species emitted from the front and rear surfaces of the foils. In (a), the pulse duration is kept constant at 1 ps while

the energy is varied between 40 and 345 J. In (b), the laser energy is kept constant at 345 J and the pulse duration is varied between 1 and 8.2 ps. In (c), both the pulse duration and the laser energy are varied to keep the laser intensity constant at $8(\pm 0.5) \times 10^{19}$ W/cm^2. Similar ion energies are observed in both directions although, on average, ions with higher velocities are detected from the front surface. The maximum ion energy is broadly found to scale as $\sqrt{I_L}$ and the same constant of proportionality is used to fit all three data sets in Fig. 3.53 (shown by the solid lines). As in the study in Sec. 3.4.5, we find no particular dependence of the maximum ion energy on the pulse duration when the intensity is held constant.

3.4.7 Long lateral electron transport

An unexpected result from the experiment described in Sec. 3.4.6 was the observation of several sources of ion emission. Multiple sources were observed for heated as well as unheated targets and for several different target materials. As explained in Paper **X**, the secondary emission is identified as originating from the edges of the target foil even though the edges are sufficiently far away from the focal spot that the expanding electron cloud cannot reach them until a long time (several ps) after the laser pulse. This leads to the conclusion that lateral electron transport continues long after the laser pulse has decayed and that electron refluxing in the foil plays a vital role for the spatio-temporal evolution of the accelerating electric fields.

The experimental arrangement is the same as in Paper **IX** (Fig. 3.51) and data from the rear side target normal Thomson spectrometer is used to illustrate the observation of multiple ion sources. Fast neutral atoms, resulting from electron-ion recombination during the flight toward the detection system are unaffected by the fields in the spectrometer and are normally used to locate the zero deflection axis of the spectrometer. In front of the spectrometer is a collimating pinhole, so while the main purpose of the spectrometer is to measure the energy spectrum of the emitted ions, it also effectively works as an ion pinhole camera. In particular, a demagnified image of the target is produced by the fast neutral atom beam on the CR39 detector. For relatively wide target foils (∼1 cm), the neutral image shows a single spot with a diameter corresponding to the projection of the pinhole. However, for smaller targets, several emission sources can be discerned, as shown by the example in Fig. 3.54 (see also Fig. 1 in Paper **X**). For this particular shot, the laser was defocused on a 10 μm heated Au foil to a 40 μm diameter (FWHM) spot and an intensity of 1×10^{19} W/cm^2. Most ions are emitted from the central region, opposite to the laser focal spot, but significant yields of ions are also observed from the edges of the 4 mm wide target

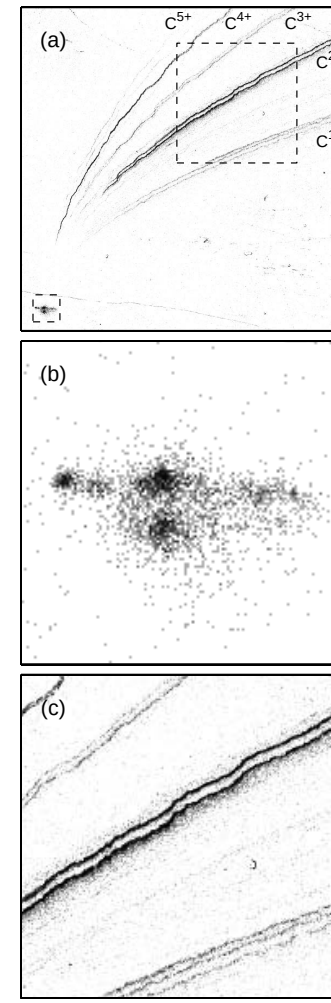

Figure 3.54. *(a) Spatial mapping of the pit distribution on the CR39 detector in the dispersion plane of a Thomson spectrometer. Mainly carbon ions are detected. Shot details are given in the text. (b) Enlarged region corresponding to fast neutral atoms that are undeflected in the spectrometer fields. Four separate ion source regions are clearly visible. (c) Enlarged region showing multiple carbon ion tracks. Each track originate from one of the source regions in (b).*

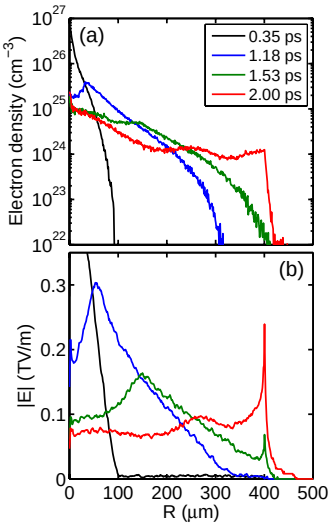

Figure 3.55. *Long lateral electron transport as observed in the* LSP *simulations in cylindrical geometry and for a target disc with 400 μm radius. (a) Electron density inside the target foil. (b) Absolute value of the electric field at the rear surface of the foil.*

and from the edge of a small 50 μm diameter witness hole which is machined in the target, 500 μm from the focal spot, for alignment purposes. These features are also reproduced as multiple tracks of many of the different charge states of carbon ions. Each track can be identified as originating from one of the four sources. By assuming field ionization by barrier suppression as being the main ionization mechanism and by identifying the highest charge state emanating from each source point, the maximum electric field strength at each source can be deduced; see Table I in Paper **X**. Determining the maximum energy of each track gives an estimate of the acceleration time at each source.

The observation of ion emission from the edges of the target implies that electrons are transported over long distances for long times after the laser pulse has passed. This has been verified in 2D cylindrical computer simulations (performed by R. Evans) using the LSP hybrid plasma simulation code [100]. This code employs a kinetic description of the energetic electrons and a fluid description of the bulk of the target. In the simulations, the target is a 10 μm thin disc with a radius of 400 μm. The laser interaction is not directly modeled, so instead a corresponding distribution of energetic electrons is created. As the electrons pass through the target, they are reflected in the expanding Debye sheath on the rear surface. The motion of the sheath leads to a reduction of the longitudinal momentum of the reflected electrons while the lateral momentum is relatively unaffected. As the electrons reflux within the foil many times, they eventually form a radially expanding charge cloud and a lateral current toward the edge of the target while a cold return current is going toward its center. Figure 3.55(a) shows the evolution of the electron density inside the bulk of the target. When the electrons reach the edge the target, the expansion is halted due to the absence of a return current and electrons are eventually reflected due to the build-up of a large electrostatic field, as shown in Fig. 3.55(b).

In Paper **X**, we use ion emission as a diagnostic of long distance electron transport and in particular we show that ion emission can provide detailed information on the strength and duration of generated electric fields. Typical diagnostics used in experimental investigations of electron transport in solid targets involve measurement of K_α emission from buried layers [101, 102] which does not give this type of information. It will be interesting to see to what extent spatially resolved measurements of ion emission will be used in the future to diagnose electron transport in solid density laser-plasma interactions.

Chapter 4

Electron acceleration

The idea to accelerate electrons in plasma waves, excited by intense laser pulses was suggested by Tajima and Dawson [103] in 1979. In their pioneering paper, they propose to use the large electric fields in a plasma wave for particle acceleration. In this scheme, the plasma wave oscillation is excited when electrons are collectively displaced by the ponderomotive force of an intense laser pulse. The plasma wave propagates with a phase velocity close to the speed of light in the wake behind the intense laser pulse (hence the term wakefield acceleration). This means that highly relativistic electrons can move in phase with the plasma wave and 'surf' the wave potential over relatively long distances.

The interest in plasma wave acceleration stems from the fact that extremely large accelerating fields can be generated. As shown in Chapter 3, electric fields of the order of several TV/m can result from intense laser-plasma interactions. This is four orders of magnitude higher than the fields achievable with current state-of-the-art superconducting RF technology. Potentially, by using a plasma, the length of future accelerators could be reduced by the corresponding factor.

In early laser wakefield acceleration experiments electron beams with continuous, Maxwellian-like energy spectra were produced [104, 105]. For most applications, a peaked distribution with a small energy spread is desirable, if not necessary. Therefore, significant interest was raised when, in 2002, a new regime of laser-wakefield acceleration (the so-called 'bubble' regime), resulting in quasi-monoenergetic electron energy distributions, was identified in kinetic plasma simulations by A. Phukov and J. Meyer-ter-Vehn [106]. Their simulations suggested that laser pulses with durations and energies beyond the capabilities of existing laser facilities were needed. However, only two years later, three laboratories in the USA, UK and France independently reported generation of quasi-monoenergetic electron beams from

laser-wakefield accelerators [107–109]. Following this important breakthrough, we have, in collaboration with scientists from the United Kingdom (Imperial College), performed systematic studies of this novel type of quasi-monoenergetic wakefield acceleration in Lund.

This chapter presents these experimental studies, performed using the Lund multi-terawatt laser as the driver, of the generation and optimization of laser-produced quasi-monoenergetic electron beams. Electrons with kinetic energies up to 200 MeV were produced in less than 2 mm acceleration length. As reported in Paper **XI**, we have found that, in the quasi-monoenergetic regime, the electron bunch originate from the first plasma wave period, and that, if the laser pulse duration is longer than half the plasma wave period, the electrons interact with the laser field during the acceleration which increases the transverse emittance along the polarization direction. A very important aspect, that needs to be addressed before these beams will be used in many prospective applications, is how to improve the stability of the acceleration process. This is discussed in Papers **XII** and **XIII**.

However, before discussing the experimental methods and results in Secs. 4.2 and 4.3, the physics of laser-wakefield accelerators is briefly outlined in Sec. 4.1.

4.1 Laser-wakefield acceleration

This section gives an overview of the main physical processes of laser-wakefield accelerators and the most important concepts, such as wave steepening, wave breaking, trapping and acceleration are introduced. The necessary conditions for generation of quasi-monoenergetic bunches are identified and the maximum electron energy gain is discussed. Finally, the propagation of ultrashort and ultraintense laser pulses in underdense plasmas are discussed.

4.1.1 Plasma waves

In a laser-wakefield accelerator, a plasma wave is excited by the ponderomotive force of the laser pulse, which pushes electrons away from regions of high intensity while the plasma ions remain immobile due to their much lower charge to mass ratio. The resulting charge displacement generates an electric field which causes the electrons to recoil and oscillate around their equilibrium positions. This oscillation has a characteristic frequency (the plasma frequency; see Sec. 3.1.3) that only depends on the equilibrium electron density, n_e. The expression for the plasma frequency is repeated here for convenience;

$$\omega_p = \sqrt{\frac{e^2 n_e}{\epsilon_0 m_e}}\,. \tag{4.1}$$

The plasma wave travels behind the laser pulse with a phase velocity that equals the group velocity of the laser pulse in the plasma. Normalized to the speed of light ($\beta_p = v/c$), the plasma wave moves with a speed;

$$\beta_p = \sqrt{1 - n_e/n_c}\,, \tag{4.2}$$

where $n_c = \epsilon_0 m_e \omega_L^2/e^2$ is the critical density for which the plasma frequency is equal to the laser frequency. The relativistic factor corresponding to the phase velocity of the plasma wave is $\gamma_p = 1/\sqrt{1-\beta_p^2} = \sqrt{n_c/n_e}$. The plasma wave has a wavelength

$$\lambda_p = 2\pi c \beta_p/\omega_p\,. \tag{4.3}$$

For typical plasma electron densities and laser wavelengths, β_p is very close to unity, and frequently, as in Papers **XI**, **XII** and **XIII**, it is ignored when estimating the plasma wavelength.

Numerical example. *The plasma wavelength, λ_p, in μm, wave velocity, β_p, relative to the speed of light, and the associated relativistic factor, γ_p, for different values of the electron density, n_e, in units of 10^{19} cm^{-3}, for a laser wavelength of 800 nm, corresponding to a critical density of 1.7×10^{21} cm^{-3}.*

n_e	β_p	γ_p	λ_p
0.1	*0.9997*	*42*	*33*
0.2	*0.9994*	*30*	*24*
0.5	*0.9986*	*19*	*15*
1	*0.9971*	*13*	*11*
2	*0.9942*	*9.3*	*7.4*
5	*0.9855*	*5.9*	*4.7*
10	*0.9709*	*4.2*	*3.2*
20	*0.9408*	*3.0*	*2.2*
50	*0.8444*	*1.9*	*1.3*
100	*0.6526*	*1.3*	*0.69*

Linear plasma waves

If the amplitude of the density perturbation, δn, associated with the plasma wave is small, $\delta n/n_e \ll 1$, the oscillation is harmonic;

$$\Delta n = \delta n \cos(k_p x - \omega_p t)\,, \tag{4.4}$$

where $k_p = 2\pi/\lambda_p$. The electric field associated with the charge perturbation is readily obtained by integration of Poisson's equation, which gives

$$\Delta E = -E_0 \left(\frac{\delta n}{n_e}\right) \sin(k_p x - \omega_p t)\,, \tag{4.5}$$

where $E_0 = e n_e/\epsilon_0 k_p$. Assuming a phase velocity close to the speed of light, so that $k_p = \omega_p/c$, we obtain

$$E_0 = mc\omega_p/e\,. \tag{4.6}$$

The peak electric field in the plasma wave increases with the magnitude of the charge displacement. For small perturbations, the electric field is a harmonic oscillation which is dephased with respect to the density perturbation by $\pi/4$ radians, as shown in Fig. 4.1(a).

Numerical example. *A 30 fs laser pulse resonantly excites a plasma wave at an electron density of $n_e = 3.4 \times 10^{18}$ cm^{-3}. At an intensity of 3×10^{18} W/cm^2 and a wavelength of 800 nm, it drives a plasma wave with a peak electric field of 200 GV/m.*

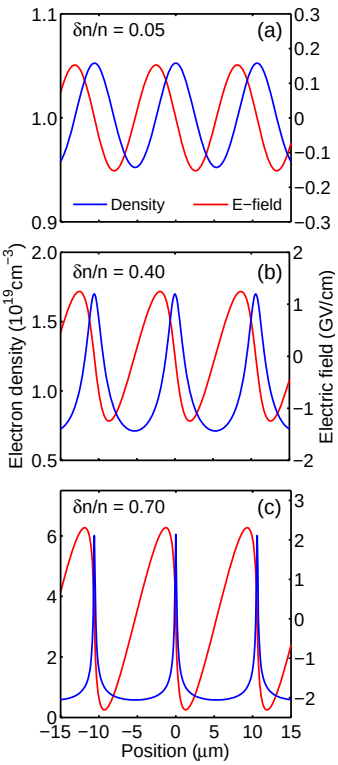

Figure 4.1. *The steepening of one-dimensional plasma waves and the resulting electric field as the magnitude of the density perturbation increases.*

Resonant plasma wave excitation

A number of theoretical articles address ponderomotive excitation of plasma waves in the laser-wakefield regime [110–112]. An important result is that there is an optimum pulse duration for which the plasma wave is resonant with the laser pulse envelope. For a Gaussian laser pulse, and for a linear plasma wave and non-relativistic laser intensities, the oscillation reaches its maximum amplitude when,

$$c\tau \approx \lambda_p/2\,, \tag{4.7}$$

where τ is the laser pulse duration (FWHM). In this non-relativistic, linear and resonant regime, the amplitude of the plasma wave grows linearly with the intensity of the laser pulse. The peak electric field is,

$$E_0 \approx 1.5\omega_p I_0/en_c c^2\,, \tag{4.8}$$

where I_0 is the laser intensity.

Non-linear plasma waves

As the laser intensity is increased, larger amounts of charge are displaced by the ponderomotive force and the amplitude of the plasma wave grows. This also means that the velocities of the electrons that make up the wave increase and, at some point, the velocities of individual electrons approaches the phase velocity of the wave. This causes the electrons to bunch up close to the peaks of the wave and the plasma wave steepens. A Fourier analysis shows that, as the amplitude of the perturbation grows, higher-order harmonics of the plasma wave oscillation are introduced and the wave form can be written [113],

$$\Delta n = n_e \sum_{m=1}^{\infty} \frac{m^m}{2^{m-1}m!} \left(\frac{\delta n}{n_e}\right)^m \cos m(k_p x - \omega_p t)\,. \tag{4.9}$$

As shown in Fig. 4.1, the waveform changes from a harmonic oscillation to a series of sharp spikes as the amplitude of the plasma oscillation increases. At the same time, the electric field waveform changes to a sawtooth function and the field reaches its maximum closer to the peak of the density oscillation. But there is a limit to the growth of the plasma wave amplitude. In particular, when $n_e \ll n_c$, the plasma wave phase velocity is close to the speed of light in vacuum and, when driven to high amplitudes, relativistic effects on the oscillating electrons become important.

Relativistic effects

At high plasma wave amplitudes, the longitudinal velocity of the oscillating plasma electrons approaches the phase velocity of the plasma wave. When $n_e \ll n_c$, this velocity is close to the speed of light and the oscillating electrons therefore experience a relativistic mass shift. This reduces the plasma frequency and the relativistic plasma wavelength becomes

$$\lambda_p' = \lambda_p \sqrt{\gamma_e}\,, \tag{4.10}$$

where γ_e is the relativistic factor of the plasma electrons which, when the electrons move at the phase velocity of the plasma wave, becomes equal to γ_p. So far, we have only considered 1D plasma waves. In a 2D (or 3D) situation, and for a focused laser pulse, the relativistic mass shift is different across the laser intensity envelope and peaks in the center of the pulse. Therefore, in the presence of the laser pulse, the relativistic plasma wavelength peaks on the laser axis, leading to curved plasma wave fronts. Figure 4.2 shows the results from a 2D particle-in-cell (PIC) simulation. The laser pulse propagates in the vertical direction toward the top of the simulation box. The color scale depicts the electron density of the plasma wave that trails behind the laser pulse.

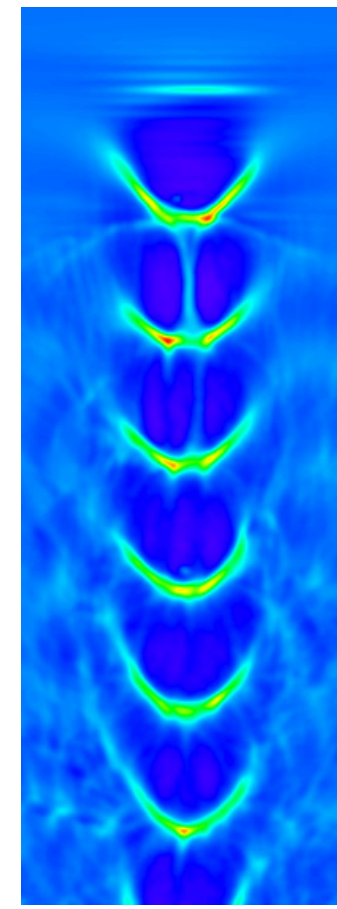

Figure 4.2. *Electron density variations in the wake of an intense laser pulse, obtained in a 2D PIC simulation using the code* OSIRIS *[114]. The laser pulse propagates toward the top of the simulation box. The curved wave fronts are due to a relativistic mass increase of the plasma electrons. Note that the laser pulse, which is shorter than the plasma wavelength, is not shown in the figure, but the electron pile-up in front of it, produced by the laser ponderomotive force, is clearly visible. Image courtesy S.P.D. Mangles.*

Pump depletion

As the laser pulse propagates through the plasma, it excites a plasma wave in its wake and energy is continuously transferred from the laser pulse to the plasma wave oscillations. At a certain point, the laser pulse is depleted and the interaction stops. We can estimate the depletion length by equating the electrostatic energy stored in the plasma wave to the energy in the laser pulse. We write the laser pulse energy as $U_L = \pi w_0^2 \tau I_0$ and the energy in the plasma wave as $U_{wave} = \pi w_0^2 L_D \frac{1}{2} \epsilon_0 E_p^2$, where E_p is the longitudinal electric field and I_0, τ and w_0 is the intensity, duration and radius of the laser pulse; respectively. The depletion length is, $L_D = 2\tau I_0 / \epsilon_0 E_0^2$. When the laser pulse resonantly excites the plasma wave, τ is given by Eq. 4.7, E_0 by Eq. 4.8, and the depletion length becomes

$$L_D \simeq \frac{n_c m c^3}{2 I_0} \gamma_p^2 \lambda_p\,. \tag{4.11}$$

This illustrates the somewhat surprising fact that, for a given spot size and pulse duration, increasing the laser pulse energy actually results in a shorter depletion length. This is due to a more efficient energy transfer from the laser pulse to the plasma wave at higher laser intensity.

4.1.2 Wave breaking

Wave breaking limits the growth of the plasma wave and the maximum electric field that can be generated. It occurs when the electrons that form the wave move with the same velocity as the wave itself. They can then be trapped and accelerated which reduces the electron density at the peak of the wave and therefore damps it. Wave breaking is important because it is a mechanism by which background plasma electrons can be injected and accelerated. If this self-injection mechanism can be controlled, it eliminates the need for complicated external injection schemes and significantly decreases the experimental complexity. The 1D relativistic wave breaking limit in a cold plasma is [115]

$$E = E_0\sqrt{2(\gamma_p - 1)}\,, \tag{4.12}$$

where E_0 is given in Eq. 4.6. Thermal effects reduce the breaking threshold [116], but also 2D and 3D effects influence the breaking. The curved plasma wavefronts in Fig. 4.2 result in large transverse electric fields and a careful analysis of the electron trajectories [117] changes the condition in Eq. 4.12 to a condition which also depends on the transverse properties of the plasma wave. Transverse wave breaking occurs at a much lower threshold than the 1D analysis shows, but it is also subtle and can inject a small amount of electrons into the plasma wave without disrupting it altogether.

4.1.3 Trapping and acceleration

It is interesting to investigate the trajectory of an electron after it has been injected into the plasma wave, and, in particular, to identify the necessary conditions for an electron to catch the plasma wave and be accelerated. Since the wave is moving at a speed close to the speed of light, the motion of the electron is transformed into the reference frame of the plasma wave using a Lorentz transformation [34]. The calculations follow [118]. Figure 4.3 shows how the electron energy, γ_e, varies as it moves over the potential of the plasma wave. Each line represents the motion of an electron with a particular injection energy. In this example, the plasma wave frame moves with $\gamma_p = 10$ ($n_e = 1.75 \times 10^{19}$ cm^{-3}), so electrons with $\gamma_e < \gamma_p$ move from right to left, while electrons with $\gamma_e > \gamma_p$ move faster than the wave, from left to right. It is clear from Fig. 4.3 that electrons with an energy above a certain lower threshold value can be trapped in the wave and periodically accelerated and decelerated. The trapped and untrapped regions are separated by the so-called *separatrix*, marked by the thick line in Fig. 4.3. The minimum energy required for trapping is

$$\gamma_{min} = \gamma_p^2\Delta\left(1 - \beta_p\sqrt{1 + 2/\gamma_p\Delta}\right) + \gamma_p\,, \tag{4.13}$$

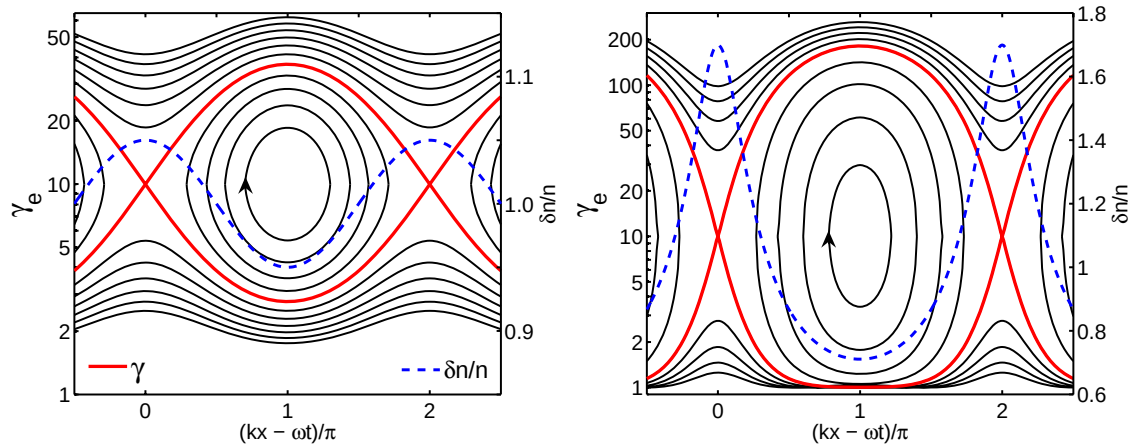

Figure 4.3. *Electron orbits in the reference frame of two different plasma waves with $\gamma_p = 10$. The left panel shows the orbits in a linear plasma wave ($\delta n/n = 0.05$) while the right panels corresponds to a non-linear plasma wave ($\delta n/n = 0.4$). The relativistic factor of the electron, γ_e, varies as it moves on the potential of the plasma wave. If the electron energy is within certain bounds, it can be trapped in the wave and periodically accelerated. If an electron is injected at the peak of the plasma wave, with a velocity corresponding to the phase velocity of the wave, it follows the orbit of the separatrix (thick solid line). When the electron reaches the center of the plasma wave period, it has reached its maximum energy and starts to decelerate.*

where $\Delta = |\phi_{max} - \phi_{min}|/\phi_0$ is the maximum potential difference of the plasma wave, normalized to $\phi_0 = mc^2/e$. For a linear plasma wave, $\Delta = 2\delta n/n_e$, and for the example in Fig. 4.3 (left panel), the trapping condition is $\gamma_{min} = 2.76$, corresponding to an electron kinetic energy of 0.9 MeV. The energy required for trapping decreases for larger amplitude waves, and for the non-linear wave in the right panel, electrons with energies as low as 1.9 keV can enter the separatrix and be trapped by the wave. The maximum energy gain also increases with the amplitude of the wave,

$$\gamma_{gain} = 2\gamma_p^2 \beta_p \Delta \sqrt{1 + 2/\gamma_p \Delta}\,, \tag{4.14}$$

Assuming a relativistic phase velocity ($\beta_p \lesssim 1$), this expression becomes $\gamma_{gain} \approx (2\gamma_p)^{3/2}\sqrt{\Delta}$ in the lower limit of small amplitude plasma waves and $\gamma_{gain} \approx 2\gamma_p^2\Delta$ in the high potential amplitude limit. In both limits, the maximum electron energy gain increases when the plasma density is reduced.

An important observation in Fig. 4.3 is that, in order to reach the maximum electron energy, the acceleration must be stopped when the electron is at the peak of its orbit. If the acceleration occurs over too long time, the particle will *dephase* with respect to the plasma wave and loose its energy again.

Particle dephasing

Numerical example. *This example is applicable in the linear laser-wakefield regime, which is different from the highly non-linear regime in Papers* ***XI*** *to* ***XIII****.*

A laser pulse with a duration of 30 fs and a wavelength of 800 nm, is focused to an intensity of 1×10^{18} *W/cm*^{2} *to resonantly excite a wave in a plasma with an electron density of* 3.4×10^{18} *cm*$^{-3}$*. Under these conditions, the dephasing length is 9.3 mm while the depletion length is 20 mm. The maximum electric field is 60 GV/m so the maximum electron energy is 600 MeV.*

Since there is a small, but not negligible, difference between the group velocity of the driving laser pulse and the accelerated electrons, the electrons eventually cross the center of the plasma wave period where the electric field changes sign. This dephasing of the electrons with respect to the plasma wave can be seen in Fig. 4.3. In the left part of the trapped particle orbits, the electrons gain energy. After they have reached their maximum energy, they enter the right part of the trajectory and loose their energy again. The final electron energy depends on where they are in their orbit when the leave the plasma wave. To estimate the dephasing length, we consider an electron with normalized velocity β_e and a plasma wave with a phase velocity β_p. If the electron is injected at the peak of the plasma wave potential (which is true when electrons are injected due to wave breaking), dephasing occurs when it has moved half a plasma wavelength longer than the wave, $\Delta L = (\beta_e - \beta_p)ct = \lambda_p/2$. The dephasing length is the length the electron moves during this time, $L_\phi = \beta_e ct = (\lambda_p/2)/(1-\beta_p/\beta_e)$. Assuming $\beta_e \approx 1$ and $n_e \ll n_c$, we obtain the 1D dephasing length,

$$L_\phi = \frac{n_c}{n_e}\lambda_p = \gamma_p^2 \lambda_p = \frac{\lambda_p^3}{\lambda_L^2}\,. \tag{4.15}$$

4.1.4 Mono-energetic electron bunch production

The key to producing mono-energetic electron beams lies in controlling the injection dynamics. If the electrons in the bunch are accelerated with an identical force over identical distance, they reach the same energy. Therefore, it is preferable to inject electrons during a short time, compared to the acceleration period, and in a well defined region in space, small compared to the electric field gradient. In the experiments described in Papers **XI** to **XIII**, self-injection occurs due to wave breaking and to obtain a monoenergetic bunch, it is necessary to stop the breaking after a short time. This can occur more or less automatically when the electric field associated with the trapped electrons becomes so large that it shields the accelerating field and terminates the injection. This effect is usually referred to as *beam loading* [119].

After injection and for a non-evolving plasma wave, the electrons follow closed orbits in momentum-phase space. This means that they are periodically accelerated and decelerated, as shown in Fig. 4.3. The energy spread is minimized by extracting the electrons at the point of highest energy. For an evolving plasma wave, the periodic phase rotation is likely to result in a large energy spread so it is preferable to extract the electrons when they reach their maximum energy for the first time.

4.1.5 Pulse propagation in underdense plasmas

Driving the plasma wave into the highly non-linear regime that is necessary for controlled wave breaking and mono-energetic bunch production, requires very short and intense laser pulses. In fact, reaching the required conditions using existing laser systems, relies on non-linear optical effects that modify the laser pulse envelope during its propagation through the plasma and act to increase the laser intensity and decrease the pulse duration. Light propagation in plasmas in general is addressed in Sec. 3.1.3. Here, propagation of an *intense pulse* is considered.

The propagation of an intense laser pulse in an underdense plasma is a complex process where the laser pulse modifies the electron density through the ponderomotive force and the modified plasma density affects the propagation of the laser pulse. Four effects are considered here; pulse compression, frequency shifts, ionization defocusing and relativistic self-focusing. The first two are effects of a longitudinal plasma density gradient, created by the ponderomotive force. The last two are effects of a transverse, intensity dependent plasma density gradient. In a typical experiment, such as the ones described in Papers **XI** to **XIII**, all mechanisms are at work simultaneously, some of which can lead to higher peak power, intensity and longer acceleration length, substantially enhancing the acceleration.

Pulse compression

When the laser pulse propagates through the plasma, the front of the pulse pushes electrons out from regions of high intensity. In the resonant laser-wakefield regime, the pulse fits within the first half plasma wave oscillation and the rear side of the pulse therefore interacts with a lower density of electrons. This means that the pulse propagates on a co-moving longitudinal electron density gradient, which translates into a gradient in the refractive index. The front of the laser pulse therefore effectively propagates with a different velocity compared to the rear. Depending on the sign of the slope of the electron density gradient, the pulse is either compressed or stretched. In the case of resonant plasma wave excitation, the laser pulse propagates on a negative gradient of the refractive index, causing the laser pulse to compress. This effect has been observed in experiments [120].

Another situation occurs when the laser pulse is so long that it covers several plasma wave periods. The electron density varies periodically under the envelope of the laser pulse which leads to a periodic compression and decompression and a modulation of the pulse envelope [121]. This modulation corresponds to sidebands in the laser frequency spectrum and by measuring the frequency shift relative to the central laser frequency, the plasma frequency can be determined.

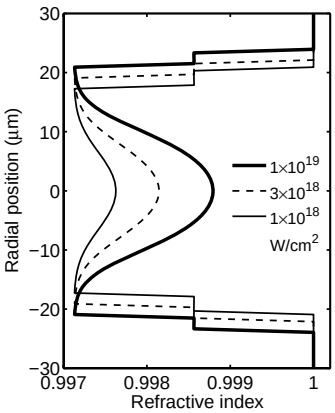

Figure 4.4. *Transverse profile of the refractive index in a He plasma with an atomic density of* $5{\times}10^{18}$ cm^{-3}*, for a Gaussian laser pulse with 800 nm wavelength and different peak intensity.*

Frequency shifts

A co-propagating longitudinal gradient in the refractive index corresponds to a variation of the phase velocity across the envelope of the laser pulse. This leads to a change in wavelength as the wavefronts of the pulse either bunch together, or disperse apart, depending on the sign of the gradient [122]. Since this phenomenon can give increased photon energies, it is sometimes referred to as photon acceleration [123]. A negative, co-propagating gradient of the refractive index results in a reduction of the laser frequency. Therefore, in the resonant laser-wakefield excitation regime, pulse compression occurs simultaneously to a red-shift of the laser wavelength. Both these effects act to increase the ponderomotive potential of the laser pulse. As discussed in Sec. 4.3.7, frequency shifts of a co-propagating probing laser pulse can be used to diagnose the plasma wave [124].

Ionization defocusing

In vacuum, diffraction causes the laser beam to quickly expand after the focal plane. At a characteristic distance from the waist of a Gaussian beam, the Rayleigh length ($z_R = \pi w_0^2/\lambda$), the transverse beam area has doubled.

In a plasma, the transverse profile of the refractive index can act to either focus or defocus the laser beam, depending on the intensity of the laser pulse. In a medium which is only partially ionized by the leading edge of the laser pulse, the electron density depends on the laser intensity across the laser focus. The refractive index is therefore lower on the central axis and is radially increasing. The plasma then acts as a negative lens and causes the laser pulse to expand faster than it would do in vacuum.

Relativistic self-focusing

In a fully ionized medium, ionization induced defocusing is avoided. Instead, another process can lead to self-focusing. When the oscillating electrons acquire relativistic energies, the relativistic mass increase locally reduces the plasma frequency, resulting in a maximum of the refractive index profile on the central axis. Figure 4.4 shows the transverse profile of the refractive index in a He plasma. The laser pulse has a Gaussian intensity profile and over the barrier ionization is assumed to be the dominant source of electrons so that He^+ and He^{2+} are formed at threshold intensities of 1.5×10^{15} W/cm^2 and 9×10^{15} W/cm^2, respectively [125]. The curvature of the refractive index profile acts as a positive lens and increases with laser intensity. Relativistic self-focusing can balance diffraction and guide the laser beam over many Rayleigh lengths. For a linearly polarized laser pulse, this

occurs at a critical power [126, 127],

$$P_c = \frac{8\pi\epsilon_0 m^2 c^5}{e^2}\frac{n_c}{n_e} \simeq 17.4\,\frac{n_c}{n_e}\ \text{GW} \tag{4.16}$$

If the laser intensity is sufficiently high, electron cavitation driven by the ponderomotive force can lead to a radially decreasing refractive index. When the effects of electron cavitation are included, the critical power threshold is lowered. Other effects that also modify the refractive index profile can counteract self-focusing. Because of the ponderomotive force, electrons pile up in front of the pulse (see Fig. 4.2) and the leading edge of the pulse experiences an effect similar to ionization defocusing. Therefore the front of the pulse erodes, while the trailing part is guided. Experimental work has shown that because of this effect, long pulses are more efficiently guided than short pulses [128, 129].

Numerical example. *For an electron density of 10^{19} cm^{-3} and a wavelength of 800 nm, the critical power for relativistic self-focusing is 3 TW.*

4.2 Experimental methods

This section describes the various techniques for plasma wave and electron beam characterization that were used to obtain the results that are reported in Papers **XI** to **XIII**. The Lund multi-terawatt laser was used as driver and a schematic picture of the experimental setup is shown in Fig. 4.5. The laser pulses are focused onto the edge of a pulsed helium gas jet by an $f/10$ off-axis parabolic mirror with a focal length of 450 mm. The electron beam profile is diagnosed by placing a scintillating screen directly in the beam path. Alternatively, the electron energy distribution is measured by letting the electrons pass through a magnetic field and registering their deflection. The different components of the arrangement are described below.

4.2.1 Gas jet target system

Generally, in laser-wakefield experiments, a sharp density gradient between the plasma medium and vacuum is required to prevent refraction of the laser beam before it reaches the high density part of the gas flow. Therefore a pulsed supersonic flow is preferable. This can be achieved by letting the gas pass through a conic nozzle at high pressure [130]. In our experiment, the gas flow is switched by a valve in which a tapered teflon plug (a poppet) is pulled back from the opening of the nozzle by a solenoid magnet. The solenoid valve, manufactured by Parker Hannifin Corporation, can operate at pressures above 100 bar but at these high pressures, the poppet tend to deform after a limited number of shots. This generates an unstable gas flow and the poppet must be changed on a regular basis.

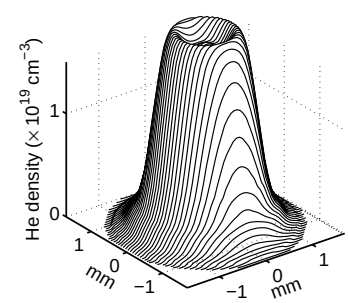

Figure 4.6. *Atomic density profile of the gas jet, measured by interferometry at 1 mm distance from the exit of the nozzle.*

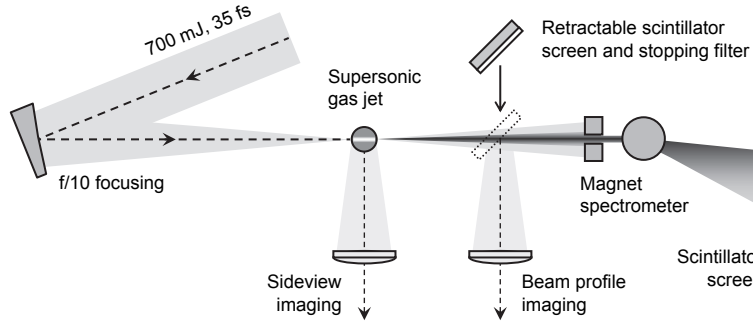

Figure 4.5. *Experimental arrangement for the experiments described in Papers **XI** to **XIII**. The 20 TW laser pulses are focused in an $f/10$ geometry onto the edge of a supersonic jet of He gas. The interaction region is imaged with high resolution onto a CCD outside the target chamber. The electron beam profile is measured by inserting a scintillating screen directly in the beam path. The electron energy spectrum is diagnosed with a magnetic field deflection spectrometer.*

4.2.2 Optical plasma diagnostics

Thomson side-scattering

As the linearly polarized laser pulse propagates through the plasma, the interaction with the plasma electrons leads to Thomson scattering [131]. The radiation source is an electromagnetic dipole so the scattered intensity peaks in a direction perpendicular to- and falls to zero parallel to the laser polarization vector. In the case of linear incoherent Thomson scattering, the intensity of the scattered radiation is proportional to the electron density and has the same wavelength as the driving laser (800 nm). Thomson scattered light is useful since it provides information on the propagation of the laser pulse through the plasma. In our experiments, side-scattered light is collected by an $f/2$ best form lens that images the interaction region with a resolution of 2 μm onto a CCD that is situated outside the target chamber. If the laser power is high enough, relativistic self-focusing balances diffraction and allows the laser beam to be guided through the plasma over a distance of several Rayleigh ranges. Figure 4.7 shows Thomson side-scattered light from such a relativistic channel. An exceptional feature of this particular image is that the laser seems to filament and be split in two beamlets close to the end of the interaction. This can occur when the laser intensity or the plasma density contains local non-uniformities that seeds a filamentation instability. Note that this is an exception. Normally, the channel is a single filament.

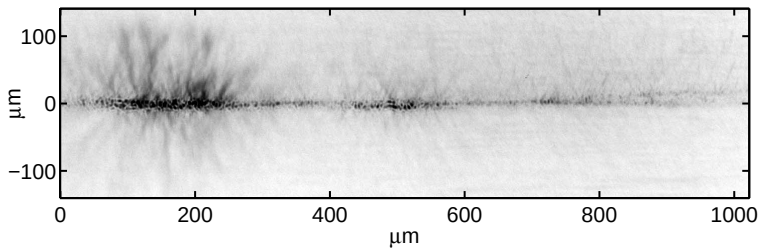

Figure 4.7. *Relativistic channel as observed in the Thomson side scattered light. The laser propagates from left to right. The length of the channel is considerably longer than the Rayleigh length (100 µm under these conditions).*

Raman forward scattering

In the experiments reported in Papers **XI** to **XIII**, the longitudinal extent of the laser pulse is matched to the plasma wavelength, leading to a resonant and efficient excitation of the plasma wave. However, if the plasma density is increased, or if the laser pulse is stretched in time, the pulse occupies several plasma wave periods. The periodic variation of the refractive index leads to a modulation of the pulse envelope, a mechanism which is similar to the self-compression mechanism described in Sec. 4.1.5. A periodic modulation of the intensity envelope in the time domain leads to sidebands in the frequency domain. In an analogy with molecular spectroscopy, the red-shifted sidebands, emanating from forward scattering, are termed Raman shifted Stokes lines [121]. Raman scattering is of particular interest because the modulation of the pulse envelope occurs with the plasma wavelength, so in the frequency domain, the shift corresponds to the plasma frequency. Therefore, Raman scattering provides a simple tool to determine the electron density in the plasma. Figure 4.8 shows two Raman shifted spectra, obtained in helium for two different backing pressures (10 and 20 bar). The shifted peaks appear at 870 and 900 nm, respectively, and since the unperturbed laser wavelength is 800 nm, this corresponds to electron densities of 1.1 and 2.0×10^{19} cm^{-3}, respectively. To facilitate these measurements, the laser pulse is stretched to ∼100 fs by increasing the grating separation in the compressor. The Raman scattered light is collected in the laser forward direction but, to avoid the blinding signal at the main laser frequency, it is collected outside the main laser cone.

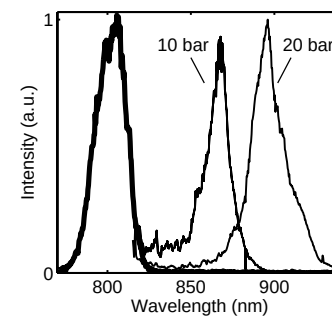

Figure 4.8. *The reference laser spectrum (thick line) and two examples of Raman shifted laser spectra, corresponding to 10 and 20 bar backing pressure. Raman spectra have been cropped at 815 nm for clarity.*

Numerical example. *At a plasma density of $n_e = 2.0 \times 10^{19}$ cm^{-3} and a laser central wavelength of 800 nm, the first three Raman shifted Stokes lines appear at 900, 1000 and 1200 nm.*

4.2.3 Electron beam diagnostics

Magnet spectrometer

We measure the electron energy distribution by deflecting the electron beam in a magnetic field. The electrons first pass through a steel collimator (either 1- or 5 mm wide) and are then deflected in an electromagnet with 38 mm circular pole pieces between which the magnetic field can be varied in the range 0 to 800 mT by adjusting the current through the solenoids. The magnetic field is mapped with a Hall probe, and the energy dependent electron deflection trajectories are calculated using a particle tracking code.

Scintillation detection

For electron detection, the scintillation from a Kodak LANEX screen is imaged onto a CCD. In this scintillator, the active material (primarily gadolinium oxysulphide) is mixed with a polymer for structural stability. The scintillation is spectrally centered at 545 nm which is well suited for efficient CCD solid state detection. Originally designed for medical applications, the response of LANEX has been well characterized for x-ray radiation, but until recently there was no calibration data available for relativistic electrons. Measurements by Glinec *et al.* [132] showed that the response is essentially flat for electrons with energies above 1 MeV. In other words, the scintillation intensity is proportional to the number of electrons per unit area.

Beam profile measurements

In a very simple arrangement, a separate LANEX screen can be inserted into the electron beam path. In front of the screen is an aluminium plate that stops low energy electrons from reaching the scintillator. The scintillation, showing the profile of the electron beam, is imaged onto a CCD camera, placed outside the interaction chamber. Since this diagnostic intercepts the electron beam, it cannot be used simultaneously with the electron spectrometer. The shield stops low energy electrons, but a drawback is that scattering inside the shielding plate smoothes the profile of the beam reaching the scintillator and limits the spatial resolution.

4.3 Results and discussions

This section summarizes the main experimental results, some of which are reported in Papers **XI**, **XII** and **XIII**. First, the narrow experimental parameter space for the generation and optimization of quasi-monoenergetic beams is identified. A particular issue is the shot-to-shot stability of various beam parameters and possibilities to improve it are discussed. It is found that, in the monoenergetic regime, electrons are injected at the back of the first plasma wave period and the duration of the electron bunch is shorter than the laser pulse.

4.3.1 Influence of electron density

Driving a plasma wave to the highly non-linear regime where partial wave breaking occurs and mono-energetic electron bunches are accelerated, requires a laser pulse that efficiently excites the plasma wave. The pulse duration should therefore be shorter than the plasma wavelength for close-to-resonant excitation. Experimentally, the plasma wavelength can be matched to the laser pulse duration by adjusting the backing pressure to the gas jet, thereby controlling the electron density in the ionized plasma.

Figure 4.9 shows three examples of electron energy spectra, illustrating the qualitative transition from a continuous- to a peaked distribution with a narrow energy spread as the electron density is reduced. This transition is the result of many effects, such as plasma wave growth, wave breaking and dephasing, all depending on the electron density. For example, if the density is so high that the laser pulse occupies several plasma wave periods, the pulse can evolve into a train of pulses due to Raman scattering, and induce wave breaking in several consecutive wave buckets. On some laser shots, electron beams with several evident peaks in the electron energy spectrum are indeed observed, as shown by the example in Fig. 4.10.

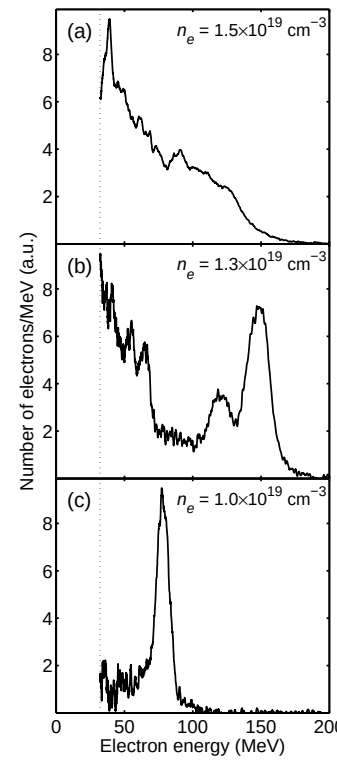

Figure 4.9. *Transition from continuous to quasi-monoenergetic energy spectrum as the electron density is decreased.*

4.3.2 Energy spread

The smallest energy spread (14% at 80 MeV for the example in Fig. 4.9(c)) is obtained at the lowest density. As shown in Fig. 4.11, there is a systematic reduction of the energy spread as the ratio between the plasma wavelength and the laser pulse duration is increased. The details of this study are reported in Paper **XII**.

Several mechanisms can contribute to the higher energy spread at higher electron densities. As discussed in Sec. 4.1.4, dephasing of the electron bunch with respect to the plasma wave can lead to an increased energy spread. At an electron density of 1×10^{19} cm^{-3}, the linear dephasing length equals the length of the 2 mm gas jet, while for densities above this value, it becomes shorter than the length of the gas jet target.

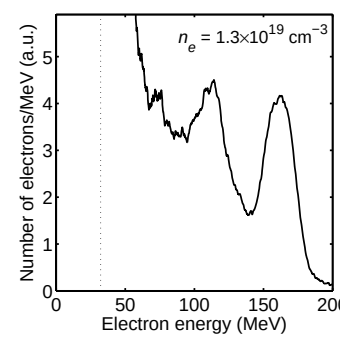

Figure 4.10. *Electron spectrum exhibiting multiple peaks, possibly emanating from breaking of several consecutive plasma wave periods.*

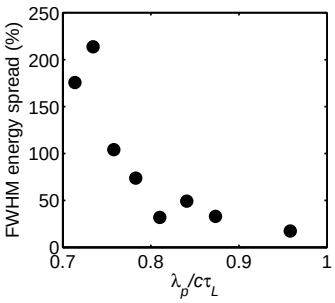

Figure 4.11. *Reducing the plasma density increases the ratio between the plasma wavelength and the laser pulse duration. This leads to a decreased energy spread of the electron energy spectrum.*

Beam loading is essential for the production of quasi-monoenergetic electron bunches since it prevents excessive injection at the back of the plasma wave period. However, it can also contribute to an *increased* energy spread since it alters the potential during the acceleration. As the electron density is increased, the degree of flattening of the wake potential due to the space charge of the electron bunch also increases.

The interaction between the electron bunch and the laser field can also increase the energy spread. As shown in Paper **XI**, the laser pulse partially overlaps with the electron bunch for the densities and pulse durations considered there. This overlap increases with increased electron density. Behind the laser pulse, the ponderomotive force forms a cavitated channel where strong radial electrostatic forces cause the electrons to perform small transverse oscillations around the propagation axis. If these *betatron* oscillations are in phase with the Doppler-shifted laser frequency, the electrons can be resonantly accelerated by the laser field. This mechanism, called Direct Laser Acceleration (DLA) [133], occurs simultaneously to the normal wakefield acceleration and can lead to an increased energy spread.

4.3.3 Stability

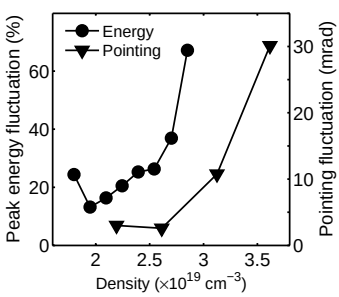

Figure 4.12. *Fluctuations of electron beam parameters as function of plasma density.*

A key issue with laser-driven wakefield accelerators is the shot-to-shot stability of important electron beam parameters such as energy, charge and pointing. The data in Fig. 4.12 shows that fluctuations of peak electron energy as well as beam pointing are minimized at low densities; close to $n_e = 2 \times 10^{19}$ cm^{-3} which corresponds to a plasma wavelength of 7.6 μm. Relativistic self-focusing occurs until the beam diameter reaches a stable value which, in this intensity regime, is close to the plasma wavelength [134]. The diffraction limited vacuum focal spot is approximately 8 μm (FWHM), so it is clear that at the lowest density, the laser spot is closely matched to the plasma wavelength. At higher densities, the matched spot size is smaller, so a higher degree of self-focusing is required before the matched spot size is reached. This leads to a higher degree of instability. Similar arguments can be applied when considering the longitudinal self-compression of the laser pulse. At $n_e = 2 \times 10^{19}$ cm^{-3}, the ratio between the plasma wavelength and the laser pulse length, $\lambda_p/c\tau$, is close to unity, but at higher plasma densities this ratio decreases. Since the pulse evolution occurs until $c\tau < \lambda_p$, a larger degree of evolution is required, leading to a higher degree of instability. This suggests that important contributions to the instabilities in the electron beam parameters originate from pulse evolution occurring prior to injection. Hence, using a matched pulse, in space and time, with sufficient intensity to inject electrons immediately upon entry into the plasma, should mitigate some of the instabilities.

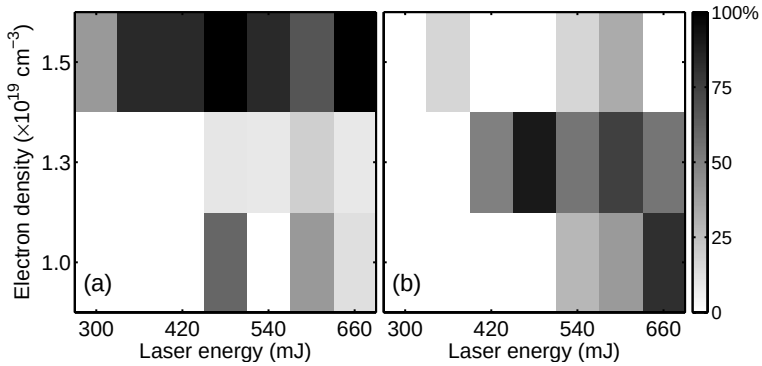

Figure 4.13. *(a) Percentage of shots yielding continuous energy spectra. (b) Percentage of shots yielding electron beams with quasi-monoenergetic features.*

4.3.4 Influence of laser energy

Both the energy spread and the fluctuations of the electron beam are minimized when the electron density is reduced. But there is a limit to the reduction of the plasma density since, to drive the plasma wave into the highly non-linear regime where wave breaking occurs, the intensity of the laser pulse must be above a certain, density dependent threshold. To investigate this, and as described in Paper **XII**, we measure the electron energy spectrum as a function of electron density and laser energy. The results are qualitatively summarized in Fig. 4.13. As expected, the character of the energy spectrum change dramatically with the electron density. At the highest electron density, most of the shots yield a continuous spectrum. At an intermediate density, quasi-monoenergetic electron beams could be consistently produced. The percentage of shots that produced an electron beam (continuous and monoenergetic) increase with laser energy. The energy required to produce a high percentage of quasi-monoenergetic beams increases with decreasing density. An optimum occurs at 1.3×10^{19} cm^{-3}. In fact, at this optimum density, the highest laser energy does not produce the most stable beams. As the laser pulse propagates through the plasma, it evolves due to self-compression and relativistic self-focusing. This evolution increases the laser intensity to the point where wave breaking and self-injection occurs. The propagation length required for this evolution is reduced for high initial intensities. For a fixed total interaction length, the acceleration length becomes longer and the electrons might dephase with the accelerating field. In addition, the higher intensity could drive the plasma wave to the point where uncontrolled breaking of several successive plasma periods occur. Both these effects lead to increased energy spread.

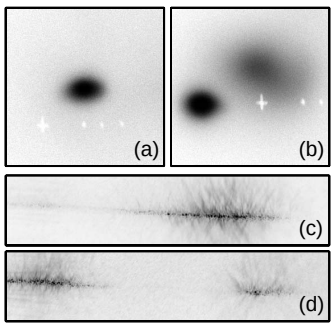

Figure 4.14. *Electron beam profiles (a), (b) and corresponding Thomson scattered images of the channel, obtained for different intensity levels of the ASE pedestal. In (a) and (c), the contrast is* 3×10^7*. In (b) and (d) it is* 2×10^6*.*

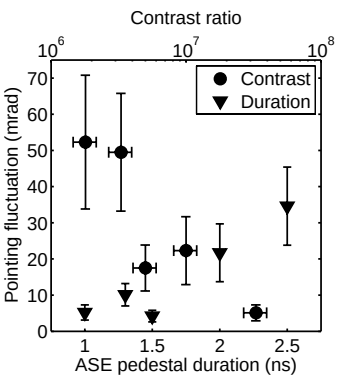

Figure 4.15. *Pointing fluctuations as function of ASE intensity and duration.*

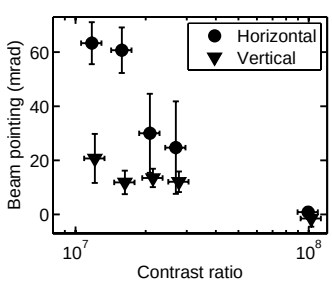

Figure 4.16. *Electron beam pointing as function of contrast.*

4.3.5 Influence of pulse contrast

At a peak intensity of the order of 10^{19} W/cm^2 and a relatively low pulse contrast of 10^6, the ASE pedestal reaches an intensity of 10^{13} W/cm^2. The ionization threshold of helium, as determined in experiments with ultrashort pulses, is about two orders of magnitude higher than this ASE intensity. For this reason, pulse contrast has historically not been considered as a crucial parameter in this type of underdense laser-plasma experiments. However, our studies, reported in Paper **XIII**, show that, in addition to the electron density and the laser energy, the laser pulse contrast can also have a significant influence on the electron beam stability. Figures 4.14(a) and (b) show two examples of beam profiles, obtained using pulses with different contrast ratios. The pulse with the best contrast ratio produces a single, well collimated electron beam. At lower contrast ratio, the electron beam is split into several beamlets with an overall larger divergence angle. As shown in Fig. 4.15, the pointing stability is severely influenced by either increasing the intensity, or the duration of the ASE pedestal. Our conclusions from these sets of measurements are that the observed electron beam instabilities originate from breakdown ionization of the He gas prior to the arrival of the main pulse. This pre-ionization and the following hydro-dynamic expansion can significantly affect the propagation of the main laser pulse. Further evidence that this is a propagation effect is seen in Fig. 4.14(c) and (d), showing the Thomson side-scattered light from the plasma channels that produced the electron beams in Fig. 4.14(a) and (b). For the low contrast level we observe a significant drop in the scattered intensity in the middle of the gas jet. This suggests a void of electrons in that region which would significantly affect both the propagation and the electron acceleration processes. Finally, while the fluctuations indeed increase, there is also a systematic motion of the electron beam centroid, as shown in Fig. 4.16. This indicates that the ASE might produce transverse electron density gradient in front of the laser pulse. Such a gradient would act to steer the laser beam off the vacuum propagation axis. Further studies are required to clarify this process.

4.3.6 Acceleration in the first plasma period

In the self-injected wakefield accelerator, background plasma electrons are injected into the accelerating fields, primarily by transverse wave breaking. In Paper **XI**, we report the first experimental evidence that in the monoenergetic regime, these electrons originate from the first plasma wave period. This also implies that the electron pulse duration is ultra-short (< 25 fs).

By optimizing the plasma density, laser energy, and laser contrast ratio, quasi-monoenergetic electron beams are reliably produced with a shot-to-shot stability that enable systematic studies of dependencies on various experimental parameters.

Figure 4.17 shows results from measurements of the transverse electron beam profile, obtained in a regime where the pulse length is longer than the plasma wavelength. The electron beam is clearly elliptical and the axis of the ellipse is close to the laser linear polarization axis. By inserting a zero-order mica half-wave plate into the laser beam, the polarization is rotated and, as shown in Fig. 4.17, the axis of the elliptic electron beam rotates as well. Although there are fluctuations, there is a clear correlation between the angle of polarization and the ellipticity axis as shown in Fig. 4.18. This implies that the laser field interacts directly with the electron bunch during the acceleration, thereby increasing its transverse emittance. The extent of the spatial overlap depends on the ratio between the pulse length and the plasma wavelength, $c\tau/\lambda_p$. When this quantity is reduced, the degree of ellipticity is also reduced, as shown in Fig. 5 in Paper **XI**. This confirms that the observed ellipticity is indeed an effect of direct interaction between the laser field and the electron bunch. It also provides evidence that the electrons originate from the first plasma period. Our interpretation that the laser field influences the transverse electron beam divergence has been reproduced in 3D particle-in-cell (PIC) simulations with almost perfect quantitative agreement with the experimental data. The details of these simulations are given in Paper **XI**. Recently, Nemeth *et al.* [135] used 3D PIC simulations to identify coherent betatron oscillations (direct laser acceleration) as the primary source of the increased transverse emittance along the polarization direction.

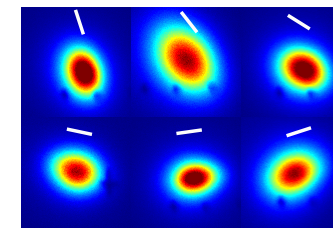

Figure 4.17. *Variation of the electron beam profile for different polarizations of the laser pulse (indicated by the white solid line).*

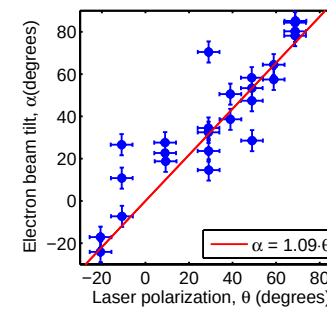

Figure 4.18. *Correlation between the electron beam ellipticity axis and the laser polarization axis.*

4.3.7 Wakefield characterization

To this point, all results relate to the very important topic of acceleration and optimization of quasi-monoenergetic electrons. This short section concentrates on a technique for characterization of the plasma wave. In the wake of the driving laser pulse, the periodic electron density variation in the plasma wave corresponds to a variation of the refractive index (Eq. 3.13). As already discussed in Sec. 4.1.5, a co-propagating longitudinal gradient of the refractive index can shift the frequency of a separate co-propagating laser pulse. The magnitude of the spectral shift depends on the steepness of the gradient and increases with propagation distance. Frequency shifts can be used as a diagnostic tool for plasma wave characterization by detecting and analyzing either the spectrum of the main high intensity laser pulse, or a collinear probe pulse, overlapping with the plasma wave behind the main pulse [124, 136].

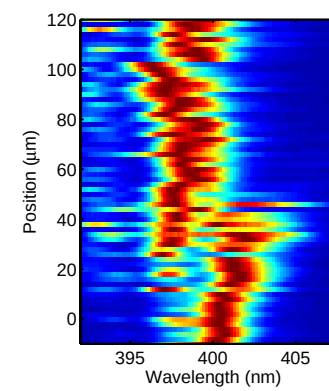

Figure 4.19. *A sequence of probe spectra, recorded for different positions in the plasma wave of the collinear probe, relative to the main laser pulse.*

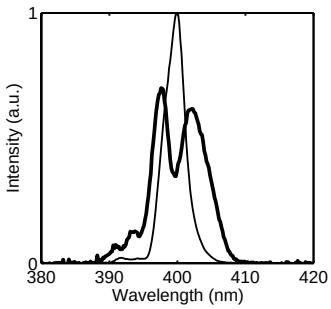

Figure 4.20. *Unperturbed (thin line) probe spectrum, obtained when the probe propagates in front of the main laser pulse. The shifted (thick line) probe spectrum is obtained when the probe pulse propagates 30 μm behind the main pulse.*

A small fraction of the main laser beam is extracted and frequency doubled before it is recombined into the main beamline again through a dichroic mirror that transmits the 400 nm probe pulse and reflects the 800 nm main pulse. During frequency doubling, the duration of the probe pulse is estimated to increase to 100 fs. The relative timing of the two pulses is varied with an optical delay line in the probe beam path. After the interaction point, the transmitted light is analyzed with an optical spectrometer as function of the distance between the two pulses in the plasma.

The composite diagram in Fig. 4.19 shows the observed frequency shifts of the probe pulse, obtained with an electron density of 1.1×10^{19} cm^{-3}. Each horizontal line is the transmitted probe spectrum, where the grayscale depicts the spectral intensity, measured for different relative positions of the probe and main pulses in the plasma. Since the length of the probe pulse (30 μm) corresponds to several λ_p (10 μm), both positive and negative shifts of the probing wavelength are present. Spectral shifts are largest when the probe travels 30 μm behind the main pulse. At this point the probe spectrum is clearly split in two peaks, at 398 nm and 402 nm, as shown in Fig. 4.20. Note that the observed shifts are not due to an amplitude modulation as in the case of Raman scattering. At the current electron density, a Raman shifted peak would be expected to appear at 416 nm.

Chapter 5

Soft x-ray lasers

The soft x-ray region of the electromagnetic spectrum falls between a few tens, down to a few tenths of a nanometer. Soft x-rays are not as energetic as medical x-rays and will not penetrate a sheet of paper. Nevertheless, this region (also called the extreme ultraviolet, XUV, region) is interesting for many applications, ranging from lithography, for fabrication of nanometer-scale objects, to holography, chemistry and biological microscopy. Of particular interest is a pulsed source of *coherent* XUV radiation with high peak brilliance and pulse energy. The need for such a source has indeed motivated large investments in a new generation of free electron lasers, driven by large scale accelerators. However, the considerable cost and limited availability of such facilities for researchers motivate a parallel development of complimentary sources.

Laser driven sources of XUV radiation have been around for a long time. In particular, plasma based soft x-ray lasers attracted considerable expectations after their first demonstration in the mid-80s. One important application that was envisioned was to characterize dense fusion plasmas by interferometry. Density measurements by interferometry are discussed for visible wavelengths in Sec. 3.3.3. However, the technology has not yet found the wide spread as first envisioned. This is largely due to the low repetition rate of the large laser systems that, until recently, were required to drive x-ray lasers to saturation. This is currently changing since new, more efficient soft x-ray laser designs have emerged, that make it possible to use relatively small, university scale, laser systems as drivers.

In the experiment described in this chapter, we use the Lund multi-terawatt laser to drive a transient collisional soft x-ray laser (SXRL), pumped in grazing incidence and based on molybdenum, lasing at 18.9 nm and operating at 10 Hz. The results are presented in Papers **XIV**, **XV** and **XVI**.

5.1 Collisional soft x-ray lasers

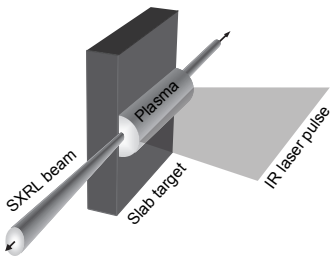

Figure 5.1. *Quasi-static collisional pumping scheme.*

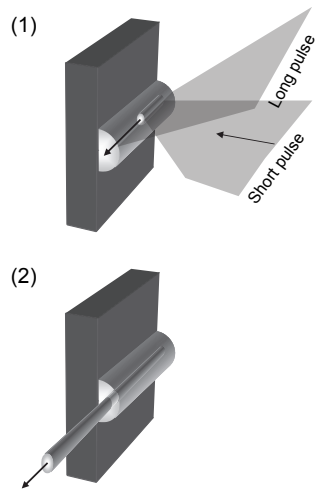

Figure 5.2. *Transient collisional traveling wave pumping scheme.*

In 1975, Elton *et al.* [137] presented the idea to use highly charged ions in a plasma as an amplifying medium for a laser in the soft x-ray region. To generate the conditions necessary for this scheme, a plasma with sufficiently high temperature and density must be created. This can be accomplished by a high power laser pulse which can be focused to obtain the required energy density to heat the plasma to the required temperature.

In 1985, Matthews *et al.* [138] demonstrated, for the first time, a collisionally pumped laser of this type by using a single laser pulse with an energy of several 100 J and a pulse duration of 0.5 ns. The laser was focused to a line on a Se solid density target and lasing was obtained by amplified spontaneous emission in a single pass along the length of the line. The Se plasma was lasing at a wavelength of 20.6 nm. For such very short wavelength transitions, the life time of the excited states is typically of the order of picoseconds. Therefore, a large fraction of the pump energy is lost in this *quasi-static collisional pumping* scheme due to spontaneous decay of the excited ions.

In 1997, Nickles *et al.* [139] demonstrated a more efficient scheme in which two laser pulses are used. A long (ns) pulse creates the plasma column while a short (ps) pulse is responsible for heating the plasma and creating the conditions necessary for lasing. In the this *transient pumping* scheme, the short pulse can create higher ionization states using less energy. Furthermore, to facilitate a long gain length, it can be applied with a tilted wavefront, i.e. in the form of a traveling wave, that heats the plasma just in front of the propagating SXRL pulse. The transient pumping scheme reduces the required laser energy to the order of 10 J.

In 2005, Keenan *et al.* [140] demonstrated the *grazing incidence pumping* (GRIP) scheme. Following their pioneering demonstration, the field of x-ray lasers is currently experiencing a very rapid development. This is largely due to the high efficiency of the GRIP scheme in which less than 1 J is needed to pump the x-ray laser. This facilitates studies using university scale and high repetition rate laser systems and this is also the scheme that is used for Papers **XIV** to **XVI**. The principle of the pumping scheme is detailed below.

For these studies, we use the same laser system as in Chapters 3 and 4, but the laser intensity and therefore also the laser-plasma interaction regime is vastly different. In the previous chapters, the laser intensity was high enough to accelerate plasma electrons to relativistic energies. At such energies, the Coulomb potential associated with other charged particles in the plasma is relatively small and collisions between the hot electrons and the ion background have a relatively small effect on the electron trajectories. In the

experiment described in this chapter, the laser pulse duration is increased by a factor 100 and the laser beam is focused to a millimeter long line. Therefore, the peak intensity is many orders of magnitude below the intensities used in the experiments described in Chapters 3 and 4, below 10^{14} W/cm^2. At this level, the ponderomotive energy of an electron is only a few eV and collisions between electrons oscillating in the laser field and plasma ions becomes the major mechanism for ionization and plasma heating.

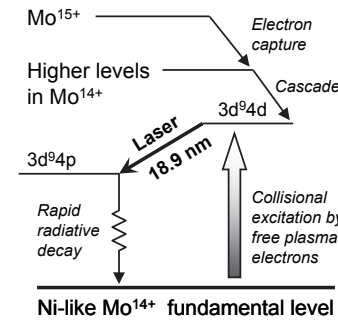

Figure 5.3. *Simplified energy level diagram of collisional excitation and laser action for a Ni-like molybdenum ion.*

5.1.1 Collisional absorption

At moderate laser intensities ($I < 10^{15}$ W/cm^2) and for relatively long pulse durations ($\tau > 1$ ps), the absorption of the laser pulse energy in the interaction with the plasma is dominated by collisions. When an energetic electron collides with the Coulomb potential of an ion, it decelerates and emits part of its energy as a burst of radiation, *Bremsstrahlung*. In the reverse process, *inverse Bremsstrahlung* or collisional absorption, a photon is absorbed by an electron during its collision with an ion or another electron. The energy which is transferred in this way from the laser field to electrons is thermalized through a large number of subsequent electron-electron or electron-ion collisions. This results in an increased plasma temperature as the coherent oscillations of the electrons in the laser field are converted to an isotropic Boltzmann velocity distribution via collisions.

5.1.2 Ionization and lasing transition

In a collisionally heated plasma, in local thermodynamic equilibrium, the density of ions of different ionization states depends on the temperature, and is obtained by solving the Saha equations [141]. The result shows that ions with closed shell electronic configurations are abundant over relatively large temperature and density ranges [142]. Therefore Ne-like ions, Ni-like ions and Pd-like ions are the major candidates as lasing ions. A higher degree of ionization implies a shorter lasing wavelength, but on the other hand the plasma must be heated to a higher temperature and therefore a higher laser power is required. In our experiment, Ni-like molybdenum is chosen as the lasing ion. The Mo^{14+} ion is excited by collisions with free electrons in the plasma, from the $3d^{10}$ ground state configuration to some state in the N shell. The ion then rapidly cascades back toward the ground state and the critical population inversion that is necessary for lasing is produced between the lower $3d^9 4p$ and the upper $3d^9 4d$ levels. Alternatively, the $3d^9 4d$ state can be populated through electron capture by a Mo^{15+} ion and subsequent cascaded deexcitation. Once population inversion is established, lasing starts from spontaneous emission at 18.9 nm.

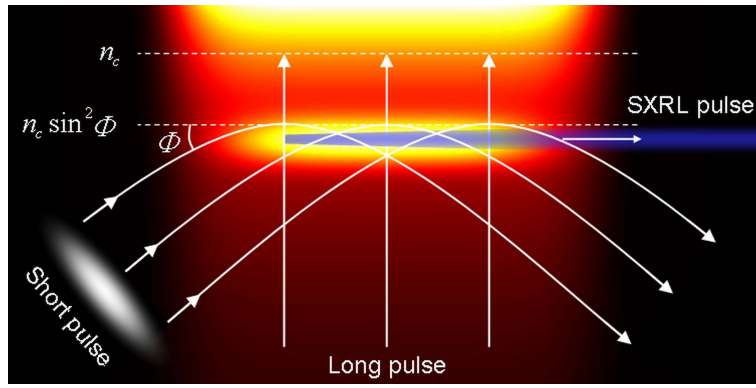

Figure 5.4. *Principle of grazing incidence pumping (GRIP). Two laser pulses are incident on the target. The long pulse creates a plasma column that expands into vacuum. After a selected time delay, the short pulse arrives at a grazing angle and heats a region of the plasma where the lasing ions appear in high abundance. By varying the grazing angle, the electron density of the heated region can be selected. The color scale depicts the electron temperature.*

5.1.3 Laser amplification

In our experiment, lasing starts from spontaneous emission and builds up in a single pass through the plasma column. The amplification of the radiation as it passes an infinitesimal volume element of length dz depends on the number of ions in the $3d^9 4p$ and $3d^9 4d$ states (N_1 and N_2, respectively) and on the cross sections, σ_s and σ_g, for spontaneous- and stimulated decay, respectively. In terms of intensity I we can write [143]

$$\frac{dI}{dz} = I(N_2 - N_1)\sigma_g + N_2\sigma_s \,. \tag{5.1}$$

For low intensities, the number of stimulated decays is relatively small and the number of excited states can be assumed to be constant so that the gain coefficient is $g_0 \approx (N_2 - N_1)\sigma_g$ and the spontaneous emissivity is $j_0 \approx N_2\sigma_s$. This implies that the intensity,

$$I(z) = (\exp(g_0 z) - 1)(j_0/g_0)\,, \tag{5.2}$$

grows exponentially with the gain-length product, $g_0 z$. As described in Paper **XIV** and Sec. 5.3.3, we determine the gain coefficient of our soft x-ray laser by varying the length of the amplifying medium and measuring the SXRL output energy.

5.1.4 Grazing incidence pumping

In the GRIP scheme, which is a variant of the transient collisional pumping scheme, two pulses are incident on the target in a non-colinear geometry, as schematically depicted in Fig. 5.4. The long pulse (LP), with a duration of a few hundred picoseconds, is focused to a line and is incident along the normal to the surface of the solid target. It ionizes the target and creates a plasma column that expands into the vacuum and contains the highly charged ions that are necessary for lasing. The short laser pulse (SP) has a duration of a few picoseconds and is incident at a grazing angle[1], Φ. The SP heats the plasma through collisions and generates a population inversion. The scale-length of the plasma column at the time of arrival of the SP, depends on the intensity of the LP and varies with the LP-SP delay, but is of the order of several tens of micrometers. At normal incidence, the SP would be reflected at the critical surface. In grazing incidence, the SP beam is continuously refracted in the plasma gradient and turns over at a lower density surface, where [33],

$$n_e = n_c \sin^2 \Phi \,. \tag{5.3}$$

The grazing incidence geometry has two major advantages. First, it results in a traveling pump wave that propagates together with the x-ray pulse in the plasma and creates the population inversion just in front of the pulse. This increases the coupling efficiency from the pump wave, via the excitation of ions, to the soft x-ray pulse since it minimizes the losses due to spontaneous emission. In addition, the grazing incidence results in an increased propagation length in the high density region of the plasma. This leads to an increased absorption of the pump energy and more efficient plasma heating. However, for very small grazing angles, refraction in the plasma gradient prevents the SP to reach the higher density layers which reduces the number density of excited ions and therefore also the gain of the laser.

Numerical example. *At a laser wavelength of 800 nm and at grazing angles of* $15°$, $19°$ *and* $21°$, *the laser beam is reflected at corresponding electron densities of 1.2, 1.8 and* 2.2×10^{20} cm^{-3}.

The optimum angle is consequently a compromise between refraction effects and coupling efficiency. The main objective of the experiment described in this chapter is to systematically investigate the influence of the GRIP angle on the laser performance.

[1]Note that, in this chapter, we follow the convention of the x-ray laser community and use the *grazing angle* instead of the *angle of incidence* which is used in all other chapters to describe the target and laser beam geometry.

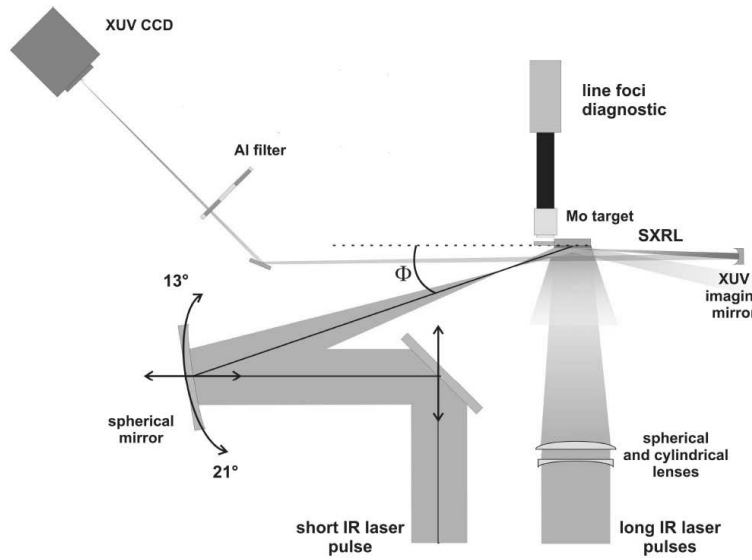

Figure 5.5. *Schematic view of the experimental setup showing the focusing geometry of the pump laser beams and the SXRL plasma imaging diagnostics. Adapted from Paper* ***XV****.*

5.2 Experimental arrangement

The Lund multi-terawatt laser (Sec. 2.1) is used as a pump laser for the SXRL. Before compression, the laser pulse is split in two parts with adjustable energy ratio using a motorized $\lambda/2$ wave plate and a polarizer. One of the pulses (the LP) remains uncompressed, with 300 ps duration, and is used to create the plasma. The other pulse (the SP) is compressed and used to heat the plasma and pump the laser transition. Normally, this laser produces 35 fs pulses, but for this experiment the compressor has been reconfigured to generate 5 ps (FWHM) pulses. The delay between the LP and the SP is adjusted with an optical delay stage in the LP beam line.

A low energy prepulse (PP) generator consisting of a $\lambda/2$ wave plate and a polarizer is installed in the LP beam path. The PP-LP delay can be adjusted with an optical delay line and the PP intensity can be adjusted by turning the wave plate. For most of the measurements during the experiment, the PP preceded the LP by 1.3 ns and contained 7% of its energy.

All beams are focused along a line on a 4 mm wide and 50 mm long molybdenum target. The LP and PP are focused under normal incidence using a combination of cylindrical and spherical lenses to a 6 mm long and 70 μm wide line and an intensity of 4×10^{11} W/cm^2 and 3×10^{10} W/cm^2, respectively, for a typical LP energy of 500 mJ. The SP is incident on the target at a grazing angle, Φ, and is focused by a spherical mirror that, since it is op-

erated in an off-axis geometry, generates a 40 μm wide astigmatic line focus on the target. The length of the focal line depends on the grazing angle but is always longer than the target width. At a 19° angle and an energy of 500 mJ, the peak intensity of the SP is 3×10^{13} W/cm^2.

A crucial point is that the position and angle of the spherical mirror and the position of the mirror before can be accurately adjusted under vacuum to facilitate a change of the grazing incidence angle while maintaining the position and orientation of the target.

The exit plane of the heated plasma is imaged onto a calibrated, back thinned, 16-bit CCD detector using a spherical mirror which is multilayer-coated for spectral selection of the laser wavelength. A set of Al filters with thickness between 1 and 6 μm are used to adjust the intensity level on the detector. The spherical mirror, which is designed and manufactured at Institut d'Optique, is operated in near normal incidence to achieve high resolution with low astigmatism. The total output energy of the SXRL is measured by integrating the signal from the calibrated CCD and correcting for the transmission of the Al filters and XUV optics.

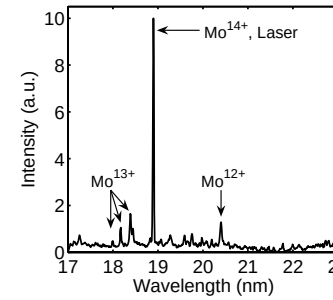

Figure 5.6. *Typical XUV spectrum under lasing conditions, taken along the propagation axis of the SXRL. The strong peak is the laser transition at 18.9 nm. The weaker peaks are from the incoherent plasma emission.*

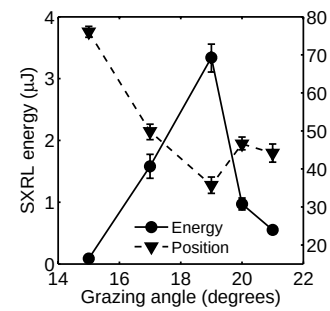

Figure 5.7. *Output energy and source position as function of the grazing angle. The LP-SP delay is 400 ps for all measurements.*

5.3 Results and discussion

Lasing is achieved at the 18.9 nm transition in Ni-like Mo^{14+}. Figure 5.6 shows the laser spectrum, measured by a flat-field spectrometer that was sampling the beam before the imaging multilayer mirror was installed. The spectrometer primarily served to find the conditions under which the plasma was lasing and this spectrum was obtained under relatively weak lasing conditions. Spectral analysis of the incoherent plasma emission confirm the presence of several other ionization states of Mo in the plasma.

5.3.1 Influence of the grazing angle

One of the key findings in the experiment is that the efficiency of the soft x-ray laser is highly dependent on the grazing angle of the heating SP. Figure 5.7 shows the output energy as function of the grazing angle. Each data point represent an average of at least 5 consecutive shots. For this data set, the LP-SP delay is fixed to 400 ps, which corresponds to the optimum measured delay for 19° as shown in the next section. The output energy has a clear optimum for 19° and reaches a maximum value of 3.3 μJ. In addition to the possibility to change the incidence angle under vacuum, a special feature of our experimental setup is that the spatial distribution of the emitting source (near-field) is imaged. Also shown in Fig. 5.7, is the distance from the source to the unperturbed target surface. The data clearly shows that

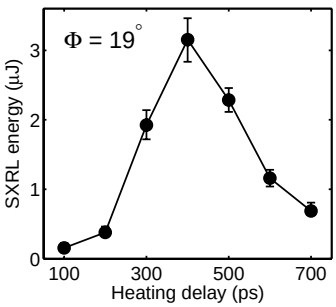

Figure 5.8. *SXRL output energy as function of LP-SP delay for a grazing angle of 19 degrees.*

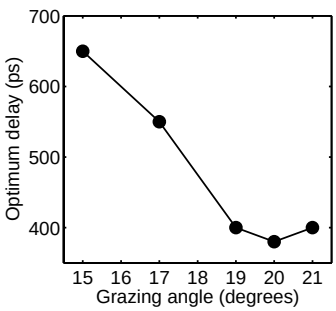

Figure 5.9. *Optimum delay between the LP and SP, for different grazing angles.*

the source moves closer to the target, i.e. toward higher electron densities, for larger angles. This is expected since the SP can penetrate deeper into the plasma for larger angles, following Eq. 5.3. The source position is closest to the target at the optimum angle but is then shifted to larger distances again for even larger angles. This is probably due to stronger refraction in the high density region of the expanded plasma. Numerical simulations under similar conditions [144] have shown that the expanding plasma has a steeper density gradient closer to the target surface than further out toward the vacuum. Therefore, even though the pulse initially penetrates deep into the plasma, it experiences a higher degree of refraction and the majority of the absorption occurs at a lower density. The optimum GRIP angle appears to be the result of a complex interplay between absorption and refraction effects at different electron densities. In addition, the abundance of Mo^{14+} ions in the absorption layer, at the time of arrival of the SP, is also highly influencing the efficiency of laser amplification.

During the experiment, many different parameters, such as the delay and the energy balance between the LP and SP, were changed. An important result is that the optimum angle seems to be relatively insensitive to these changes, although the output energy varies significantly.

5.3.2 Influence of the short pulse delay

As discussed in the previous section, the density profile of the expanding plasma has a significant influence on the propagation and refraction of the heating SP. For a given LP intensity, the density profile of the expanding plasma, at the time of arrival of the SP, depends on the delay between the two pulses since the density gradient decreases during expansion, mainly along the horizontal axis normal to the target surface. To study the influence of different scale lengths on the SXRL generation, we vary the LP-SP delay at the optimum angle ($\Phi = 19°$). As shown in Fig. 5.8, the SXRL output energy exhibits a clear optimum for a delay of 400 ps. Below this optimum value, the plasma has not had time to expand sufficiently and the steep density gradient causes the pump laser to refract in the plasma which decreases the coupling efficiency. Above the optimum value, the plasma has expanded far into the vacuum, resulting in a long density gradient at the arrival time of the heating pulse. This is presumably good for the propagation of the SP but, during the expansion, the plasma also adiabatically cools down, resulting in significant recombination and a depletion of the population of lasing ions. This reduces the gain and efficiency of the soft x-ray laser.

In conclusion, the optimum delay for soft-x-ray laser emission appears to be a compromise between refraction effects for short delays and adiabatic plasma cooling for longer delays.

When varying the delay at different grazing angles, we find that there is a different optimum delay for each angle. As shown in Fig. 5.9, smaller grazing angles require longer delays to reach the optimum plasma conditions. At smaller angles, refraction in the plasma gradient is more important. This means that, for very shallow angles, longer delays are required so that the plasma has time to expand and produce a smooth density profile prior to the arrival of the heating pulse.

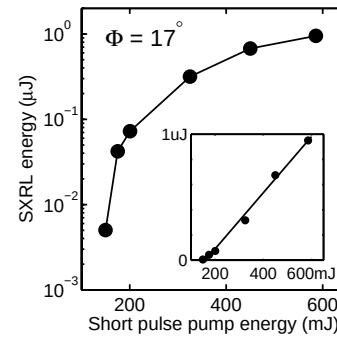

Figure 5.10. *SXRL output energy as function of heating energy in the SP. The inset shows the same data, but on a linear scale. The linear fit represents a slope efficiency of* 2×10^{-6}.

5.3.3 Estimation of gain and efficiency

The energy conversion efficiency is a very important parameter when comparing different alternative sources of XUV radiation. We have made estimates of the slope efficiency and of the maximum total efficiency. Keeping all other parameters constant, Fig. 5.10 shows the output energy of the SXRL as function of the heating SP energy, obtained at a grazing angle of 17° and with a LP energy of 500 mJ. Under these conditions, 150 mJ constitutes a lower cut-off SP pumping energy and no laser emission is observed below this value. For higher pumping energies, the output energy grows almost linearly with the SP energy, as shown by the inset in Fig. 5.10. The linear increase gives a slope efficiency of $\eta_{slope} = 2.2 \times 10^{-6}$. At the optimum grazing angle (19°), the maximum SXRL energy is 3.3 μJ, for a total pumping energy (LP and SP) of 1.0 J. This gives a total efficiency of $\eta_{max} = 3.3 \times 10^{-6}$. By operating the pump laser at 10 Hz, as described in the next section, this efficiency facilitates an average power of more than 30 μW. Estimating the SXRL pulse duration to be a few ps [145] gives a peak power of the order of MW. By varying the length of the gain medium, we have also measured the output energy as function of amplification length. This gives an estimated gain of $g \approx 45$ cm^{-1} and, for the full width of the target, a gain-length product of $\sim$18.

5.3.4 10 Hz operation

The low repetition rate of soft x-ray lasers has for a long time been one of the limiting factors for their use in applications. Historically, the repetition rate of transient collisional soft x-ray lasers has been at most a few shots per hour, restricted by the time required to cool down the amplifiers of the large laser systems needed to drive the SXRL. With the introduction of the GRIP technique, the energy required to drive the x-ray laser is reduced and smaller scale laser systems with higher repetition rates can be used as pump sources.

The Lund multi-terawatt laser system runs at 10 Hz and in principle also the SXRL could be operated at this repetition rate. However, most part of the experiment was conducted on a single-

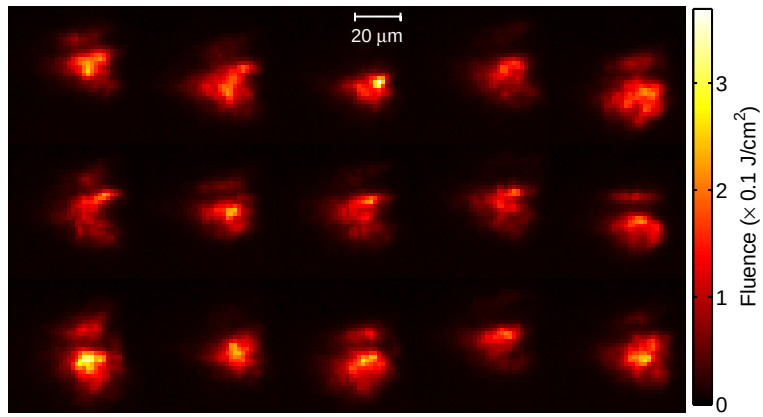

Figure 5.11. *Stability of the spatial distribution of the gain region for 15 consecutive shots, acquired at 10 Hz during 1.5 s for a stationary target. The color scale depicts the fluence of the SXRL beam as it exits the plasma.*

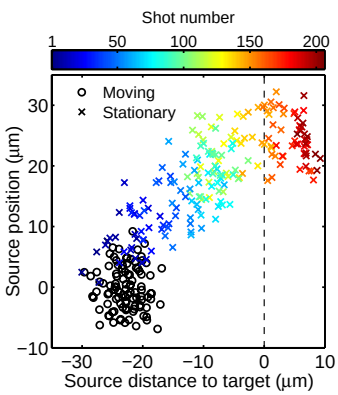

Figure 5.12. *Position of the gain region centroid relative to the initial target surface for stationary and moving targets.*

shot basis, with a shot rate that was determined by the readout time of the diagnostics (a few seconds). By restricting the readout of the CCD to a small region of interest, the frame rate of the camera was matched to the 10 Hz repetition rate of the pump laser.

To test the 10 Hz operation of the x-ray laser, the target is first translated in the vertical direction at a constant rate of 0.4 mm/s during 10 s (100 shots), to supply a fresh target surface for every shot. Then the target is stopped and 200 shots are acquired during 20 s on the same target position. Figure 5.11 shows the fluence distribution within the SXRL gain region for 15 consecutive shots, acquired during 1.5 s for the stationary target. As long as a fresh target is supplied for every shot, the position of the gain region is relatively constant, as shown in Fig. 5.12. When the target is stopped, every laser shot ablates a certain amount of material. Therefore, as shown in Fig. 5.12, the source position moves at a steady rate toward the initial target surface. Somewhat unexpectedly, we also find that both the SXRL output energy and the shot-to-shot stability improve significantly when a large amount of target material has been ablated.

As discussed in Paper **XVI**, several effects could contribute to the improved efficiency. Repeated shots on the same target position results in a linear crater, or a notch, at the position of the laser beams. The shape of the notch influences the plasma expansion and could help guiding the heating pulse to improve the overlap of the two pulses. In particular, the transverse confinement of the plasma in the crater could also lead to a higher plasma density in the heated region. In turn, a higher density of lasing ions leads to a higher output energy of the SXRL.

Chapter 6

Summary and perspectives

The work presented in this thesis investigates the physics of novel and potentially very compact laser-driven sources of intense beams of particles and short-wavelength radiation. It has been shown that a single high-power laser system can be used for a variety of purposes and by careful selection of the laser-plasma interaction conditions, high quality beams of either fast ions, relativistic electrons or coherent x-rays can be efficiently generated[1].

Proton and heavy ion acceleration

Experimental investigations of laser-driven acceleration of protons and heavy ions from thin solid foil targets is described in Chapter 3. The influence of many different experimental parameters, such as amplified spontaneous emission (ASE) (Papers **I**, **II** and **III**), is studied. Using the ultrahigh contrast pulses from the Lund multi-terawatt laser, highly efficient acceleration is obtained from targets as thin as 20 nm (Paper **V**). Using the Vulcan Petawatt laser, we investigate the scaling of the maximum ion energy with the intensity and duration of the laser pulse and obtain proton energies up to 55 MeV (Paper **VII**). By heating the target foil prior to and during the laser shot, highly charged heavy ions are accelerated (Paper **IX**). It is found that long lateral electron transport can lead to ion acceleration very far from the laser focus (Paper **X**). Novel schemes, involving multiple laser pulses, are also developed to facilitate control and optimization of the ion beams (Papers **IV** and **VI**).

When this work started in 2004, the first unexpected observations of beams of MeV ions, had been published only a few years earlier [22–25] and conflicting ideas of the main mechanisms of acceleration appeared in academic journals. In Lund, the first

[1] Other kinds of particles, such as neutrons [146], positrons [147] and γ-rays [8], can also be generated in intense laser-plasma interactions, but this has not been part of the current thesis work.

steps towards controlling important experimental parameters for the acceleration were taken during my first months as a doctorate student.

Since then, several important advancements have been made. They include, in addition to the ones reported on in this thesis, for example, experimental demonstrations of two techniques for generation of quasi-monoenergetic ion beams [85, 86] and an ultrafast technique for ion beam focusing and energy selection [148]. As laser technology continues to develop, intensities in the ultrarelativistic regime will eventually become available [149]. In this regime, the extreme photon pressure associated with the focused laser pulse can be efficiently converted to directed ion energy, leading to the generation of very dense, quasi-monoenergetic and highly relativistic ion bunches [47, 150, 151]. Recently, it has been found in numerical simulations that, by using circularly polarized laser pulses, this very promising regime might be reached using existing laser facilities [152, 153].

Electron acceleration

The experiments described in Chapter 4 aim to investigate a new regime of laser-wakefield acceleration in which electron beams with narrow energy spread can be generated. Electrons are accelerated up to 200 MeV in less than 2 mm acceleration length. It is found that, in this regime, the electrons are injected by wave breaking in the first plasma wave period and that, during acceleration, the electron bunch interacts with the laser field, resulting in a slight increase of the transverse emittance along the laser polarization direction (Paper **XI**). Our studies also show that reducing the required amounts of nonlinear spatio-temporal self-evolution of the laser pulse envelope leads to an increased shot-to-shot stability of important electron beam parameters (Paper **XII**). By minimizing the intensity and duration of the ASE pedestal, the stability is improved even further (Paper **XIII**).

In Lund, the first experiment leading to stable generation of quasi-monoenergetic electron beams was performed in 2005, one year after the publication of the three seminal papers on this new regime of acceleration [107–109]. Since then, the subject has attracted significant international interest and by now, quasi-monoenergetic electron beams are produced in many different laboratories worldwide [154–157]. Several major achievements have been made, such as the acceleration of quasi-monoenergetic bunches up to one GeV [158], and the demonstration of a technique for generation of electron beams with tunable kinetic energies [159]. Current research is focused on several different topics, for example, improving the stability, increasing the output energies to the multi-GeV regime, and developments towards a laser-driven free electron laser [160].

Soft x-ray lasers

In the experiments described in Chapter 5, two laser beams from the Lund multi-terawatt laser are used to pump a soft x-ray laser in grazing incidence. Lasing is achieved in Ni-like molybdenum at a wavelength of 18.9 nm and optimized output energies up to 3 μJ are obtained at a repetition rate of 10 Hz. The influence of many important experimental parameters are investigated, such as the grazing angle and the time delay between the two pulses (Papers **XIV** and **XV**). In addition, 10 Hz operation of the soft x-ray laser is demonstrated and characterized (Paper **XVI**).

X-ray lasers, based on optical field ionization, were studied in Lund during the 1990s. The present experiment, which was performed within a year after the pioneering demonstration of the grazing incidence pumping (GRIP) scheme by Keenan *et al.* [140], is a major step forward in terms of average x-ray laser output power. Currently, the field is drawing considerable attention since the highly efficient GRIP scheme facilitates studies using table-top laser systems [145, 161–163]. The interest partly stems from the very high peak spectral brightness of the x-ray laser pulses that can be obtained with this relatively cheap and compact source, which actually outperforms the light generated in undulators at much more expensive synchrotron facilities.

In our experiments, spontaneous emission seeded the laser transition. Current international developments are aiming to improve the spatial coherence of the soft x-ray laser by using high-harmonics, generated in a separate gas target by a third laser pulse, to seed the soft x-ray plasma amplifier [164–166].

Role of the Author

In all experiments performed using the Lund multi-terawatt laser (Papers **I**–**V**, **XI**–**XVI**), I was jointly responsible for the operation of the laser system and I contributed to the experimental work. In all experiments using the Vulcan Petawatt laser (Papers **VII**–**X**), I was jointly responsible for target area operations (as deputy officer), including all work inside the interaction chamber.

I **Laser-accelerated protons with energy-dependent beam direction**
This paper reports the first observation of an energy dependent shift of the proton emission direction. It is shown that the deflection originates from a surface deformation, induced by a shock wave which is driven by amplified spontaneous emission.

I had an active part in planning, setting up and performing the experiment. I wrote a large fraction of the program for the automatic target positioning system that was developed for this experiment. I performed part of the data evaluation and analysis. I was also very active in preparing the manuscript.

II **High-intensity laser-driven proton acceleration: influence of pulse contrast**
In this paper we discuss the influence of the laser pulse contrast ratio on proton acceleration.

I took active part in planning, setting up and performing the experiment. I performed part of the data analysis, produced several of the figures in the paper and contributed to the manuscript. I also designed and programmed the scanning and pit counting microscope system that was used for automatic readout of the CR39 detectors.

III **Influence of shockwaves on laser-driven proton acceleration**
This paper presents the results from a parametric follow-up study, aiming to investigate the influence of ASE-driven shock waves. The preliminary observations reported in Paper **I** are strengthened by new data and improved modeling.

I planned and performed a large part of the measurements while D. Batani performed the simulations. I did all analysis and modeling of the experimental data and the simulations. I made all the figures and wrote the manuscript.

IV **Active steering of laser-accelerated ion beams**
A separate laser pulse is used to drive a shock and locally shape the target foil. This is used to control the emission direction of the proton beam.

I and Y. Glinec were responsible for planning and leading the experiment. I contributed to the implementation and optimization of the preamplifier and saturable absorbed that was used to enhance the contrast of the laser pulses. I did most of the data analysis. I made most of the figures and wrote the paper.

V **Enhanced proton beams from ultrathin targets driven by high contrast laser pulses**
This paper describes an experiment in which we used plasma mirrors to facilitate highly efficient acceleration from sub-μm thick target foils.

I was highly involved in all aspects of the experiment. I did most of the data analysis and I took an active part in the preparation of the manuscript.

VI **Active manipulation of the spatial energy distribution of laser-accelerated proton beams**
In an experiment using the 100 TW arm of the Vulcan laser, a separate laser beam was used to improve both the spatial quality and the maximum energy of the proton beam.

I was involved both in the experiment and in the discussions on the interpretation of the results. I also contributed to the manuscript.

VII **Scaling of proton acceleration driven by petawatt-laser–plasma interactions**
The scaling of the proton energies with laser intensity and pulse duration is investigated in the ultrahigh intensity regime. A slower scaling than previous theories predicted is found. The experimental data is used to improve the theoretical modeling.

I had an active role in the experiment and I contributed to discussions on the interpretation of the data. I contributed to the writing of the paper.

VIII **Detection of short lived radioisotopes as a fast diagnostic for intense laser–solid interactions**
A technique for diagnosing laser-accelerated protons using induced activation of short-lived radioisotopes is described.

I contributed mainly by setting up the equipment inside the Petawatt target chamber and to a certain extent in the preparation of the manuscript.

IX **Low- and medium-mass ion acceleration driven by petawatt laser plasma interactions**
This paper describes results from an experiment in which the Vulcan Petawatt laser was used to accelerate highly charged ions from heated targets.

I was fully involved in the experiment. In particular, I was responsible for the operation of the Thomson spectrometers. I contributed to the paper.

X **Lateral electron transport in high-intensity laser-irradiated foils diagnosed by ion emission**
Ion emission is observed from multiple sources, far from the focal spot, during an experiment at Vulcan Petawatt laser. The phenomenon is explained as being the result of electrons propagating along the surface of the target.

I was fully involved in the experiment, in particular in the search of the cause of the multiple ion sources. I took part in the discussions leading to the conclusions. I contributed to the manuscript.

XI **Laser-wakefield acceleration of monoenergetic electron beams in the first plasma-wave period**
This paper reports the observation of an elliptic profile of the quasi-monoenergetic electron beam. This discovery was used to elucidate important properties of the acceleration mechanism.

I was fully involved in all parts of the experiment, including setup, laser operations and data analysis. I also participated in the discussions leading to the reported findings and I took part in the preparation of the manuscript.

XII **On the stability of laser wakefield electron accelerators in the monoenergetic regime**
The conditions leading to quasi-monoenergetic electron beams are investigated. It is found that by matching the focusing geometry and the pulse duration to the plasma wavelength, the shot-to-shot stability is improved.

I was fully involved in all parts of the experiment, including setup, laser operations, data acquisitions and analysis.

XIII **Effect of laser contrast ratio on electron beam stability in laser wakefield acceleration experiments**
This paper reports a study of electron beams accelerated using two different lasers with different contrast ratios.

I was fully involved in all parts of the experiment on the Lund multi-terawatt laser, including setting up, data acquisition and data analysis.

XIV **Optimization toward a high-average-brightness soft-x-ray laser pumped at grazing incidence**
This paper presents the first results from the implementation and optimization of a soft x-ray laser, pumped in grazing incidence by the Lund multi-terawatt laser.

I was highly involved in all aspects of the experiment, including setting up, laser operations and data acquisition. I also contributed to the manuscript.

XV **Characterization of a transient collisional Ni-like molybdenum soft x-ray laser pumped in grazing incidence**
This paper presents the experimental details and additional data from the study in Paper **XIV**.

I was highly involved all aspects of the experiment, including setting up, laser operations and data acquisition.

XVI **Quantitative study of 10 Hz operation of a soft x-ray laser – energy stability and target considerations**
This paper reports on a study of 10 Hz operation of the soft x-ray laser discussed in Paper **XIV**.

I was highly involved in the experiment and I contributed to the manuscript.

Acknowledgements

The work presented in this thesis is to a large extent the result from fruitful collaborations with many people from around the world. I would like to thank all my co-authors of the papers that have resulted from these joint efforts.

First of all, I would like to thank my supervisor, Claes-Göran Wahlström, for giving me responsibilities and support and for always keeping his door open for discussions. Sune Svanberg, my co-supervisor and head of the division, for radiating such enthusiasm and creating a very hospitable and friendly working environment.

Special thanks goes to all my colleagues at the Atomic Physics division, and in particular to past and present members of our small group, Filip Lindau, Yannick Glinec, Christian Homann, Matthias Burza and Guillaume Genoud. It has been a pleasure to work with you all. Thanks Filip for enduring all those experiments with me both in Sweden and in the UK, it was exciting and eventful times. Thanks Yannick for interesting discussions, I learned so many things.

Special thanks also to Anders Persson, for always being willing to help and for his impressive skills in making seemingly broken things work, in particular high-power lasers.

I have had the privilege to work with several highly competent researchers in international collaborations. In particular from Strathclyde University, Imperial College, Central Laser Facility and Queens University in the United Kingdom; from LIXAM, LPGP and LOA in France; from University of Milan in Italy and from GSI in Germany. Thank you everybody for nice joint work, I hope we will work together again in the future. Special thanks to Paul McKenna, David Neely, Stuart Mangles and David Carroll with whom I worked most closely. Thanks Paul, and thanks David for fruitful work in Sweden and for giving me the opportunity to work on several experimental campaigns at Vulcan. It was important.

Very special thanks to all my friends and my family, who have supported and inspired me over these years.

Finally, my warmest thanks goes to my gorgeous, precious and understanding wife. Susanna, I will always love you.

References

1. T. E. Cowan, J. Fuchs, H. Ruhl, A. Kemp, P. Audebert, M. Roth, R. Stephens, I. Barton, A. Blazevic, E. Brambrink, J. Cobble, J. Fernandez, J.-C. Gauthier, M. Geissel, M. Hegelich, J. Kaae, S. Karsch, G. P. Le Sage, S. Letzring, M. Manclossi, S. Meyroneinc, A. Newkirk, H. Pepin and N. Renard-LeGalloudec. *Ultralow emittance, multi-MeV proton beams from a laser virtual-cathode plasma accelerator.* Phys. Rev. Lett. **92**, 204801 (2004).

2. M. Borghesi, D. H. Campbell, A. Schiavi, M. G. Haines, O. Willi, A. J. MacKinnon, P. Patel, L. A. Gizzi, M. Galimberti, R. J. Clarke, F. Pegoraro, H. Ruhl and S. Bulanov. *Electric field detection in laser-plasma interaction experiments via the proton imaging technique.* Phys. Plasmas **9**, 2214 (2002).

3. S. V. Bulanov and V. S. Khoroshkov. *Feasibility of using laser ion accelerators in proton therapy.* Plasma Phys. Rep. **28**, 453 (2002).

4. K. W. D. Ledingham, P. McKenna, T. McCanny, S. Shimizu, J. M. Yang, L. Robson, J. Zweit, J. M. Gillies, J. Bailey, G. N. Chimon, R. J. Clarke, D. Neely, P. A. Norreys, J. L. Collier, R. P. Singhal, M. S. Wei, S. P. D. Mangles, P. Nilson, K. Krushelnick and M. Zepf. *High power laser production of short-lived isotopes for positron emission tomography.* J. Phys. D: Appl. Phys. **37**, 2341 (2004).

5. M. Roth, T. E. Cowan, M. H. Key, S. P. Hatchett, C. Brown, W. Fountain, J. Johnson, D. M. Pennington, R. A. Snavely, S. C. Wilks, K. Yasuike, H. Ruhl, F. Pegoraro, S. V. Bulanov, E. M. Campbell, M. D. Perry and H. Powell. *Fast ignition by intense laser-accelerated proton beams.* Phys. Rev. Lett. **86**, 436 (2001).

6. K. Krushelnick, E. L. Clark, R. Allott, F. N. Beg, C. N. Danson, A. Machacek, V. Malka, Z. Najmudin, D. Neely, P. A. Norreys, M. R. Salvati, M. I. K. Santala, M. Tatarakis, I. Watts, M. Zepf and A. E. Dangor. *Ultrahigh-intensity laser-produced plasmas as a compact heavy ion injection source.* IEEE Trans. Plasma Sci. **28**, 1184 (2000).

7. W. P. Leemans, C. G. R. Geddes, J. Faure, Cs. Tóth, J. van Tilborg, C. B. Schroeder, E. Esarey, G. Fubiani, D. Auerbach, B. Marcelis, M. A. Carnahan, R. A. Kaindl, J. Byrd and M. C. Martin. *Observation of terahertz emission from a laser-plasma accelerated electron bunch crossing a plasma-vacuum boundary.* Phys. Rev. Lett. **91**, 074802 (2003).

8. Y. Glinec, J. Faure, L. Le Dain, S. Darbon, T. Hosokai, J. J. Santos, E. Lefebvre, J. P. Rousseau, F. Burgy, B. Mercier and V. Malka. *High-resolution gamma-ray radiography produced by a laser-plasma driven electron source.* Phys. Rev. Lett. **94**, 025003 (2005).

9. D. Strickland and G. Mourou. *Compression of amplified chirped optical pulses.* Opt. Commun. **56**, 219 (1985).

10. S. Backus, C. G. Durfee III, M. M. Murnane and H. C. Kapteyn. *High power ultrafast lasers.* Rev. Sci. Instrum. **69**, 1207 (1998).

11. D. E. Spence, J. M. Evans, W. E. Sleat and W. Sibbett. *Regeneratively initiated self-mode-locked Ti:sapphire laser.* Opt. Lett. **16**, 1762 (1991).

12. C. N. Danson, P. A. Brummitt, R. J. Clarke, J. L. Collier, B. Fell, A. J. Frackiewicz, S. Hancock, S. Hawkes, C. Hernandez-Gomez, P. Holligan, M. H. R. Hutchinson, W. J. Lester A. Kidd, I. O. Musgrave, D. Neely, D. R. Neville, P. A. Norreys, D. A. Pepler, C. J. Reason, W. Shaikh, T. B. Winstone, R. W. W. Wyatt and B. E. Wyborn. *Vulcan Petawatt–an ultra-high-intensity interaction facility.* Nucl. Fusion **44**, 239 (2004).

13. C. N. Danson, P. A. Brummitt, R. J. Clarke, J. L. Collier, B. Fell, A. J. Frackiewicz, S. Hawkes, C. Hernandez-Gomez, P. Holligan, M. H. R. Hutchinson, A. Kidd, W. J. Lester, I. O. Musgrave, D. Neely, D. R. Neville, P. A. Norreys, D. A. Pepler, C. J. Reason, W. Shaikh, T. B. Winstone, R. W. W. Wyatt and B. E. Wyborn. *Vulcan petawatt: Design, operation and interactions at* 5×10^{20} *Wcm*$^{-2}$. Laser Part. Beams **23**, 87 (2005).

14. A. Dubietis, G. Jonusauskas and A. Piskarskas. *Powerful femtosecond pulse generation by chirped and stretched pulse parametric amplification in BBO crystal.* Opt. Commun. **88**, 437 (1992).

15. I. N. Ross, P. Matousek, M. Towrie, A. J. Langley and J. L. Collier. *The prospects for ultrashort pulse duration and ultrahigh intensity using optical parametric chirped pulse amplifiers.* Opt. Commun. **144**, 125 (1997).

16. J. Collier, C. Hernandez-Gomez, I. N. Ross, P. Matousek, C. N. Danson and J. Walczak. *Evaluation of an ultrabroadband high-gain amplification technique for chirped pulse amplification facilities.* Appl. Opt. **38**, 7486 (1999).

17. P. Tournois. *Acousto-optic programmable dispersive filter for adaptive compensation of group delay time dispersion in laser systems.* Opt. Commun. **140**, 245 (1997).

18. C. Ziener, P. S. Foster, E. J. Divall, C. J. Hooker, M. H. R. Hutchinson, A. J. Langley and D. Neely. *Specular reflectivity of plasma mirrors as a function of intensity, pulse duration, and angle of incidence.* J. Appl. Phys. **93**, 768 (2003).

19. H. C. Kapteyn, M. M. Murnane, A. Szoke and R. W. Falcone. *Prepulse energy suppression for high-energy ultrashort pulses using self-induced plasma shuttering.* Opt. Lett. **16**, 490 (1991).

20. G. Doumy, F. Quere, O. Gobert, M. Perdrix, Ph. Martin, P. Audebert, J. C. Gauthier, J.-P. Geindre and T. Wittmann. *Complete characterization of a plasma mirror for the production of high-contrast ultraintense laser pulses.* Phys. Rev. E **69**, 026402 (2004).

21. S. J. Gitomer, R. D. Jones, F. Begay, A. W. Ehler, J. F. Kephart and R. Kristal. *Fast ions and hot electrons in the laser–plasma interaction.* Physics of Fluids **29**, 2679 (1986).

22. R. A. Snavely, M. H. Key, S. P. Hatchett, T. E. Cowan, M. Roth, T. W. Phillips, M. A. Stoyer, E. A. Henry, T. C. Sangster, M. S. Singh, S. C. Wilks, A. MacKinnon, A. Offenberger, D. M. Pennington, K. Yasuike, A. B. Langdon, B. F. Lasinski, J. Johnson, M. D. Perry and E. M. Campbell. *Intense high-energy proton beams from petawatt-laser irradiation of solids.* Phys. Rev. Lett. **85**, 2945 (2000).

23. E. L. Clark, K. Krushelnick, J. R. Davies, M. Zepf, M. Tatarakis, F. N. Beg, A. Machacek, P. A. Norreys, M. I. K. Santala, I. Watts and A. E. Dangor. *Measurements of energetic proton transport through magnetized plasma from intense laser interactions with solids.* Phys. Rev. Lett. **84**, 670 (2000).

24. E. L. Clark, K. Krushelnick, M. Zepf, F. N. Beg, M. Tatarakis, A. Machacek, M. I. K. Santala, I. Watts, P. A. Norreys and A. E. Dangor. *Energetic heavy-ion and proton generation from ultraintense laser-plasma interactions with solids.* Phys. Rev. Lett. **85**, 1654 (2000).

25. A. Maksimchuk, S. Gu, K. Flippo, D. Umstadter and V. Yu. Bychenkov. *Forward ion acceleration in thin films driven by a high-intensity laser.* Phys. Rev. Lett. **84**, 4108 (2000).

26. M. Allen, P. K. Patel, A. Mackinnon, D. P., S. Wilks and E. Morse. *Direct experimental evidence of back-surface ion acceleration from laser-irradiated gold foils.* Phys. Rev. Lett. **93**, 265004 (2004).

27. J. Fuchs, Y. Sentoku, S. Karsch, J. Cobble, P. Audebert, A. Kemp, A. Nikroo, P. Antici, E. Brambrink, A. Blazevic, E. M. Campbell, J. C. Fernández, J.-C. Gauthier, M. Geissel, M. Hegelich, H. Pépin, H. Popescu, N. Renard-LeGalloudec, M. Roth, J. Schreiber, R. Stephens and T. E. Cowan. *Comparison of laser ion acceleration from the front and rear surfaces of thin foils.* Phys. Rev. Lett. **94**, 045004 (2005).

28. M. Borghesi, J. Fuchs, S. V. Bulanov, A. J. MacKinnon, P. K. Patel and M. Roth. *Fast ion generation by high-intensity laser irradiation of solid targets and applications.* Fusion Sci. Technol. **49**, 412 (2006).

29. A. L. Galkin, V. V. Korobkin, M. Yu. Romanovsky and O. B. Shiryaev. *Dynamics of an electron driven by relativistically intense laser radiation.* Phys. Plasmas **15**, 023104 (2008).

30. S. C. Wilks and W. L. Kruer. *Absorption of ultrashort, ultra-intense laser light by solids and overdense plasmas.* IEEE J. Quantum. Electron. **33**, 1954 (1997).

31. F. V. Hartemann, S. N. Fochs, G. P. Le Sage, N. C. Luhmann, J. G. Woodworth, M. D. Perry, Y. J. Chen and A. K. Kerman. *Nonlinear ponderomotive scattering of relativistic electrons by an intense laser field at focus.* Phys. Rev. E **51**, 4833 (1995).

32. F. V. Hartemann, J. R. Van Meter, A. L. Troha, E. C. Landahl, N. C. Luhmann, H. A. Baldis, Atul Gupta and A. K. Kerman. *Three-dimensional relativistic electron scattering in an ultrahigh-intensity laser focus.* Phys. Rev. E **58**, 5001 (1998).

33. W. Kruer. *The physics of laser plasma interactions.* Westview Press, Oxford, reprint edition (2003).

34. J. D. Jackson. *Classical electrodynamics.* John Wiley and Sons Inc, New York, 3rd edition (1999).

35. S. C. Wilks, W. L. Kruer, M. Tabak and A. B. Langdon. *Absorption of ultra-intense laser pulses.* Phys. Rev. Lett. **69**, 1383 (1992).

36. M. I. K. Santala, M. Zepf, I. Watts, F. N. Beg, E. Clark, M. Tatarakis, K. Krushelnick, A. E. Dangor, T. McCanny, I. Spencer, R. P. Singhal, K. W. D. Ledingham, S. C. Wilks, A. C. Machacek, J. S. Wark, R. Allott, R. J. Clarke and P. A. Norreys. *Effect of the plasma density scale length on the direction of fast electrons in relativistic laser–solid interactions.* Phys. Rev. Lett. **84**, 1459 (2000).

37. F. Brandl, G. Pretzler, D. Habs and E. Fill. *Cerenkov radiation diagnostics of hot electrons generated by fs-laser interaction with solid targets.* Europhys. Lett. **61**, 632 (2003).

38. M. H. Key, M. D. Cable, T. E. Cowan, K. G. Estabrook, B. A. Hammel, S. P. Hatchett, E. A. Henry, D. E. Hinkel, J. D. Kilkenny, J. A. Koch, W. L. Kruer, A. B. Langdon, B. F. Lasinski, R. W. Lee, B. J. MacGowan, A. MacKinnon, J. D. Moody, M. J. Moran, A. A. Offenberger, D. M. Pennington, M. D. Perry, T. J. Phillips, T. C. Sangster, M. S. Singh, M. A. Stoyer, M. Tabak, G. L. Tietbohl, M. Tsukamoto, K. Wharton and S. C. Wilks. *Hot electron production and heating by hot electrons in fast ignitor research.* Phys. Plasmas **5**, 1966 (1998).

39. J. Yu, Z. Jiang, J. C. Kieffer and A. Krol. *Hard X-ray emission in high intensity femtosecond laser–target interaction.* Phys. Plasmas **6**, 1318 (1999).

40. F. N. Beg, A. R. Bell, A. E. Dangor, C. N. Danson, A. P. Fews, M. E. Glinsky, B. A. Hammel, P. Lee, P. A. Norreys and M. Tatarakis. *A study of picosecond laser–solid interactions up to* 10^{19} *W cm*$^{-2}$. Phys. Plasmas **4**, 447 (1997).

41. F. Brunel. *Not-so-resonant, resonant absorption.* Phys. Rev. Lett. **59**, 52 (1987).

42. H. Alfvén. *On the motion of cosmic rays in interstellar space.* Phys. Rev. **55**, 425 (1939).

43. E. S. Weibel. *Spontaneously growing transverse waves in a plasma due to an anisotropic velocity distribution.* Phys. Rev. Lett. **2**, 83 (1959).

44. E. d'Humieres, E. Lefebvre, L. Gremillet and V. Malka. *Proton acceleration mechanisms in high-intensity laser interaction with thin foils.* Phys. Plasmas **12**, 062704 (2005).

45. Y. Sentoku, T. E. Cowan, A. Kemp and H. Ruhl. *High energy proton acceleration in interaction of short laser pulse with dense plasma target.* Phys. Plasmas **10**, 2009 (2003).

46. L. O. Silva, M. Marti, J. R. Davies, R. A. Fonseca, C. Ren, F. S. Tsung and W. B. Mori. *Proton shock acceleration in laser-plasma interactions.* Phys. Rev. Lett. **92**, 015002 (2004).

47. T. Esirkepov, M. Borghesi, S. V. Bulanov, G. Mourou and T. Tajima. *Highly efficient relativistic-ion generation in the laser-piston regime.* Phys. Rev. Lett. **92**, 175003 (2004).

48. S. C. Wilks, A. B. Langdon, T. E. Cowan, M. Roth, M. Singh, S. Hatchett, M. H. Key, D. Pennington, A. MacKinnon and R. A. Snavely. *Energetic proton generation in ultra-intense laser–solid interactions.* Phys. Plasmas **8**, 542 (2001).

49. F. F. Chen. *Introduction to plasma physics and controlled fusion.* Kluwer Academic Publishers Group, Dordrecht, 2nd revised edition (1984).

50. M. Widner, I. Alexeff and W. D. Jones. *Plasma expansion into a vacuum.* Phys. Fluids **14**, 795 (1971).

51. J. E. Crow, P. L. Auer and J. E. Allen. *The expansion of a plasma into a vacuum.* J. Plasma Phys. **14**, 65 (1975).

52. J. Denavit. *Collisionless plasma expansion into a vacuum.* Phys. Fluids **22**, 1384 (1979).

53. M. A. True, James R. Albritton and E. A. Williams. *Fast ion production by suprathermal electrons in laser fusion plasmas.* Phys. Fluids **24**, 1885 (1981).

54. P. Mora. *Plasma expansion into a vacuum.* Phys. Rev. Lett. **90**, 185002 (2003).

55. P. Mora. *Thin-foil expansion into a vacuum.* Phys. Rev. E **72**, 056401 (2005).

56. M. Borghesi, A. J. Mackinnon, D. H. Campbell, D. G. Hicks, S. Kar, P. K. Patel, D. Price, L. Romagnani, A. Schiavi and O. Willi. *Multi-MeV proton source investigations in ultraintense laser-foil interactions.* Phys. Rev. Lett. **92**, 055003 (2004).

57. A. J. Mackinnon, M. Borghesi, S. Hatchett, M. H. Key, P. K. Patel, H. Campbell, A. Schiavi, R. Snavely, S. C. Wilks and O. Willi. *Effect of plasma scale length on multi-MeV proton production by intense laser pulses.* Phys. Rev. Lett. **86**, 1769 (2001).

58. J. Fuchs, C. A. Cecchetti, M. Borghesi, T. Grismayer, E. d'Humières, P. Antici, S. Atzeni, P. Mora, A. Pipahl, L. Romagnani, A. Schiavi, Y. Sentoku, T. Toncian, P. Audebert and O. Willi. *Laser-foil acceleration of high-energy protons in small-scale plasma gradients.* Phys. Rev. Lett. **99**, 015002 (2007).

59. T. Grismayer and P. Mora. *Influence of a finite initial ion density gradient on plasma expansion into a vacuum.* Phys. Plasmas **13**, 032103 (2006).

60. A. P. L. Robinson, D. Neely, P. McKenna and R. G. Evans. *Spectral control in proton acceleration with multiple laser pulses.* Plasma Phys. Control. Fusion **49**, 373 (2007).

61. D. L. Henshaw. *Applications of CR-39 nuclear track detector in medicine and technology.* Phys. Tech. **13**, 266 (1982).

62. Track Analysis Systems Limited, H. H. Wills Physics Laboratory, Bristol, UK. URL `http://www.phy.bris.ac.uk/research/TASL/home.html`.

63. F. H. Seguin, J. A. Frenje, C. K. Li, D. G. Hicks, S. Kurebayashi, J. R. Rygg, B.-E. Schwartz, R. D. Petrasso, S. Roberts, J. M. Soures, D. D. Meyerhofer, T. C. Sangster, J. P. Knauer, C. Sorce, V. Yu. Glebov, C. Stoeckl, T. W. Phillips, R. J. Leeper, K. Fletcher and S. Padalino. *Spectrometry of charged particles from inertial-confinement-fusion plasmas.* Rev. Sci. Instrum. **74**, 975 (2003).

64. S. Gaillard, J. Fuchs, N. Renard-Le Galloudec and T. E. Cowan. *Study of saturation of CR39 nuclear track detectors at high ion fluence and of associated artifact patterns.* Rev. Sci. Instrum. **78**, 013304 (2007).

65. W. L. McLaughlin, J. M. Puhl, M. Al-Sheikhly, C. A. Christou, A. Miller, A. Kovcs, L. Wojnarovits and D. F. Lewis. *Novel radiochromic films for clinical dosimetry.* Radiat. Prot. Dosimetry **66**, 263 (1996).

66. EXFOR database at the International Atomic Energy Agency (IAEA). URL `http://www-nds.iaea.org`.

67. I. Spencer, K. W. D. Ledingham, R. P. Singhal, T. McCanny, P. McKenna, E. L. Clark, K. Krushelnick, M. Zepf, F. N. Beg, M. Tatarakis, A. E. Dangor, P. A. Norreys, R. J. Clarke, R. M. Allott and I. N. Ross. *Laser generation of proton beams for the production of short-lived positron emitting radioisotopes*. Nucl. Instrum. Methods B **183** (2001).

68. M. I. K. Santala, M. Zepf, F. N. Beg, E. L. Clark, A. E. Dangor, K. Krushelnick, M. Tatarakis, I. Watts, K. W. D. Ledingham, T. McCanny, I. Spencer, A. C. Machacek, R. Allott, R. J. Clarke and P. A. Norreys. *Production of radioactive nuclides by energetic protons generated from intense laser-plasma interactions*. Appl. Phys. Lett. **78**, 19 (2001).

69. J. M. Yang, P. McKenna, K. W. D. Ledingham, T. McCanny, S. Shimizu, L. Robson, R. J. Clarke, D. Neely, P. A. Norreys, M.-S. Wei, K. Krushelnick, P. Nilson, S. P. D. Mangles and R. P. Singhal. *Nuclear reactions in copper induced by protons from a petawatt laser-foil interaction*. Appl. Phys. Lett. **84**, 675 (2004).

70. K. W. D. Ledingham. *Laser induced nuclear physics and applications*. Nucl. Phys. A **752**, 633 (2005).

71. National Institute of Science and Technology, PSTAR database. URL `http://www.physics.nist.gov/PhysRefData/Star/Text/PSTAR.html`.

72. J. J. Thomson. Philos. Mag. **21** (1911).

73. J. F. Ziegler, J. P. Biersack and U. Littmark. *The stopping and range of ions in solids*. Pergamon Press, New York (1985).

74. R. Benattar, C. Popovics and R. Sigel. *Polarized light interferometer for laser fusion studies*. Rev. Sci. Instrum. **50**, 1583 (1979).

75. E. Hecht. *Optics*. Addison-Wesley, 4 edition (2001).

76. M. Hipp and P. Reiterer. *User Manual for IDEA 1.00: Software for Interferometrical Data Evaluation*. Institut für Experimentalphysik, Technische Universität Graz (1999).

77. M. Kaluza, J. Schreiber, M. I. K. Santala, G. D. Tsakiris, K. Eidmann, J. Meyer-ter Vehn and K. J. Witte. *Influence of the laser prepulse on proton acceleration in thin-foil experiments*. Phys. Rev. Lett. **93**, 045003 (2004).

78. R. Ramis, R. Schmalz and J. Meyer-Ter-Vehn. *MULTI - A computer code for one-dimensional multigroup radiation hydrodynamics*. Comput. Phys. Commun. **49**, 475 (1988).

79. M. Roth, A. Blazevic, M. Geissel, T. Schlegel, T. E. Cowan, M. Allen, J.-C. Gauthier, P. Audebert, J. Fuchs, J. Meyer ter Vehn, M. Hegelich, S. Karsch and A. Pukhov. *Energetic ions generated by laser pulses: A detailed study on target properties*. Phys. Rev. ST Accel. Beams **5**, 061301 (2002).

80. J. Lindl. *Development of the indirect-drive approach to inertial confinement fusion and the target physics basis for ignition and gain*. Phys. Plasmas **2**, 3933 (1995).

81. S. Eliezer. *Interaction of high power lasers with plasmas.* Institute of Physics publishing, Bristol, 1st edition (2001).

82. J. Schreiber, M. Kaluza, F. Grüner, U. Schramm, B.M. Hegelich, J. Cobble, M. Geissler, E. Brambrink, J. Fuchs, P. Audebert, D. Habs and K. Witte. *Source-size measurements and charge distributions of ions accelerated from thin foils irradiated by high-intensity laser pulses.* Appl. Phys. B **79**, 1041 (2004).

83. A. J. Mackinnon, Y. Sentoku, P. K. Patel, D. W. Price, S. Hatchett, M. H. Key, C. Andersen, R. Snavely and R. R. Freeman. *Enhancement of proton acceleration by hot-electron recirculation in thin foils irradiated by ultraintense laser pulses.* Phys. Rev. Lett. **88**, 215006 (2002).

84. T. Esirkepov, S. V. Bulanov, K. Nishihara, T. Tajima, F. Pegoraro, V. S. Khoroshkov, K. Mima, H. Daido, Y. Kato, Y. Kitagawa, K. Nagai and S. Sakabe. *Proposed double-layer target for the generation of high-quality laser-accelerated ion beams.* Phys. Rev. Lett. **89**, 175003 (2002).

85. H. Schwoerer, S. Pfotenhauer, O. Jackel, K.-U. Amthor, B. Liesfeld, W. Ziegler, R. Sauerbrey, K. W. D. Ledingham and T. Esirkepov. *Laser-plasma acceleration of quasi-monoenergetic protons from microstructured targets.* Nature **439**, 445 (2006).

86. B. M. Hegelich, B. J. Albright, J. Cobble, K. Flippo, S. Letzring, M. Paffett, H. Ruhl, J. Schreiber, R. K. Schulze and J. C. Fernndez. *Laser acceleration of quasi-monoenergetic MeV ion beams.* Nature **439**, 441 (2006).

87. A. G. R. Thomas, S. P. D. Mangles, Z. Najmudin, M. C. Kaluza, C. D. Murphy and K. Krushelnick. *Measurements of wave-breaking radiation from a laser-wakefield accelerator.* Phys. Rev. Lett. **98**, 054802 (2007).

88. J. S. Green, V. M. Ovchinnikov, R. G. Evans, K. U. Akli, H. Azechi, F. N. Beg, C. Bellei, R. R. Freeman, H. Habara, R. Heathcote, M. H. Key, J. A. King, K. L. Lancaster, N. C. Lopes, T. Ma, A. J. MacKinnon, K. Markey, A. McPhee, Z. Najmudin, P. Nilson, R. Onofrei, R. Stephens, K. Takeda, K. A. Tanaka, W. Theobald, T. Tanimoto, J. Waugh, L. Van Woerkom, N. C. Woolsey, M. Zepf, J. R. Davies and P. A. Norreys. *Effect of laser intensity on fast-electron-beam divergence in solid-density plasmas.* Phys. Rev. Lett. **100**, 015003 (2008).

89. M. Allen, Y. Sentoku, P. Audebert, A. Blazevic, T. Cowan, J. Fuchs, J. C. Gauthier, M. Geissel, M. Hegelich, S. Karsch, E. Morse, P. K. Patel and M. Roth. *Proton spectra from ultraintense laser–plasma interaction with thin foils: Experiments, theory, and simulation.* Phys. Plasmas **10**, 3283 (2003).

90. Y. Oishi, T. Nayuki, T. Fujii, Y. Takizawa, X. Wang, T. Yamazaki, K. Nemoto, T. Kayoiji, T. Sekiya, K. Horioka, Y. Okano, Y. Hironaka, K. G. Nakamura, K. Kondo and A. A. Andreev. *Dependence on laser intensity and pulse duration in proton acceleration by irradiation of ultrashort laser pulses on a Cu foil target.* Phys. Plasmas **12**, 073102 (2005).

91. E. Fourkal, I. Velchev and C.-M. Ma. *Coulomb explosion effect and the maximum energy of protons accelerated by high-power lasers.* Phys. Rev. E **71**, 036412 (2005).

92. J. Schreiber, F. Bell, F. Grüner, U. Schramm, M. Geissler, M. Schnürer, S. Ter-Avetisyan, B. M. Hegelich, J. Cobble, E. Brambrink, J. Fuchs, P. Audebert and D. Habs. *Analytical model for ion acceleration by high-intensity laser pulses.* Phys. Rev. Lett. **97**, 045005 (2006).

93. T. Esirkepov, M. Yamagiwa and T. Tajima. *Laser ion-acceleration scaling laws seen in multiparametric particle-in-cell simulations.* Phys. Rev. Lett. **96**, 105001 (2006).

94. J. Fuchs, P. Antici, E. D'Humieres, E. Lefebvre, M. Borghesi, E. Brambrink, C. A. Cecchetti, M. Kaluza, V. Malka, M. Manclossi, S. Meyroneinc, P. Mora, J. Schreiber, T. Toncian, H. Pepin and R. Audebert. *Laser-driven proton scaling laws and new paths towards energy increase.* Nature Phys. **2**, 48 (2006).

95. V. Malka, S. Fritzler, E. Lefebvre, E. d'Humières, R. Ferrand, G. Grillon, C. Albaret, S. Meyroneinc, J.-P. Chambaret, A. Antonetti and D. Hulin. *Practicability of protontherapy using compact laser systems.* Med. Phys. **31**, 1587 (2004).

96. M. Hegelich, S. Karsch, G. Pretzler, D. Habs, K. Witte, W. Guenther, M. Allen, A. Blazevic, J. Fuchs, J. C. Gauthier, M. Geissel, P. Audebert, T. Cowan and M. Roth. *MeV ion jets from short-pulse-laser interaction with thin foils.* Phys. Rev. Lett. **89**, 085002 (2002).

97. B. M. Hegelich, B. Albright, P. Audebert, A. Blazevic, E. Brambrink, J. Cobble, T. Cowan, J. Fuchs, J. C. Gauthier, C. Gautier, M. Geissel, D. Habs, R. Johnson, S. Karsch, A. Kemp, S. Letzring, M. Roth, U. Schramm, J. Schreiber, K. J. Witte and J. C. Fernandez. *Spectral properties of laser-accelerated mid-Z MeV/u ion beams.* Phys. Plasmas **12**, 056314 (2005).

98. P. McKenna, K. W. D. Ledingham, J. M. Yang, L. Robson, T. McCanny, S. Shimizu, R. J. Clarke, D. Neely, K. Spohr, R. Chapman, R. P. Singhal, K. Krushelnick, M. S. Wei and P. A. Norreys. *Characterization of proton and heavier ion acceleration in ultrahigh-intensity laser interactions with heated target foils.* Phys. Rev. E **70**, 036405 (2004).

99. T. A. Carlson, C. W. Nestor, Jr., N. Wasserman and J. D. McDowell. *Calculated ionization potentials for multiply charged ions.* At. Data **2**, 63 (1970).

100. D. R. Welch, D. V. Rose, B. V. Oliver and R. E. Clark. *Simulation techniques for heavy ion fusion chamber transport.* Nucl. Instrum. Methods A **464**, 134 (2001).

101. S. D. Baton, D. Batani, M. Manclossi, A. Morace, D. Piazza, A. Benuzzi-Mounaix, M. Koenig, P. Guillou, B. Loupias, J. Fuchs, F. Amiranoff, M. Rabec Le Gloahec, H. Popescu, C. Rousseaux, M. Borghesi, C. Cecchetti, R. Kodama, T. Norimatsu, M. Nakatsutsumi and Y. Aglitskiy. *Recent experiments on electron transport in high-intensity laser matter interaction.* Plasma Phys. Control. Fusion **47**, B777 (2005).

102. P. K. Patel, M. H. Key, A. J. Mackinnon, R. Berry, M. Borghesi, D. M. Chambers, H. Chen, R. Clarke, C. Damian, R. Eagleton, R. Freeman, S. Glenzer, G. Gregori, R. Heathcote, D. Hey, N. Izumi, S. Kar, J. King, A. Nikroo, A. Niles, H.-S. Park, J. Pasley, N. Patel, R. Shepherd, R. A. Snavely, D. Steinman, C. Stoeckl, M. Storm, W. Theobald, R. Town, R. Van Maren, S. C. Wilks and B. Zhang. *Integrated laser-target interaction experiments on the RAL petawatt laser.* Plasma Phys. Control. Fusion **47**, B833 (2005).

103. T. Tajima and J. M. Dawson. *Laser electron accelerator.* Phys. Rev. Lett. **43**, 267 (1979).

104. A. Modena, Z. Najmudin, A. Dangor, C. Clayton, K. A. Marsh, C. Joshi, V. Malka, C. Darrow, C. Danson, D. Neely and F. Walsh. *Electron acceleration from the breaking of relativistic plasma waves.* Nature **377**, 606 (1995).

105. V. Malka, S. Fritzler, E. Lefebvre, M.-M. Aleonard, F. Burgy, J.-P. Chambaret, J.-F. Chemin, K. Krushelnick, G. Malka, S. P. D. Mangles, Z. Najmudin, M. Pittman, J.-P. Rousseau, J.-N. Scheurer, B. Walton and A. E. Dangor. *Electron acceleration by a wake field forced by an intense ultrashort laser pulse.* Science **298**, 1596 (2002).

106. A. Pukhov and J. Meyer ter Vehn. *Laser wake field acceleration: the highly non-linear broken-wave regime.* Appl. Phys. B: Lasers Opt. **V74**, 355 (2002).

107. S. P. D. Mangles, C. D. Murphy, Z. Najmudin, A. G. R. Thomas, J. L. Collier, A. E. Dangor, E. J. Divall, P. S. Foster, J. G. Gallacher, C. J. Hooker, D. A. Jaroszynski, A. J. Langley, W. B. Mori, P. A. Norreys, F. S. Tsung, R. Viskup, B. R. Walton and K. Krushelnick. *Monoenergetic beams of relativistic electrons from intense laser-plasma interactions.* Nature **431**, 535 (2004).

108. J. Faure, Y. Glinec, A. Pukhov, S. Kiselev, S. Gordienko, E. Lefebvre, J.-P. Rousseau, F. Burgy and V. Malka. *A laser-plasma accelerator producing monoenergetic electron beams.* Nature **431**, 541 (2004).

109. C. G. R. Geddes, Cs. Toth, J. van Tilborg, E. Esarey, C. B. Schroeder, D. Bruhwiler, C. Nieter, J. Cary and W. P. Leemans. *High-quality electron beams from a laser wakefield accelerator using plasma-channel guiding.* Nature **431**, 538 (2004).

110. L. M. Gorbunov and V. I. Kirsanov. *The excitation of plasma waves by an electromagnetic wave packet.* Zh. Eksp. Teor. Fiz. **93**, 509 (1987).

111. P. Sprangle, E. Esarey, A. Ting and G. Joyce. *Laser wakefield acceleration and relativistic optical guiding.* Appl. Phys. Lett. **53**, 2146 (1988).

112. E. Esarey, P. Sprangle, J. Krall and A. Ting. *Overview of plasma-based accelerator concepts.* IEEE Trans. Plasma Sci. **24**, 252 (1996).

113. E. A. Jackson. *Nonlinear oscillations in a cold plasma.* Phys. Fluids **3**, 831 (1960).

114. R. A. Fonseca, L. O. Silva, F. S. Tsung, V. K. Decyk, W. Lu, C. Ren, W. B. Mori, S. Deng, S. Lee, T. Katsouleas and J. C. Adam. *OSIRIS: A three-dimensional, fully relativistic particle in cell code for modeling plasma based accelerators.* Computational Science - ICCS 2002 **III**, 342 (2002).

115. A. Akhiezer and R. Polovin. *Theory of wave motion of an electron plasma.* JETP **3**, 696 (1956).

116. T. Katsouleas and W. B. Mori. *Wave-breaking amplitude of relativistic oscillations in a thermal plasma.* Phys. Rev. Lett. **61**, 90 (1988).

117. S. V. Bulanov, F. Pegoraro, A. M. Pukhov and A. S. Sakharov. *Transverse-wake wave breaking.* Phys. Rev. Lett. **78**, 4205 (1997).

118. P. Mora and F. Amiranoff. *Electron acceleration in a relativistic electron plasma wave.* J. Appl. Phys. **66**, 3476 (1989).

119. T. Katsouleas, S. Wilks, P. Chen, J. M. Dawson and J. J. Su. *Beam loading in plasma accelerators.* Part. Accel. **22**, 81 (1987).

120. J. Faure, Y. Glinec, J. J. Santos, F. Ewald, J.-P. Rousseau, S. Kiselev, A. Pukhov, T. Hosokai and V. Malka. *Observation of laser-pulse shortening in nonlinear plasma waves.* Phys. Rev. Lett. **95**, 205003 (2005).

121. W. B. Mori, C. D. Decker, D. E. Hinkel and T. Katsouleas. *Raman forward scattering of short-pulse high-intensity lasers.* Phys. Rev. Lett. **72**, 1482 (1994).

122. E. Esarey, A. Ting and P. Sprangle. *Frequency shifts induced in laser pulses by plasma waves.* Phys. Rev. A **42**, 3526 (1990).

123. S. C. Wilks, J. M. Dawson, W. B. Mori, T. Katsouleas and M. E. Jones. *Photon accelerator.* Phys. Rev. Lett. **62**, 2600 (1989).

124. J. M. Dias, L. O. Silva and J. T. Mendonça. *Photon acceleration versus frequency-domain interferometry for laser wakefield diagnostics.* Phys. Rev. ST Accel. Beams **1**, 031301 (1998).

125. U. Mohideen, M. H. Sher, H. W. K. Tom, G. D. Aumiller, O. R. Wood, R. R. Freeman, J. Boker and P. H. Bucksbaum. *High intensity above-threshold ionization of He.* Phys. Rev. Lett. **71**, 509 (1993).

126. G.-Z. Sun, E. Ott, Y. C. Lee and P. Guzdar. *Self-focusing of short intense pulses in plasmas.* Phys. Fluids **30**, 526 (1987).

127. P. Sprangle, E. Esarey and A. Ting. *Nonlinear interaction of intense laser pulses in plasmas.* Phys. Rev. A **41**, 4463 (1990).

128. C. Delfin, V. Lokhnygin, J. Mauritsson, A. Sjögren, C.-G. Wahlström, A. Pukhov and G. D. Tsakiris. *Influence of laser pulse duration on relativistic channels.* Phys. Plasmas **9**, 937 (2002).

129. J. Faure, V. Malka, J.-R. Marquès, P.-G. David, F. Amiranoff, K. Ta Phuoc and A. Rousse. *Effects of pulse duration on self-focusing of ultrashort lasers in underdense plasmas.* Phys. Plasmas **9**, 756 (2002).

130. S. Semushin and V. Malka. *High density gas jet nozzle design for laser target production.* Rev. Sci. Instrum. **72**, 2961 (2001).

131. J. J. Thomson. *Conduction of electricity through gases.* Cambridge University Press, Cambridge, (1906).

132. Y. Glinec, J. Faure, A. Guemnie-Tafo, V. Malka, H. Monard, J. P. Larbre, V. De Waele, J. L. Marignier and M. Mostafavi. *Absolute calibration for a broad range single shot electron spectrometer.* Rev. Sci. Instrum. **77**, 103301 (2006).

133. A. Pukhov, Z.-M. Sheng and J. Meyer-Ter-Vehn. *Particle acceleration in relativistic laser channels.* Phys. Plasmas **6**, 2847 (1999).

134. A. G. R. Thomas, Z. Najmudin, S. P. D. Mangles, C. D. Murphy, A. E. Dangor, C. Kamperidis, K. L. Lancaster, W. B. Mori, P. A. Norreys, W. Rozmus and K. Krushelnick. *Effect of laser-focusing conditions on propagation and monoenergetic electron production in laser-wakefield accelerators.* Phys. Rev. Lett. **98**, 095004 (2007).

135. K. Németh, B. Shen, Y. Li, H. Shang, R. Crowell, K. C. Harkay and J. R. Cary. *Laser-driven coherent betatron oscillation in a laser-wakefield cavity.* Phys. Rev. Lett. **100**, 095002 (2008).

136. C. D. Murphy, R. Trines, J. Vieira, A. J. W. Reitsma, R. Bingham, J. L. Collier, E. J. Divall, P. S. Foster, C. J. Hooker, A. J. Langley, P. A. Norreys, R. A. Fonseca, F. Fiuza, L. O. Silva, J. T. Mendonça, W. B. Mori, J. G. Gallacher, R. Viskup, D. A. Jaroszynski, S. P. D. Mangles, A. G. R. Thomas, K. Krushelnick and Z. Najmudin. *Evidence of photon acceleration by laser wake fields.* Phys. Plasmas **13**, 033108 (2006).

137. R. C. Elton. *Quasi-stationary population inversion on K alpha transitions.* Appl. Opt. **14**, 2243 (1975).

138. D. L. Matthews, P. L. Hagelstein, M. D. Rosen, M. J. Eckart, N. M. Ceglio, A. U. Hazi, H. Medecki, B. J. MacGowan, J. E. Trebes, B. L. Whitten, E. M. Campbell, C. W. Hatcher, A. M. Hawryluk, R. L. Kauffman, L. D. Pleasance, G. Rambach, J. H. Scofield, G. Stone and T. A. Weaver. *Demonstration of a soft X-ray amplifier.* Phys. Rev. Lett. **54**, 110 (1985).

139. P. V. Nickles, V. N. Shlyaptsev, M. Kalachnikov, M. Schnrer, I. Will and W. Sandner. *Short pulse X-ray laser at 32.6 nm based on transient gain in Ne-like titanium.* Phys. Rev. Lett. **78**, 2748 (1997).

140. R. Keenan, J. Dunn, P. K. Patel, D. F. Price, R. F. Smith and V. N. Shlyaptsev. *High-repetition-rate grazing-incidence pumped X-ray laser operating at 18.9 nm.* Phys. Rev. Lett. **94**, 103901 (2005).

141. M. N. Saha. *On a physical theory of stellar spectra.* R. Soc. L. Proc. A **99**, 135 (1921).

142. H. Daido. *Review of soft X-ray laser researches and developments.* Rep. Prog. Phys. **65**, 1513 (2002).

143. O. Svelto. *Priciples of lasers.* Plenum Press, New York, 4th edition (1998).

144. G. J. Pert. *Optimizing the performance of nickel-like collisionally pumped x-ray lasers.* Phys. Rev. A **73**, 033809 (2006).

145. A. Weith, M. A. Larotonda, Y. Wang, B. M. Luther, D. Alessi, M. C. Marconi, J. J. Rocca and J. Dunn. *Continuous high-repetition-rate operation of collisional soft-x-ray lasers with solid targets.* Opt. Lett. **31**, 1994 (2006).

146. P. McKenna, K. W. D. Ledingham, S. Shimizu, J. M. Yang, L. Robson, T. McCanny, J. Galy, J. Magill, R. J. Clarke, D. Neely, P. A. Norreys, R. P. Singhal, K. Krushelnick and M. S. Wei. *Broad energy spectrum of laser-accelerated protons for spallation-related physics.* Phys. Rev. Lett. **94**, 084801 (2005).

147. C. Gahn, G. D. Tsakiris, G. Pretzler, K. J. Witte, P. Thirolf, D. Habs, C. Delfin and C.-G. Wahlström. *Generation of MeV electrons and positrons with femtosecond pulses from a table-top laser system.* Phys. Plasmas **9**, 987 (2002).

148. T. Toncian, M. Borghesi, J. Fuchs, E. d'Humieres, P. Antici, P. Audebert, E. Brambrink, C. A. Cecchetti, A. Pipahl, L. Romagnani and O. Willi. *Ultrafast laser-driven microlens to focus and energy-select mega-electron volt protons.* Science **312**, 410 (2006).

149. G. Mourou, T. Tajima and S. V. Bulanov. *Optics in the relativistic regime.* Rev. Mod. Phys. **78**, 309 (2006).

150. W. Yu, H. Xu, F. He, M. Y. Yu, S. Ishiguro, J. Zhang and A. Y. Wong. *Direct acceleration of solid-density plasma bunch by ultraintense laser.* Phys. Rev. E **72**, 046401 (2005).

151. F. Pegoraro and S. V. Bulanov. *Photon bubbles and ion acceleration in a plasma dominated by the radiation pressure of an electromagnetic pulse.* Phys. Rev. Lett. **99**, 065002 (2007).

152. A. P. L. Robinson, M. Zepf, S. Kar, R. G. Evans and C. Bellei. *Radiation pressure acceleration of thin foils with circularly polarized laser pulses.* New J. Phys. **10**, 013021 (2008).

153. O. Klimo, J. Psikal, J. Limpouch and V. T. Tikhonchuk. *Monoenergetic ion beams from ultrathin foils irradiated by ultrahigh-contrast circularly polarized laser pulses.* Phys. Rev. ST Accel. Beams **11**, 031301 (2008).

154. E. Miura, K. Koyama, S. Kato, N. Saito, M. Adachi, Y. Kawada, T. Nakamura and M. Tanimoto. *Demonstration of quasi-monoenergetic electron-beam generation in laser-driven plasma acceleration.* Appl. Phys. Lett. **86**, 251501 (2005).

155. B. Hidding, K.-U. Amthor, B. Liesfeld, H. Schwoerer, S. Karsch, M. Geissler, L. Veisz, K. Schmid, J. G. Gallacher, S. P. Jamison, D. Jaroszynski, G. Pretzler and R. Sauerbrey. *Generation of quasimonoenergetic electron bunches with 80-fs laser pulses.* Phys. Rev. Lett. **96**, 105004 (2006).

156. C.-T. Hsieh, C.-M. Huang, C.-L. Chang, Y.-C. Ho, Y.-S. Chen, J.-Y. Lin, J. Wang and S.-Y. Chen. *Tomography of injection and acceleration of monoenergetic electrons in a laser-wakefield accelerator.* Phys. Rev. Lett. **96**, 095001 (2006).

157. T. Hosokai, K. Kinoshita, T. Ohkubo, A. Maekawa, M. Uesaka, A. Zhidkov, A. Yamazaki, H. Kotaki, M. Kando, K. Nakajima, S. V. Bulanov, P. Tomassini, A. Giulietti and D. Giulietti. *Observation of strong correlation between quasimonoenergetic electron beam generation by laser wakefield and laser guiding inside a preplasma cavity.* Phys. Rev. E **73**, 036407 (2006).

158. W. P. Leemans, B. Nagler, A. J. Gonsalves, C. Tóth, K. Nakamura, C. G. R. Geddes, E. Esarey, C. B. Schroeder and S. M. Hooker. *GeV electron beams from a centimetre-scale accelerator.* Nature Phys. **2**, 696 (2006).

159. J. Faure, C. Rechatin, A. Norlin, A. Lifschitz, Y. Glinec and V. Malka. *Controlled injection and acceleration of electrons in plasma wakefields by colliding laser pulses.* Nature **444**, 737 (2006).

160. H.-P. Schlenvoigt, A. Haupt, K. Debus, F. Budde, O. Jackel, S. Pfotenhauer, H. Schwoerer, E. Rohwer, J. G. Gallacher, E. Brunetti, R. P. Shanks, S. M. Wiggins and D. A. Jaroszynski. *A compact synchrotron radiation source driven by a laser-plasma wakefield accelerator.* Nature Phys. **4**, 1745 (2008).

161. B. M. Luther, Y. Wang, M. A. Larotonda, D. Alessi, M. Berrill, M. C. Marconi, J. J. Rocca and V. N. Shlyaptsev. *Saturated high-repetition-rate 18.9-nm tabletop laser in nickel-like molybdenum.* Opt. Lett. **30**, 165 (2005).

162. Y. Wang, M. A. Larotonda, B. M. Luther, D. Alessi, M. Berrill, V. N. Shlyaptsev and J. J. Rocca. *Demonstration of high-repetition-rate tabletop soft-x-ray lasers with saturated output at wavelengths down to 13.9 nm and gain down to 10.9 nm.* Phys. Rev. A **72**, 053807 (2005).

163. J. Tümmler, K. A. Janulewicz, G. Priebe and P. V. Nickles. *10-Hz grazing–incidence pumped Ni-like Mo x-ray laser*. Phys. Rev. E **72**, 037401 (2005).

164. Y. Wang, E. Granados, M. A. Larotonda, M. Berrill, B. M. Luther, D. Patel, C. S. Menoni and J. J. Rocca. *High-brightness injection-seeded soft-x-ray-laser amplifier using a solid target*. Phys. Rev. Lett. **97**, 123901 (2006).

165. F. Pedaci, Y. Wang, M. Berrill, B. Luther, E. Granados and J. J. Rocca. *Highly coherent injection-seeded 13.2 nm tabletop soft x-ray laser*. Opt. Lett. **33**, 491 (2008).

166. Y. Wang, E. Granados, F. Pedaci, D. Alessi, B. Luther, M. Berrill and J. J. Rocca. *Phase-coherent, injection-seeded, table-top soft-X-ray lasers at 18.9 nm and 13.9 nm*. Nature Phot. **2**, 1749 (2008).

Papers

Paper I

Laser-accelerated protons with energy-dependent beam direction

F. Lindau, O. Lundh, A. Persson, P. McKenna, K. Osvay, D. Batani and C.-G. Wahlström.

Physical Review Letters **95**, 175002 (2005).

PRL 95, 175002 (2005) PHYSICAL REVIEW LETTERS week ending 21 OCTOBER 2005

Laser-Accelerated Protons with Energy-Dependent Beam Direction

F. Lindau,[1] O. Lundh,[1] A. Persson,[1] P. McKenna,[2] K. Osvay,[1,*] D. Batani,[3,†] and C.-G. Wahlström[1]

[1]*Department of Physics, Lund Institute of Technology, P.O. Box 118, S-22100 Lund, Sweden*
[2]*Department of Physics, University of Strathclyde, Glasgow G4 0NG, United Kingdom*
[3]*Dipartimento di Fisica "G. Occhialini," Università di Milano Bicocca, Piazza della Scienza 3, 20126 Milano, Italy*

(Received 24 June 2004; published 19 October 2005)

The spatial distribution of protons, accelerated by intense femtosecond laser pulses interacting with thin target foils under oblique irradiation are investigated. Under certain conditions, the proton beams are directed away from the target normal. This deviation is towards the laser forward direction, with an angle that increases with the level and duration of the amplified spontaneous emission pedestal before the main laser pulse. In addition, for a given laser pulse, this beam deviation increases with proton energy. The observations are discussed in terms of different electron acceleration mechanisms and target normal sheath acceleration, in combination with a laser-controllable shock wave locally deforming the target rear surface.

DOI: 10.1103/PhysRevLett.95.175002 PACS numbers: 52.38.Kd, 29.27.Fh, 52.35.Tc, 52.40.Kh

The generation of intense beams of energetic protons using short-pulse high-intensity lasers has recently attracted great interest. One of the most characteristic features of short-pulse laser acceleration of protons from thin solid targets is the directed beams emerging from the back of the target, in the target normal direction, and with a divergence decreasing with increasing proton energy [1]. With the laser focused obliquely onto the target, Krushelnick *et al.* [2] found that under certain conditions two separate spatial distributions could be observed in the proton emission. Deviation from target normal was observed also by Zepf *et al.* [3] on some of the laser shots in their investigations.

We present in this Letter a study on the spatial distribution of laser-accelerated protons. In particular, we study systematically the direction of the proton beam, as a function of various target and laser parameters, with the laser focused obliquely onto the target foil. We find that the proton beams are not always directed along the target normal, but under certain conditions steered towards the laser forward direction. We also show, for the first time, that the angle of deviation depends on the proton energy, and that it can be optically controlled by varying the intensity and duration of the ASE (amplified spontaneous emission) pedestal.

The experiments are performed with the 10 Hz multiterawatt femtosecond laser at the Lund Laser Centre. It is a Ti:sapphire system delivering 35 fs pulses of up to 35 TW at 800 nm. Important features of this system are that it allows the level and duration of the ASE pedestal, as well as the final pulse energy, to be continuously varied. The ratio between the peak and pedestal intensities, being the temporal contrast, is measured in the flat part of the pedestal before the main pulse, using a third order autocorrelator. (The ASE intensity is estimated from the measured contrast value and the estimated peak intensity.) Fast Pockels cells are incorporated in the system to enable efficient suppression of any prepulses and to facilitate control of the duration of the ASE pedestal—in the range 1.0–4.5 ns.

An $f/3$, off-axis parabolic mirror is used to focus the laser beam to a ~ 10 μm diameter spot ($1/e^2$). From the spot size, pulse duration, and pulse energy (700 mJ on target), we infer a peak intensity exceeding 10^{19} W/cm^2. At the focus, target foils of different materials and thicknesses are mounted for p-polarized irradiation at 45° angle of incidence.

The spatial distribution of the laser-accelerated protons is diagnosed with CR-39 nuclear track detectors, sensitive to protons but insensitive to electrons and x rays [4], placed 25 mm behind the target and oriented parallel to the target foil. A filter mask is positioned directly in front of the detector plates. This enables measurement of the spatial distributions of protons above chosen threshold energies; see Fig. 1(a).

With this setup we detect a broad energy distribution of protons, extending beyond 4 MeV, in a beam which is always in the plane of the laser beam and the target normal. Most unexpectedly, we find that under certain target and laser conditions, the proton beams are directed away from the target normal, towards the laser direction, by an angle that increases with proton energy. This is illustrated in Fig. 1(d) by a typical example obtained with 6 μm Al target.

In order to investigate these observations further, we perform a series of experiments where we systematically vary the target thickness, pedestal duration, and contrast ratio (pedestal intensity). The results are illustrated in Fig. 2, where data from typical, representative CR-39 detector plates, recorded during the same experimental runs are compared. These show that the observed energy-dependent beam deviation, away from target normal, can be optically controlled by carefully selecting the level and duration of the ASE pedestal. For a 6 μm Al target and a

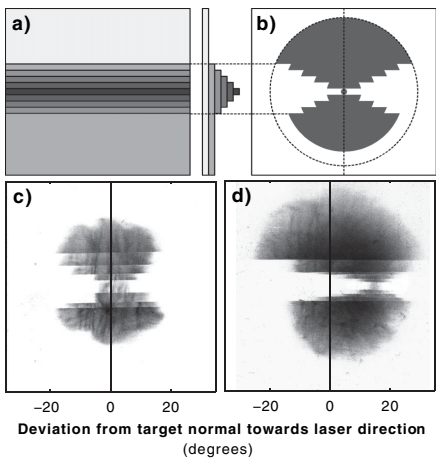

FIG. 1. (a) An Al filter mask is placed in front of the CR-39 plates to enable measurement of both the proton spatial and energy distributions. The expected pattern on the detector plates is schematically illustrated in (b), assuming a proton beam directed along the target normal and with a divergence decreasing with increasing proton energy. The observed distributions are illustrated by two representative examples obtained with (c) 12 μm and (d) 6 μm Al target. These examples clearly show that the proton beam under some conditions is centered along the target normal, and under other conditions shifted away, towards the laser direction, with an angle of deviation increasing with proton energy. The filter thickness used in the two cases are different, corresponding to a maximum threshold energy of 2.5 and 4.8 MeV in (c) and (d), respectively.

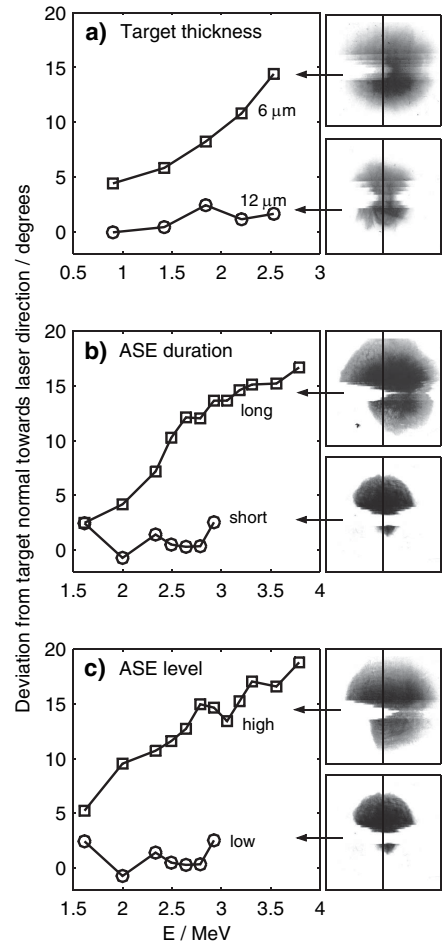

FIG. 2. Deviation from target normal for protons above different threshold energies. The lines through the images on the right indicate target normal direction. With the pedestal duration increased by 1 ns from its minimum value and a contrast of 3×10^7, the target thickness is varied in (a) from 12 to 6 μm. With 6 μm target thickness and a setting with minimum pedestal duration ($\sim$ 1 ns) and a contrast of 3×10^7, (b) illustrates the effect of increasing the pedestal duration by 1 ns and (c) of decreasing the contrast (increasing the ASE level) to 6×10^6, corresponding to an estimated ASE intensity of 5×10^{12} W/cm^2.

sufficiently low ASE level, proton beam steering requires the ASE pedestal to be extended in time beyond its minimum value. Alternatively, with a minimum pedestal duration (1 ns), the ASE level must be increased beyond its minimum value ($\sim 1 \times 10^{12}$ W/cm^2). In addition to the systematic trends observed regarding beam directions, we find that the smallest beam divergence is obtained with the shortest pedestal and the best contrast. This is illustrated by the cases shown in Figs. 2(b) and 2(c), where the divergence increases with ASE duration and level, respectively. The dependency on target thickness, illustrated in Fig. 2(a), indicates that the observed beam steering cannot be due to processes occurring on the target front surface only. In addition, not shown in Fig. 2 are our findings that energy-dependent beam deviations are observed also with 12 μm targets if the pedestal duration, or intensity, is increased sufficiently beyond its minimum value, and that with a too high ASE level no protons with energy above 1.6 MeV are observed with 6 μm targets.

The observed beam deviation from target normal might at first appear to be in conflict with the target normal sheath acceleration, TNSA, mechanism [5], by which the proton beams are emitted normal to the target rear surface. However, as discussed by Wilks *et al.* [5] and demonstrated by Roth *et al.* [6], this mechanism facilitates proton beam manipulation (focusing and defocusing) by using targets with curved rear surfaces. With this in mind, we propose the following explanation for the observed beam deflection: a shock wave is launched into the target, along the target normal, by the ablation pressure induced on the front surface by the ASE pedestal. When this shock wave

reaches the back side it gives rise to a dynamic expansion of the rear surface, which thus becomes convex with a time-dependent curvature. In experiments performed with the laser at normal incidence, this would, at most, result in an increased beam divergence.

To understand the beam deflection observed in our experiments, performed at 45° angle of incidence, we need to consider also the direction of the electrons heated by the laser at the target front surface. Different acceleration mechanisms exist and have different relative importance at different laser intensities and preplasma conditions. At ''low'' intensities, or steep plasma density gradients, resonant absorption dominates, accelerating electrons predominately along the target normal. At higher (relativistic) intensities and sufficiently large preplasmas, electrons are accelerated also in the laser forward direction by the $\mathbf{v} \times \mathbf{B}$ force of the intense laser radiation. This leads to the generation of two distinct electron distributions, along the target normal and in the forward laser propagation direction. This was first studied by Santala *et al.* [7], exploring the relative importance of the plasma density scale length on the two electron distributions. Later, Brandl *et al.* [8] showed that at high intensities, the highest electron energies are in the forward directed distribution. In our study the size of the preplasma varies with the ASE conditions. Simulations using the code MULTI, discussed below, show that the size, as determined by the distance from the ablation front to the critical density, ranges from a few μm at the lowest ASE levels and shortest durations, to 10–20 μm for the higher ASE intensities. Under the ASE conditions leading to the observed energy-dependent proton direction, the preplasma thus supports both heating mechanisms. However, we emphasize that the varying preplasma conditions alone cannot explain the experimental observations, in particular, not the dependence on target thickness of the ASE controlled proton beam deviation.

The electron distributions produced by the two different mechanisms both have certain angular spreads, so at the rear surface they can partly overlap. However, the center positions are different. If the rear surface has had time to expand, and become convex before the arrival of the main pulse, the central part of the two electron distributions will therefore leave the surface where the ''local target normal'' is pointing in different directions. In particular, the most energetic, forward accelerated electrons will leave the target surface where the local target normal is steered towards the laser forward direction (see inset of Fig. 3). The most energetic protons will consequently be accelerated, by TNSA, in this direction, while the low-energy proton distribution will mainly be defocused by the convex target surface. The curvature of the rear surface, and the partly overlapping electron distributions, result in a continuous spread of proton directions and not two separate beams.

The breakout of a shock wave at the rear target surface is frequently assumed to ruin the steep density gradient and thus prohibit efficient rear surface ion acceleration. A key

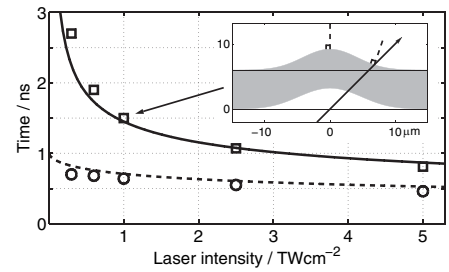

FIG. 3. The time required for a laser-driven shock to pass through a 6 μm Al target is plotted as a function of the laser (ASE) intensity (dashed line), as well as the total time for the shock to pass through the target and for the rear surface to expand 3 μm into vacuum (solid line). The analytical results are compared with results of 1D-hydrodynamic simulations giving the shock breakout time (circles) and the expansion time up to 3 μm (squares). The inset illustrates the results from 2D-hydrodynamic simulations, showing the ablation front at the front target surface and the expansion of the rear surface before the arrival of the main pulse. The arrow points in the direction of the laser propagation axis. The intensity and duration of the ASE pedestal match the indicated data point in the main figure.

point in the proposed explanation of our observations is therefore the assumption that, within our range of target and laser-pedestal parameters, an ASE-driven shock wave can give rise to a deformation of the target rear surface without melting it. In aluminum, the shock pressure P required to reach melting along the Hugoniot is approximately 1.2 Mbar (=120 GPa) [9]. This pressure corresponds to a melting temperature along the Hugoniot of about 5200 K (0.45 eV), much higher than even the boiling temperature for Al in standard conditions (2792 K). Such a change of regime in shock dynamics was recently studied experimentally using optical diagnostics [10].

The shock wave is driven by laser ablation on the front surface. Ablation pressure scales with laser intensity approximately as $I^{2/3}$ and, for Al and our laser wavelength, a pressure of 1.2 Mbar is reached at $\approx 4.2 \times 10^{12}$ W/cm^2 [11,12]. In our experiments we vary, and measure, the ASE contrast over more than 1 order of magnitude, with 3×10^7 being the highest value. With the peak laser intensity estimated to 3×10^{19} W/cm^2, this gives a variable pedestal intensity ranging from 1×10^{12} W/cm^2 to several times 10^{13} W/cm^2. This range of ASE intensities thus allows shock waves with shock temperatures below as well as above the melting point of the compressed target material to be studied.

Next we estimate the time required for the shock to pass through the target and to develop a rear surface curvature. At very low pressures, the shock velocity u_s is close to the bulk sound velocity c_0 but increases with shock pressure. The shock velocity is related to the particle velocity u_p as $u_s = c_0 + \alpha \times u_p$ ($\alpha = 1.21$, and $c_0 = 6.0$ μm/ns in Al [9]). The particle velocity and the shock wave velocity are

related through the momentum conservation relation $\rho_0 u_s u_p = P$, where ρ_0 is the initial target density and P the shock pressure. When the shock wave reaches the rear surface of the solid target, the free surface starts moving into vacuum with a velocity $u_{FS} \approx 2u_p$ while a rarefaction wave is backscattered into the medium [13]. In Fig. 3 we plot, as functions of laser intensity, the time it takes for a shock wave to pass through a 6 μm thick target and for the rear surface, with velocity u_{FS}, to move 3 μm, as an example of deformation giving a significant target curvature. (We assume a temporally flattop intensity profile for the ASE pedestal.) The analytic results are verified by hydrodynamic simulations performed with the code MULTI [14] and equation-of-state data for Al from [9]. We find good agreement between the analytical results and the hydrodynamic simulation. In addition, the MULTI simulations confirm that at these intensities, the density profile at the rear surface remains a step function during the expansion. From this figure we find that, with the ASE intensity corresponding to our best contrast, $\sim 1 \times 10^{12}$ W/cm^2, and our minimum ASE duration, 1 ns, there will not be time to produce the given rear surface deformation before the arrival of the main pulse. But by increasing either the ASE duration by 1 ns or the shock pressure (ASE intensity) to the maximum pressure without melting, 1.2 Mbar (4.2×10^{12} W/cm^2), the rear surface will have time to deform before the arrival of the main pulse. These estimates also show that an increase in target thickness requires an increase in pedestal duration, or in ASE intensity, for the same beam deviation to be observed as with thinner targets. These dependencies, with respect to ASE intensity, pedestal duration, and target thickness all agree qualitatively with the trends observed experimentally and illustrated in Fig. 2.

In order to verify that the rear surface deformation is consistent with the observed proton deflection, we perform two-dimensional hydrodynamic simulations using the code MULTI-2D [15] with parameters chosen to mimic the experimental conditions (flattop laser intensity profile with 14 μm $1/e^2$ diameter Gaussian spot, target simulated with data from the Sesame tables). One example of the results is shown in the inset of Fig. 3. The limits of the gray regions correspond to the position of the surface where the mass density equals the initial mass density in the solid, unperturbed, target. The ''local target normal,'' where the laser axis exits the rear surface, deviates from the global target normal, towards the laser forward direction, in agreement with the observed proton beam deflections. More detailed comparisons between experimental results and modeling will be published separately.

The findings reported in this Letter have immediate implication in a variety of situations. First, they directly influence the proper design of experimental studies. For example, Thomson parabola ion spectrometers are frequently employed to diagnose the accelerated ions. Whereas this technique supports measurement of the continuous energy distribution of the ions, it is limited to sampling a small solid angle. The results of the present study clearly show that the positioning of the ion spectrometer can influence the recorded energy distribution. Second, the present result addresses the fundamental processes involved in the transfer of laser energy to energetic protons, via energetic and directed electrons. Further studies of these energy-dependent beam directions should allow the different processes involved to be further disentangled and understood, which is of utmost importance for efficient optimization of the beam properties. Finally, they open new perspective for novel applications, where active control of the divergence, direction, and spatial energy distribution of beams of laser-accelerated ions are essential. It is conceivable, for example, that the observed phenomenon could be used to tailor the beams such that ions of selected energy are preferentially deflected or focused in specific directions.

We acknowledge the support from the Swedish Research Council, the Knut and Alice Wallenberg foundation, the EU Access to Large-Scale Facility Programme (HPRI-CT-1999-00041 and RII3-CT-2003-506350 Laserlab Europe), and the EU SHARP project (HPRI-CT-2001-50037). P. McK. gratefully acknowledges Royal Society of Edinburgh support. Stimulating discussions with K. Ledingham, S. Svanberg, R. Ramis, and S. Atzeni are also acknowledged.

*Present address: Department of Optics and Quantum Electronics, University of Szeged, Szeged 6701, Hungary.
†On leave at LOA, Ecole Polytechnique, Palaiseau, France.

[1] R. A. Snavely *et al.*, Phys. Rev. Lett. **85**, 2945 (2000).
[2] K. Krushelnick *et al.*, Phys. Plasmas **7**, 2055 (2000).
[3] M. Zepf *et al.*, Phys. Plasmas **8**, 2323 (2001).
[4] F. H. Seguin *et al.*, Rev. Sci. Instrum. **74**, 975 (2003).
[5] S. C. Wilks *et al.*, Phys. Plasmas **8**, 542 (2001).
[6] M. Roth *et al.*, Plasma Phys. Controlled Fusion **44**, B99 (2002).
[7] M. I. K. Santala *et al.*, Phys. Rev. Lett. **84**, 1459 (2000).
[8] F. Brandl *et al.*, Europhys. Lett. **61**, 632 (2003).
[9] Sesame tables 3712 and 3717 for Al, from T4 Group LANL, SESAME Report on the Los Alamos Equation-of-State Library, Report No. LALP-83-4, 1983.
[10] A. Benuzzi-Mounaix *et al.*, Phys. Rev. E **70**, 045401 (2004).
[11] D. C. Swift *et al.*, Phys. Rev. E **69**, 036406 (2004).
[12] J. Lindl, Phys. Plasmas **2**, 3933 (1995).
[13] Ya. B. Zeldovich and Yu. P. Raizer, *Physics of Shock Waves and High Temperature Hydrodynamic Phenomena* (Academic Press, New York, 1967).
[14] R. Ramis, R. Schmalz, and J. Meyer-ter-Vehn, Comput. Phys. Commun. **49**, 475 (1988).
[15] R. Ramis and J. Meyer-ter-Vehn, Max-Planck-Institut für Quantenoptik, Report No. MPQ174, 1992.

Paper II

High-intensity laser-driven proton acceleration: influence of pulse contrast

P. McKenna, F. Lindau, O. Lundh, D. Neely, A. Persson and C.-G. Wahlström.

Philosophical Transactions of the Royal Society A **364**, 711 (2006).

PHILOSOPHICAL TRANSACTIONS OF THE ROYAL SOCIETY A

Phil. Trans. R. Soc. A (2006) **364**, 711–723
doi:10.1098/rsta.2005.1733
Published online 25 January 2006

High-intensity laser-driven proton acceleration: influence of pulse contrast

By Paul McKenna[1,*], Filip Lindau[2], Olle Lundh[2], David Neely[3], Anders Persson[2] and Claes-Göran Wahlström[2]

[1]*SUPA, Department of Physics, University of Strathclyde, 107 Rottenrow, Glasgow G4 0NG, UK*
[2]*Department of Physics, Lund Institute of Technology, PO Box 118, 221 00 Lund, Sweden*
[3]*Central Laser Facility, Rutherford Appleton Laboratory, Chilton, Didcot, Oxon OX11 0QX, UK*

Proton acceleration from the interaction of ultra-short laser pulses with thin foil targets at intensities greater than $10^{18}\,\mathrm{W\,cm^{-2}}$ is discussed. An overview of the physical processes giving rise to the generation of protons with multi-MeV energies, in well defined beams with excellent spatial quality, is presented. Specifically, the discussion centres on the influence of laser pulse contrast on the spatial and energy distributions of accelerated proton beams. Results from an ongoing experimental investigation of proton acceleration using the 10 Hz multi-terawatt Ti : sapphire laser (35 fs, 35 TW) at the Lund Laser Centre are discussed. It is demonstrated that a window of amplified spontaneous emission (ASE) conditions exist, for which the direction of proton emission is sensitive to the ASE-pedestal preceding the peak of the laser pulse, and that by significantly improving the temporal contrast, using plasma mirrors, efficient proton acceleration is observed from target foils with thickness less than 50 nm.

Keywords: laser-particle acceleration; proton beam; laser–plasma interactions

1. Background

Ion acceleration driven by intense laser–plasma interactions has been observed for more than two decades. Gitomer *et al.* (1986) provides a review of early ion measurements with long pulse (nanosecond) CO_2 lasers. In these experiments, at focused intensities of approximately $10^{16}\,\mathrm{W\,cm^{-2}}$, protons and carbon ions were accelerated to energies of the order of tens of keV. It was found that the source of the ions was hydro-carbon or water contamination layers on the surfaces of the thin foil targets irradiated by the laser, and that the acceleration mechanism was driven by charge separation within the laser-produced plasma.

In recent years, there has been a renewed interest in laser-driven ion acceleration due to the availability of high-intensity laser pulses (greater than

* Author for correspondence (p.mckenna@phys.strath.ac.uk).

One contribution of 15 to a Discussion Meeting Issue ‘Laser-driven particle acclerators: new sources of energetic particles and radiation’.

10^{18} W cm^{-2}) with sub-picosecond duration, made possible by the introduction of chirped pulse amplification (CPA). Proton acceleration to tens of MeV energies and in low divergent beams of excellent quality has been demonstrated (Clark *et al.* 2000*a*; Snavely *et al.* 2000). Heavier ions have also been observed, with energies up to hundreds of MeV (Clark *et al.* 2000*b*; Hegelich *et al.* 2002). Laser-generated ion beams have a number of desirable properties. It has been shown experimentally that proton beams are generated with low transverse and longitudinal emittance (about 100 fold better than beams produced from typical RF accelerators; Cowan *et al.* 2004). The ions are produced in short bunches of high brightness with a measured efficiency of conversion from laser energy to ions as high as 12% (Snavely *et al.* 2000). An interesting application of laser-driven protons is to probe the evolution of electric fields within a plasma (Borghesi *et al.* 2002). These techniques have even been applied to measure the spatial and temporal evolution of the electrostatic fields responsible for laser-driven ion acceleration. Other proposed applications of this potentially compact ion source include ion radiotherapy (Bulanov *et al.* 2002), isotope production for medical imaging techniques (Ledingham *et al.* 2004) and as injectors for the next generation of ion accelerators (Krushelnick *et al.* 2000). The need to optimize and control ion acceleration for many of these applications has motivated a number of research groups worldwide to investigate laser-driven proton and heavier ion acceleration.

In this paper, we discuss aspects of our present understanding of the mechanisms leading to ion acceleration in the interaction of high-intensity laser pulses with thin foil targets, and highlight examples of some of the recent progress made in this research area. Specifically, we discuss the influence of the temporal contrast of the laser pulse on ion acceleration, and illustrate our discussion with results from an ongoing research campaign on laser-driven proton acceleration at the Lund Laser Centre (LLC) in Sweden.

2. Ion acceleration mechanisms

We begin by noting that the high energy ions that are produced by laser–plasma interactions are not directly accelerated by the laser pulse—this would require much higher focused intensities (greater than 10^{22} W cm^{-2}) than are currently available. Instead, ion acceleration occurs due to the build up of electrostatic fields, resulting from charge separation due to the laser pulse driving electron motion inside the irradiated target. By creating and heating a plasma, the laser pulse drives ion acceleration. Although a variety of target types, including gas, water droplets, clusters, thin foils and thick solid targets, have been used to demonstrate the acceleration of ions (Mendonca *et al.* 2001), the highest quality ion beams are observed with thin foil targets.

When a high-intensity laser pulse is focused onto a surface of a target foil, the leading edge of the laser pulse (or the amplified spontaneous emission (ASE)-pedestal) ionizes the target (at intensities of approximately 10^{12} W cm^{-2}) leading to an expanding plasma, with an exponentially decreasing density at increasing distance from the target surface. The peak of the laser pulse propagates in the expanding plasma until it reaches a critical plasma density (approximately 10^{21} cm^{-3}), at which the plasma frequency (collective electron

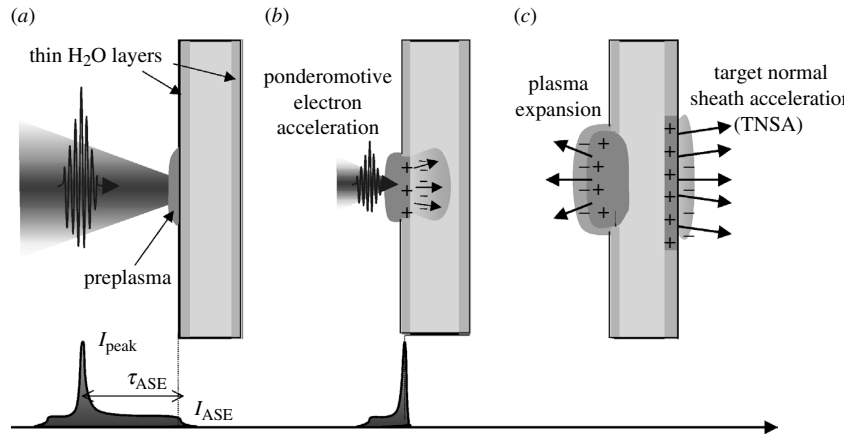

Figure 1. The main ion acceleration mechanisms in the interaction of a high-intensity laser pulse with a thin foil target. (*a*) The ASE-pedestal arriving at the target surface, prior to the peak of the laser pulse, creates a plasma. (*b*) The peak intensity of the laser pulse interacts with the preformed plasma, ponderomotively accelerating electrons into the target and creating a space charge separation, leading to ion acceleration. (*c*) The accelerated electrons emerge from the target rear surface, forming an electron sheath with micron-scale Debye length. The resulting quasi-static electric field, of the order of TV m^{-1}, leads to ionization and ion acceleration to multi-MeV energies (the TNSA mechanism). Plasma expansion at the target front surface leads to ion acceleration in the backward direction.

motion against the ion background) cancels the propagation of an electromagnetic wave. The main laser–plasma interaction occurs at this critical density surface. The plasma electrons react to the ponderomotive potential of the focused laser light, and are pushed from regions of high laser intensity to regions of lower intensity. A number of important electron acceleration mechanisms have been identified. At lower intensities, of the order of 10^{16} W cm^{-2}, and short plasma scale lengths, resonant absorption dominates, leading to electron acceleration in the direction of the density gradient. At higher intensities, greater than 10^{18} W cm^{-2} for laser light at wavelength of approximately 1 μm, relativistic laser–plasma interactions occur. The $\boldsymbol{v}\times\boldsymbol{B}$ component of the Lorentz force then leads to electron acceleration in the laser propagation direction, with electron energies corresponding to MeV temperatures. If a high-intensity, *p*-polarized laser pulse is focused onto a target foil at an angle other than target normal, two distributions of electrons (resulting from the two acceleration mechanisms) will thus be driven into the foil in different directions. This has been demonstrated experimentally (Santala *et al.* 2000; Brandl *et al.* 2003). We also note that in order to sustain large currents of hot electrons moving forward, return currents of cold electrons are produced to overcome the Alfvén limit.

Separation of the accelerated electrons from the ion background within the plasma creates electrostatic fields which accelerate the ions. At least two ion acceleration schemes have been put forward to explain experimental observations, and are summarized in figure 1. Ponderomotive electron acceleration produces an electrostatic field on the laser-irradiated surface, resulting in the

acceleration of ions from the front side of the target, passing through the target and forming a beam in the forward direction (Clark *et al.* 2000*a*). The hot electron populations which are accelerated through the target foil form an electron sheath at the rear surface, resulting in field ionization and ion acceleration—the target normal sheath acceleration model (TNSA; Wilks *et al.* 2001). The quasi-static electric fields (approximately $kT_{\mathrm{hot}}/e\lambda_{\mathrm{D}}$, where kT_{hot} is the hot electron temperature and λ_{D} is the Debye length) can reach values greater than $10^{12}\,\mathrm{V\,m^{-1}}$, leading to ion energies in the MeV range for micron scale Debye lengths. Because of the presence of hydrocarbon and water vapour on the surfaces of the foils (for experiments performed at typical vacuums of approximately 10^{-5} mbar), protons are usually observed in large numbers, and due to their high charge-to-mass ratio they are more efficiently accelerated than heavier ion species and effectively screen the electric acceleration fields experienced by heavier ions. Recent studies have shown that in order to efficiently accelerate heavier ions the proton source layers should be removed from the target foil by heating or ablation (Hegelich *et al.* 2002; McKenna *et al.* 2004). In addition to ion acceleration in the forward direction (direction of laser propagation), we note that plasma expansion at the front surface of the target foil can also lead to ion acceleration in the backward direction. The energies and other properties of accelerated ions depend strongly on the parameters of the charge separation, and this is currently the subject of intense experimental and theoretical research programmes.

3. Effects of laser pulse contrast on ion acceleration

Laser pulse intensity contrast is a measure of the ratio of the intensity of laser light in the peak of the laser pulse to the background intensity. An important contributory factor to the background light is ASE, which is produced when inherent background light gets amplified due to the gain in the amplifying crystals. The ASE forms a pedestal extending of the order of nanoseconds before and after the peak of the laser pulse, as shown schematically in figure 1*a*, where the peak intensity is denoted I_{peak} and I_{ASE} and τ_{ASE} denote the level and duration of the ASE pedestal prior to the peak of the pulse, respectively. The background may also contain pre-pulses arising from, for example, incomplete compression of the CPA pulse through higher order phase errors or spectral clipping. In this discussion article, we specifically consider the effects of the ASE pedestal on ion acceleration.

An ASE-pedestal arriving at the surface of a target foil will generate X-rays which can heat the bulk of the target. If the target foil is sufficiently thin, the target rear surface is radiatively heated. In addition, the ablation pressure due to the arrival of the ASE-pedestal on the surface of the foil launches a shock wave into the target. Again, if the target foil is sufficiently thin for the shock wave to propagate through the foil before the peak of the laser pulse arrives on target, expansion of the target rear surface can result. Both processes can ruin the steep density gradient on the target rear surface required for ion acceleration by the TNSA mechanism.

The optimum target thickness for efficient proton acceleration, without inducing an expansion of the target rear surface, depends not only on the laser pulse parameters, but also the target density. For the purposes of illustrating our

discussion, however, we consider only Al, which has been widely shown to be a suitable target material for efficient proton acceleration. Many of the reported measurements on laser-driven proton acceleration have involved laser pulses with typical contrast in the range 10^5–10^7. As a result, Al target foils with thickness greater than a few microns are usually employed to ensure that the ASE-pedestal does not induce an expansion of the target rear surface (Roth *et al.* 2002). Using laser pulses with contrast of approximately 10^6, for example, Spencer and co-workers (McKenna *et al.* 2002; Spencer *et al.* 2003) observed the highest proton energies from Al target foils of thicknesses of approximately 12 μm, with a sharp cut-off with thinner foils. With pulses of contrast better than 2×10^7, Kaluza *et al.* (2004) have shown that the optimum target thickness for proton acceleration decreases with the duration of the ASE-pedestal—with a minimum pedestal duration of 0.5 ns an optimum Al thickness of 2 μm was observed to produce protons with energies up to ∼3.5 MeV. They further report that with targets below the optimum thickness the spatial profile of the proton beam becomes blurred—consistent with an expansion of the target rear surface.

The expansion of the target rear surface is sensitive to both the level and duration of the ASE-pedestal prior to the peak of the pulse. Let us consider, for example, a laser pulse with a peak focused intensity of 10^{19} W cm^{-2} and with a pedestal duration of 1 ns and intensity of approximately 10^{13} W cm^{-2}. This ASE-pedestal produces an ablation pressure of greater than 2 Mbar and launches a shock wave of velocity ∼10 μm ns^{-1} into an Al target foil. Assuming a constant shock velocity (ignoring expansion of the shock wave within the target), the shock wave will reach the rear surface, of target foils with thickness less than 10 μm, prior to the arrival of the peak of the laser pulse on target and, therefore, the formation of the electron sheath responsible for ion acceleration at the target rear surface. A reduction in the pedestal duration or ASE intensity (resulting in a slower shock wave) reduces the lower limit of the target thickness before shock breakout on the rear surface results.

A pulse contrast of between 10^5 and 10^7 is typical of high-power laser systems. A measurement of proton acceleration with laser pulses with exceptional temporal contrast of 10^{10} was reported (Mackinnon *et al.* 2002) using the JanUSP laser (at the Lawrence Livermore National Laboratory, USA). With this contrast, a dramatic enhancement in measured proton energy was observed when decreasing target thickness below a certain threshold. This was attributed to electron recirculation inside thin foil targets. While the laser pulse is present, electrons generated at the laser focus are reflected from the Debye sheath built up at the target surfaces and recirculate within the target, enhancing the electrostatic fields responsible for ion acceleration. With a peak intensity of 1×10^{20} W cm^{-2}, Mackinnon *et al.* (2002) observed proton energies up to 24 MeV from Al targets with thickness down to 3 μm. Such an enhancement due to recirculation in thin foil targets motivates research using even thinner targets.

In the remainder of this article, we discuss progress made in an ongoing research programme at the Lund Laser Center to investigate proton acceleration as a function of various laser and target parameters. In particular, we discuss a transition window of ASE-pedestal conditions, for which shock breakout modifies the properties of the accelerated ion beam, without resulting in evaporative expansion of the target rear surface. We also discuss a progression towards ion acceleration from ultra-thin targets under ultra-high contrast conditions, facilitated by the use of plasma mirrors.

4. Experimental approach at the Lund Laser Centre

We use the 10 Hz, multi-terawatt, femtosecond laser at the LLC, which can deliver pulses of 1.0 J in 35 fs at a wavelength of 800 nm. The laser system is described elsewhere (Lundh *et al.* in preparation). Importantly, a total of four Pockels cells are used to efficiently suppress any pre-pulses and to facilitate control of the duration of the ASE pedestal, in the range 1.0–4.5 ns. The system is also equipped with an acousto-optic pulse shaper for spectral and temporal control of the seed pulses from the oscillator. The amplitude of the acoustic wave launched into the acousto-optic crystal determines diffraction efficiency of this device. Thereby, the seed energy to the first amplification stage, a regenerative amplifier, can be continuously controlled. Because of its high gain, the bulk of the ASE is produced in the regenerative amplifier. Increasing the seed energy to the amplifier, other things kept constant, lowers the amount of ASE produced by it. The pulse energy from the final amplifier remains unchanged, as it operates in saturation. The temporal contrast is measured in the flat part of the pedestal, approximately 100 ps before the main pulse, using a third order autocorrelator, and the ASE intensity is estimated from the measured contrast and the estimated peak intensity. On the nanosecond timescale, the temporal profile is measured with a fast photo diode and oscilloscope. Figure 2 shows a typical temporal profile of the laser pulse.

The laser pulses are focused onto thin foils at 45° angle of incidence by a $f/3$, off-axis parabolic mirror to a focal spot with a $1/e^2$ focal spot diameter of 7 μm, as illustrated in figure 3. A peak intensity on target exceeding 10^{19} W cm^{-2} is inferred from the measured spot size, pulse energy and pulse duration. Target foils are mounted in a multi-target holder to facilitate systematic investigation of proton acceleration as a function of target parameters. An alternative mode of operation involving a plasma mirror (Ziener *et al.* 2003; Dromey *et al.* 2004), to further extend the contrast range available with this laser, is illustrated in the inset of figure 3.

CR-39 nuclear track detector, which is sensitive to ions, but insensitive to electrons and X-rays, is used to diagnose the spatial distribution of the proton beam in the energy range 0.1–11 MeV (1 mm thick CR-39 plates). A CR-39 plate feeder system (not shown in figure 3) enables the proton beam profiles to be recorded on up to 20 laser shots for each pump down cycle of the target vacuum chamber. The proton stopping power in Al (figure 4*a*) is used to determine the spatial profile of the protons above selected threshold energies. An Al filter mask with increasing thickness (figure 4*b*) is employed directly in front of the detector plates. The filters also serve to stop heavier ions from reaching the CR-39 and protect it from target debris.

Proton energy distribution measurements are made using a Thomson parabola ion spectrometer and two compact magnetic spectrometers (figure 3). For both types of spectrometer the dispersed proton beam is again detected using CR-39, but with a thin Al filter, in direct contact, to remove heavier ions and to slow down fast protons for effective detection and analysis. The spectrometers have a line of sight to the laser focal spot in the plane of the laser beam and the target normal, and can be used at a wide range of angles with respect to the target normal.

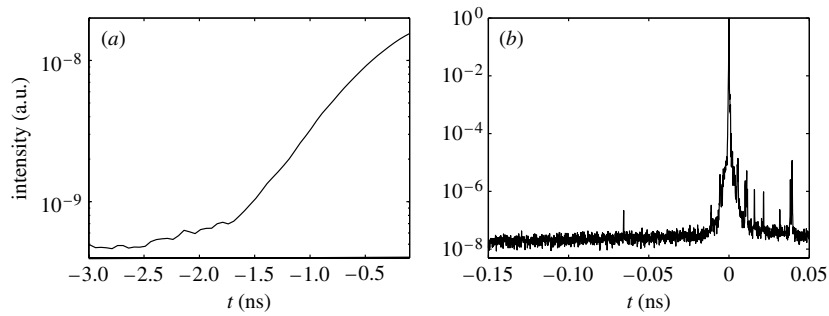

Figure 2. Representative example of temporal profile measurements of the laser pulse, using a fast photo diode (*a*) and a third order autocorrelator (*b*).

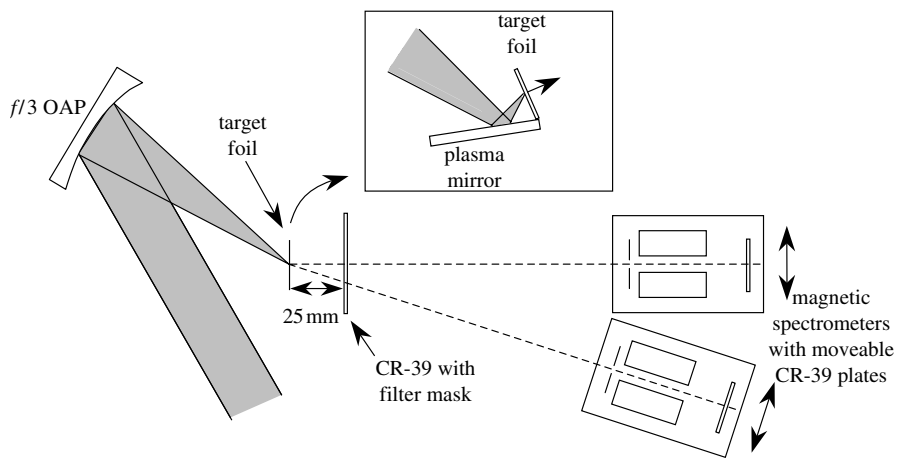

Figure 3. Schematic illustration of the experimental arrangement employed to investigate laser-driven proton acceleration. The spatial and energy distributions of beams of protons accelerated in the forward direction are measured using CR-39 with a filter mask (figure 4) and two magnetic spectrometers and a Thomson parabola spectrometer (not shown). Inset: the addition of a plasma mirror is used to achieve higher laser pulse contrast. The plasma mirror (a glass plate) is positioned such that the intensity of the ASE-pedestal is below the ionization threshold of the glass and is therefore transmitted. A plasma is created by the rising edge of the peak of the laser pulse and reflects the main laser pulse, with the bulk of the energy, onto the target foil.

5. Measured sensitivity of proton emission to ASE-pedestal

We measure proton beam spectral distributions and spatial profiles for a range of target foil thicknesses, as a function of ASE-pedestal intensity and duration. Typically, we observe a broad energy distribution of protons, extending beyond 4.5 MeV. As an example, the proton energy spectrum, emitted along target normal, from a 6 μm Al foil irradiated at a few 10^{19} W cm^{-2} is shown in figure 5. We do not specifically investigate the relative contributions to the measured

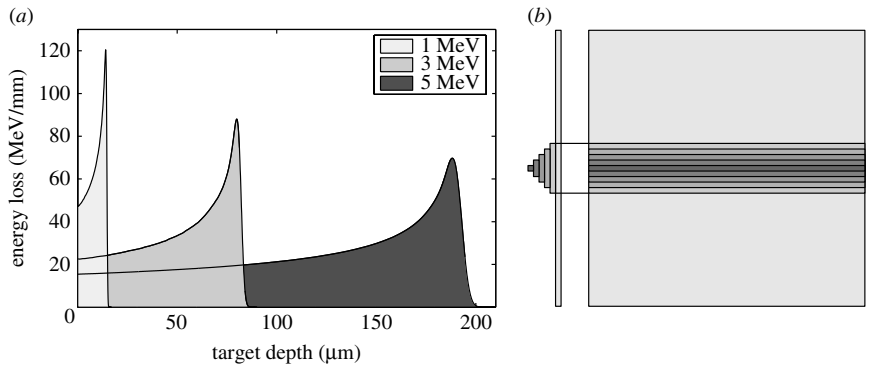

Figure 4. (*a*) Proton stopping powers in aluminium. (*b*) The stepped aluminium filter arrangement placed in front of the CR-39 to enable measurement of the proton spatial distributions above selected energy thresholds.

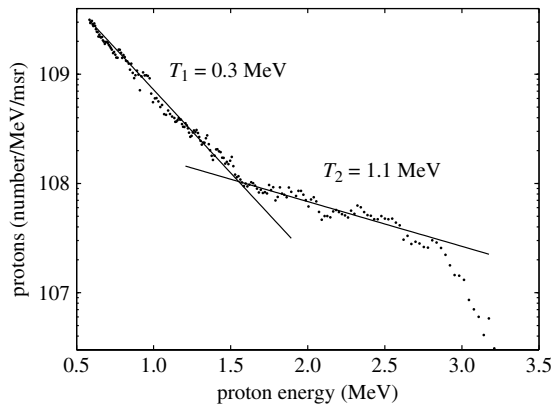

Figure 5. A typical proton energy spectrum, observed by irradiating a 6 μm thick Al foil at a few 10^{19} W cm^{-2}. The spectrum comprises of two Boltzmann-like distributions with temperatures of 0.3 and 1.1 MeV.

proton beam resulting from the front and rear side acceleration mechanisms previously discussed, but note that simulations by Sentoku *et al.* (2003) predict a maximum energy of approximately 7.5 MeV due to the rear surface acceleration process, and less than 1 MeV for protons originating from the front surface, for the 35 fs pulse duration used in this work.

Typical examples of our recordings of the spatial profiles of the proton beam above selected energies, as a function of Al target foil thickness and laser pulse contrast, are summarized in figure 6. We observe that, independent of target thickness, the proton beam is always emitted in the plane of the laser beam and the target normal, and in agreement with previous observations (Snavely *et al.* 2000), we also observe that the angular divergence of the collimated beams decreases with increasing proton energy. Importantly, similar to Kaluza *et al.*

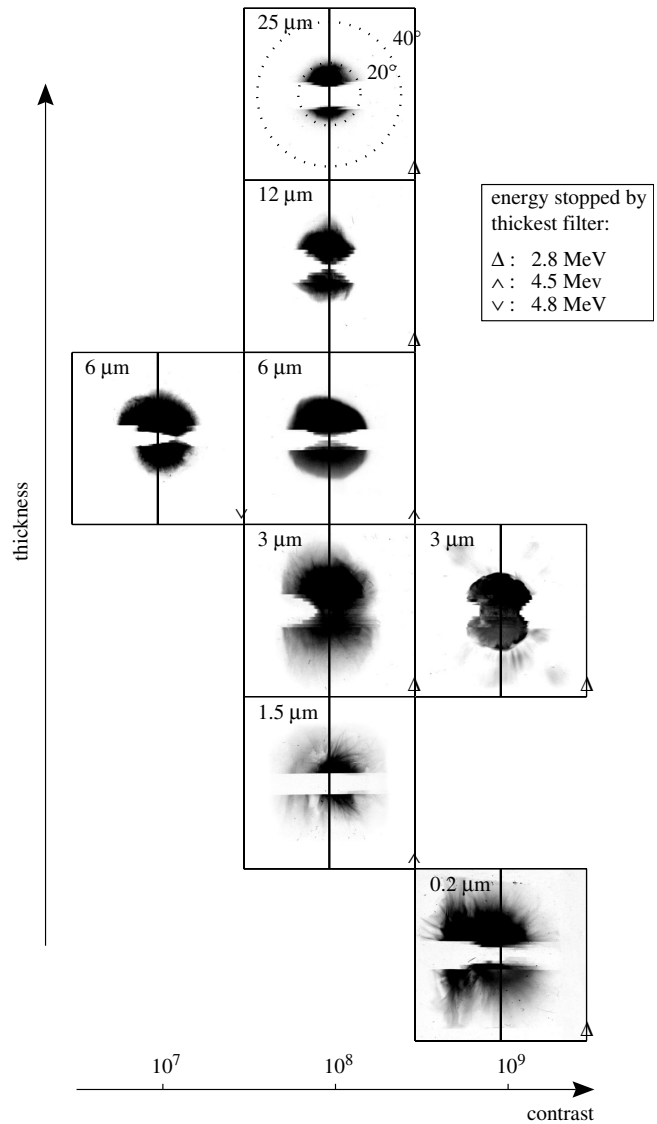

Figure 6. Representative examples of spatial and energy distributions of proton beams, as a function of Al target foil thickness and laser pulse contrast. Al filters, as illustrated in figure 4, are used. The laser pulse contrast of 10^9 was obtained using a plasma mirror with reflectivity of the order of 50%. The two circles, shown for the 25 µm result, correspond to the 20° and 40° half-angles of the divergence of the proton beam, and are applicable to all examples. The vertical lines correspond to the target normal. At laser pulse contrasts of 10^7 and 10^8 it is observed that the high-energy component of the proton beam is shifted away from the target normal, towards the laser direction (to the right of the distribution), for the 6 and 3 µm thick targets, respectively. The angle of deviation is found to increase with proton energy.

(2004), we observe that the optimum target thickness for proton acceleration is sensitive to the duration of the ASE-pedestal. We further observe that it is also sensitive to ASE intensity.

Consider the example profiles recorded with laser pulses of contrast $\sim 10^8$ (with ASE level a few 10^{11} W cm^{-2} and duration 1 ns) in figure 6. We observe proton beams centred on the target normal direction for all proton energies from targets with thickness 6 μm or greater. With the same laser conditions, and with a target thickness of 1.5 μm, we observe a reduction in the homogeneity of the proton beam and begin to observe structure in the beam profile. We also observe a significant reduction in the energy of emitted protons. This is consistent with our understanding that for a sufficiently thin target the ASE-pedestal will ruin the steep density gradient required on the target rear surface for efficient ion acceleration, and that there is an optimum foil thickness for given laser contrast conditions (approximately 3–6 μm for the case considered).

Of particular interest is our reported observation (Lindau *et al.* 2005) that for a certain window of ASE-pedestal conditions we observe a deflection of the high-energy component of the emitted proton beam, away from the target normal and towards the laser direction. This is illustrated in figure 6 for the 6 μm Al target at a laser pulse contrast of 10^7, and 3 μm target at contrast 10^8. The observation is explained in terms of proton acceleration from a target rear surface which is undergoing dynamic expansion due to breakout of the shock wave, launched by the ablation pressure on the front surface by the arrival of the ASE pedestal (Lindau *et al.* 2005). Irradiation of a target foil with *p*-polarized pulses at 45° angle of incidence ponderomotively drives electrons in the laser forward direction, leading to sheath formation in a region of the target rear surface where the localized target normal is directed away from the global target normal. The highest energy protons, produced at the peak of the sheath field are thus accelerated in a direction away from the global target normal. With laser pulses of contrast 10^8, this deviation is not observed for the 6 μm target, but is observed for 3 μm and thinner targets. For 6 μm thick Al foils, we find that threshold ASE-pedestal intensity and duration conditions are reached with laser pulses of contrast between 10^8 and 10^7, corresponding to shock breakout on the rear surface and leading to the observed deflection. For 3 μm thick Al foils the threshold conditions are lower, resulting in the observed high-energy proton deviation with pulses of 10^8 contrast.

Our observations show that a window of ASE conditions exists, for a given target thickness, in which shock break out modifies the spatial distribution of the accelerated proton beam, without destroying the steep density gradient required by the TNSA acceleration mechanism. This model of a dynamic deformation of the target rear surface, induced by a shock wave with Mbar pressures and velocity of the order of μm ns^{-1} is supported by simulations using the hydrodynamic code MULTI (Lundh *et al.* in preparation).

6. Proton acceleration with ultra-high contrast laser pulses

We routinely obtain pulses with a temporal contrast of approximately 1.0×10^8 from the multi-terawatt LLC laser. With this contrast, and a minimum pedestal duration of 1.0 ns, we observe protons with energy extending beyond 4.5 MeV,

from Al target foils of thickness down to 0.2 μm. Motivated by the observed enhancement in proton numbers and energies reported by Mackinnon *et al.* (2002), and attributed to electron recirculation within thin foils, we extend our investigation to even higher contrast and thinner targets.

Enhanced contrast pulses are produced by inserting a plasma mirror (Ziener *et al.* 2003; Dromey *et al.* 2004) into the focusing beam, as illustrated in the inset of figure 3. A planar plasma mirror was operated at 45° in *p*-polarization giving a measured energy reflectivity of 41%. The ASE intensity on the plasma mirror is less than 10^8 W cm^{-2}, which is well below the threshold for plasma formation. By calculating the ratio of ASE reflectivity to main pulse reflectivity, we estimate a contrast enhancement of 45. This leads to a contrast on target of up to 10^{10}.

We find that, by increasing the contrast by more than one order of magnitude, we can decrease the target thickness, for which we observe high energy well-defined proton beams, by more than one order of magnitude (Neely *et al.* in preparation). In fact, with laser pulses with temporal contrast better than 10^9 we observe protons with multi-MeV energies from Al target foils with thickness less than 50 nm. We also find that, as illustrated in figure 6, the increased contrast has the effect of 'switching-off' the proton deviation observed, at a contrast of 10^8, with a 3 μm Al target. This is expected due to the associated reduction in ASE-pedestal intensity and hence the ablation pressure and velocity of the resulting shock wave launched in the target.

7. Summary and future challenges

We conclude that the temporal contrast of the laser pulse plays an important role in laser-driven ion acceleration from thin foil targets. Our experimental programme has led directly to the observation that for a target foil of a given thickness, threshold ASE-pedestal intensities and durations exist, above which an ASE-induced shock wave can lead to non-evaporative deformation of the target rear surface and a resulting change in the direction of proton emission. This observation points to a laser controllable manipulation of the proton beam profile. This is achieved without the need for precision pre-manufactured targets and, therefore, in principle, can be performed at high repetition rates.

In addition, at the start of our research programme we would not have imagined that we would observe well-defined, energetic proton beams from target foils with thickness ranging over 3 orders of magnitude—from 50 μm to below 50 nm. The fact that we observe efficient ion acceleration from ultra-thin targets raises interesting questions regarding the electron transport and ion acceleration processes at work, and opens up exciting directions for our ongoing research programme. We anticipate further experimentation, possibly involving double plasma mirrors, to extend our investigations of the influence of laser contrast on ion acceleration and to elucidate the acceleration mechanisms with even thinner target foils, approaching the skin depth (approximately 8 nm) for 800 nm laser light absorption.

In general, the advances made in understanding the parameters affecting proton acceleration, and to some extent manipulating the proton beam, encourage the view that this potentially compact and unique source of ions may become useful for

a number of potential applications. Further experimental and theoretical research is required to optimize and control laser-driven ions. An important challenge remains to find the parameters which control the accelerated ion energy distribution, to enable high-quality beams of quasi-monoenergetic ions to be produced.

We acknowledge the financial support by the Access to Research Infrastructures activity in the Sixth Framework Programme of the EU (contract RII3-CT-2003-506350, Laserlab Europe) and by the Swedish Research Council. P.McK. acknowledges the award of a Royal Society of Edinburgh Personal Fellowship.

References

Borghesi, M. *et al.* 2002 Electric field detection in laser–plasma interaction experiments via the proton imaging technique. *Phys. Plasmas* **9**, 2214. (doi:10.1063/1.1459457)

Brandl, F., Pretzler, G., Habs, D. & Fill, E. 2003 Cerenkov radiation diagnostics of hot electrons generated by fs–laser interactions with solid targets. *Europhys. Lett.* **61**, 632. (doi:10.1209/epl/i2003-00118-y)

Bulanov, S. V., Esirkepov, T. Z., Khoroshkov, V. S., Kunetsov, A. V. & Pegoraro, F. 2002 Oncological hadrontherapy with laser ion accelerators. *Phys. Lett. A* **299**, 240. (doi:10.1016/S0375-9601(02)00521-2)

Clark, E. L. *et al.* 2000*a* Measurements of energetic proton transport through magnetized plasma from intense laser interactions with solids. *Phys. Rev. Lett.* **84**, 670. (doi:10.1103/PhysRevLett.84.670)

Clark, E. L. *et al.* 2000*b* Energetic heavy-ion and proton generation from ultra-intense laser–plasma interactions with solids. *Phys. Rev. Lett.* **85**, 1654. (doi:10.1103/PhysRevLett.85.1654)

Cowan, T. *et al.* 2004 Ultralow emittance, multi-MeV proton beams from a laser virtual-cathode plasma accelerator. *Phys. Rev. Lett.* **92**, 204 801. (doi:10.1103/PhysRevLett.92.204801)

Dromey, B., Kar, S., Zepf, M. & Foster, P. S. 2004 The plasma mirror—a subpicosecond optical switch for ultrahigh power lasers. *Rev. Sci. Instrum.* **75**, 645. (doi:10.1063/1.1646737)

Gitomer, S. J., Jones, R. D., Begay, F., Ehler, A. W., Kephart, J. F. & Kristal, R. 1986 Fast ions and hot electrons in the laser–plasma interaction. *Phys. Fluids* **29**, 2679. (doi:10.1063/1.865510)

Hegelich, M. *et al.* 2002 MeV ion jets from short–pulse–laser interaction with thin foils. *Phys. Rev. Lett.* **89**, 085 002. (doi:10.1103/PhysRevLett.89.085002)

Kaluza, M., Schreiber, J., Santala, M. I. K., Tsakiris, G. D., Eidmann, K., Meyer-ter-Vehn, J. & Witte, K. J. 2004 Influence of the laser prepulse on proton acceleration in thin-foil experiments. *Phys. Rev. Lett.* **93**, 045 003. (doi:10.1103/PhysRevLett.93.045003)

Krushelnick, K. *et al.* 2000 Ultrahigh-intensity laser-produced plasmas as a compact heavy ion injection source. *IEEE Trans. Plasma Sci.* **28**, 1184. (doi:10.1109/27.893296)

Ledingham, K. W. D. *et al.* 2004 High power laser production of short-lived isotopes for positron emission tomography. *J. Phys. D: Appl. Phys.* **37**, 2341. (doi:10.1088/0022-3727/37/16/019)

Lindau, F., Lundh, O., Persson, A., McKenna, P., Osvay, K., Batani, D. & Wahlström, C.-G. 2005 Laser-accelerated protons with energy dependent beam direction. *Phys. Rev. Lett.* **95**, 175002.

Lundh, O., Lindau, F., McKenna, P., Persson, A. & Wahlström, C.-G. In preparation.

Mackinnon, A. J., Sentoku, Y., Patel, P. K., Price, D. W., Hatchett, S. P., Key, M. H., Andersen, C., Snavely, R. A. & Freeman, R. R. 2002 Enhancement of proton acceleration by hot-electron recirculation in thin foils irradiated by ultraintense laser pulses. *Phys. Rev. Lett.* **88**, 215 006. (doi:10.1103/PhysRevLett.88.215006)

McKenna, P. *et al.* 2002 Characterization of multiterawatt laser–solid interactions for proton acceleration. *Rev. Sci. Instrum.* **73**, 4176. (doi:10.1063/1.1516855)

McKenna, P. *et al.* 2004 Proton and heavier ion acceleration in ultrahigh intensity laser-interactions with heated target foils. *Phys. Rev. E* **70**, 036 405. (doi:10.1103/PhysRevE.70.036405)

Mendonca, J. T., Davies, J. R. & Eloy, M. 2001 Proton and neutron sources using terawatt lasers. *Meas. Sci. Technol.* **12**, 1801.

Neely, D., Foster, P., Lindau, F., Lundh, O., McKenna, P., Persson, A. & Wahlström, C.-G. In preparation.

Roth, M. *et al.* 2002 Energetic ions generated by laser pulses: a detailed study on target properties. *Phys. Rev. Spec. Topics—Accel. Beams* **5**, 061 301. (doi:10.1103/PhysRevSTAB.5.061301)

Santala, M. I. K. *et al.* 2000 Effect of the plasma density scale length on the direction of fast electrons in relativistic laser–solid interactions. *Phys. Rev. Lett.* **84**, 1459. (doi:10.1103/PhysRevLett.84.1459)

Sentoku, Y., Cowan, T. E., Kemp, A. & Ruhl, H. 2003 High energy proton acceleration in interaction of short laser pulse with dense plasma target. *Phys. Plasmas* **10**, 2009. (doi:10.1063/1.1556298)

Snavely, R. A. *et al.* 2000 Intense high-energy proton beams from petawatt-laser irradiation of solids. *Phys. Rev. Lett.* **85**, 2945. (doi:10.1103/PhysRevLett.85.2945)

Spencer, I. *et al.* 2003 Experimental study of proton emission from 60 fs, 200 mJ high rep-rate 'table-top' laser pulses interacting with solid targets. *Phys. Rev. E* **67**, 046 402. (doi:10.1103/PhysRevE.67.046402)

Wilks, S. C. *et al.* 2001 Energetic proton generation in ultra-intense laser–solid interactions. *Phys. Plasmas* **8**, 542. (doi:10.1063/1.1333697)

Ziener, C., Foster, P. S., Divall, E. J., Hooker, C. J., Hutchinson, M. H. R., Langley, A. J. & Neely, D. 2003 Specular reflectivity of plasma mirrors as a function of intensity, pulse duration, and angle of incidence. *J. Appl. Phys.* **93**, 768. (doi:10.1063/1.1525062)

Paper III

Influence of shockwaves on laser-driven proton acceleration

O. Lundh, F. Lindau, A. Persson, P. McKenna, D. Batani and C.-G. Wahlström.

Physical Review E **76**, 026404 (2007).

PHYSICAL REVIEW E **76**, 026404 (2007)

Influence of shock waves on laser-driven proton acceleration

O. Lundh, F. Lindau, A. Persson, and C.-G. Wahlström
Department of Physics, Lund University, P.O. Box 118, S-22100 Lund, Sweden

P. McKenna
SUPA, Department of Physics, University of Strathclyde, Glasgow G4 0NG, United Kingdom

D. Batani
Dipartimento di Fisica, Università di Milano Bicocca, Piazza della Scienza 3, 20126 Milano, Italy
(Received 3 May 2007; published 28 August 2007)

The influence of shock waves, driven by amplified spontaneous emission (ASE), on laser-accelerated proton beams is investigated. A local deformation, produced by a cold shock wave launched by the ablation pressure of the ASE pedestal, can under oblique laser irradiation significantly direct the proton beam toward the laser axis. This can be understood in the frame of target normal sheath acceleration as proton emission from an area of the target where the local target normal is shifted toward the laser axis. Hydrodynamic simulations and experimental data show that there exists a window in laser and target parameter space where the target can be significantly deformed and yet facilitate efficient proton acceleration. The dependence of the magnitude of the deflection on target material, foil thickness, and ASE pedestal intensity and duration is experimentally investigated. The deflection angle is found to increase with increasing ASE intensity and duration and decrease with increasing target thickness. In a comparison between aluminum and copper target foils, aluminum is found to yield a larger proton beam deflection. An analytic model is successfully used to predict the proton emission direction.

DOI: 10.1103/PhysRevE.76.026404 PACS number(s): 52.38.Kd, 52.35.Tc, 52.38.Mf, 29.27.Fh

I. INTRODUCTION

Laser-driven proton and heavy ion acceleration is an area of research that currently attracts significant scientific interest. The particle beams produced in these experiments have a number of attractive characteristics, such as high laser to particle beam conversion efficiency [1], very low emittance [2], and a small virtual source size [3]. Proposed applications of this possibly compact ion beam source include ion radiotherapy for cancer treatment [4], isotope production for medical imaging techniques [5], and injectors for future ion accelerators [6]. These applications have different requirements with regards to ion energy, conversion efficiency, and beam quality and, before they can be realized, a better understanding of the underlying processes must be established so that the ion beam can be appropriately optimized.

In a typical experiment, a high power laser pulse is tightly focused on the surface of a thin foil to an intensity exceeding 10^{19} W/cm^2. The laser interacts preferentially with plasma electrons (to accelerate ions directly requires higher intensities than are currently available) and, according to a number of different mechanisms, a population of hot electrons with a Maxwellian temperature of typically a few MeV is generated. These electrons traverse the target and build up exceptionally high electrostatic fields ($\sim$TV/m) at the surfaces of the foil. Atoms on the target surface experience the field and are rapidly field-ionized and accelerated. The magnitude of the electric field depends on the electron temperature and density. For a given laser pulse it is possible to increase the hot electron density on the rear surface of the target by decreasing the foil thickness. This minimizes the geometrical spreading of the electron beam during the transport through the target and consequently the highest proton energies and the highest conversion efficiencies are reached by using very thin foils [1]. However, there are limits as to how thin foils can be used in order to optimize the proton beam. The most severely limiting factor in experiments is the fact that, due to the large gain in the laser system and amplified spontaneous emission (ASE) in the amplifiers, a nanosecond pedestal precedes the main pulse. When focused, this pedestal can become so intense that it significantly changes the properties of the target prior to the main pulse arrival. The effects induced by the ASE pedestal varies with intensity. Even at a relatively low intensity ($\sim 10^{10}$ W/cm^2), material at the target front surface is evaporated and partially ionized prior to the main pulse arrival. As this preplasma expands into vacuum, the initially sharp target density profile is smoothed on the front of the foil. This has important implications for the mechanisms of proton acceleration. In fact, it has been shown theoretically and experimentally that the acceleration is most effective for a steep ion density gradient, whereas a long ion density scale length severely limits the maximum proton energy [7,8]. The presence of a preplasma at the front of the target might therefore explain why the most energetic protons have been observed to originate from the rear surface of the foil [9]. At medium ASE intensities ($\sim 10^{12}$ W/cm^2) not only the front but also the bulk of the target is significantly influenced. The preplasma has in this case such a high temperature that the front side plasma expansion launches a compressional shock wave into the target. Given enough time, it will break through the rear surface of the foil and significantly influence the properties of the proton emitting region [10–13]. At even higher ASE intensities ($>10^{13}$ W/cm^2), the shock is strong enough to induce phase

transitions and even evaporate the target material. After shock breakout, this effect might create a long ion density scale length also at the rear surface, thereby terminating the proton acceleration. To avoid this and to eliminate other rear surface effects, most experimenters choose the foil thickness so that the shock front is still inside the target when the main pulse arrives.

In this article, we present a study of laser-driven proton acceleration under conditions where the ASE pedestal strongly influences the acceleration mechanisms. Between the region in laser and target parameter space where the shock has no time to break out and the region where the shock breakout ruins the steep density gradient at the rear surface, we identify a region where the shock is strong enough to significantly deform the rear surface, but yet not strong enough to terminate the proton emission. We further show that this effect can be used to manipulate the beam direction, and discuss its potentials for optical target manipulation and beam focusing.

The paper is organized as follows. In Sec. II we discuss the generation, propagation, and breakout of ASE-driven shocks and, in particular, the dependencies on target material and laser intensity. In Sec. III we describe the experimental setup and methods used for proton acceleration and how we control the ASE duration and intensity. We present the experimental results and discuss these with respect to analytical and numerical predictions in Sec. IV. Finally, in Sec. V we conclude.

II. INFLUENCE OF ASE-DRIVEN SHOCK WAVES

In this section, we discuss how ASE-driven shock waves change the properties of a thin foil target prior to the main interaction. Our discussion is based on analytical calculations and hydrodynamic simulations using the code MULTI [14], assuming a rectangular ASE temporal pulse shape.

A. Shock propagation and breakout

Figure 1 shows the result of a one-dimensional (1D) hydrodynamic simulation of the interaction between a 3 ns long ASE pedestal of medium intensity (1×10^{12} W/cm^2) and a 6 μm thick aluminum foil target. The laser hits the target at time zero and heats the plasma formed on the front side of the foil. The heated plasma expands out into the vacuum and in doing so it exerts a 30 GPa (0.3 Mbar) pressure on the remaining target. Because of this rocket effect, a shock is launched into the target. The shock wave moves with a constant velocity until it reaches the rear surface where shock breakout occurs. The rear surface then starts to expand while a rarefaction wave is backscattered into the target. The laser continues to push on the front side so the net effect is that, after shock breakout, the target is moving with a speed of typically a few μm/ns.

The scaling of the induced pressure with laser intensity has been shown to be relatively insensitive to target material [15] and can be approximated as [16]

$$P = \zeta I^{2/3}, \tag{1}$$

where the pressure P is in Pa and intensity I in W/m^2. ζ is a material specific constant which is, for a laser wavelength of

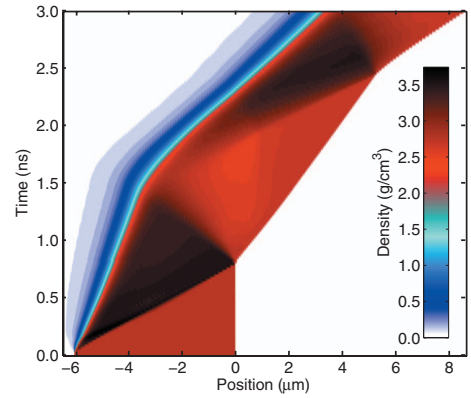

FIG. 1. (Color online) Time evolution of the density of a 6 μm aluminum target shocked by laser pulse with a constant intensity of 1×10^{12} W/cm^2. Laser ablation launches a shock at the target front which propagates inside the target at a constant speed of 7.8 μm/ns. Behind the shock front, the target is compressed to 1.4 times the initial density. The shock breaks through the rear surface 0.8 ns after the laser hit the target front and the rear surface then starts to expand with a velocity of 3.1 μm/ns, while a rarefaction wave is backscattered into the target.

0.8 μm, close to unity. For a shocked material, initially at rest, the state behind the shock front is governed by the mass and momentum conservation laws, and by an experimentally validated linear relationship between the shock and particle velocities, v_s and v_p,

$$\rho_0 v_s = \rho(v_s - v_p), \tag{2a}$$

$$P = \rho_0 v_s v_p, \tag{2b}$$

$$v_s = c_0 + \alpha v_p, \tag{2c}$$

where ρ_0 and ρ are the densities of the unperturbed and compressed material, respectively, P is the shock pressure, c_0 is the sound velocity, and α is an empirical material constant [17]. Table I gives experimental values of c_0 and α for some typical target materials, common in proton acceleration experiments. Solving Eqs. (2a)–(2c) gives the particle and shock velocities,

$$v_s = \frac{c_0}{2}(\sqrt{1+x}+1), \tag{3a}$$

$$v_p = \frac{c_0}{2\alpha}(\sqrt{1+x}-1), \tag{3b}$$

where $x=(4\alpha/\rho_0 c_0^2)P$. When the shock breaks through, the rear surface starts to expand with a velocity $v_{exp}=2v_p$. This relation is appropriate for relatively weak shocks, i.e., when no phase transitions are induced. Figure 2 shows the position of the shock front inside a 6 μm target and the position of the rear surface after shock breakout. Assuming $\zeta=1.0$ and 0.75 J$^{1/3}$s$^{2/3}$m$^{-5/3}$ in Cu and Al, respectively, gives good

TABLE I. Experimental values [17,18] of c_0 and α for common proton acceleration target materials with initial density ρ_0 and atomic number Z. P_m is the pressure required for melting along the Hugoniot and T_m is the associated temperature [19–23].

Element	Z	ρ_0 (g/cm^3)	c_0 (μm/ns)	α	P_m (GPa)	T_m (K)
Al	13	2.70	5.24	1.40	170	5700
Ti	22	4.53	4.91	1.02		
Fe	26	7.86	3.77	1.65	260	6100
Cu	29	8.93	3.94	1.49	270	5600
Pd	46	11.99	4.01	1.55	265	5800
Sn	50	7.29	2.59	1.49	49	1300
Au	79	19.30	3.08	1.56	280	
Mylar		0.92	2.76	1.59		

agreement between simulation data and analytical calculations. As expected, the shock travels faster through Al than through Cu and reaches the rear surface at earlier times. After breakout, the expansion velocity is also higher for Al than for Cu. Therefore, for a given laser intensity, an Al target is always more affected than a Cu target.

B. Induced phase transitions

An important observation from the simulation in Fig. 1 is that, at the rear surface of the foil, the target surface-to-vacuum boundary remains sharp after the shock breakout. In contrast, simulations at higher laser intensities, shown in Fig. 3, confirm that shock breakout can result in a destruction of the sharp density gradient. A key point, when discussing proton acceleration from shocked targets, is therefore that it has been established, both theoretically and in experiments, that the proton energy is highest for sharp target boundaries [7,8]. So, to achieve efficient rear surface acceleration from a shocked target, the shock driving laser intensity needs to be adjusted to produce a relatively cold, plastic deformation. Figure 4 shows how the melting point of aluminum and copper increases as the pressure increases. When a material is compressed by a shock, the state of the compressed material is described by the Hugoniot curve, also shown in Fig. 4. Note that this curve does not show a transition trajectory of the material as the pressure is being ramped, but rather the final state behind the front of a shock of a certain pressure. The intersection of the melting curve and the Hugoniot curve gives the pressure required for shock melting. In combina-

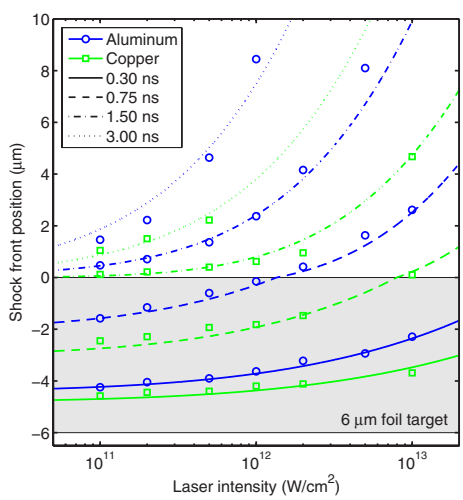

FIG. 2. (Color online) Shock front position inside a 6 μm target and the position of the rear surface after breakout. Simulation results (symbols) are in reasonably good agreement with analytical calculations (lines). The shock speed is increasing with laser intensity, but is lower in Cu than in Al.

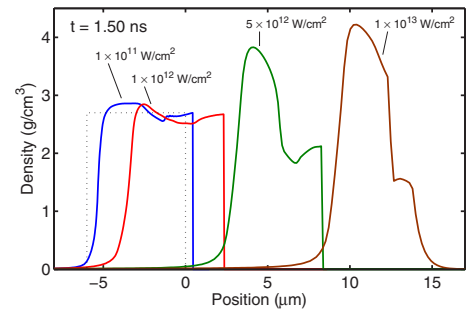

FIG. 3. (Color online) Density profile of a 6 μm thick aluminum target after 1.5 ns for different laser intensities. The dotted line shows the unperturbed density profile. At 1×10^{12} W/cm^2, laser ablation generates a relatively cold and plastic deformation of the target. Increasing the intensity one order of magnitude heats the shocked material and creates a density ramp at the rear surface. Such a ramp has been shown to decrease the maximum proton energy.

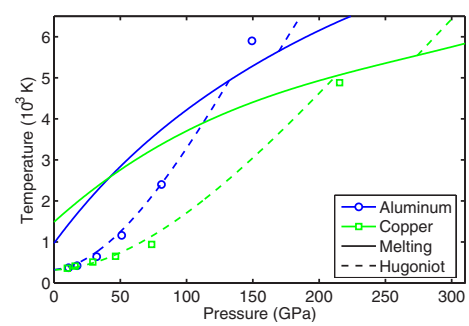

FIG. 4. (Color online) Temperature just behind the shock front in the center of a 6 μm target, obtained using the code MULTI. The simulation data (symbols) compares well with the shock-release model (dashed), proposed by Dai *et al.* [19], for assessing the melting on Hugoniots of metals. The intersection of the melting (solid) and Hugoniot (dashed) curves gives an estimate of the pressure below which the shocked target is in a solid phase.

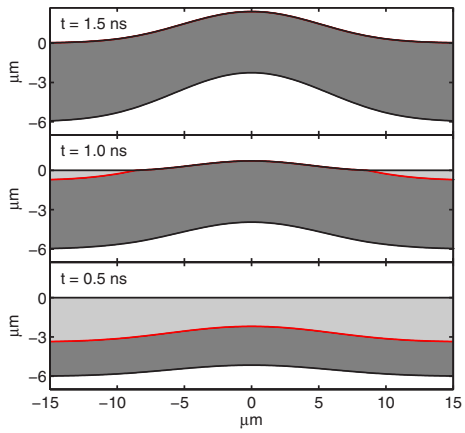

FIG. 5. (Color online) Analytical calculation of the propagation and breakout of a shock wave, driven in a 6 μm aluminum target by a 1×10^{12} W/cm^2 ASE pedestal, with a 10 μm (FWHM) Gaussian focal spot. The dark gray area between the shock front and the ablation front is the compressed target. The degree of compression varies along the radial coordinate and is a consequence of different shock pressure. Not shown is the low density coronal plasma in the lower white region that drives the shock wave.

tion with the intensity-pressure relation in Eq. (1), this gives an estimate of the laser intensity below which the shock produces a plastic deformation with a sharp rear surface density gradient, facilitating efficient ion acceleration.

C. Two-dimensional effects

So far we have only considered the propagation of a planar (1D) shock. In reality, the ASE intensity varies over the focal region so that the highest shock pressure, and consequently the largest rear surface deformation, occurs in the center of the focus. Important for proton acceleration is the geometrical shape of the target foil. To model the time dependent shape, we assume that the shock pressure depends only on the local intensity and that the lateral shock spreading can be neglected. This assumption is realistic for relatively thin targets as compared to the focal spot diameter. Assuming a Gaussian laser intensity distribution and using Eqs. (1), (2a)–(2c), (3a), and (3b), Fig. 5 shows the results from an analytical calculation of the shock front propagation and the expansion following shock breakout. These results compare reasonably well with the results from the corresponding 2D hydrodynamic simulation and will be used in Sec. IV D to estimate the shape of the deformed target foil and the direction of the accelerated proton beam.

III. EXPERIMENTAL METHOD

The experiments are performed with the 10 Hz multiterawatt femtosecond laser at the Lund Laser Centre. It is a Ti:sapphire system, operating at 800 nm, capable of delivering 35 fs pulses of up to 30 TW on target. The system is based on chirped pulse amplification and incorporates a regenerative amplifier for preamplification and two multipass amplifiers. The regenerative preamplifier has a gain of almost 10^8 and special caution is devoted to the optimization of this amplifier on a day-to-day basis in order to minimize the ASE intensity of the compressed pulses to around 10^{-8} of the main pulse peak intensity.

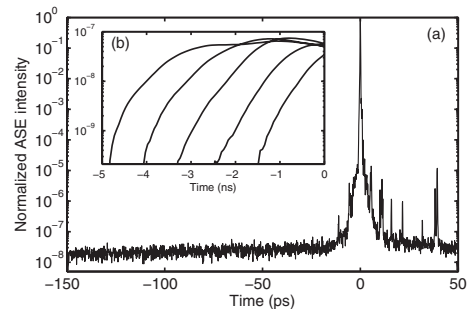

FIG. 6. (a) High dynamic range third order autocorrelation measurement of the laser pulse profile. On this time scale, the laser intensity is constant until it starts to rise 15 ps before the main pulse. The ASE pedestal intensity is measured 100 ps before the main pulse. (b) The ASE pedestal duration is controlled by selecting the timing of the gating Pockels cells relative to the main laser pulse. The photodiode measurements have been normalized to corresponding third order autocorrelations.

A. Control of amplified spontaneous emission

The temporal pulse shape is diagnosed on a picosecond time scale by a high dynamic range third order autocorrelator (Sequoia, Amplitude Technologies). A typical temporal profile is shown in Fig. 6(a). On this time scale, the laser intensity is reasonably constant until it starts rising 15 ps before the main pulse. Consequently, we quote the ASE intensity as the intensity in the flat part of this pedestal, as measured 100 ps before the main pulse.

The ASE pedestal is diagnosed on a nanosecond time scale by a fast photodiode and a high bandwith oscilloscope. Three synchronized pulse cleaning Pockels cells, each of which has a rise time of 1.0 ns, are incorporated in the system. Figure 6(b) shows the ASE pedestal for different timing of these optical gates relative to the main pulse. The photodiode measurements are normalized to simultaneous third order autocorrelations. On a nanosecond time scale, the ASE intensity closely follows the opening of the Pockels cells. Hereafter, we refer to the ASE duration as the time between the half maximum of the rising edge of the ASE pedestal and the peak of the main pulse.

The contrast ratio between the main pulse intensity and the ASE intensity is highly dependent on the energy that seeds the regenerative amplifier. The laser system incorporates an acousto-optic programmable dispersive filter (Dazzler, Fastlite). This device, positioned at the oscillator output, is normally used to precompensate for high order dispersion and gain narrowing in the amplifier chain, but it

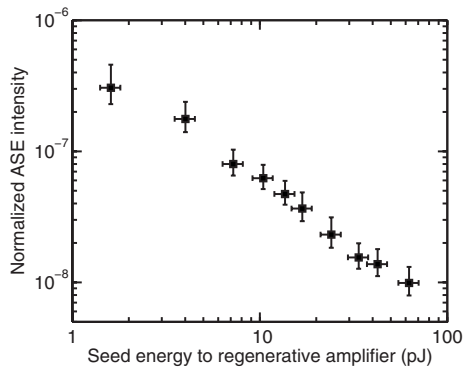

FIG. 7. By controlling the seed energy to the regenerative amplifier, it is possible to control the ASE intensity of the amplified laser pulse.

can also be used as a programmable attenuator in order to control the seed energy to the regenerative amplifier via the filter control software. Figure 7 shows the dependence of the ASE intensity on the seed energy to the regenerative amplifier. This method for adjusting of the ASE intensity does not affect the main pulse duration or the energy.

B. Experimental arrangement

A schematic of the experimental setup is shown in Fig. 8. In this study, pulses with a total energy of 700 mJ, a duration of 35 fs [full width at half maximum (FWHM)], and a 50 mm diameter enter the vacuum target chamber. The laser beam is focused by an $f/3$ off-axis parabolic mirror to an 8 μm (FWHM) focal spot, giving an inferred peak intensity of 2×10^{19} W/cm^2. Target foils of different materials and thicknesses are positioned in the focal plane for p-polarized

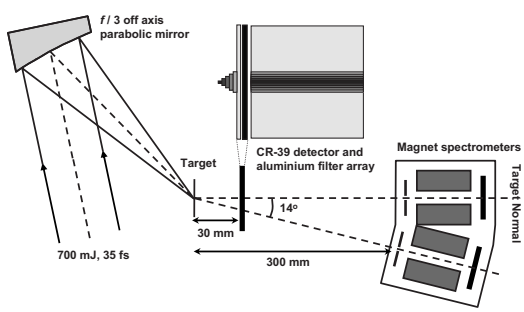

FIG. 8. Schematic of the experimental arrangement showing the geometry and the proton diagnostics. The laser is focused by an $f/3$ off axis parabola onto a thin foil target. A filter mask consisting of stripes of Al foil of different thicknesses enables measurement of the spatial profile above chosen threshold proton energies. Alternatively, two magnetic spectrometers register the proton energy spectrum along the target normal direction and at 14° toward the laser axis.

irradiation at a 45° angle of incidence. The target holder can be loaded with up to 50 individual foil targets.

C. Target positioning system

Prior to each full power shot, the intensity distribution of a collinear alignment beam, reflected off the target surface, is captured by an imaging system as a function of the longitudinal position of the target foil. Irregularities on the target foil surface produce speckles in the reflected beam. The speckle size is determined through Fourier image analysis and the target position that produces the largest speckles, i.e., the focal position, is found through a polynomial fit to the calculated values. The acquisition and analysis are fully automated and controlled from a LABVIEW interface. The system facilitates reproducible positioning of solid targets in the focal plane to within a Rayleigh range. An additional feature of this positioning system is that it provides information on the local surface orientation of each individual target through the direction of the reflected alignment beam. This allows the angle of incidence to be adjusted to be exactly the same for each shot.

D. Proton beam diagnostics

In order to diagnose the proton beam, we use CR39 nuclear track detectors, sensitive to protons and ions but insensitive to electrons and x rays [24]. The spatial distribution is captured by a 50×50 mm plate of CR39, positioned 30 mm from the target. A filter mask, consisting of stripes of aluminum with different thickness, is placed directly in front of the detector plate. This enables simultaneous measurement of the spatial distribution of protons above different threshold energies. A feeding mechanism allows up to 20 consecutive shots to be recorded on different detector plates before the vacuum chamber must be opened and the detectors replaced. Alternatively, when the plate feeder is removed, the energy spectrum can be registered on CR39 detectors behind two compact magnetic spectrometers, positioned 300 mm from the target, in the target normal direction and at 14° toward the laser axis.

IV. EXPERIMENTAL RESULTS AND DISCUSSION

Under conditions where the ASE has no influence on the rear target surface, we obtain a well defined proton beam with a continuous energy spectrum extending up to a few MeV; see Figs. 9(a) and 9(b). The beam is centered on the target normal axis and has a divergence that decreases with increasing energy.

A. Influence of shock waves

Figures 9(c) and 9(d) show the energy spectrum and spatial distribution of proton beams, accelerated under conditions where an ASE-driven shock wave strongly influences the shape of the rear surface. The beam is significantly shifted toward the laser direction with a deflection angle that increases with proton energy.

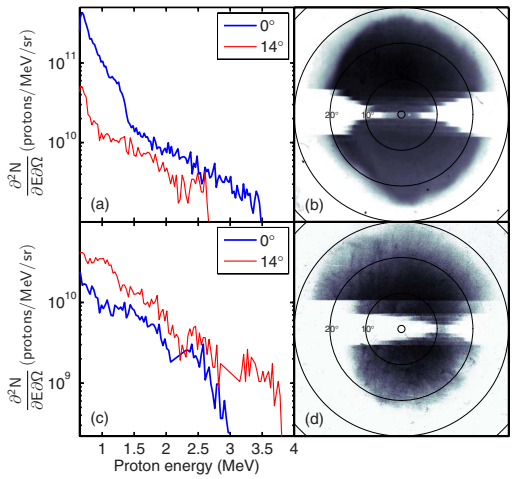

FIG. 9. (Color online) [(a),(c)] Energy spectra and [(b),(d)] spatial distributions of proton beams obtained using 6 μm Al foils. In (a) and (b), the ASE has no influence on the rear surface (τ_{ASE} =0.5 ns, $I_{ASE}=2\times10^{11}$ W/cm^2) and the most energetic protons are emitted along the target normal. In (c) and (d), the amount of ASE has been increased (τ_{ASE}=1.5 ns, $I_{ASE}=2\times10^{12}$ W/cm^2) and the most energetic protons are shifted toward the laser axis. The filter arrays in (b) and (d) are different and correspond to a maximum cutoff energy of 2.8 MeV and 4.8 MeV, respectively.

The phenomenon may be explained by considering the effects of an ASE-driven shock wave in combination with the oblique incidence of the main laser pulse; see Fig. 10. Given an ASE pedestal of sufficient intensity and duration, the initially planar target is deformed into a convex profile before the main pulse arrives. The main laser pulse, incident at 45°, accelerates electrons according to a number of different mechanisms. The relative importance of these mechanisms varies with the laser intensity and the preplasma conditions. At low intensities and steep plasma gradients, resonance absorption dominates and electrons are accelerated predominantly along the target normal, whereas at high intensities and long plasma scale lengths, electrons are accelerated primarily in the laser direction [25]. Other experiments have confirmed that, under our experimental conditions, two populations of hot electrons are created [26] and that the most energetic population, heated by the $v\times B$ force of the intense laser field, is directed along the laser direction.

When the electrons reach the rear surface, they are asymmetrically distributed over the deformation. In particular, the most energetic electrons appear in an area of the target where the local target normal points away from the global target normal. Hence the direction of the strongest electric field is also shifted and the most energetic protons are steered toward the laser axis. Low energy protons are emitted from a much larger area [2], so for these the deformation has a defocusing effect rather than a steering effect.

The proton beam in Fig. 9(d) is significantly influenced by the ASE-driven shock, but has a well defined structure. The most energetic protons (>4.8 MeV) are shifted by 13° but are still emitted within a 4° cone. To produce a high energy proton beam with a good beam quality, such as the examples in Figs. 9(b) and 9(d), requires an initially cold emitting surface at the time the hot electrons are created. Not illustrated here is the fact that increasing the ASE intensity or duration beyond certain limits locally disrupts the target, producing an inferior beam quality or even terminating the proton emission altogether.

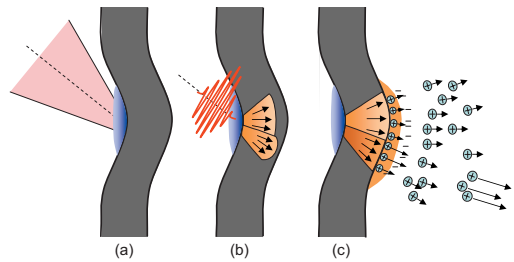

FIG. 10. (Color online) Sequential illustration of proton acceleration in a shocked target. (a) Prior to the main pulse arrival, the ablation pressure induced by the ASE deforms the target foil. (b) The main pulse arrives under oblique incidence and generates a population of hot electrons. (c) The most energetic electrons traverse the target and set up a strong electric field in an area where the local target normal is shifted toward the laser axis, away from the global target normal. Consequently, during the plasma expansion, the most energetic protons are accelerated in a direction that is shifted toward the laser axis, with an angle that increases with the magnitude of the local deformation.

B. Influence of target properties

Next, the influence of the target material and thickness on the magnitude of the proton deflection is investigated. Keeping the laser properties constant, the thickness of aluminum and copper target foils is varied; see Fig. 11. For a laser contrast ratio of 1×10^7, the inferred ASE intensity is 2×10^{12} W/cm^2. At this intensity, the shock velocity is estimated to be 9 μm/ns in Al and 6 μm/ns in Cu. For a 1 ns long ASE pedestal, the shock has not yet reached the rear surface of 12 μm foils when the main pulse arrives and, consequently, no proton beam deflection is observed for either Cu or Al foils. For the 6 μm foils, the shock has reached the rear surface of both the Cu and Al foils before the main pulse arrives. After shock breakout, the rear surface expands with a velocity of 5 μm/ns in Al and 3 μm/ns in Cu. This means that the 6 μm Al foil is deformed by 2 μm and indeed we observe the onset of an energy dependent proton beam emission. However, for 6 μm Cu, we observe only a very small deflection since, even though the shock breaks through, there is no time for expansion before the main pulse arrives. Finally, for the 3 μm foils, the Al foil is deformed by 3 μm, giving an even larger deflection than the 6 μm Al foil. The 3 μm Cu foil is deformed by 1.5 μm, giving a deflection slightly smaller than the 6 μm Al foil. In conclusion, beams emitted from thinner foils are more de-

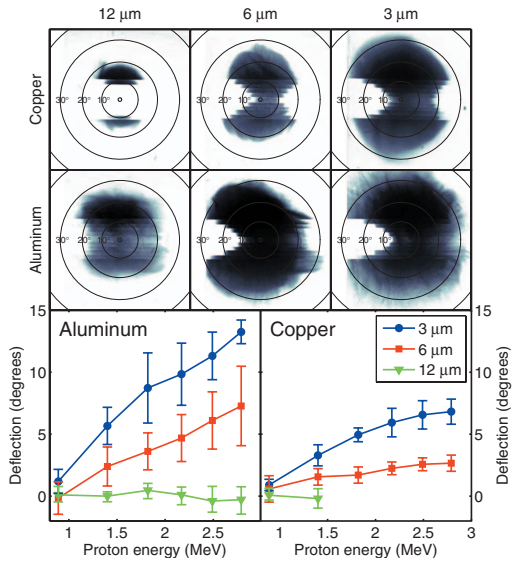

FIG. 11. (Color online) Influence of the target properties on the energy dependent emission direction. The ASE pedestal intensity and duration is 2×10^{12} W/cm^2 and 1 ns, respectively. The panels in the top and middle rows show representative proton beams, obtained from Al and Cu foils of different thicknesses. The complete data set is compiled in the two bottom diagrams, where the error bars denote the standard deviation taken over three consecutive shots.

flected since they have more time to expand after breakout. Beams emitted from Al foils are more deflected than beams emitted from the denser Cu foils because of the difference in shock and expansion velocity.

C. Influence of ASE pedestal properties

The onset of an energy dependent proton emission direction depends on the relation between the target thickness, the shock velocity, and the ASE pedestal duration. In turn, the shock velocity is determined by the ASE intensity through Eqs. (1), (3a), and (3b). For a given thickness, a skewed proton beam can be obtained by either increasing the ASE pedestal duration or the intensity. Figure 12 shows data from three representative shots on 6 μm Al for three different ASE conditions. First, the contrast ratio is set to 3×10^7, giving an inferred shock driving intensity of 6×10^{11} W/cm^2. In Al, the corresponding shock and expansion velocities are 7 μm/ns and 3 μm/ns, respectively. For a short, 1 ns pedestal, we get a maximum deformation of 0.4 μm yielding a very small or no proton beam deflection. However, increasing the ASE duration to 2 ns gives a calculated deformation of 3 μm and a significant beam deflection. Increasing the inferred ASE intensity to 4×10^{12} W/cm^2 gives a calculated shock velocity of 10 μm/ns and an expansion velocity of 7 μm/ns. A 1 ns ASE pedestal at this increased intensity should therefore also produce a 3 μm

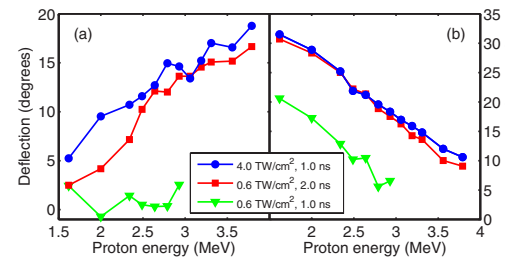

FIG. 12. (Color online) Influence of the ASE intensity and duration on (a) the energy dependent proton beam deflection toward the laser axis and (b) on the half apex angle of the emission cone.

maximum deformation. Indeed, as shown in Fig. 12(a), the intense but short pedestal generates a proton beam deflection of magnitude similar to the weak but long pedestal.

Closely correlated with the onset of an energy dependent proton emission direction is an increase in beam divergence. As shown in Fig. 12(b), increasing the ASE duration or intensity produces a proton beam with significantly larger divergence. This phenomenon can also be observed in the representative examples in Fig. 11, where the target thickness is decreased. The increased divergence could be interpreted as resulting from the breakout of an ASE-driven shock wave. It has been shown in simulations and in experiments that a concave rear surface acts to focus the emitted proton beam [27,28]. In the same way, a convex rear surface, produced by the breakout of a shock, could be expected to defocus the proton beam, thereby increasing the beam divergence.

D. Prediction of the emission direction

The proton beam deflection angle is directly related to the lateral and longitudinal extent of the foil deformation. The longitudinal extent is determined by the expansion velocity and the time available for the expansion, while the lateral extent is determined by the size of the focal spot. To probe the dynamics of the foil deformation the pulse contrast is set to 1×10^8, giving an inferred ASE intensity of 2×10^{11} W/cm^2. Using a single layer Al filter in front of the CR39 detector plate, the emission direction of protons above 2.5 MeV from 6 μm Al foils is measured as a function of the ASE duration. As shown in Fig. 13, the proton beam is emitted along the target normal, until the shock breaks through the rear surface. After this point, the beam is steered away from the target normal with an angle that increases with increasing pedestal duration. Also shown in Fig. 13 is the time dependent deflection angle for proton beams produced in 6 μm Cu targets. As expected, the shock appears to break out at a later time and, after that point, the deflection angle increases at a slower rate than for the Al foil. These observations are consistent with slower shock and expansion velocities in Cu as compared to Al.

In order to do a quantitative prediction of the beam deflection angle, we estimate the shape of the rear surface using the model described in Sec. II C. The inset in Fig. 13 shows the calculated shape for a 2.0 ns long ASE pedestal with an

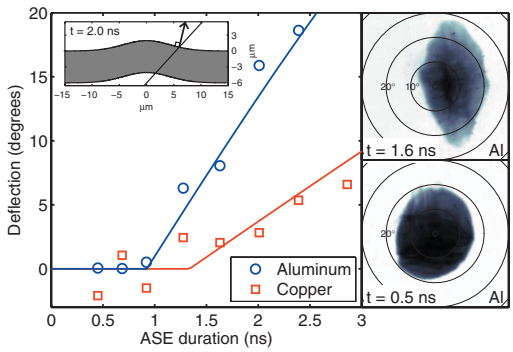

FIG. 13. (Color online) Proton beam deflection toward the laser axis as a function of ASE duration. The target is 6 μm Al and Cu and the inferred ASE intensity is 2×10^{11} W/cm^2. As shown in the bottom right panel, the proton beam stays on the target normal axis for the shortest ASE pedestal. After shock breakout, the proton beam is steered toward the laser axis as shown in the top right panel. The inset shows the calculated shape of the foil for a 2.0 ns long ASE pedestal. The modeled emission direction (solid lines) is the calculated target normal direction at the point where the laser axis intersects the rear surface.

intensity of 2×10^{11} W/cm^2. The proton emission direction is calculated as the direction of the local target normal where the laser axis, incident at 45°, intersects the rear surface. In this model, we have only one free parameter: the ASE intensity distribution. With the peak ASE intensity fixed at 2×10^{11} W/cm^2, we assume a Gaussian intensity distribution and fit the width of this function to the Al data set. This gives an inferred ASE spot diameter of 8 μm (FWHM), the same as the measured spot size. Keeping the parameters of the ASE we change only the material constants (ρ_0, c_0, and α) and apply the model to the Cu data set. This gives excellent agreement with the experimental observations, as shown in Fig. 13.

V. CONCLUSION

We have demonstrated the possibility of using the intrinsic ASE pedestal to shape a thin foil and thereby control the proton emission angle. A natural extension to this work is to increase the contrast ratio of the laser to a level where the ASE has only a minor effect and instead use a secondary, independently configurable, laser pulse in order to shape the target and thereby optically control the proton emission. It is, for example, conceivable that, by using a ring-shaped steering pulse, it would be possible to control not only the direction but also the divergence of the proton beam. This could open interesting prospects for future high repetition rate laser-based proton accelerators.

We acknowledge support from the Swedish Research Council, the Knut and Alice Wallenberg Foundation, and the EU Access to Research Infrastructures Programme (RII3-CT-2003-506350 Laserlab Europe).

[1] D. Neely *et al.*, Appl. Phys. Lett. **89**, 021502 (2006).
[2] T. E. Cowan *et al.*, Phys. Rev. Lett. **92**, 204801 (2004).
[3] M. Borghesi, A. J. MacKinnon, D. H. Campbell, D. G. Hicks, S. Kar, P. K. Patel, D. Price, L. Romagnani, A. Schiavi, and O. Willi, Phys. Rev. Lett. **92**, 055003 (2004).
[4] S. V. Bulanov and V. S. Khoroshkov, Plasma Phys. Rep. **28**, 453 (2002).
[5] K. W. D. Ledingham *et al.*, J. Phys. D **37**, 2341 (2004).
[6] K. Krushelnick *et al.*, IEEE Trans. Plasma Sci. **28**, 1184 (2000).
[7] T. Grismayer and P. Mora, Phys. Plasmas **13**, 032103 (2006).
[8] A. J. Mackinnon, M. Borghesi, S. Hatchett, M. H. Key, P. K. Patel, H. Campbell, A. Schiavi, R. Snavely, S. C. Wilks, and O. Willi, Phys. Rev. Lett. **86**, 1769 (2001).
[9] M. Allen, P. K. Patel, A. Mackinnon, D. Price, S. Wilks, and E. Morse, Phys. Rev. Lett. **93**, 265004 (2004).
[10] F. Lindau, O. Lundh, A. Persson, P. McKenna, K. Osvay, D. Batani, and C. G. Wahlström, Phys. Rev. Lett. **95**, 175002 (2005).
[11] P. McKenna *et al.*, Philos. Trans. R. Soc. London, Ser. A **364**, 711 (2006).
[12] M. Kaluza, J. Schreiber, M. I. K. Santala, G. D. Tsakiris, K. Eidmann, J. Meyer-ter-Vehn, and K. J. Witte, Phys. Rev. Lett. **93**, 045003 (2004).
[13] M. H. Xu *et al.*, Phys. Plasmas **13**, 104507 (2006).
[14] R. Ramis, R. Schmalz, and J. Meyer-Ter-Vehn, Comput. Phys. Commun. **49**, 475 (1988).
[15] D. C. Swift, T. E. Tierney IV, R. A. Kopp, and J. T. Gammel, Phys. Rev. E **69**, 036406 (2004).
[16] J. Lindl, Phys. Plasmas **2**, 3933 (1995).
[17] *LASL Shock Hugoniot Data*, edited by S. P. Marsh (University of California Press, Berkeley, 1980).
[18] S. Eliezer, Plasma Phys. Controlled Fusion **45**, 181 (2003).
[19] C. Dai, H. Tan, and H. Geng, J. Appl. Phys. **92**, 5019 (2002).
[20] J. H. Nguyen and N. C. Holmes, Nature (London) **427**, 339 (2004).
[21] J.-W. Jeong and K. J. Chang, J. Phys.: Condens. Matter **11**, 3799 (1999).
[22] M. Werdiger *et al.*, Laser Part. Beams **17**, 547 (1999).
[23] C. W. Greeff and M. J. Graf, Phys. Rev. B **69**, 054107 (2004).
[24] F. H. Seguin *et al.*, Rev. Sci. Instrum. **74**, 975 (2003).
[25] M. I. K. Santala *et al.*, Phys. Rev. Lett. **84**, 1459 (2000).
[26] F. Brandl *et al.*, Europhys. Lett. **61**, 632 (2003).
[27] S. C. Wilks *et al.*, Phys. Plasmas **8**, 542 (2001).
[28] P. K. Patel, A. J. Mackinnon, M. H. Key, T. E. Cowan, M. E. Foord, M. Allen, D. F. Price, H. Ruhl, P. T. Springer, and R. Stephens, Phys. Rev. Lett. **91**, 125004 (2003).

Paper IV

Active steering of laser-accelerated ion beams

O. Lundh, Y. Glinec, C. Homann, F. Lindau, A. Persson,
C.-G. Wahlström, P. McKenna and D. C. Carroll.

Applied Physics Letters **92**, 011504 (2008).

APPLIED PHYSICS LETTERS **92**, 011504 (2008)

Active steering of laser-accelerated ion beams

O. Lundh,[a] Y. Glinec, C. Homann, F. Lindau, A. Persson, and C.-G. Wahlström
Department of Physics, Lund University, P.O. Box 118, S-22100 Lund, Sweden

D. C. Carroll and P. McKenna
SUPA, Department of Physics, University of Strathclyde, Glasgow G4 0NG, United Kingdom

(Received 15 September 2007; accepted 17 December 2007; published online 10 January 2008)

A technique for optical control of the spatial distribution of laser-accelerated ion beams is presented. An ultrashort laser pulse, tightly focused to relativistic intensities on a thin foil target, drives a beam of MeV ions. An auxiliary, nanosecond laser pulse drives a shock and locally deforms the initially flat target prior to the main pulse interaction. By changing the properties of the shock-driving laser pulse, the normal direction of the ion emitting surface is locally manipulated and the emission direction is thereby controlled. In the future, this method could be used to achieve dynamic control of the ion beam divergence. © *2008 American Institute of Physics*. [DOI: 10.1063/1.2832765]

Proton and heavy ion acceleration, driven by ultraintense laser-plasma interactions in thin foil targets is currently drawing significant scientific interest. The generated beams have several attractive characteristics, such as high laser-to-particle energy conversion efficiency,[1] very low emittance,[2] and a small virtual source size.[3] Proposed applications of this potentially compact ion beam source include ion radiotherapy for cancer treatment,[4] isotope production for medical imaging techniques,[5] injectors for large accelerators,[6] and ignitors in laser-driven inertial confinement fusion.[7]

Many different mechanisms can lead to the generation of fast ion beams.[8] At an intensity of the order of 10^{19} W/cm^2, rear surface sheath acceleration dominates and generates the most energetic particles.[9] Electrons, heated to MeV temperatures by the intense laser field at the front, traverse the thin foil target and establish exceptionally high (~TV/m) electrostatic fields at the rear surface. Hydrogen atoms, present on the target surface under typical experimental vacuum conditions, are rapidly field ionized and the protons accelerated. The direction of the accelerating field is defined by the target geometry and, for a plane target foil, the emitted proton beam is centered on the target normal axis, regardless of the laser incidence angle. By shaping the rear surface, it is possible to control the proton emission. In particular, numerical simulations and experiments have shown that a prefabricated concave or convex rear surface produce converging or diverging proton beams, respectively.[9–11] It has also been shown that the target foil can be significantly deformed by a shock wave, launched by amplified spontaneous emission (ASE) prior to the main pulse arrival, and that this dynamic deformation can, under oblique laser irradiation, significantly shift the proton beam emission direction.[12,13] The first method for controlling the proton beam divergence requires prefabricated curved targets, a potential drawback for future applications requiring ultrathin targets[14] and high repetition rates. The second method facilitates dynamic control of the emission direction using standard flat foils, but is limited since the position and the spatial intensity distribution of the ASE are difficult to control independently of the main pulse. In the present experiment, schematically illustrated in Fig. 1, a separate nanosecond laser pulse is used to drive a shock and locally shape the target foil prior to the main pulse interaction. By careful selection of the intensity, arrival time and position of this steering pulse relative to the main pulse, we control the local slope of the target rear surface and gain active control of the proton emission direction.

The experiment is performed using the 10 Hz multiterawatt laser at the Lund Laser Centre in Sweden. It is a Ti:sapphire system, based on the chirped pulse amplification scheme and operating at 800 nm, delivering for this experiment 600 mJ of laser energy on the target in a 45 fs [full width at half maximum (FWHM)] pulse. The laser beam is focused using an $f/3$ off-axis parabolic mirror to a 5 μm (FWHM) spot, yielding an inferred peak intensity exceeding 4×10^{19} W/cm^2. In focus, 3 μm thick aluminum foils are positioned for p-polarized irradiation at 30° angle of incidence in the horizontal plane. To minimize the influence of ASE, a preamplifier and a saturable absorber for temporal pulse cleaning was added to the laser system to provide a main pulse to ASE intensity contrast ratio greater than 10^{10} at 1 ns and 10^9 at 50 ps before the main pulse. These exceptional ASE conditions allow experiments using an artificial prepulse with intensity below 10^{11} W/cm^2.

The shock driving steering beam is produced using a frequency doubled (yttrium aluminum garnet) Nd:YAG laser.

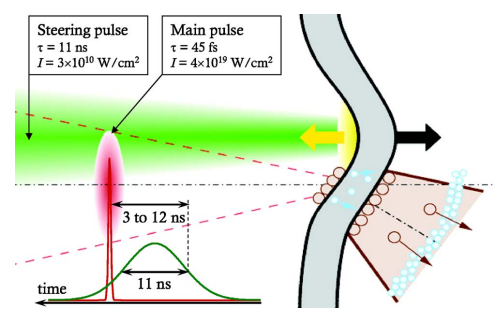

FIG. 1. (Color online) Schematic illustration of the described method for active manipulation of laser accelerated ion beams. Prior to the main pulse interaction, a low intensity pulse ionizes and ablates the front surface of the thin foil target. The induced ablation pressure shocks and locally deforms the foil, shifting the emission direction of the proton beam generated by the high intensity laser pulse.

[a]Electronic mail: olle.lundh@fysik.lth.se.

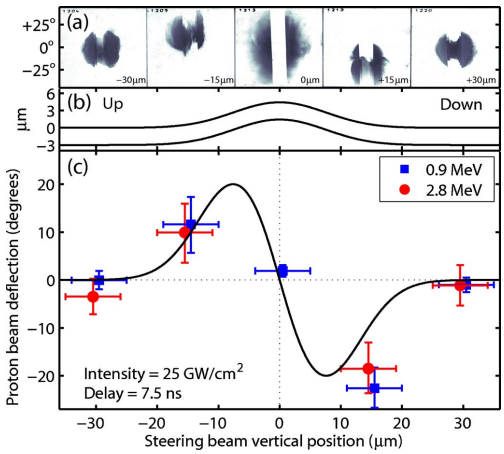

FIG. 2. (Color online) Proton beam deflection as function of the vertical position of the horizontal line focus relative to the high-intensity focal spot. Error bars indicate the relative beam positioning accuracy and the total spread of the deflection data over three consecutive shots. Representative data in (a) illustrates the quality of the deflected proton beams. The calculated shape of the foil when the main pulse arrives on target is shown in (b). The normal direction to this curve, the solid line in (c), fits the data very well.

An 11 ns (FWHM) laser pulse is delivered on the target with an energy up to 50 mJ at 532 nm. To control the arrival time of the steering pulse, the Q switch in the Nd:YAG oscillator is electronically synchronized to the main laser pulse with a pulse-to-pulse jitter less than 200 ps. The relative delay between the main pulse and the half maximum of the rising edge of the steering pulse is varied between 3 and 12 ns. The steering beam is focused by a 200 mm focal length doublet lens, which has been rotated around the vertical axis in order to produce a horizontal line focus, 14 μm wide and 230 μm long. In this simplified geometry, proton deflection is expected only in the vertical plane.

The spatial distribution of the proton beam is diagnosed using CR39 plastic track detectors, covered by stripes of aluminum stopping filters in order to facilitate simultaneous recording of the spatial distribution above several threshold energies, up to 2.8 MeV.[12]

The steering pulse arrives on the target prior to the main pulse and creates a plasma at the front surface. As the hot plasma is ejected into the vacuum, the induced ablation pressure locally shocks and deforms the target. The magnitude of the deformation depends on the driving laser intensity and on the time available for the target expansion following shock breakout. The emission direction of protons, accelerated from the deformed rear surface by the high-intensity laser pulse, depends on the local target normal direction.[9] To demonstrate active control of the proton emission direction, we systematically vary the intensity, delay, and position of the steering pulse.

Keeping all other parameters constant, we first scan the vertical position of the horizontal line focus relative to the high-intensity focal spot. As shown in Fig. 2, we see no effect when the distance between the main pulse and the steering pulse is 30 μm. This means that the width of the emitting region and the width of the local deformation do not overlap. When the steering pulse is positioned at ±15 μm, the proton beam is significantly deflected. As expected, the protons are steered upward when the steering pulse is below the main pulse and vice versa. Note that protons of different energies are steered by approximately the same amount. This full beam steering is fundamentally different from the energy dependent beam deflection obtained previously using the intrinsic ASE pedestal[12,13] and indicates that the entire proton source fits on the slope of the deformation. We also note that the number of protons in the deflected proton beams remain similar to the undeflected beams. When the two pulses overlap on the target, the divergence of the low energy part of the proton beam is significantly increased in the vertical direction. We interpret this to be due to the cylindrically convex shape of the emitting rear surface.[13] The absence of higher proton energies indicates that under these conditions, the area close to the peak of the deformation is not suitable for efficient acceleration. A reasonable explanation is the long preplasma scale length resulting from the ablation of the target front. This could increase the divergence of the electron beam driven into the target by the high intensity laser pulse but also reduce the front side reflection of refluxing electrons. Both effects reduce the electron density in the sheath at the rear surface and, thereby, also the magnitude of the accelerating field.

To model the proton emission direction we employ the quasi-two-dimensional scheme presented in Ref. 13. The magnitude of the deformation depends on the time available for the laser-driven shock to transit the target and for expansion following shock breakout. The shock velocity, $u_s = c_0/2(\sqrt{1+\eta}+1)$, and the expansion velocity, $u_e = c_0/\alpha(\sqrt{1+\eta}-1)$, are derived from the equation of state of the target material. Here, $\eta=(4\alpha/\rho_0 c_0^2)P$ depends linearly on the laser induced ablation pressure P, ρ_0 is the density, c_0 is the sound speed, and α is a dimensionless parameter of the order of unity. Neglecting transverse shock spreading and using a rectangular approximation of the laser pulse shape, the shape of the rear surface is $z(x,t)=\max(0,\{t-[L/u_s(x)]\}u_e(x))$, where t is the delay between the two laser pulses, x is the vertical position, and L is the target thickness. The induced pressure distribution (in pascal) is assumed to follow the intensity distribution (in $\mathrm{W/m^2}$) as $P(x)=1.3I(x)^{2/3}$, according to the scaling given by Lindl.[15]

Using tabulated data for aluminum ($\rho_0=2.7\ \mathrm{g/cm^3}$, $c_0=5240$ m/s, and $\alpha=1.40$) and a Gaussian intensity distribution with a 14 μm full width at half maximum, the shape of the target foil at the time of the main pulse arrival on target is calculated [see Fig. 2(b)]. The direction of the local target normal, shown by the solid line in Fig. 2(c), fits the measured data very well. The model indirectly gives an upper limit to the proton source size. The region in which the proton beam is steered has a width of 40 μm so the proton emitting area must be smaller than 20 μm for protons above the detection threshold (0.9 MeV). This is small compared to previous studies.[2] The reasons are the thinner targets and shorter pulses used in this experiment. We can estimate the expected source size by simply assuming that electrons, injected at angle θ, recirculate inside the target during the laser pulse and are ballistically reflected at the surfaces. After the laser pulse has passed, we estimate the sheath radius at the rear as $R=r+(c\tau+L)\tan\theta$. Here, r is the focal spot radius and θ is the half opening angle of the injected electron dis-

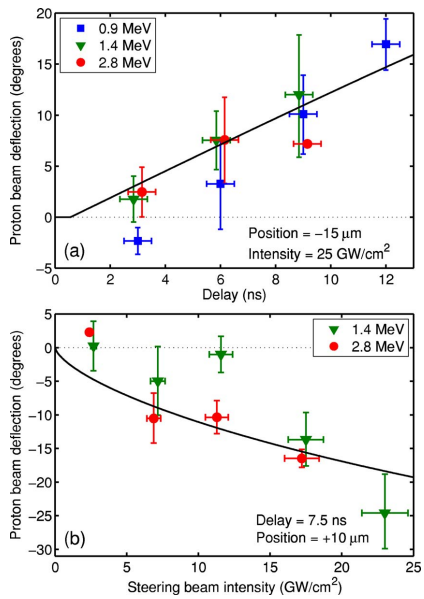

FIG. 3. (Color online) Deflection of protons of different energies as function of (a) delay and (b) intensity of the steering pulse. When the line focus is below the main pulse, protons are steered upward and vice versa. Vertical error bars show the total spread of the deflection data over three consecutive shots. The summed uncertainty due to drift and pulse-to-pulse fluctuations are shown by the horizontal error bars.

tribution. For a full opening angle of 30° and our experimental parameters, the predicted sheath diameter is 14 μm, which agrees well with our experimental observations.

We now keep the steering beam fixed at a 15 μm offset below the main focal spot and vary the relative delay between the two pulses [see Fig. 3(a)]. As expected, the proton beam is deflected upward with a magnitude that increases with increasing delay. As in Fig. 2, the magnitude of the deflection does not vary significantly for protons of different energies and the analytical model fits the data very well. Note that prior to shock breakout, we expect no proton beam deflection since the rear surface is unperturbed. Finally, we vary the intensity of the steering beam [see Fig. 3(b)]. Note that, even though the model qualitatively fits the data, target ionization is not included and at laser intensities close to or below the ionization threshold, the induced ablation pressure cannot be accurately estimated.

In conclusion, we have demonstrated a method for optical control of the spatial distribution of laser-accelerated proton beams. In this letter, we concentrated on the first-order application of the method, beam steering, but by using tailored intensity distributions, other aspects of the spatial distribution should be possible to control. We expect that a ring shaped beam can control the ion beam divergence and that the dynamic change of the target curvature can bring the proton beam to focus at an adjustable distance from the foil. Such control is very interesting for many applications such as studies of isochoric heating of dense plasmas and for the fast ignition approach to inertial confinement fusion. In addition, by controlling the divergence directly at the source, a higher charge could be delivered into the limited acceptance angle of the injection optics in a large accelerator.

The authors acknowledge discussions with D. Neely and financial support from the Swedish Research Council and the Knut and Alice Wallenberg Foundation. C.H. was supported by the Marie Curie EST MAXLAS program. P.McK. and D.C. acknowledge the support from the COST P-14 program.

[1]L. Robson, P. Simpson, R. Clarke, K. W. D. Ledingham, F. Lindau, O. Lundh, T. McCanny, P. Mora, D. Neely, C.-G. Wahlstrom, M. Zepf, and P. McKenna, Nat. Phys. **3**, 58 (2007).
[2]T. E. Cowan, J. Fuchs, H. Ruhl, A. Kemp, P. Audebert, M. Roth, R. Stephens, I. Barton, A. Blazevic, E. Brambrink, J. Cobble, J. Fernandez, J.-C. Gauthier, M. Geissel, M. Hegelich, J. Kaae, S. Karsch, G. P. LeSage, S. Letzring, M. Manclossi, S. Meyroneinc, A. Newkirk, H. Pepin, and N. Renard–LeGalloudec, Phys. Rev. Lett. **92**, 204801 (2004).
[3]M. Borghesi, A. J. Mackinnon, D. H. Campbell, D. G. Hicks, S. Kar, P. K. Patel, D. Price, L. Romagnani, A. Schiavi, and O. Willi, Phys. Rev. Lett. **92**, 055003 (2004).
[4]S. V. Bulanov and V. S. Khoroshkov, Plasma Phys. Rep. **28**, 453 (2002).
[5]K. W. D. Ledingham, P. McKenna, T. McCanny, S. Shimizu, J. M. Yang, L. Robson, J. Zweit, J. M. Gillies, J. Bailey, G. N. Chimon, R. J. Clarke, D. Neely, P. A. Norreys, J. L. Collier, R. P. Singhal, M. S. Wei, S. P. D. Mangles, P. Nilson, K. Krushelnick, and M. Zepf, J. Phys. D **37**, 2341 (2004).
[6]K. Krushelnick, E. L. Clark, R. Allott, F. N. Beg, C. N. Danson, A. Machacek, V. Malka, Z. Najmudin, D. Neely, P. A. Norreys, M. R. Salvati, M. I. K. Santala, M. Tatarakis, I. Watts, M. Zepf, and A. E. Dangor, IEEE Trans. Plasma Sci. **28**, 1184 (2000).
[7]M. Roth, T. E. Cowan, M. H. Key, S. P. Hatchett, C. Brown, W. Fountain, J. Johnson, D. M. Pennington, R. A. Snavely, S. C. Wilks, K. Yasuike, H. Ruhl, F. Pegoraro, S. V. Bulanov, E. M. Campbell, M. D. Perry, and H. Powell, Phys. Rev. Lett. **86**, 436 (2001).
[8]M. Borghesi, J. Fuchs, S. V. Bulanov, A. J. MacKinnon, P. K. Patel, and M. Roth, Fusion Sci. Technol. **49**, 412 (2006).
[9]S. C. Wilks, A. B. Langdon, T. E. Cowan, M. Roth, M. Singh, S. Hatchett, M. H. Key, D. Pennington, A. MacKinnon, and R. A. Snavely, Phys. Plasmas **8**, 542 (2001).
[10]P. K. Patel, A. J. Mackinnon, M. H. Key, T. E. Cowan, M. E. Foord, M. Allen, D. F. Price, H. Ruhl, P. T. Springer, and R. Stephens, Phys. Rev. Lett. **91**, 125004 (2003).
[11]F. N. Beg, M. S. Wei, A. E. Dangor, A. Gopal, M. Tatarakis, K. Krushelnick, P. Gibbon, E. L. Clark, R. G. Evans, K. L. Lancaster, P. A. Norreys, K. W. D. Ledingham, P. McKenna, and M. Zepf, Appl. Phys. Lett. **84**, 2766 (2004).
[12]F. Lindau, O. Lundh, A. Persson, P. McKenna, K. Osvay, D. Batani, and C.-G. Wahlstrom, Phys. Rev. Lett. **95**, 175002 (2005).
[13]O. Lundh, F. Lindau, A. Persson, C.-G. Wahlstrom, P. McKenna, and D. Batani, Phys. Rev. E **76**, 026404 (2007).
[14]D. Neely, P. Foster, A. Robinson, F. Lindau, O. Lundh, A. Persson, C.-G. Wahlstrom, and P. McKenna, Appl. Phys. Lett. **89**, 021502 (2006).
[15]J. Lindl, Phys. Plasmas **2**, 3933 (1995).

Paper V

Enhanced proton beams from ultrathin targets driven by high contrast laser pulses

D. Neely, P. Foster, A. Robinson, F. Lindau, O. Lundh, A. Persson, C.-G. Wahlström and P. McKenna.

Applied Physics Letters **89**, 021502 (2006).

APPLIED PHYSICS LETTERS **89**, 021502 (2006)

Enhanced proton beams from ultrathin targets driven by high contrast laser pulses

D. Neely,[a] P. Foster, and A. Robinson
Central Laser Facility, Rutherford Appleton Laboratory, Chilton, Didcot, Oxon OX11 0QX, United Kingdom

F. Lindau, O. Lundh, A. Persson, and C.-G. Wahlström
Department of Physics, Lund Institute of Technology, P.O. Box 118, S-221 00 Lund, Sweden

P. McKenna
SUPA, Department of Physics, University of Strathclyde, Glasgow G4 0NG, United Kingdom

(Received 14 March 2006; accepted 22 May 2006; published online 13 July 2006)

The generation of proton beams from ultrathin targets, down to 20 nm in thickness, driven with ultrahigh contrast laser pulses is explored. The conversion efficiency from laser energy into protons increases as the foil thickness is decreased, with good beam quality and high efficiencies of 1% being achieved, for protons with kinetic energy exceeding 0.9 MeV, for 100 nm thick aluminum foils at intensities of 10^{19} W/cm^2 with 33 fs, 0.3 J pulses. To minimize amplified spontaneous emission (ASE) induced effects disrupting the acceleration mechanism, exceptional laser to ASE intensity contrasts of up to 10^{10} are achieved by introducing a plasma mirror to the high contrast 10 Hz multiterawatt laser at the Lund Laser Centre. It is shown that for a given laser energy on target, regimes of higher laser-to-proton energy conversion efficiency can be accessed with increasing contrast. The increasing efficiency as the target thickness decreases is closely correlated to an increasing proton temperature. © *2006 American Institute of Physics*.
[DOI: 10.1063/1.2220011]

Significant progress has recently been made in the production of low-divergence beams of MeV protons from the interaction between short pulse, high intensity laser radiation, and thin target foils. Such laser-driven ion beams will potentially find numerous uses in the fields of physics, materials science, and medicine.[1,2] However, important work remains, for example, to increase the maximum proton energy and to optimize the laser-to-proton energy conversion efficiency. Studies along these lines are presently the focus of many research programs worldwide.

The main mechanism behind the highest energy protons is target normal sheath acceleration[3] (TNSA) at the rear surface. In particular, with a hydrogen containing layer on the target surface, always present under the vacuum conditions normally available for laser-plasma experiments, the dominant accelerated ion species is proton, due to their high charge to mass ratio. The highest electron density at the rear surface, and consequently highest acceleration field, is expected for ultrathin targets of a conducting material. As the target thickness is decreased, transverse spreading of the hot electrons inside the target is reduced, resulting in a higher rear surface charge density.[4] In addition, if the thickness is less than $\tau c/2$ (τ is the laser pulse duration and c the speed of light), electron recirculation within the target during the laser pulse may further enhance the acceleration field at the rear surface.[5] Finally, for very high intensities and ultrathin targets, relativistic transparency allows part of the laser pulse to be transmitted through the target and contribute to increased electron heating.[6] However, there are limits to this decrease in target thickness in order to optimize proton acceleration. The most severe limiting factor in experiments is the presence of laser prepulses or a pedestal of amplified spontaneous emission (ASE), affecting the conditions on the target rear surface prior to the arrival of the main laser pulse.[7,8] An induced density gradient can drastically reduce the effectiveness of the TNSA mechanism.[9] The thinner the target, the more sensitive it is to such prepulses. For a given peak laser intensity, the optimum target thickness is thus related to the laser temporal contrast, defined as the ratio between the intensity of the main pulse to that of the pedestal or prepulse. Most experiments reported in the literature are limited to targets with thickness in the range from a few micrometers to several tens of micrometers.

Previous investigations using medium contrast Ti:sapphire laser systems,[4,10] have demonstrated a gradual increase in maximum proton energy observed E_{max} as the target thickness was decreased. For example, Kaluza *et al.* with a laser contrast of 10^7 demonstrate an increase in proton energy with decreasing target thickness down to 2 μm. The increase was attributed to reduced transverse spreading of the hot electrons inside the target. Mackinnon *et al.*,[5] using a laser with a contrast of 10^{10}, demonstrated significant enhancement in E_{max} as the target thickness was decreased below $\tau c/2$ ($\sim$10 μm in their case). This increase was attributed to electron recirculation. In the studies by Kaluza *et al.*,[4] the same drastic enhancement was not observed, possibly because ASE induced density gradients of the target rear surface disrupted the proton acceleration before the recirculation mechanism became effective.

Motivated by these earlier studies we embark on a program of work examining proton acceleration from surface contamination layers on ultrathin target substrates. In particular, we study the influence of target thickness on the laser-to-proton energy conversion efficiency and energy distribution. In this letter we report results with Al targets and ultrahigh contrast laser pulses, allowing us to extend the in-

[a]Electronic mail: d.neely@rl.ac.uk

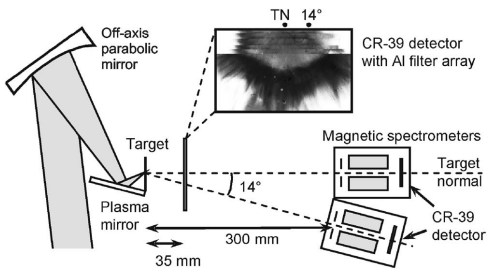

FIG. 1. Schematic of the experimental arrangement showing the plasma mirror geometry and proton diagnostics. The spatial profile monitor only sampled the lower portion of the beam, enabling the magnetic spectrometers situated in the horizontal plane to be operated simultaneously. The inset shows the spatial profile data from a 50 nm foil shot, corresponding to the star in Fig. 2. A filter mask consisting of strips of Al foil with different thicknesses, each stopping protons below a threshold energy, gives a staircase energy response in the vertical direction for the spatial profile.

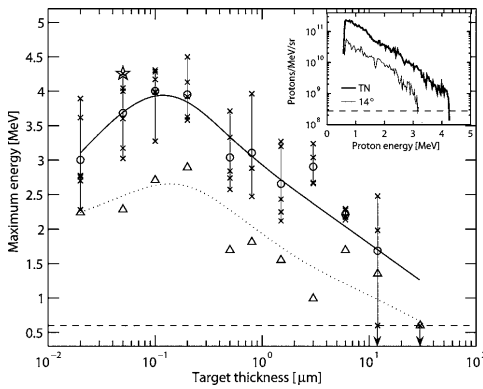

FIG. 2. Maximum proton energies obtained as a function of Al target thickness for on-target contrasts of 10^{10} (crosses). The solid line is a trend line fitted to the on-axis average for each thickness (circles). The 14° average data are represented by the triangles and the dotted trend line. The dashed line represents the detection limit. The inset shows typical proton spectra for the shot represented by the star symbol.

vestigations to significantly thinner targets than previously reported.

The experiment employs the 10 Hz, 800 nm multiterawatt laser system at the Lund Laser Centre (LLC),[7] which delivers 33 fs pulses with a 1 ns duration ASE, at an intensity contrast of 2×10^8. When this laser is focused to an intensity of $\sim10^{19}$ W/cm^2, the ASE pedestal typically launches an ~8 μm/ns shock wave into Al target foils.[7,8] Therefore, to drive targets thinner than 1 μm, contrasts $>10^8$ (or pedestals of much shorter duration) are necessary to maintain an undisturbed target rear surface. To achieve such conditions in the present study we use a plasma mirror.[11] The transition from low to high reflectivity of a plasma mirror can be set to occur as the main pulse rises out of the ASE background approximately a few tens of picosecond before the peak of the pulse. The ASE pedestal is thus transmitted, resulting in a significant increase in temporal contrast in the reflected part of the pulse. Previous plasma mirror studies[12] have demonstrated that it is possible to obtain high contrast and high reflectivity without adding any phase errors by carefully selecting the appropriate irradiance conditions.

We operate our uncoated glass plasma mirror at 45° angle of incidence, in a *P*-polarized geometry, 3 mm from the laser focus. At this point the ASE intensity onto the plasma mirror is always below 10^8 W/cm^2, while the peak laser pulse intensity exceeds 10^{15} W/cm^2. In this configuration we measure a reflectivity of $41\pm3\%$. The contrast enhancement, calculated as the ratio of ASE reflectivity to main pulse reflectivity, is 45 under these conditions leading to an on-target contrast of 10^{10}. The laser pulse is focused onto thin Al foils at 30° angle of incidence by an $f/3$, off-axis parabolic mirror, via the plasma mirror, as illustrated in Fig. 1. With a pulse energy, after the plasma mirror, of 0.3 J and a $1/e^2$ focal spot diameter of 10 μm, the peak intensity on target reaches 10^{19} W/cm^2. In this configuration, and with an ASE contrast of 1×10^{10}, a data set comprising of over 50 shots is obtained for a wide range of target thickness, enabling trends to be clearly identified. The rear surface proton beam emission is sampled by three diagnostics, two magnetic spectrometers operating at deflection angles $\phi=0°$ and 14° with respect to target normal, and a half beam "spatial profile monitor"[8] consisting of a CR-39 track detector covered with an array of Al filters.

Proton spectra from Al foils in the range of 20 nm–30 μm are recorded and a typical example of the 0° and 14° emissions is shown in the inset in Fig. 2. The maximum detectable proton energy (E_{max}) is plotted as a function of target thickness in Fig. 2. The average E_{max} for a given foil thickness increases from 0.6 MeV with 30 μm thick foils to 4 MeV with 0.1 μm and then decreases slightly to 3 MeV for 0.02 μm thickness targets. The shot-to-shot variations under nominally identical conditions at a given foil thickness have an average standard deviation of 12%. It is believed that this is partly due to variation within the proton contamination layer or intensity modulations within the focal spot and will be studied in future experiments.

Proton acceleration using the same incident energy on target but at a lower contrast of 5×10^7 reveals that E_{max} is always lower when using the lower contrast pulse, although comparable for targets thicker than a few micrometers.

The proton spectra show an almost single temperature Boltzmann-like distribution (see inset in Fig. 2.). The number of protons/MeV/Sr, $N(E,\phi)$, can be fitted by a simple distribution of the form $N(E,\phi)=N_0(\phi)\exp[-E/T(\phi)]$, where E is the proton energy in MeV, $N_0(\phi)=N(0,\phi)$ extrapolated from the data to $E=0$, and $T(\phi)$ is the temperature in MeV of the distribution. A plot of the fitted temperatures as a function of target thickness is shown in Fig. 3. The data clearly show an increase in the effective temperature of the protons as the target thickness decreases, with the temperature rising from 0.2 MeV at 12 μm to a maximum temperature of 0.65 MeV for targets of thickness of 0.1 μm and then falling to 0.4 MeV for 0.02 μm targets. $N_0(0)$ is approximately independent of target thickness with an average value of 10^{12} protons/MeV/Sr.

The 14° proton spectra follow similar trends to the target normal data in terms of temperature in the majority of shots. However, in a small number of shots (3 out of 50) an off-axis peaked energy spectrum was observed. The angular divergence of the proton beams generally decreases with increasing proton energy, with the ratio $E_{max}(0)/E_{max}$ (14°) having an average of 1.5 and a standard deviation of 0.4. This ratio

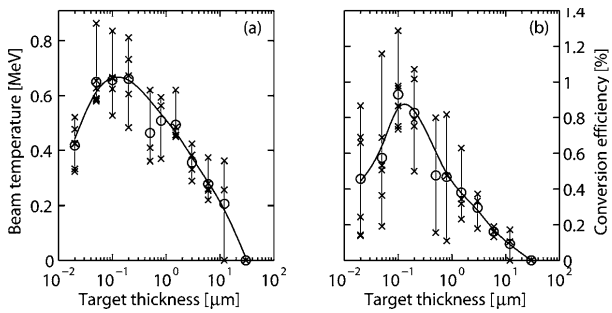

FIG. 3. The effective temperature (a) and energy conversion efficiency to protons with $E>0.9$ MeV (b) of the proton distribution as a function of target thickness. Both curves show maxima for targets of ~100 nm thickness.

does not show any correlation with target thickness. The energy of the energetic part of the proton beam is obtained by integrating the proton beam angular distribution spectrally and spatially for $E>0.9$ MeV, corresponding to the detection threshold of the spatial profile monitor. The beam profile is obtained for each shot by combining the data from the two spectrometers and the spatial profile monitor using cubic spline interpolation. Dividing by the incident drive energy gives the efficiency of conversion into energetic protons, as shown in Fig. 3. The energy transferred into protons of energy above 0.9 MeV increases rapidly with decreasing target thickness and reaches an optimum of ~1% for submicron targets.

Although $N_0(0)$ and divergence show no systematic trends with target thickness, the maximum observed proton energy and beam efficiency exhibit clear trends. The number of accelerated protons increases by approximately a factor of 10 and their average energy also increases as the targets are thinned. It is believed that increasing rear surface hot electron temperatures and densities are enabling these higher proton beam temperatures to be achieved using thinner targets. The observed dependence of E_{max} on target thickness may have different origins in different ranges of thickness. Above a few micrometers, the increase in E_{max} with a decrease in thickness might be dominated by geometrical effects with a decrease in transverse spreading of the hot electrons during transit through the target, as observed by Kaluza *et al.*.[4] Due to the higher contrast available, the thickness can be decreased to even thinner targets in the present study, and we reach a regime where transverse spreading should be negligible. Here E_{max} continues to increase, possibly due to an increasing role of recirculation with decreasing target thickness.[5] It is not expected that self-induced transparency and electron heating by the transmitted fraction of the laser pulse[6] play a significant role at these intensities. Below about 100 nm, we find a decrease in E_{max}, resulting in a clear optimum in thickness. This decrease could be due to the finite temporal contrast on the picosecond time scale, given by the shoulders of the main pulse rather than to ASE or separate prepulses. Establishing the relative contributions of the different effects, including recirculation, refluxing, conduction, and return current inhibitions will be undertaken in future experimental and theoretical studies.

In conclusion, a laser-to-proton beam energy conversion efficiency of 1%, for protons with $E>0.9$ MeV, is obtained for the first time with a short pulse Ti:sapphire laser and pulse energy as low as 0.3 J on target. With a contrast of 10^{10}, the optimum target thickness is found to be as thin as 100 nm. The results show a significant enhancement in proton beam scaling with a variation in target thickness and clearly demonstrate the benefits of using an ultrahigh contrast laser to drive thin targets.

This work was supported by the Access to Research Infrastructures under the Sixth EU Framework Programme contract (RII3-CT-2003-506350, Laserlab Europe), by the Swedish Research Council and the UK Council for the Central Laboratories of the Research Councils.

[1]S. V. Bulanov, T. Z. Esirkepov, V. S. Khoroshkov, A. V. Kunetsov, and F. Pegoraro, Phys. Lett. A **299**, 240 (2002).
[2]M. Roth, E. Brambrink, P. Audebert, M. Basko, A. Blazevic, R. Clarke, J. Cobble, T. E. Cowan, J. Fernandez, J. Fuchs, M. Hegelich, K. Ledingham, L. G. Logan, D. Neely, H. Ruhl, and M. Schollmeier, Plasma Phys. Controlled Fusion **47**, B841 (2005).
[3]S. C. Wilks, A. B. Langdon, T. E. Cowan, M. Roth, M. S. Singh, S. P. Hatchett, M. H. Key, D. M. Pennington, A. J. Mackinnon, and R. A. Snavely, Phys. Plasmas **8**, 542 (2001).
[4]M. Kaluza, J. Schreiber, M. I. K. Santala, G. D. Tsakiris, K. Eidmann, J. Meyer-ter-Vehn, and K. J. Witte, Phys. Rev. Lett. **93**, 045003 (2004).
[5]A. J. Mackinnon, Y. Sentoku, P. K. Patel, D. W. Price, S. P. Hatchett, M. H. Key, C. Andersen, R. A. Snavely, and R. R. Freeman, Phys. Rev. Lett. **88**, 215006 (2002).
[6]E. d'Humiere, E. Lefebvre, L. Grémillet, and V. Malka, Phys. Plasmas **12**, 062704 (2005).
[7]F. Lindau, O. Lundh, A. Persson, P. McKenna, K. Osvay, D. Batani, and C.-G. Wahlström, Phys. Rev. Lett. **95**, 175002 (2005).
[8]P. McKenna, F. Lindau, O. Lundh, D. Neely, A. Persson, and C.-G. Wahlström, Philos. Trans. R. Soc. London, Ser. A **364**, 711 (2006).
[9]A. J. Mackinnon, M. Borghesi, S. P. Hatchett, M. H. Key, P. K. Patel, H. Campbell, A. Schiavi, R. A. Snavely, S. C. Wilks, and O. Willi, Phys. Rev. Lett. **86**, 1769 (2001).
[10]I. Spencer, K. W. D. Ledingham, P. McKenna, T. McCanny, R. P. Singhal, K. Krushelnick, E. L. Clark, P. A. Norreys, R. J. Clarke, D. Neely, A. J. Langley, E. J. Divall, C. H. Hooker, and J. R. Davies, Phys. Rev. E **67**, 046402 (2003).
[11]G. Doumy, F. Quere, O. Gobert, M. Perdrix, Ph. Martin, P. Audebert, J.-C. Gauthier, J.-P. Geindre, and T. Wittmann, Phys. Rev. E **69**, 026402 (2004).
[12]C. Ziener, P. S. Foster, E. J. Divall, C. H. Hooker, M. H. R. Hutchinson, A. J. Langley, and D. Neely, J. Appl. Phys. **93**, 768 (2003).

Paper VI

Active manipulation of the spatial energy distribution of laser-accelerated proton beams

D. C. Carroll, P. McKenna, O. Lundh, F. Lindau, C.-G. Wahlström, S. Bandyopadhyay, D. Pepler, D. Neely, S. Kar, P. T. Simpson, K. Markey, M. Zepf, C. Bellei, R. G. Evans, R. Redaelli, D. Batani, M. H. Xu and Y. T. Li.

Physical Review E **76**, 065401(R) (2007).

RAPID COMMUNICATIONS

PHYSICAL REVIEW E **76**, 065401(R) (2007)

Active manipulation of the spatial energy distribution of laser-accelerated proton beams

D. C. Carroll and P. McKenna*
SUPA, Department of Physics, University of Strathclyde, Glasgow G4 0NG, United Kingdom

O. Lundh, F. Lindau, and C.-G. Wahlström
Department of Physics, Lund University, P.O. Box 118, S-22100 Lund, Sweden

S. Bandyopadhyay, D. Pepler, and D. Neely
STFC, Rutherford Appleton Laboratory, Didcot OX11 0QX, United Kingdom

S. Kar, P. T. Simpson, K. Markey, and M. Zepf
School of Mathematics and Physics, Queen's University Belfast, Belfast BT7 1NN, United Kingdom

C. Bellei and R. G. Evans
The Blackett Laboratory, Imperial College London, London, SW7 2AZ, United Kingdom

R. Redaelli and D. Batani
Dipartimento di Fisica, Università di Milano Bicocca, 20126 Milano, Italy

M. H. Xu and Y. T. Li
Beijing National Laboratory for Condensed Matter Physics, Institute of Physics, Chinese Academy of Sciences, Beijing 100080, China
(Received 9 July 2007; revised manuscript received 28 September 2007; published 12 December 2007)

The spatial energy distributions of beams of protons accelerated by ultrahigh intensity ($>10^{19}$ W/cm^2) picosecond laser pulse interactions with thin foil targets are investigated. Using separate, low intensity ($<10^{13}$ W/cm^2) nanosecond laser pulses, focused onto the front surface of the target foil prior to the arrival of the high intensity pulse, it is demonstrated that the proton beam profile can be actively manipulated. In particular, results obtained with an annular intensity distribution at the focus of the low intensity beam are presented, showing smooth proton beams with a sharp circular boundary at all energies, which represents a significant improvement in the beam quality compared to irradiation with the picosecond beam alone.

DOI: 10.1103/PhysRevE.76.065401 PACS number(s): 52.38.Kd, 41.75.Jv, 52.50.Jm

The use of ultraintense ($>10^{19}$ W/cm^2) laser pulses to drive multi-MeV ion acceleration has generated a lot of international interest recently [1]. Many of the exciting possible applications of these ion beams would benefit from active control of the properties of the beam. It has recently been demonstrated experimentally that it is possible to optically change the direction of the proton beam [2,3], and it has been shown theoretically that it should be possible to change the spectral distribution of the beam by use of a double laser pulse arrangement [4].

In this paper we present a study on the active manipulation of the spatial distribution of laser accelerated protons using separate low intensity laser pulses. In particular, we report conditions for which smooth beams with sharp circular boundaries at all energies are consistently produced, and show that the divergence properties of the ion beam can be actively manipulated. We show that with the addition of a second low intensity laser pulse, we obtain not only an improvement in the spatial quality of the beam, but also an increase in beam flux and energy.

The experiment is performed using multiple beams from the Vulcan laser at the Rutherford Appleton Laboratory. A chirped pulse amplified (CPA) pulse of 1 ps duration [full width at half maximum (FWHM)] and up to 90 J energy is used to drive the proton acceleration. The 1053 nm wavelength beam is focused using an off-axis $f/3$ parabolic mirror. A plasma mirror [5] is positioned in the focusing beam to suppress the intensity of the amplified spontaneous emission to less than 10^{12} W/cm^2. The mirror is operated at 15° angle of incidence, in a *P*-polarized geometry, and has a measured reflectivity of 55%, giving a pulse energy on target of up to 50 J. The beam is incident onto target at an angle of 5° and the spot size at focus is 9 μm (FWHM), resulting in a peak intensity of up to 4×10^{19} W/cm^2. The targets are planar Cu foils of 5, 12.5, and 20 μm thickness, and with a measured average peak-to-mean surface roughness of ~0.7 μm. The arrangement is illustrated schematically in Fig. 1.

A low energy (<5 J), 1053 nm wavelength pulse with a temporal profile approximating a flat-top distribution with a duration of 6 ns is used to drive ablation on the front surface of the target foil. The leading edge of the pulse arrives on target 3.5 ns prior to the arrival of the CPA pulse. The "ablation" pulse is focused using an $f/10$ lens and is incident at an angle of 25° onto target. A binary phase plate is positioned in the beam, in order to produce an annular distribution of laser light at focus, with a mean diameter of 460 μm and a thickness of ~35 μm, as shown in the inset of Fig. 1. The phase plate is a glass (borosilicate) substrate, on which a surface relief has been produced (using photolithography).

*Author to whom correspondence should be addressed. p.mckenna@phys.strath.ac.uk

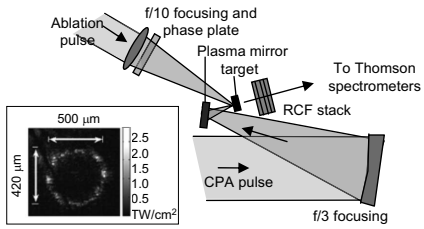

FIG. 1. Schematic diagram of the experiment. Proton acceleration is driven by a high intensity CPA pulse, which is focused using a $f/3$ off-axis parabolic mirror, with contrast enhancement provided by a plasma mirror positioned in the focusing beam. A binary phase plate introduced into the beam path of a separate low energy ("ablation") pulse, which is focused using an $f/10$ lens, is used to produce a low intensity ring of laser light centered on the CPA focus. The measured spatial intensity distribution at the focus of the ablation pulse is shown in the inset. The proton spatial energy distribution is measured using a stack of RCF film and ion charge and spectral distributions are measured using Thomson ion spectrometers.

This induces a designed phase distribution in the laser beam transversing it, leading to the desired intensity distribution in the focus. The distribution of light produced around the ring varies in intensity between 3×10^{11} and 3×10^{12} W/cm^2.

The spatial distribution of the accelerated proton beam is measured simultaneously for different proton energies using a stack of radiochromic films (RCFs), which are preferentially sensitive to protons [6]. We confirm that the dose measured in the RCFs is predominately due to protons by introducing a periodical pattern in the intensity distribution of the proton beam using an absorbing mesh positioned behind the target on some shots. Each RCF in the stack measures the spatial distribution of the deposited dose for protons above an energy defined by the total thickness of the preceding stack layers. The stack is positioned 30 mm from the target and a slot machined in it provides a line of sight to an array of Thomson ion spectrometers.

With this arrangement, and in the absence of the ablation pulse, we detect the emission of proton beams with broad energy distributions from the rear of the targets. Using 5 μm-thick Cu targets, the energy distribution typically reaches up to 12 MeV, but when increasing the thickness to 20 μm, the maximum energy decreases to 9 MeV and the beam divergence reduces. Representative examples of spatial distributions, obtained with 5 and 20 μm targets, are shown in Figs. 2(a) and 2(c), respectively. Spatial modulations are typically observed in the proton dose, and may arise due to the roughness of the Cu target surface, modulations in the ultrahigh intensity drive laser beam, and/or instabilities in electron transport through the foil [7].

With the addition of the ablation beam, focused to produce the annular intensity distribution shown in the inset of Fig. 1, while using identical CPA beam and target parameters, we observe a significant improvement in the spatial distribution of the accelerated proton beam, together with increases in proton flux (typically about a factor of 3) and

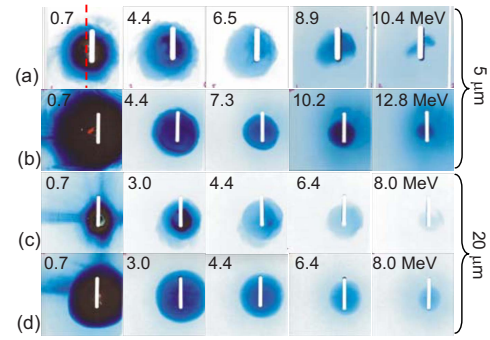

FIG. 2. (Color online) Representative examples of the measured proton spatial and energy distributions using RCF, obtained with a 5-μm target (a) without and (b) with the "ablation ring" pulse; and the corresponding results for a 20-μm target are shown in (c) and (d), respectively. The calculated intensity of the CPA pulse was between 2×10^{19} and 3×10^{19} W/cm^2 for all shots. These examples clearly show that the proton beam profile becomes more circular and more uniformly distributed in the presence of the low intensity ablation beam at both target thicknesses. The dashed line in (a) corresponds to the position of the lineout profiles sampled in Fig. 3, and applies to all RCFs in (a) and (b).

maximum proton energy. Corresponding measurements for the 5 and 20 μm targets are shown in Figs. 2(b) and 2(d), respectively. Consistently we observe that with the ablation "ring" present, the profile of the proton beam becomes more like a "top-hat" distribution with a sharper circular boundary for most of the energy range. We quantify the improvement in the flatness of the beam by sampling the proton dose distribution in the region corresponding to 50% of the beam area, at the center of the beam, at each measured energy in the range 3.0–8.8 MeV. We find that the standard deviation of the proton dose in the film from a flat distribution varies from 54% of the mean value, at the lower energy, to 11% at the higher energy, when the target is irradiated by the CPA beam only. When the ablation pulse is added, the corresponding values are 16% and 4%, respectively. Examples of beam profile lineouts as a function of energy, with and without the ablation pulse, are shown in Fig. 3.

Our findings can be interpreted in the framework of the

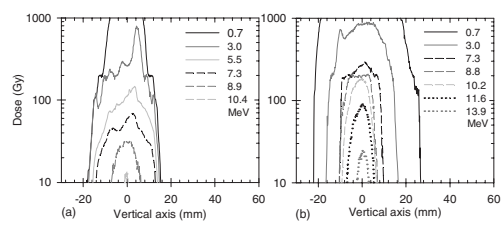

FIG. 3. Beam profile lineouts (along the position of the dashed line in Fig. 2) as a function of proton energy for the 5-μm target results shown in Fig. 2; (a) without and (b) with the ablation pulse.

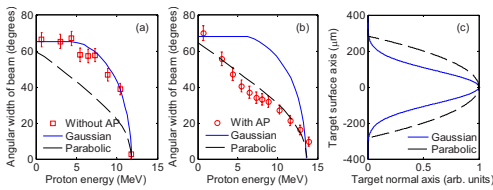

FIG. 4. (Color online) (a) Symbols correspond to the measured angular envelope of the proton beam as a function of proton energy for the 5-μm target sample measurements of Fig. 2, *without* the ablation pulse (AP); (b) corresponding measurements *with* the ablation pulse. The lines are the calculated divergence as a function of energy using the Gaussian (solid blue line) and the parabolic (dashed black line) sheath spatial distributions shown in (c). With the CPA beam only, a Gaussian distribution with a FWHM of 220 μm reproduces the experimental results, as shown in (a), whereas a better fit to the experimental measurements in the presence of the long pulse ablation beam is obtained with a parabolic function with a FWHM of 400 μm, as shown in (b). The ratio of the peak electric fields used in the simulation results shown in (a) and (b) is 0.9, as defined by the maximum measured proton energies.

target normal sheath acceleration (TNSA) mechanism [8]. Fast electrons, which are accelerated through the target by the CPA laser pulse, become electrostatically confined to the target rear surface, building a sheath with a quasi-static charge separation field, which ionizes and accelerates atoms at the rear surface. Protons are accelerated normal to isodensity contours in the sheath [6], and hence the measured spatial profile of the accelerated proton beam is sensitive to the shape of the sheath. The spatial profile of the sheath, and hence the ion front, is typically Gaussian shaped, as inferred from measurements by Fuchs *et al.* [6] and shown experimentally by Romagnani *et al.* [9]. Our observations of a change to the spatial profile of the proton beam can thus be interpreted as a change to the shape of the sheath, induced by the presence of the ablation beam.

Evidence of a change in the sheath shape is inferred from observed changes to the angular divergence as a function of energy. It has previously been shown, with single CPA beam irradiation of a target foil, that the angular envelope of the proton beam decreases with energy [10–12], and that this is due to a decrease in size of the emission region near the peak of the Gaussian-shaped electron sheath [12,1]. We find that the divergence characteristics of the proton beam changes significantly in the presence of the annular ablation beam, as shown in the example measurements of Figs. 2–4. The representative measurements in Fig. 4 illustrate the changes to the full angular envelope of the proton beam as a function of energy induced by the addition of the ablation beam. In the absence of the ablation ring, we consistently observe that the spatial extent of the beam is fairly constant for low proton energies and decreases only at the highest energies. This manifests itself in the plateau-like distribution at low energies in Fig. 4(a) and is quite different to the near-linear dependence of the divergence on proton energy consistently observed with the ablation ring present, Fig. 4(b), for otherwise identical target and laser conditions.

The measured changes to the proton beam divergence as a function of energy can be explained by changes to the spatial distribution of the sheath. To illustrate this, we devise a model to determine the sheath shape by fitting to the experimental measurements. The model calculates the spatial distribution of the expanding ion front, and the divergence and energy of protons produced along the ion front, as a function of time for a defined spatial and temporal distribution of the electric field. The temporal profile of the electric field is assumed to be Gaussian with a FWHM equal to 1.2 ps—similar to the laser pulse duration. The peak strength of the field is chosen to reproduce the maximum detected energy of the accelerated protons. The model uses the threshold field for the ionization of hydrogen (assuming field ionization to be the dominant ionization mechanism at the rear surface of the target) to define the spatial extent of the proton source as a function of time. The ion front expands into vacuum and the velocity components and hence proton energy as a function of radius from the center of the sheath, at each temporal step (0.1 ps steps over a 4 ps range defined by the temporal profile of the electric field), is determined. The local normal at each point along the ion front surface is calculated as it evolves spatially and temporally, to determine the angle of proton emission.

Based on the measured sheath distributions reported by Romagnani *et al.* [8], for foil irradiation with a single CPA beam, we begin by assuming that the sheath shape has the form of a Gaussian distribution. We find a good fit to the experimental measurements, as shown in Fig. 4(a), when the FWHM of the distribution is equal to 220 μm. The spatial distribution of the sheath is shown in Fig. 4(c). Next, we consider what kind of change to the sheath shape would give rise to the measured changes in the divergence as a function of proton energy, when the ablation pulse is added. We find very good agreement with the experimental data, as shown in Fig. 4(b), when an inverse parabolic sheath profile with a FWHM of 400 μm is used [Fig. 4(c)]. We note that an inverse parabolic profile of the ion front is used by Brambrink *et al.* [11] in their modeling of ion divergence from laser-irradiated foil targets. With the ablation beam present, a slightly higher maximum electric field strength is required to produce the higher proton energies observed, and hence, for comparison, the calculated divergence as a function of energy for both sheath distributions and both peak electric fields are shown in Figs. 4(a) and 4(b).

The shape and lateral extent of the sheath, and the uniformity and spatial profile of the proton beam, are determined by a number of properties, including the number and distribution of hot electrons generated at the target front surface and accelerated into the foil, and the transport, including refluxing [13] of the hot electrons within the foil. Our findings that, with the ablation beam present, the ion front distribution and the profile of the proton beam changes, suggests that the properties of the hot electron generation at the front surface and/or the lateral spreading of the hot electrons within the foil are modified. The fact that the proton flux and maximum proton energy are consistently observed to increase in the presence of the ablation pulse suggests an increase in absorption of laser energy in the preformed plasma. In addition, in a separate investigation, using a similar ex-

Paper VII

Scaling of proton acceleration driven by petawatt-laser–plasma interactions

L. Robson, P. T. Simpson, P. McKenna, K. W. D. Ledingham, R. J. Clarke, T. McCanny, D. Neely, O. Lundh, F. Lindau, C.-G. Wahlström and M. Zepf.

Nature Physics **3**, 58 (2007).

ARTICLES

Scaling of proton acceleration driven by petawatt-laser–plasma interactions

L. ROBSON[1,2], P. T. SIMPSON[3], R. J. CLARKE[1,4], K. W. D. LEDINGHAM[1,2], F. LINDAU[5], O. LUNDH[5], T. McCANNY[1], P. MORA[6], D. NEELY[4], C.-G. WAHLSTRÖM[5], M. ZEPF[3] AND P. McKENNA[1,4]*

[1]SUPA, Department of Physics, University of Strathclyde, Glasgow G4 0NG, UK
[2]AWE plc, Aldermaston, Reading RG7 4PR, UK
[3]Department of Physics and Astronomy, Queen's University Belfast, Belfast BT7 1NN, UK
[4]CCLRC, Rutherford Appleton Laboratory, Chilton, Didcot, OX14 0QX, UK
[5]Department of Physics, Lund University, PO Box 118, S-221 00 Lund, Sweden
[6]Centre de Physique Théorique, Ecole Polytechnique, CNRS, 91128 Palaiseau, France
*e-mail: p.mckenna@phys.strath.ac.uk

Published online: 10 December 2006; doi:10.1038/nphys476

The possibility of using high-power lasers to generate high-quality beams of energetic ions is attracting large global interest. The prospect of using laser-accelerated protons in medicine attracts particular interest, as these schemes may lead to compact and relatively low-cost sources. Among the challenges remaining before these sources can be used in medicine is to increase the numbers and energies of the ions accelerated. Here, we extend the energy and intensity range over which proton scaling is experimentally investigated, up to 400 J and 6×10^{20} W cm^{-2} respectively, and find a slower proton scaling than previously predicted. With the aid of plasma-expansion simulation tools, our results suggest the importance of time-dependent and multidimensional effects in predicting the maximum proton energy in this ultrahigh-intensity regime. The implications of our new understanding of proton scaling for potential medical applications are discussed.

Multi-MeV ion acceleration from laser-irradiated thin target foils is an area that has received considerable interest over the past few years and has been widely examined both experimentally and theoretically. When an ultraintense ($>10^{18}$ W cm^{-2}) laser pulse is incident onto a thin target foil, protons, arising from hydrogenated contamination layers on the surfaces of the foil, are accelerated owing to electric-field formation[1–3]. Field gradients of the order of MV μm^{-1} are produced owing to charge separation of laser-accelerated hot electrons and the ionized target. Protons with energies up to 60 MeV (refs 1,2) and heavier ions with energies up to ~7 MeV per nucleon[4–6] have been measured. The proton beams have a number of unique properties including high brightness (~10^{12} ions in picosecond-scale bunches) and ultralow emittance[7]. Potential applications of this laser-based source of ions include medical isotope production (for example, for positron emission tomography—PET)[8–10], proton oncology[11,12], proton imaging[13], injection into large-ion accelerators[14], studies relating to nuclear spallation physics[15] and as a fast ignitor beam for laser-driven fusion[16].

Regarding the potential applications to medicine, for example, the idea of using lasers as a future source of high-energy protons for oncology has been discussed by several groups[11,12]. However, the treatment of deep-seated tumours requires proton energies of ~200 MeV, which still requires medium- to large-scale accelerator facilities. To produce intense radioisotope sources for PET ($>10^9$ Bq of ^{11}C or ^{18}F are commonly used per patient dose), a large number of protons with energy ~10 MeV is required. Spencer *et al.*[8] reported the idea of using laser-based protons for PET and recently Ledingham *et al.*[10] measured up to 10^7 Bq of ^{11}C and 10^5 Bq of ^{18}F produced by laser-accelerated protons. Determination of the feasibility of using future high-power lasers as drivers of proton acceleration for application to oncology or PET isotope production requires investigation of the scaling of laser-accelerated proton energies and yields as a function of laser parameters such as intensity, energy and pulse duration.

Several experimental[17,18] and theoretical[19–21] results are reported on the maximum achievable proton energy as a function of various laser pulse parameters. Two recent papers specifically address this in some detail. Oishi *et al.*[22] investigate proton scaling using ultrashort (55 to 400 fs) lasers at intensities ranging from 8.5×10^{17} to 1.1×10^{19} W cm^{-2} and Fuchs *et al.*[23] addresses laser-driven proton scaling using pulses with durations in the range 0.15–10 ps and intensities from 10^{18} to 6×10^{19} W cm^{-2}. Fuchs *et al.*[23] uses the plasma-expansion model described by Mora[24] to predict that a proton energy of 200 MeV could be achieved at an intensity of about 5×10^{20} W cm^{-2} (for a laser pulse of picosecond duration). Other groups have used particle-in-cell simulations to predict, for example, energies up to 380 MeV at a peak laser intensity of 2×10^{21} W cm^{-2} (ref. 12) and 173 MeV at 1.2×10^{21} W cm^{-2} (ref. 25).

Here, we extend experimentally the energy and intensity range over which proton scaling is parametrically investigated, up to 400 J and 6×10^{20} W cm^{-2} respectively. We report on the scaling of the maximum proton energy and the laser-to-proton energy-conversion efficiency in the higher energy and intensity regime, and for laser pulse durations up to 10 ps. We find that our results are not consistent with previous predictions, and in particular the increase of the maximum proton energy is much slower than previously thought. We compare our findings with predictions of the Mora[24] one-dimensional isothermal plasma-expansion model,

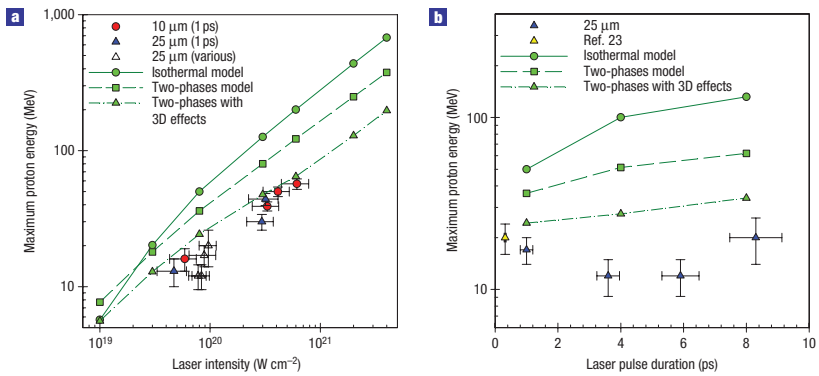

Figure 1 The laser-accelerated maximum proton energy as a function of laser intensity and pulse duration. a, Maximum proton energy detected as a function of laser intensity, by variation of the laser energy and with a constant pulse duration of 1 ps for Al targets with thicknesses of 10 μm (red circles) and 25 μm (blue triangles). The open triangles correspond to laser shots on 25 μm targets for which the energy and pulse duration are both varied. **b**, Maximum proton energy detected as a function of laser pulse duration by variation of the laser energy to maintain a given intensity of 8×10^{19} W cm^{-2}. For comparison, a data point (yellow triangle) at a similar intensity of 6×10^{19} W cm^{-2} from Fuchs *et al.*[23] is included. The green circles (with the solid line) are the predictions of the isothermal plasma-expansion model described by Mora[24]. The green squares (with the dashed line) correspond to results from a revised form of this one-dimensional model, using two phases of electron temperature changes, as described in the main text. The green triangles (with the dash–dot line) correspond to results using the same model with three-dimensional effects mimicked (details in the main text). The error bars on the maximum proton energy arise from combining counting statistics with errors in the deconvolution of the proton energy spectra. The error bars on the laser intensity are a combination of the measurement uncertainty in laser pulse energy and estimated shot-to-shot fluctuations in pulse duration. The error bars on the laser pulse duration are based on estimated shot-to-shot fluctuation.

and introduce revised forms of the model, which involve two phases of electron temperature, and mimic three-dimensional effects, and find that results with these revised models are in better agreement with our experimental results. We discuss the implications of our new understanding of proton scaling for potential applications in medicine.

Two parameters of interest, the maximum proton energy and the laser-to-proton energy-conversion efficiency, are examined as a function of various laser parameters and we present results on the scaling of each in turn. The maximum proton energy, E_{pmax}, measured as a function of laser intensity from 4×10^{19} W cm^{-2} to 6×10^{20} W cm^{-2} is shown in Fig. 1a, for Al targets with thicknesses of 10 μm and 25 μm. In this parameter scan, the pulse duration, τ_{L}, is held constant at 1 ps, and the laser energy, E_{L}, and therefore intensity, I, are varied. Values for E_{pmax} range from ∼10 MeV at 4×10^{19} W cm^{-2} to ∼55 MeV at 6×10^{20} W cm^{-2}. A simple power scaling of the form $E_{\mathrm{pmax}} = a \times I^{b}$ with $b = 0.5 \pm 0.1$ provides a good fit to the complete data set (individual fits for 10 μm and 25 μm targets are obtained with $b = 0.5$ and 0.6 respectively). This indicates that the maximum proton energy is proportional to the fast-electron temperature, which scales as the ponderomotive potential ($\propto (I\lambda^2)^{1/2}$) (ref. 26). The result is in very good agreement with proton energy measurements reported by Clark *et al.*[17] and Allen *et al.*[18] at intensities between 10^{18} W cm^{-2} and 10^{20} W cm^{-2}.

In a different parameter scan, the laser intensity is held constant and the pulse duration and energy are varied. The maximum proton energy as a function of τ_{L} in the range 1–8 ps, for constant $I = (8 \pm 1) \times 10^{19}$ W cm^{-2} and with a corresponding variation in E_{L} up to a maximum of 400 J, is shown in Fig. 1b. E_{pmax} is observed to change only from 19 MeV at 1 ps to 24 MeV at 8 ps.

Figure 2 shows the conversion efficiency of the laser energy to proton energy for various laser parameters. The conversion efficiency is calculated by measuring the total energy in the proton beam, integrating from 4 MeV (lower energy threshold limit of the diagnostic) to E_{pmax}, and dividing by the laser pulse energy. Measured conversion efficiencies as a function of laser energy (and therefore intensity) at constant pulse duration (1 ps) are shown in Fig. 2a. Efficiencies of between 0.2% and 6.0% are observed and compare well with values previously reported for low repetition rate, ultraintense laser systems[6,27,28]. We measure a linear dependence on the laser energy. The thinner, 10 μm, target shows higher energy-conversion efficiencies at all laser energies, in agreement with previous studies[22,23]. Figure 2b shows the variation in efficiency as a function of pulse duration—for the parameter scan in which the pulse energy is varied to maintain a fixed intensity of $(8 \pm 1) \times 10^{19}$ W cm^{-2}. The proton conversion efficiency shows only a weak dependence on pulse length, increasing from 0.7% at 1 ps to 1.5% at 8 ps. Although the shots are nominally at the same intensity, there is a variation of 22% (not represented in the figure), which may account for the dip at 3.6 ps.

At the lower end of our intensity range our measurements are in good agreement with results reported by Fuchs *et al.*[23]. In both cases, the maximum proton energy is ∼20 MeV for an intensity of around 6×10^{19} W cm^{-2} to 8×10^{19} W cm^{-2}. However, we find that the scaling relations reported by Fuchs *et al.*[23], for the maximum proton energy and conversion efficiency, as a function of laser intensity (up to 6×10^{19} W cm^{-2}) and pulse duration, are not valid for the higher intensity regime of the present measurements. For example, Fuchs *et al.*[23] report an increase from 1.5 MeV to 6 MeV when increasing the pulse duration by only a factor of 2, from 150 to 300 fs (at intensity 10^{19} W cm^{-2}). Energy increases of this magnitude are not observed as a function of pulse duration at the higher intensities and longer τ_{L} of the present study.

The experimental measurements reported by Fuchs *et al.*[23] are in good agreement with calculations using a one-dimensional isothermal plasma-expansion model described by Mora (2003)[24].

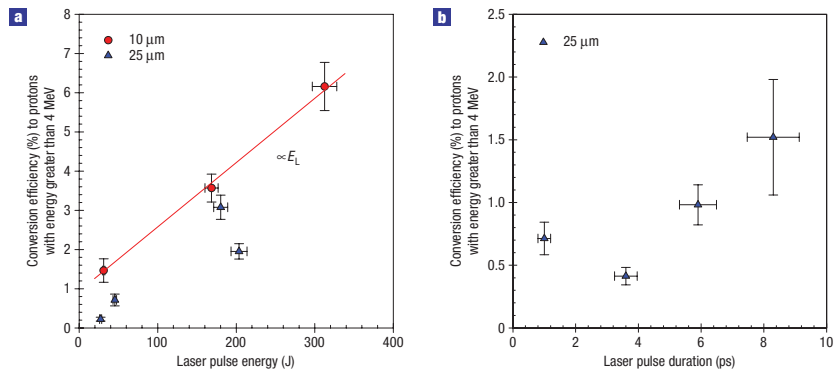

Figure 2 The laser-to-proton energy-conversion efficiency as a function of laser energy and pulse duration. a,**b**, Energy-conversion efficiency (as a percentage) from laser pulse to protons with energies greater than 4 MeV, as a function of laser energy for constant pulse duration of 1 ps (**a**) and laser pulse duration by variation of laser energy to maintain a given intensity of 8×10^{19} W cm^{-2} (**b**). A linear relationship between conversion efficiency and laser energy is observed, with a higher efficiency for the thinner target. The error bars on the laser-to-proton energy-conversion efficiency are a combination of the error in the measurement of laser pulse energy and uncertainties in the proton energy and numbers arising from the deconvolution of the proton energy spectra. The error bars on laser energy represent the uncertainty in the energy measurement. The error bars on the laser pulse duration are based on estimated shot-to-shot fluctuation.

We carry out similar calculations using this model to determine the predicted scaling in the higher intensity regime explored experimentally in the present study, and find that this model greatly overestimates the maximum proton energies, as shown in Fig. 1.

Next, we used a revised form of the Mora (2003)[24] model, where the isothermal assumption is replaced by a more realistic temporal variation of the hot-electron temperature driving the ion acceleration. More specifically, we use a two-phases model, where the electron temperature first rises linearly on the pulse duration timescale, and then decreases adiabatically as described by Mora (2005)[29]. The effect of the beginning of the first phase is to produce a finite density gradient at the back of the foil, which reduces the efficiency of the acceleration during the periods corresponding to the peak of the electron temperature and to the second phase[30]. The maximum proton energies calculated with this one-dimensional two-phases model are also shown in Fig. 1. It is found that although the maximum energies are reduced with respect to the predictions of the isothermal model, they are still about a factor of three higher than the measured maximum proton energies.

In addition, to mimic some three-dimensional effects, such as the radial expansion of the hot-electron population, which are not normally included in the model, we stop the acceleration in the second ('cooling') phase when the plasma longitudinal expansion becomes equal to twice the calculated initial lateral extension of the plasma sheath at the back of the target. We find that this somewhat crude model gives a better agreement between the maximum proton energies predicted and the experimental results, as shown in Fig. 1.

Although the Mora (2003) isothermal expansion model[24] provides a good fit to the maximum proton energies for intensities up to 6×10^{19} W cm^{-2} as observed and reported by Fuchs *et al.*[23], for intensities up to an order of magnitude higher our simulations suggest that a more realistic temperature-varying model is required and that multidimensional effects become important. Figure 1a shows that the predictions using the isothermal model and the two-phases model converge at lower intensities, around 10^{19} Wcm^{-2}. In this intensity regime, the plasma expansion is quasi-one-dimensional during the pulse duration. With increasing intensity, multidimensional effects become increasingly more important because the longitudinal excursion of the fast ions at the back of the foil becomes of the order of the transverse plasma size in a shorter time.

We are also aware of a recent publication by Schreiber *et al.*[20] describing an analytical model and predictions that agree partially with our data. In this model, for a fixed laser power (or intensity for constant focal spot size), increasing the pulse energy and duration do not result in an increase in ion energy once an optimum pulse duration (predicted by the model to be between 30 and 100 fs for the energy range of the present study) is exceeded. The same model also predicts the scaling of E_{pmax} with $I^{0.5}$ as observed in Fig. 1a. However, similar to the simple one-dimensional isothermal expansion model by Mora[24], the proton energies predicted by this model are considerably higher than those measured.

Further experimental investigation to separate the geometrical effects of the laser spot size from the intensity, and to elucidate the role of electron acceleration, will enable deeper understanding of the physical mechanisms affecting the observed scaling laws for the sheath acceleration scheme. In addition, two other predicted acceleration mechanisms at higher intensities, laser-driven shock acceleration[31] above 10^{21} W cm^{-2} and acceleration by radiation pressure[32] above 10^{23} W cm^{-2}, need to be investigated in future studies at higher laser intensities.

Exploring the predictions of the revised two-phases model, with multidimensional effects, at even higher intensities we find that it predicts that 200 MeV protons, required for oncology, should be achievable with 1 ps laser pulses focused to 4×10^{21} Wcm^{-2} (with a 25 μm Al target). Although this is much higher than previously predicted using the isothermal model[23], it is close to the intensity requirements predicted in some particle-in-cell simulations (see, for example, refs 21,25). We note however that this corresponds to the conditions required to reach 200 MeV and that even higher intensities are required to produce the number of 200 MeV protons required for oncology.

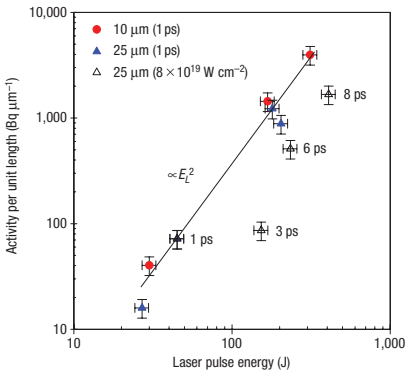

Figure 3 Proton-induced activation scaling with laser parameters. Measured ^{63}Zn activity (per unit length of activation foil) in the first Cu foil in the diagnostic stack as a function of laser energy for a constant pulse duration of 1 ps (filled symbols) and for a constant laser intensity of 8×10^{19} W cm^{-2} (open symbols). The vertical error bars are a combination of counting statistics and uncertainty in the detector calibration efficiency. The horizontal error bars represent the uncertainty in the laser pulse energy measurement.

Proton-induced nuclear activation of stacked Cu foils is used to measure the proton energy spectrum. The scaling of the measured ^{63}Cu(p,n)^{63}Zn reactions as a function of laser parameters is of interest for the potential application of laser-accelerated protons to radioisotope production. The ^{63}Zn activity (per unit length) in the first Cu foil in the diagnostic stack is plotted in Fig. 3 revealing a power dependence on laser energy, with an exponent of 2 (for fixed τ_L). A similar scaling of activity with respect to laser energy is inferred when τ_L is varied to produce a constant laser intensity. This is unsurprising as the total energy in the proton beam scales as E_L^2—the energy-conversion efficiency (total proton beam energy normalized to laser pulse energy) scales linearly with E_L, Fig. 2a. We note that previous measurements of the scaling of ^{11}B(p,n)^{11}C reactions with respect to laser pulse energy can be fitted with a power law with an exponent of ∼3 (ref. 10). The cross-section for this reaction is peaked at the lower energy of ∼6 MeV compared with ∼13 MeV for the ^{63}Cu(p,n)^{63}Zn reaction measured in this work. Therefore, the scaling of the number of ^{11}B(p,n)^{11}C reactions is more sensitive to increases in the number of protons in the low-energy region of the spectrum. The present results further highlight the importance of laser pulse energy for laser-driven radioisotope production.

METHODS

The Vulcan petawatt laser at the Rutherford Appleton Laboratory, UK, is used in this study. It delivers pulses of wavelength, λ, equal to 1.054 μm, *p*-polarized and incident at an angle of 45° onto the target foil. The pulse energy delivered to the target is varied between 20 and 400 J and the pulse duration is varied, by altering the grating separation in the stretcher, from 1 to 8 ps. With an $f/3$ off-axis parabolic mirror focusing to a 6-μm-diameter spot size at full-width at half-maximum (assumed to remain constant for all shots), intensities in the range 4×10^{19} to 6×10^{20} W cm^{-2} are produced. The level of amplified spontaneous emission, ASE, (background light that is amplified owing to the gain in the laser-amplifying crystals) is measured, with a fast photodiode and oscilloscope, to be 10^{-7} of the peak pulse intensity at a few nanoseconds before the peak of the main pulse, and 10^{-6} of the peak pulse intensity at a few picoseconds, as measured with a third-order autocorrelator. The laser-irradiated targets are 8 mm × 4 mm pieces of aluminium, of two thicknesses, 10 μm and 25 μm. ASE-induced effects have previously been shown to affect the spatial distribution and reduce the maximum energy of ions accelerated from thin targets[33,34]. Here, the highest proton energies are measured with the thinner target, demonstrating that the laser contrast ratio is sufficient to prevent ASE-induced effects from adversely affecting the target.

Nuclear activation of Cu is used as the main diagnostic of multi-MeV proton acceleration. Stacks of Cu pieces, each 5 × 5 cm and of varying thickness (25 to 1,000 μm), are positioned 5 cm from the rear of the target and centred on the target normal axis. The lower energy threshold is ∼4 MeV, as defined by the threshold of the ^{63}Cu(p,n)^{63}Zn nuclear reaction. The upper energy threshold is defined by the stack thickness and exceeds 80 MeV. The measured activity of ^{63}Zn in each Cu foil is convoluted with the energy-dependent cross-section and stopping power of protons in Cu to generate the proton energy spectrum for each laser pulse condition[8]. The ^{63}Zn isotope decays with a characteristic half-life of 38.1 min, predominantly by positron emission, and the 511 keV gamma-rays signature of positron annihilation is measured using two 3 inch × 3 inch NaI–photomultiplier tube counters operated in coincidence. Nuclear activation as a diagnostic enables the energy distribution to be measured over the entire proton beam, similar to the use of stacked dosimetry film as a proton diagnostic[23]. We define the maximum proton energy, E_{pmax}, as the energy corresponding to the lower number threshold, which is 10^6 protons MeV^{-1} sr^{-1}. In contrast, a Thomson parabola ion spectrometer with a CR-39 detector, commonly used in experiments of this type, enables single-particle detection, but is limited to sampling a small solid angle of the beam, typically $<10^{-7}$ sr, resulting in a detection limit typically $>10^7$ protons MeV^{-1} sr^{-1}.

Received 11 August 2006; accepted 1 November 2006; published 10 December 2006.

References

1. Clark, E. L. *et al.* Measurements of energetic proton transport through magnetized plasma from intense laser interactions with solids. *Phys. Rev. Lett.* **84**, 670–673 (2000).
2. Snavely, R. A. *et al.* Intense high-energy proton beams from petawatt-laser irradiation of solids. *Phys. Rev. Lett.* **85**, 2945–2948 (2000).
3. Wilks, S. C. *et al.* Energetic proton generation in ultra-intense laser-solid interactions. *Phys. Plasmas* **8**, 542–549 (2001).
4. Hegelich, M. *et al.* MeV ion jets from short-pulse-laser interaction with thin foils. *Phys. Rev. Lett.* **89**, 085002 (2002).
5. McKenna, P. *et al.* Demonstration of fusion-evaporation and direct-interaction nuclear reactions using high intensity laser-plasma-accelerated ion beams. *Phys. Rev. Lett.* **91**, 075006 (2003).
6. McKenna, P. *et al.* Proton and heavier ion acceleration in ultrahigh intensity laser-interactions with heated target foils. *Phys. Rev. E* **70**, 036405 (2004).
7. Cowan, T. *et al.* Ultralow emittance, multi-MeV proton beams from a laser virtual-cathode plasma accelerator. *Phys. Rev. Lett.* **92**, 204801 (2004).
8. Spencer, I. *et al.* Laser generation of proton beams for the production of short-lived positron emitting radioisotopes. *Nucl. Instrum. Methods Phys. Res. B* **183**, 449–458 (2001).
9. Fritzler, S. *et al.* Proton beams generated with high-intensity lasers: Applications to PET isotope production. *Appl. Phys. Lett.* **83**, 3039–3041 (2003).
10. Ledingham, K. W. D. *et al.* High power laser production of short-lived isotopes for positron emission tomography. *J. Phys. D* **37**, 2341–2345 (2004).
11. Bulanov, S. V. *et al.* Oncological hadrontherapy with laser ion accelerators. *Phys. Lett. A* **299**, 240–247 (2002).
12. Malka, V. *et al.* Practicality of proton therapy using compact laser systems. *Med. Phys.* **31**, 1587–1592 (2004).
13. Borghesi, M. *et al.* Electric field detection in laser-plasma interaction experiments via the proton imaging technique. *Phys. Plasmas* **9**, 2214–2220 (2002).
14. Krushelnick, K. *et al.* Ultrahigh-intensity laser-produced plasmas as a compact heavy ion injection source. *IEEE Trans. Plasma Sci.* **28**, 1184–1189 (2000).
15. McKenna, P. *et al.* Broad energy spectrum of laser-accelerated protons for spallation-related physics. *Phys. Rev. Lett.* **94**, 084801 (2005).
16. Roth, M. *et al.* Fast ignition by intense laser-accelerated proton beams. *Phys. Rev. Lett.* **86**, 436–439 (2001).
17. Clark, E. L. *et al.* Energetic heavy-ion and proton generation from ultra-intense laser-plasma interactions with solids. *Phys. Rev. Lett.* **85**, 1654–1657 (2000).
18. Allen, M. *et al.* Proton spectra from ultraintense laser-plasma interaction with thin foils: Experiments, theory, and simulation. *Phys. Plasmas* **10**, 3283–3289 (2003).
19. Fourkal, E., Velchev, I. & Ma, C.-M. Coulomb explosion effect and the maximum energy of protons accelerated by high-power lasers. *Phys. Rev. E* **71**, 036412 (2005).
20. Schreiber, J. *et al.* Analytical model for ion acceleration by high-intensity laser pulses. *Phys. Rev. Lett.* **97**, 045005 (2006).
21. Esirkepov, T. Z., Yamagiwa, M. & Tajima, T. Laser ion-acceleration scaling laws seen in multiparametric particle-in-cell simulations. *Phys. Rev. Lett.* **96**, 105001 (2006).
22. Oishi, Y. *et al.* Dependence on laser intensity and pulse duration in proton acceleration by irradiation of ultrashort laser pulses on a Cu foil target. *Phys. Plasmas* **12**, 073102 (2005).
23. Fuchs, J. *et al.* Laser-driven proton acceleration: scaling laws and new paths towards energy increase. *Nature Phys.* **2**, 48–54 (2006).
24. Mora, P. Plasma expansion into a vacuum. *Phys. Rev. Lett.* **90**, 185002 (2003).
25. Schwoerer, H. *et al.* Laser-plasma acceleration of quasi-monoenergetic protons with microstructured targets. *Nature* **439**, 445–448 (2006).
26. Wilks, S. C. *et al.* Absorption of ultra-intense laser pulses. *Phys. Rev. Lett.* **69**, 1383–1386 (1992).
27. Zepf, M. *et al.* Proton acceleration from high-intensity laser interactions with thin foil targets. *Phys. Rev. Lett.* **90**, 064801 (2003).
28. Roth, M. *et al.* Energetic ions generated by laser pulses: A detailed study on target properties. *Phys. Rev. Special Topics-Accelerators and Beams* **5**, 061301 (2002).

29. Mora, P. Thin-foil expansion into a vacuum. *Phys. Rev. E* **72**, 056401 (2005).
30. Grismayer, T. & Mora, P. Influence of a finite initial ion density gradient on plasma expansion into a vacuum. *Phys. Plasmas* **13**, 032103 (2006).
31. Silva, L. O. *et al.* Proton shock acceleration in laser-plasma interactions. *Phys. Rev. Lett.* **92**, 015002 (2004).
32. Esirkepov, T. Z. *et al.* Highly efficient relativistic-ion generation in the laser-piston regime. *Phys. Rev. Lett.* **92**, 175003 (2004).
33. Lindau, F. *et al.* Laser-accelerated protons with energy dependent beam direction. *Phys. Rev. Lett.* **95**, 175002 (2005).
34. Kaluza, M. *et al.* Influence of the laser prepulse on proton acceleration in thin-foil experiments. *Phys. Rev. Lett.* **93**, 045003 (2004).

Acknowledgements

The authors would like to acknowledge the scientific and technical expertise of the personnel at the Vulcan High Power Laser Facility. O.L. and F.L. acknowledge support from the COST programme. M.Z. holds a Royal Society Wolfson Research Merit Award.
Correspondence and requests for materials should be addressed to P.M.

Competing financial interests

The authors declare that they have no competing financial interests.

Paper VIII

Detection of short lived radioisotopes as a fast diagnostic for intense laser–solid interactions

R. J. Clarke, K. W. D Ledingham, P. McKenna, L. Robson, T. McCanny, D. Neely, F. Lindau, O. Lundh, C.-G. Wahlström, P. T. Simpson and M. Zepf.

Applied Physics Letters **89**, 141117 (2006).

APPLIED PHYSICS LETTERS **89**, 141117 (2006)

Detection of short lived radioisotopes as a fast diagnostic for intense laser-solid interactions

R. J. Clarke,[a),b)] K. W. D. Ledingham,[c)] P. McKenna,[a)] L. Robson,[c)] and T. McCanny
SUPA, Department of Physics, University of Strathclyde, Glasgow G4 0NG, Scotland, United Kingdom

D. Neely
CCLRC Rutherford Appleton Laboratory, Chilton, Didcot, Oxfordshire OX11 OQX, United Kingdom

O. Lundh, F. Lindau, and C.-G. Wahlström
Department of Physics, Lund Institute of Technology, P.O. Box 118, S-221 00 Lund, Sweden

P. T. Simpson and M. Zepf
Department of Physics and Astronomy, Queens University Belfast, Belfast BT7 1NN, Northern Ireland, United Kingdom

(Received 3 April 2006; accepted 22 August 2006; published online 3 October 2006)

As a diagnostic of high-intensity laser interactions ($>10^{19}$ W cm^{-2}), the detection of radioactive isotopes is regularly used for the characterization of proton, neutron, ion, and photon beams. This involves sample removal from the interaction chamber and time consuming post shot analysis using NaI coincidence counting or Ge detectors. This letter describes the use of *in situ* detectors to measure laser-driven (p,n) reactions in ^{27}Al as an almost real-time diagnostic for proton acceleration. The produced ^{27}Si isotope decays with a 4.16 s half-life by the predominantly $\beta+$ emission, producing a strong 511 keV annihilation peak. © *2006 American Institute of Physics*.
[DOI: 10.1063/1.2358940]

The diagnostics of fast ions from intense laser-solid interactions are historically Thomson parabolas[1–3] or stacks of radiochromic film and nuclear track detectors interdispersed with energy filtering foils.[4,5] However, recently it has been shown that the production of short lived isotopes can be used as an efficient diagnostic for high-intensity laser interactions in the relativistic regime above 10^{19} W cm^{-2} where laser produced nuclear reactions occur.[6–8] This is particularly useful as a diagnostic for gamma and proton production.[4,5,9–11] For example, most (γ,n) reactions have typical thresholds of ~10 MeV, and for multiple (γ,mn) reactions, the production of each successive neutron typically requires an extra 10 MeV. Clearly, a $(\gamma,7n)$ reaction can diagnose photon energies >70 MeV. Giant resonance (γ,n) cross sections increase in value with increasing A number, and are typically 50–100 mb in the mid-Z region. (p,n) reactions are very useful for the production of radioisotopes and typically have lower thresholds, as low as 2–3 MeV, and cross sections which can exceed hundreds of millibarns. Isotopes commonly used for laser-plasma diagnostics are ^{63}Cu (p,n) ^{63}Zn ($t_{1/2}$=38 min) and ^{63}Cu (γ,n) ^{62}Cu ($t_{1/2}$=10 min). The samples are removed from the interaction chamber and analyzed off line using techniques such as coincidence counting, hence the choice of a half-life within the 10–60 min region. The detection of half-lives of a few minutes is precluded as the time for access into the interaction vessels after a shot and vacuum let-up typically exceeds 10 min. Fast pneumatic transfer systems, commonly used in conventional reactors and accelerators, can extract samples within seconds but have not yet been adopted in a laser facility.

This letter describes the demonstration of the production and subsequent detection of the short lived ^{27}Si isotope using a (p,n) reaction in high purity ^{27}Al as a method to diagnose energetic protons accelerated in a laser plasma. The analyzing detector is housed within the interaction chamber, negating the need to remove the sample. ^{27}Si has a 4.16 s half-life and with a maximum ^{27}Al (p,n) ^{27}Si cross section at ~8 MeV; this process becomes an almost real-time diagnostic for the detection of high-energy protons. The half-life needs to be short to enable measurements soon after the shot, yet long enough for the detector to recover from the initial laser-target interaction, which produces a large gamma flash.

The experiment was performed on the Vulcan petawatt laser at Rutherford Appleton Laboratory.[12] The experiment used an $f/3$ parabolic focussing optic and plasma mirrors to enhance the laser contrast. On-target laser conditions were ~200 J in ~1 ps, producing an on-target intensity of ~1×10^{20} W cm^{-2}. The laser was incident on 20 μm thick gold targets at 40° to the target normal. The 1 mm thick aluminum sample (catcher) was placed at approximately 20 cm from target, covered by a 500 μm thick aluminum plate to stop activated target debris from being deposited on the catcher—highlighted as a problem during preliminary shots. To penetrate this debris shield, the proton energy must exceed 9 MeV. Coupled with the energy required to exceed the threshold value for the ^{27}Al (p,n) ^{27}Si reaction, the system responded to a minimum proton energy of 11 MeV.

The layout is shown in Fig. 1. The catcher was held by an electromagnetic solenoid which when released allowed it to drop via guide rails to a lead shielded NaI detector lying ~30 cm below the target plane. The 3 in. diameter Scionix 76B76/3 NaI detector with VD141-E1 base was biased with 800 V. The signal from the detector was routed through an ORTEC 675 spectroscopy amplifier with 0.5 μs integration and differentiation time constants. A Canberra Multiport 2

[a)]Also at: CCLRC Rutherford Appleton Laboratory, Chilton, Didcot, Oxfordshire OX11 OQX, UK.
[b)]Electronic mail: r.j.clarke@rl.ac.uk
[c)]Also at: AWE, Aldermaston, Reading, RG7 4PR, UK.

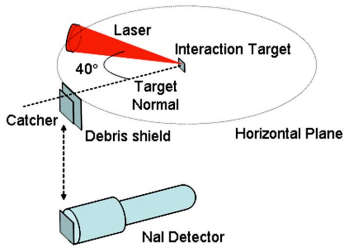

FIG. 1. (Color online) Detector and sample setup. The NaI detector is shown without the surrounding shielding for clarity.

multichannel analyzer (MCA), operating in multiscale mode, was used for data acquisition, with 10 ms dwell time per channel. The MCA has a dead time of 2 μs, matching the signal saturation observed in the experiment. Calibration of the detector using a ^{22}Na source gave a detector efficiency of 30%. Lead shielding surrounding the detector was used to reduce the effect of the large picoseconds duration gamma flash produced by MeV electrons in the target, commonly observed during high-intensity interactions. Even with this shielding in place, spectra show a gamma flash saturating the detector ($\sim$1000 counts) with a recovery time of $\sim$0.5 s.

Figure 2 shows the data from an unoptimized shot. The ^{27}Si component is clearly visible in the data, and the insets show the 511 keV emission line from β+ decay (top), along with the recovery of the detector before the sample was dropped (bottom). Successful shots were also performed by remotely viewing the catcher over a small solid angle.

Typical activities observed during laser-driven medical isotope production experiments[13] show the generation of $\sim 10^{10}$ radioactive nuclei from (p,n) reactions on ^{11}B. The generated isotope of ^{11}C, with a half-life of $\sim$20 min, produces activities in the order of 10^6 Bq at $t=0$. The ^{27}Si, generated through the ^{27}Al (p,n) reaction, has a half-life of 4.16 s and the difference in half-life is much greater than the difference in cross section. This results in very large counting rates and requires heavy filtering between sample and detector to reduce the detector dead time and saturation of the photomultiplier tube (PMT). A thinner sample could also be used to limit the activity, but for these measurements a 1 cm thick lead filter was used between the catcher and detector, reducing the signal by a factor of 6. Figure 3 shows

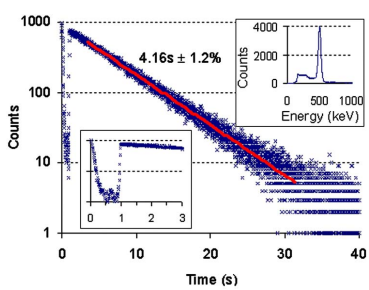

FIG. 2. (Color online) Data and fit to ^{27}Si decay. Top inset—spectrum showing 511 keV γ ray from β+ emission. Bottom inset—response to prompt γ flash and recovery before the catcher is dropped. Detector dead time has been compensated.

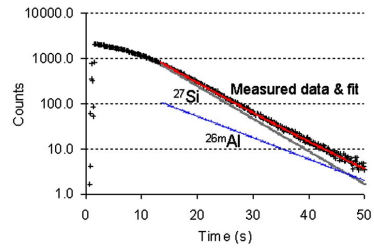

FIG. 3. (Color online) Saturated data showing ^{27}Si (4.16 s) and ^{26m}Al (6.34 s) components with combined fit. Counts at $t=0$ are calculated at $\sim$6500 (^{27}Si) and $\sim$450 (^{26m}Al) using a 10 ms dwell time. Detector dead time has been compensated.

data from the same experimental arrangement but under more optimal proton production conditions, resulting in the saturation of the PMT. With such high activity, it is possible to identify a second active component, matching the 6.34 s half-life of ^{26m}Al. This can be generated through $(p,p+n)$, (p,d), (γ,n), or $(n,2n)$ reactions in the aluminum catcher. It is likely that the $(p,p+n)$ or (p,d) reaction dominates this production as the high-energy neutron and gamma yields should be relatively low for the target type used. The cross sections for reactions are shown in Fig. 4, though no available data were found for the $(p,p+n)$ or (p,d) reactions. Calculations indicate a reaction threshold of 11.23 MeV for the (p,d) reaction and 13.54 MeV for the $(p,p+n)$ reaction, hence the (p,d) reaction is more likely if the reactions have similar cross sections. The observation of both the ^{27}Si and ^{26m}Al components may in the future allow rapid temperature measurements to be performed using the two different energies to fit an ion temperature[14] assuming a Boltzmann-like energy distribution. This is an important aspect of the future work, as the use of the (p,n) generated ^{27}Si in a single catcher will only derive proton numbers at a single energy, as selected by the thickness of the debris filter. The diagnostic will therefore not derive a proton spectral measurement similar to that achieved through detector stacks.[4,5]

The presented method opens up a new approach for the diagnosis of proton, ion, photon, and neutrons on a much faster time scale than at present. Though this is extremely useful for low repetition, high-intensity lasers, it opens up the possibility for experiments on future high repetition facilities of typically 10 Hz where shot rates will be limited by the time taken to analyze diagnostic data. For these types of facilities, half-lives in the region of 10–100 ms will be re-

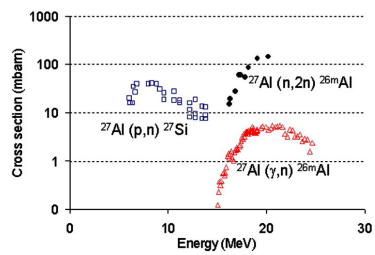

FIG. 4. (Color online) Cross section data for ^{27}Al (p,n) ^{27}Si (Ref. 16), ^{27}Al $(n,2n)$ ^{26m}Al (Ref. 17), and ^{27}Al (γ,n) ^{26m}Al (Ref. 18).

TABLE I. Examples of short half-life reactions (Ref. 19).

Reaction	Half-life	Threshold (MeV)
^{23}Na (p,n) ^{23}Mg	11.32 s	5.05
^{27}Al (p,n) ^{27}Si	4.16 s	5.80
^{39}K (p,n) ^{39}Ca	860 ms	7.50
^{40}Ca (γ,n) ^{39}Ca	860 ms	15.64
^{28}Si (p,n) ^{28}P	270 ms	15.66
^{40}Ca (p,n) ^{40}Sc	182 ms	15.49

quired. Possible examples are listed in Table I. Reactions on this time scale will also need to make use of much faster amplifiers and detectors with recovery times below tens of milliseconds to reduce the observed dead times caused by the built-in electronics. Two techniques have been demonstrated for the detection of short lived isotopes—utilizing a moveable catcher or by remote viewing of a stationary catcher. Both principles have been achieved with the high activities observed on aluminum, and even higher activities are expected with shorter half-life isotopes.

Finally, the use of short half-life radioisotopes to generate a spatially resolvable system for particle detection is suggested to enable real-time access to the acquired data. The generated radioisotopes in the catcher can be imaged via contact radiography, providing a spatially resolved detector. This requires the use of newly developed camera technology such as pixelated CdTe or Ge detectors capable of detecting 511 keV $\beta+$ annihilation gamma rays emitted from short half-life radioisotopes. The advantage over scintillators is that the prompt gamma flash does not need to be gated out as the half life of activated nuclei in the catcher is much larger than the evolution of the gamma flash. The catcher material can also be optimized to appropriately match the half-life to the integration period of the camera. If the signal is recorded in real time, a spatially resolved image will form after the initial gamma flash has subsided. The number of generated radioisotopes can also be derived from the decay of the recorded images. Additionally, a saturated signal will become resolvable as the catcher decays, making the dynamic range extremely large. This technique could be a route towards instantaneously accessing laser-plasma proton radiography data,[15] crucial for high repetition laser facilities, though limitations generated by the observed gamma flash will also have to be addressed. This potential issue may not, however, be a serious threat, as high repetition facilities typically use low energies with ultrashort pulses, seriously reducing the gamma flash in comparison to the data acquired on the Vulcan facility with energies exceeding 200 J on target. The associated electromagnetic pulse (EMP) issues for any charge-coupled device system will also be reduced, which have caused some problems on ultrahigh-intensity laser systems such as Vulcan when used close to target. In these situations, true EMP shielding for the electronics and gating of the detector may need to be employed, possibly reducing the capable repetition rates.

The authors would like to acknowledge the scientific and technical expertise at the Vulcan High Power Laser facility. One of the authors (K.W.D.L.) acknowledges discussions with F. Hannachi and J. F. Chemin on fast nuclear diagnostics. Another author (P.McK.) acknowledges the award of a Royal Society of Edinburgh Personal Fellowship. One of the authors (M.Z.) is a holder of the Royal Society Wolfson Merit Award.

[1] J. J. Thomson, Philos. Mag. **21**, 225 (1911).
[2] S. Sakabe, T. Mochizuki, T. Yamanaka, and C. Yamanaka, Rev. Sci. Instrum. **51**, 1314 (1980).
[3] E. L. Clark, K. Krushelnick, M. Zepf, F. N. Beg, M. Tatarakis, A. Machacek, M. I. K. Santala, I. Watts, P. A. Norreys, and A. E. Dangor, Phys. Rev. Lett. **85**, 1654 (2000).
[4] M. Zepf, E. L. Clark, K. Krushelnick, F. N. Beg, C. Escoda, A. E. Dangor, M. I. K. Santala, M. Tatarakis, I. F. Watts, P. A. Norreys, R. J. Clarke, J. R. Davies, M. A. Sinclair, R. D. Edwards, T. J. Goldsack, I. Spencer, and K. W. D. Ledingham, Phys. Plasmas **8**, 2323 (2001).
[5] I. Spencer, K. W. D. Ledingham, R. P. Singal, T. McCanney, P. McKenna, E. L. Clark, K. Krushelnick, M. Zepf, F. N. Beg, M. Tatarakis, A. E. Dangor, P. A. Norreys, R. J. Clarke, R. M. Allott, and I. N. Ross, Nucl. Instrum. Methods Phys. Res. B **183**, 449 (2001).
[6] K. W. D. Ledingham, P. McKenna, and R. P. Singhal, Science **300**, 1107 (2003).
[7] P. McKenna, K. W. D. Ledingham, T. McCanny, R. P. Singhal, I. Spencer, M. I. K. Santala, F. N. Beg, K. Krushelnick, M. Tatarakis, M. S. Wei, E. L. Clark, R. J. Clarke, K. L. Lancaster, P. A. Norreys, K. Spohr, R. Chapman, and M. Zepf, Phys. Rev. Lett. **91**, 075006 (2003).
[8] F. Amiranoff, Meas. Sci. Technol. **12**, 1795 (2001).
[9] P. McKenna, K. W. D. Ledingham, S. Shimizu, J. M. Yang, L. Robson, T. McCanny, J. Galy, J. Magill, R. J. Clarke, D. Neely, P. A. Norreys, R. P. Singhal, K. Krushelnick, and M. S. Wei, Phys. Rev. Lett. **94**, 084801 (2005).
[10] S. P. Hatchett, C. G. Brown, T. E. Cowen, E. A. Henry, J. S. Jonson, M. H. Key, J. A. Koch, A. B. Langdon, B. F. Lasinsky, R. W. Lee, A. J. Mackinnon, D. M. Pennington, M. D. Perry, T. W. Philips, M. Roth, T. C. Sangster, M. S. Singh, R. A. Snavely, M. A. Stoyer, S. C. Wilks, and K. Yasuike, Phys. Plasmas **7**, 2076 (2000).
[11] P. A. Norreys, M. Santala, E. Clark, M. Zepf, I. Watts, F. N. Beg, K. Krushelnick, M. Tatarakis, A. E. Dangor, X. Fang, P. Graham, T. McCanny, R. P. Singhal, K. W. D. Ledingham, A. Creswell, D. C. W. Sanderson, J. Magill, A. Machacek, J. S. Wark, R. Allott, B. Kennedy, and D. Neely, Phys. Plasmas **6**, 2150 (1999).
[12] C. N. Danson, P. A. Brummitt, R. J. Clarke, J. L. Collier, B. Fell, A. J. Frackiewicz, S. Hancock, S. Hawkes, C. Hernandez-Gomez, P. Holligan, M. H. R. Hutchinson, A. Kidd, W. J. Lester, I. O. Musgrave, D. Neely, D. R. Neville, P. A. Norreys, D. A. Pepler, C. J. Reason, W. Shaikh, T. B. Winstone, R. W. W. Wyatt, and B. E. Wyborn, Nucl. Fusion **44**, S239 (2004).
[13] K. W. D. Ledingham, P. McKenna, T. McCanny, S. Shimizu, J. M. Yang, L. Robson, J. Zweit, J. M. Gillies, J. Bailey, G. N. Chimon, R. J. Clarke, D. Neely, P. A. Norreys, J. L. Collier, R. P. Singhal, M. S. Wei, S. P. D. Mangles, P. Nilson, K. Krushelnick, and M. Zepf, J. Phys. D **37**, 2341 (2004).
[14] J. M. Yang, P. McKenna, K. W. D. Ledingham, T. McCanney, L. Robson, S. Shimizu, R. P. Singhal, M. S. Wei, K. Krushelnick, R. J. Clarke, D. Neely, and P. A. Norreys, J. Appl. Phys. **96**, 6912 (2004).
[15] A. J. Mackinnon, P. K. Patel, R. P. Town, M. J. Edwards, T. Phillips, S. C. Lerner, D. W. Price, D. Hicks, M. H. Key, S. Hatchett, S. C. Wilks, M. Borghesi, L. Romagnani, S. Kar, T. Toncian, G. Pretzler, O. Willi, M. Koenig, E. Martinolli, S. Lepape, A. Benuzzi-Mounaix, P. Audebert, J. C. Gauthier, J. King, R. Snavely, R. R. Freeman, and T. Boehlly, Rev. Sci. Instrum. **75**, 3531 (2004).
[16] J. D. Anderson, S. D. Bloom, C. Wong, W. F. Hornyak, and V. A. Madsen, Phys. Rev. **177**, 1416 (1969).
[17] G. S. Mani, G. J. Mccallum, and A. T. G. Ferguson, Nucl. Phys. **19**, 535 (1960).
[18] M. N. Thompson, J. M. Taylor, B. M. Spicer, and J. E. E. Baglin, Nucl. Phys. **64**, 486 (1965).
[19] QCALC, *Q*-value calculator, NNDC, Brookhaven National Laboratory.

Paper IX

Low- and medium-mass ion acceleration driven by petawatt laser plasma interactions

P. McKenna, F. Lindau, O. Lundh, D. C. Carroll, R. J. Clarke, K. W. D. Ledingham, T. McCanny, D. Neely, A. P. L. Robson, P. T. Simpson, C.-G. Wahlström and M. Zepf.

Plasma Physics and Controlled Fusion **49**, B223 (2007).

IOP PUBLISHING PLASMA PHYSICS AND CONTROLLED FUSION

Plasma Phys. Control. Fusion **49** (2007) B223–B231 doi:10.1088/0741-3335/49/12B/S20

Low- and medium-mass ion acceleration driven by petawatt laser plasma interactions

P McKenna[1], F Lindau[2], O Lundh[2], D C Carroll[1], R J Clarke[3], K W D Ledingham[1,5], T McCanny[1], D Neely[3], A P L Robinson[3], L Robson[1,5], P T Simpson[4], C-G Wahlström[2] and M Zepf[4]

[1] SUPA, Department of Physics, University of Strathclyde, Glasgow G4 0NG, UK
[2] Department of Physics, Lund University, PO Box 118, S-22100 Lund, Sweden
[3] STFC, Rutherford Appleton Laboratory, Chilton, Didcot, Oxon OX11 0QX, UK
[4] Department of Physics and Astronomy, Queen's University Belfast, Belfast BT7 1NN, UK

E-mail: p.mckenna@phys.strath.ac.uk

Received 6 July 2007
Published 15 November 2007
Online at stacks.iop.org/PPCF/49/B223

Abstract

An experimental investigation of low- and medium-mass ion acceleration from resistively heated thin foil targets, irradiated by picosecond laser pulses at intensities up to $5 \times 10^{20}\,\mathrm{W\,cm^{-2}}$, is reported. It is found that the spectral distributions of ions, up to multi-MeV/nucleon energies, accelerated from the rear surface of the target are broadly consistent with previously reported measurements made at intensities up to $5 \times 10^{19}\,\mathrm{W\,cm^{-2}}$. Properties of the backward-directed beams of ions accelerated from the target front surface are also measured, and it is found that, compared with the rear surface, higher ion numbers and charges, and similar ion energies are produced. Additionally, the scaling of the maximum ion energy as a function of ion charge and laser intensity are measured and compared with the predictions of a numerical model.

(Some figures in this article are in colour only in the electronic version)

1. Introduction

In recent years the application of ultra-intense ($>10^{19}\,\mathrm{W\,cm^{-2}}$) laser pulses to drive multi-MeV proton and heavier ion acceleration has generated a lot of international interest [1–3]. High quality beams of ions with ultra-low emittance have been measured, from the rear surface of thin foil targets [4, 5], and recently it has been demonstrated that it is possible to produce quasi-monoenergetic beams of ions [6–9].

[5] Also at AWE plc, Aldermaston, Reading, RG7 4PR, UK.

The acceleration of multiply-charged ions has been investigated using long (∼ns) and, recently, short (ps and sub-ps) laser pulses—see [1, 2] and references therein. Heavy ions, for example Ta and Au of ion charge states up to 38+ and 33+, respectively, with energy of the order of 1 MeV, were demonstrated at subrelativistic intensities of $\sim 5 \times 10^{16}\,\mathrm{W\,cm^{-2}}$ using terawatt laser pulses with 1 ps duration [10, 11]. The main acceleration mechanism of the backward-directed ions investigated in these studies is skin-layer ponderomotive acceleration (S-LPA) [12]. Multiply charged fast ions generated by ultra-intense laser pulses have also been investigated, for both forward- [13–16] and backward-directed beams [17, 18]. The target normal sheath acceleration (TNSA) mechanism has been proposed to explain forward-directed ion acceleration at the rear surface [19]. Compared with subrelativistic intensity laser pulses, higher ion energies, up to ∼5 MeV/nucleon, are observed with ultra-intense pulses, although high numbers of ions of high charge states are recorded in both cases.

In this paper we report a characterization of low- and medium-mass ion acceleration from thin palladium target foils, heated to reduce hydrogen-containing surface contaminations, and irradiated at ultra-high intensities up to $5 \times 10^{20}\,\mathrm{W\,cm^{-2}}$ using picosecond pulses from a petawatt-class laser. We verify that many of the main properties of the rear surface ion beam are similar to measurements reported previously for lower intensities. We extend the study to include a characterization of ion acceleration at the target front, and also report on measurements and modelling of the scaling of the maximum ion energy with charge and with laser intensity.

2. Experimental method

The petawatt beam line of the Vulcan laser at the Rutherford Appleton Laboratory, UK, is used in this experiment. It is a Nd:glass laser (wavelength 1.05 μm) which can deliver pulses with energy up to 500 J in 0.5 ps duration. Pulse energies and durations in the range 40 to 375 J (on target) and 1 to 8 ps (FWHM), respectively, are used. The pulse duration was controlled by moving a grating in the pulse stretcher. An $f/3$ off-axis parabolic mirror is used to focus the p-polarized laser pulses onto palladium target foils at a 45° angle of incidence. The peak laser pulse intensity is varied between 5×10^{19} and $5 \times 10^{20}\,\mathrm{W\,cm^{-2}}$. The measured ratio of the level of the amplified spontaneous emission (ASE) relative to the peak intensity is 10^{-7} at a few nanoseconds and 10^{-6} at a few picoseconds prior to the peak of the pulse. As ASE-induced radiation heating and shock waves can affect the TNSA mechanism [20–22], a fixed target thickness of 25 μm is chosen to minimize these effects, whilst ensuring efficient transport of hot electrons through the target to establish the sheath on the rear surface.

Identical Thomson ion spectrometers are positioned on both sides of the target, along the axis normal to the surface and at ±10° from the target normal in the plane of incidence. The spectrometers have parallel electric and magnetic fields to separate ions with different charge-to-mass ratios (q/m) into energy-dispersed tracks. The peak magnetic field is 0.6 T and the electrostatic field varies from 3.0 to 0.3 $\mathrm{kV\,mm^{-1}}$ over a distance of 200 mm [23]. The solid angles defined by the entrance apertures to the spectrometers are in the range 5×10^{-9} to 2×10^{-8} Sr. A CR-39 plastic track detector is positioned in the dispersion plane of each spectrometer to record the ion q/m and energy distributions. CR-39 is insensitive to electrons and photons, and is 100% efficient at detecting ions with energy above ∼100 keV and below a limit defined by the thickness of the plastic. The 1 mm-thick CR-39 used in this experiment detects protons with energy up to ∼10 MeV and carbon, oxygen and palladium ions with energy up to 19, 22 and 47 MeV/nucleon, respectively. Higher energy ions (with range longer than 1 mm) pass through the CR-39 without leaving clear tracks. Each ion stopped in the CR-39 damages the plastic and after etching in NaOH solution a corresponding 'pit'

(of typical diameter in the range 5–20 μm) is observed. An automated scanning microscope with pit recognition and analysis software [24] is used to digitize the spatial distribution of the pits. Ions of a given q/m produce a single signature parabolic track of pits in the CR-39. The measured tracks are identified by matching them to simulated ion trajectories, using the known electric and magnetic field distributions in the spectrometers, and the ion energy spectra extracted.

Under vacuum conditions typical of experiments of this type ($\sim 10^{-5}$ mbar), hydrocarbons and water vapour form thin contamination layers on the target surface, providing a source of protons, and carbon and oxygen ions. Having the largest q/m, protons are accelerated more effectively than other, heavier, ions. The protons at the leading edge of the ion front screen the accelerating field acting on the heavier ions [13], and previous studies have shown that these ions are more efficiently accelerated when the source of the protons is removed [13, 14, 18]. Target heating has been shown to be an effective method [14] for reducing the hydrogenated contamination layers on the surfaces of the target and we adopt this technique to ensure uniform cleaning of both target surfaces. The targets are resistively heated to 1000 °C for 10 minutes immediately prior to and during the laser shot. In agreement with previous observations, we find that under these conditions ions heavier than protons are efficiently accelerated. Large numbers of palladium and oxygen ions are observed, together with weak traces of carbon ions.

3. Results

3.1. Comparison of front and rear surface ion acceleration

We measure the energy and charge distributions of ions detected in the spectrometers positioned at the front and rear sides of the target, for a range of laser pulse parameters, and observe similar maximum energies (multi-MeV/nucleon) of ions accelerated in both directions. Ions with charge states up to O^{6+} and Pd^{18+}, which correspond to closed shell electron configurations, are measured in the rear spectrometers at the highest laser intensity (5×10^{20} W cm^{-2}). Because a 25 μm Pd target foil will stop oxygen and palladium ions of $\sim$5.3 and $\sim$7.8 MeV/nucleon, respectively, we assume that all ions detected in the rear spectrometers are accelerated from the rear surface. Assuming field ionization by barrier suppression is the dominant ionization mechanism at the rear surface [13], a field strength of $\sim 2 \times 10^{12}$ V m^{-1} is needed to produce the observed ions [25]. Ions with much higher charge states are observed in the spectrometers positioned at the front side of the target, including fully stripped oxygen and up to Pd^{30+}. These higher charge state ions are likely produced by the intense fields in the laser pulse itself or through collisional ionization in the hot plasma generated there [26].

We find that the shapes of the ion energy spectra measured at the front and at the rear of the target are broadly similar. Example spectra for selected charge states of oxygen and palladium are shown in figures 1(*a*) and (*b*), respectively. These spectra were measured along the target normal axis at the front of a heated Pd foil irradiated by a 122 J, 1 ps laser pulse. The spectra exhibit features similar to those previously reported [14, 16, 17]. Notably, the energy distribution shifts to higher energies with increasing charge. The energy spectra of the lower charge state ions are typically broad, Maxwellian-like, distributions and the higher charges exhibit plateau-like distributions which partially overlap the spectra of the lower charge state ions. Integrations of the energy spectra for all the measured charge states of palladium and oxygen for this representative laser shot are shown in figure 1(*c*) and (*d*) for the rear and front, respectively. Similarly to Schreiber *et al* [16], we find that the integrated spectra for ions at the rear of the target can be fitted with a double exponential distribution. The mean energies of the colder and hotter parts of the integrated spectra are $\sim$0.1 MeV/nucleon and

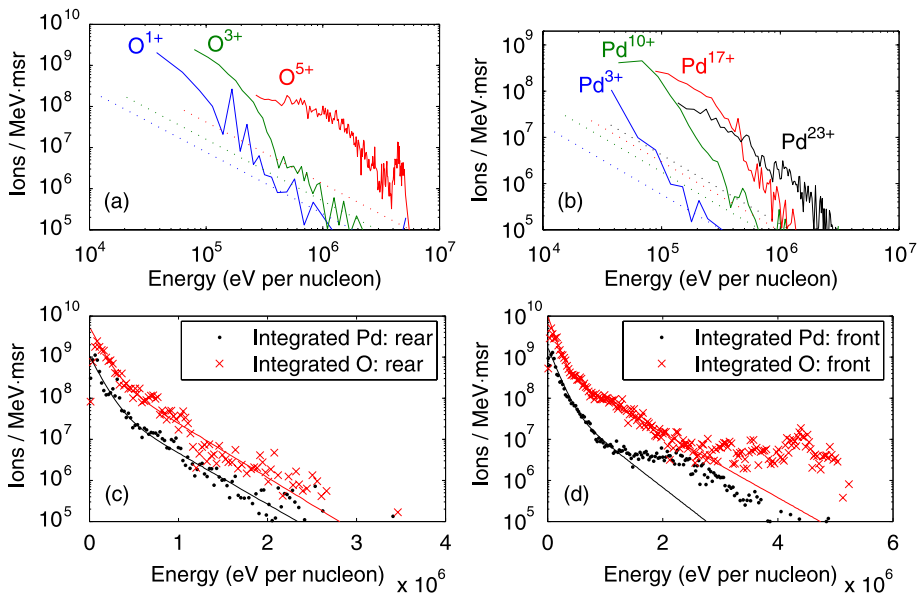

Figure 1. Example oxygen (*a*) and palladium (*b*) energy spectra measured along target normal at the front surface of a heated palladium target irradiated by a 122 J, 1 ps, 2×10^{20} W cm^{-2} laser pulse. The solid lines are the measured spectra and the dotted lines correspond to the background level (lower detection threshold), as measured by sampling the pit distribution in equivalent regions of the CR-39, either side of the ion tracks; (*c*) and (*d*) are the integrated numbers of all palladium and oxygen ions measured at the rear and front of the target foil, respectively. The symbols are the experimental data and the solid curves correspond to fits made with a double exponential function, with 'cold' and 'hot' mean energies of 0.1 and 0.35 MeV/nucleon, respectively, for both Pd and O at the target rear, and 0.1 MeV/nucleon for the lower mean energy at the target front.

∼0.35 MeV/nucleon, respectively, for both the oxygen and palladium ions. The mean energy of the colder part of the corresponding integrated spectra at the front is also ∼0.1 MeV/nucleon, but the spectra depart from the double exponential distribution at high energies. The high energy component results from the higher charged ions produced at the front, with energy distributions shifted to higher energies.

An example of the measured variation of the maximum detected ion energy, $E_{\max}$, and the total energy of each ion species, E_{tot}, as a function of q/m are plotted in figures 2(*a*) and (*b*), respectively. A similar scaling of both $E_{\max}$ and E_{tot} are observed on both sides of the target. The total energy in the portion of the ion beam sampled along the target normal at the target front is more than a factor of 5 higher than that measured along target normal at the rear (69 J Sr^{-1} compared with 13 J Sr^{-1}). We do not measure the spatial profile of the ion beam. However, measurement of the spatial profile of proton emission from unheated 25 μm thick Al targets, using dosimetry film, reveals a beam size corresponding to ∼0.25 Sr at the rear of the target (for protons with energy of ∼5 MeV). Assuming a similar, or slightly smaller divergence for heavier ions (as reported by Brambrink *et al* [15]), yields an estimated conversion efficiency of laser to ion energy at the target rear of ∼3%. This is consistent with reported measurements of conversion efficiency into protons from unheated Al targets under the same laser conditions [27]. A corresponding estimate of the conversion efficiency at the front surface is not made due to asymmetry in the spatial profile of the proton and ion beam, as discussed below. We note, from our measurements, that typically between 70% and 80% of

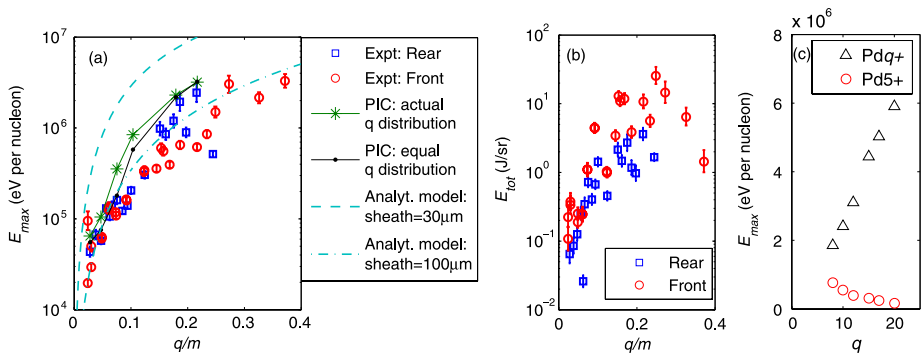

Figure 2. (*a*) Maximum ion energy, $E_{\max}$, and (*b*) total integrated ion energy, E_{tot}, as a function of charge-to-mass ratio, measured along the target normal axis at the front and rear sides of a heated palladium target irradiated by a 122 J, 1 ps, 2×10^{20} W cm^{-2} laser pulse. Similar maximum ion energies are measured on both sides of the target, while higher charges and total ion energies are measured at the front surface. The error bars are determined from the energy resolution of the spectrometer. The filled symbols with lines in (*a*) are results from numerical PIC simulations using the model described in the main text. The green points (stars with line) result when the ion charge distribution approximates the measured charge distribution, and the black points (dots with line) result when ion population is equally distributed across all charges. Also shown in (*a*) are the predictions of the analytical model described by Schreiber *et al* [33] for sheath radii of 30 μm (cyan dashed line) and 100 μm (cyan dot-dash line). (*c*) Results from numerical PIC simulations involving only two charges (with equal population), Pd^{5+} and Pd^{q+} where q is varied from 8 to 20. The maximum energy of the higher q/m ion increases with increasing charge, whereas the energy of the lower q/m ion decreases.

the total ion energy is carried by palladium ions, with the reminder as ions from contaminants, principally oxygen.

A number of acceleration mechanisms may contribute to efficient backward-directed ion acceleration from the target front surface. It has been shown that S-LPA is an efficient mechanism of backward ion acceleration [10–12], and this mechanism may contribute to the ion acceleration at the front of the target observed here. A Debye sheath is formed at the front surface of the target (in addition to the rear) and this may also contribute to the observed backward-directed ions, by a mechanism similar to TNSA. Because significant refluxing of electrons within the target foil [28] is expected (the distance travelled by relativistic electrons during the laser pulse duration, $\sim$300 μm, is much larger than twice the target thickness), the quasistatic electric fields formed on both surfaces will be enhanced. It is expected that the larger plasma density gradient scale length at the front surface, compared with the rear, would result in lower maximum ion energies [29]. A steepening of the density gradient at the focus of the ultra-intense laser pulse may however aid front surface acceleration. Ion acceleration may also be aided by electron stochastic heating within the preformed plasma at the front surface [30].

Although, as discussed above, no direct measurement of the spatial profile of the ion beam is made, measurement of ion emission at $\pm 10^{\circ}$ relative to the target normal axis on both sides of the targets enables partial characterization of the angular emission of ions from the target. Consistently we observe that similar numbers and maximum energies of ions are detected in both off-axis spectrometers at the target rear, and we conclude that the beam of ions emitted from the target rear surface is centred on the target normal axis, as expected from the TNSA mechanism [19]. By contrast, we typically observe asymmetry in the ion beam profile at the target front, particularly for the longer pulse duration measurements (greater than 3 ps), for

which the beam is shifted towards the axis of the incoming laser beam. The 'shape' of the ablated plume on the target front surface, in which the hot electron cloud expands to establish the sheath field, is subject to processes such as 'hole-boring' in which the relativistic critical density surface at the focus of the laser pulse is pushed inwards (into the target), whilst the ablated plume expands outwards into vacuum. This is further complicated due to the 45° angle of laser incidence onto target.

3.2. Ion energy scaling as a function of charge

In order to determine to what extent the measured scaling of ion energy with charge (figure 2(*a*)) is predicted by numerical modelling and how it depends on the initial charge state distribution, we model the ion expansion from the target rear surface using a one dimensional explicit particle-in-cell (PIC) code [31]. A linear interpolation is used for particle and grid weighting and the electric field obeys Gauss' Law. The simulation space involves a grid of 20 000 spatial points with a cell size of 2 nm. The target has a thickness of 4 μm, with a top-hat density profile (i.e. initially sharp interfaces) and an ion density of 2×10^{28} m^{-3} (i.e. ∼0.3 times the density of Pd). The electron density is set to give overall charge neutrality. The 'laser' pulse has a $\sin^2$ envelope function, with pulse duration 200 fs (FWHM), wavelength 1 μm and intensity equal to 2×10^{20} W cm^{-2}. These parameters are chosen to keep the electron density sufficiently low so that the simulation run-time is feasible, and so that the pulse duration and target thickness are scaled by a similar order. The dynamics of six ion species with a mass of 1.78×10^{-25} kg (^{106}Pd) and charges 3, 5, 8, 11, 19 and 23 are modelled in each simulation.

Results from two of the simulations are shown in figure 2(*a*). The green symbols (stars with line) represent the result when the input charge population distribution closely matches the measured distribution, and the black symbols (dots with line) represent the result when the ion population is equally distributed across the six charges sampled. We note that, as expected, the charge distribution influences the energy scaling as a function of charge, but that both results broadly reproduce the measured scaling (blue squares), with good agreement particularly for the lowest and highest charges.

To further investigate the interplay between the acceleration of ions with different charges, and in particular the screening effect of high charge ions on the field acting on lower q/m ions, we perform a series of simulation runs with an equal mixture of Pd^{5+} and one other Pd ion charge state in the range 8 to 20. The absolute energy in the results for this set of simulations is overestimated because a much thinner target (1 μm) is used to enhance particle statistics. Nevertheless, the results, shown in figure 2(*c*), illustrate that an increase in energy of the higher q/m species is observed as its charge increases, whilst the energy of the low q/m ion (Pd^{5+}) experiences a decrease in maximum energy. A higher charge results in a higher maximum energy for the highest q/m species [32]. Since the field decays as $1/\omega_{pi}t$, where ω_{pi} (the ion plasma frequency) $\propto \sqrt{q}$ [32], with increasing q/m the electric field decays more rapidly and the lower q/m species (Pd^{5+}) is accelerated to successively lower energy. In this way the ion energy scaling with q/m is likely to be a complicated function of the ionization dynamics, and as we illustrate in figure 2(*a*), the ionization charge distribution.

We note that Schreiber *et al* [33] describes an analytical model which, although does not include screening effects nor consider the ionization charge distribution, gives good agreement with experimental measurements of ion acceleration as a function of charge, in the intensity range up to 6×10^{19} W cm^{-2}. We apply this model to determine the predicted scaling of the maximum ion energies as a function of q/m for the laser parameters explored in the present study, and find that the predicted energies are higher than experimentally observed, as shown in the example measurement in figure 2(*a*). We note however that a sheath radius of 30 μm is

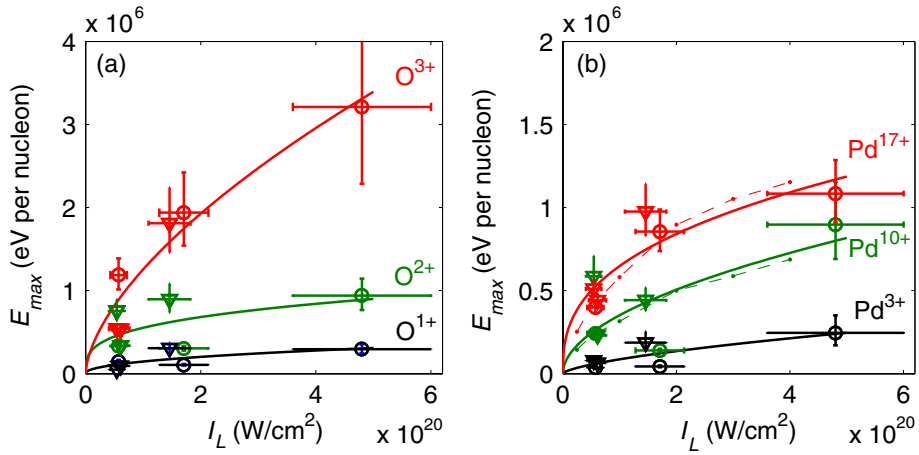

Figure 3. Maximum energy of sample (*a*) oxygen and (*b*) palladium ions as a function of laser intensity. Open symbols are experimental measurements, where triangles correspond to variation of pulse duration for approximately constant laser energy and circles correspond to variation of laser energy for constant pulse duration. The error bars on the maximum energy arise from the energy resolution of the spectrometer and the error bars on the laser intensity are a combination of measurement uncertainty in laser pulse energy and shot-to-shot fluctuations in pulse duration. The solid lines correspond to individual power fits to the data for each ion and the mean value of the exponent of the power fits is 0.5. The closed symbols and dashed lines in (*b*) are results from a numerical model, for Pd^{10+} and Pd^{17+}, normalized to the experimental data, in good agreement with the observed scaling.

used in the model (calculated based on the laser focal spot size and the cone angle of electron transport within the target). When we increase the sheath radius to 100 μm we obtain a much better fit to our experimental data for 1 ps pulse duration (as also shown in figure 2(*a*)), whereas a sheath radius of the order of 500 μm is required to provide a good fit to the data for the longer pulse duration of 8 ps. This is consistent with the idea of increased lateral spreading of the electron sheath [34] due to the increased number of cycles of refluxing electrons for the longer pulse duration.

3.3. Ion scaling as a function of laser intensity

We investigate the scaling of the maximum energies of oxygen and palladium ions accelerated as a function of laser intensity in the range 5×10^{19} to 5×10^{20} W cm^{-2}. Specifically, over a series of six shots, we vary the laser energy from 40 to 375 J for a fixed pulse duration of 1 ps, and also vary the pulse duration from 1 to 8 ps for approximately constant laser pulse energy (345 ± 30 J).

Figure 3 shows the scaling of the maximum detected energy, $E_{\max}$, of sample oxygen and palladium ions at the target rear. The highest q/m ion that we observe for all six shots is O^{3+}, and we measure a clear increase in the maximum energy of this ion with increasing laser intensity. We find no systematic change in the scaling observed for different q/m ions individually when applying simple power fits. Furthermore, we find that the mean value of the exponents of the individual power fits is 0.5. This suggests that the maximum detected ion energy is proportional to the fast electron temperature ($\propto \sqrt{(I\lambda^2)}$), independent of q/m. The same scaling has been reported for proton maximum energies for similar laser conditions [17,27,35], and for helium-like carbon and fluorine ions at laser intensities up to $\sim 5 \times 10^{19}$ W cm^{-2} [14].

Paper X

Lateral electron transport in high-intensity laser-irradiated foils diagnosed by ion emission

P. McKenna, D. C. Carroll, R. J. Clarke, R. G. Evans, K. W. D. Ledingham, F. Lindau, O. Lundh, T. McCanny, D. Neely, A. P. L. Robinson, L. Robson, P. T. Simpson, C.-G. Wahlström and M. Zepf.

Physical Review Letters **98**, 145001 (2007).

PRL 98, 145001 (2007) PHYSICAL REVIEW LETTERS week ending 6 APRIL 2007

Lateral Electron Transport in High-Intensity Laser-Irradiated Foils Diagnosed by Ion Emission

P. McKenna,[1,2,*] D. C. Carroll,[1] R. J. Clarke,[2] R. G. Evans,[2,5] K. W. D. Ledingham,[1,†] F. Lindau,[3] O. Lundh,[3] T. McCanny,[1] D. Neely,[2] A. P. L. Robinson,[2] L. Robson,[1,†] P. T. Simpson,[4] C.-G. Wahlström,[3] and M. Zepf[4]

[1]*SUPA, Department of Physics, University of Strathclyde, Glasgow G4 0NG, United Kingdom*
[2]*CCLRC, Rutherford Appleton Laboratory, Chilton, Didcot, Oxon OX14 0QX, United Kingdom*
[3]*Department of Physics, Lund University, P.O. Box 118, S-22100 Lund, Sweden*
[4]*Department of Physics and Astronomy, Queen's University Belfast, Belfast BT7 1NN, United Kingdom*
[5]*Department of Physics, Imperial College, London, SW7 2AZ, United Kingdom*

(Received 16 December 2006; published 4 April 2007)

An experimental investigation of lateral electron transport in thin metallic foil targets irradiated by ultraintense ($\geq 10^{19}$ W/cm^2) laser pulses is reported. Two-dimensional spatially resolved ion emission measurements are used to quantify electric-field generation resulting from electron transport. The measurement of large electric fields ($\sim$0.1 TV/m) millimeters from the laser focus reveals that lateral energy transport continues long after the laser pulse has decayed. Numerical simulations confirm a very strong enhancement of electron density and electric field at the edges of the target.

DOI: 10.1103/PhysRevLett.98.145001 PACS numbers: 52.50.Jm, 41.75.Jv, 52.70.Nc

The study of fast electron generation and transport in intense laser interactions with dense plasma is of fundamental importance for the fast ignition approach to inertial fusion [1]. It is also important for the optimization of high power laser-driven ion [2–5] and x-ray sources [6]. One of the factors influencing the efficiency of longitudinal energy transport in a laser-irradiated target is the degree of lateral spreading of the energetic electron population. In the 1980s experimental and theoretical investigations, at laser intensities up to $\sim 10^{16}$ W/cm^2, revealed that of the order of 30% of the absorbed laser energy is transported laterally by energetic electrons [7–9]. Recently there has been significant interest in electron transport along the surface of targets irradiated by ultraintense ($>10^{18}$ W/cm^2) laser pulses [10–12], in relation to the physics of cone guided schemes for fast ignition [13].

In this Letter we present an experimental investigation of lateral electron transport in ultraintense laser-irradiated foils, diagnosed via spatially resolved measurements of multi-MeV ion emission. The principal diagnostics used in experimental investigations of electron transport in solid targets typically involve, for example, measurement of $K\alpha$ emission from buried layers [14,15]. Ion emission has previously been used to investigate electron energy transport through a solid target [16] and field dynamics at the rear of a target foil, opposite to the laser focal spot [17,18]. Here we observe and measure ion emission from the edges of thin target foils, where the edges are sufficiently far away from the focal spot that the expanding electron cloud cannot reach them until a long time after the laser pulse. We use this ion emission to make quantitative measurements of the 2D spatial distribution of electric-field (E-field) formation due to lateral electron transport in the foil. Our experimental measurements and simulations using the LSP code [an implicit particle-in-cell (PIC) model with fluid background] [19] reveal enhanced electron densities and E fields at solid-vacuum boundaries, and shed light on the dynamics of the expansion of the electron cloud.

The experiment used the Vulcan laser at the Rutherford Appleton Laboratory, UK. Pulses of wavelength 1.053 μm, energy up to 400 J and duration 1 ps (FWHM) are focused using an $f/3$ off-axis parabola to intensities up to 6×10^{20} W/cm^2. The level of the amplified spontaneous emission (ASE) is measured to be 10^{-7} and 10^{-6} of the peak laser intensity at a few nanoseconds and a few picoseconds prior to the peak of the pulse, respectively. The pulses are p polarized and incident onto target at 45°. A schematic of the experiment arrangement is shown in Fig. 1(a).

The targets are 10 μm thick planar Au and Al foils of size 4 mm $\times$ 10 mm. Foils with 50 μm diameter "witness" holes machined 500 μm from the laser focus are also used. The Au targets are resistively heated to 1000 °C for 10 min prior to and during laser irradiation to reduce the hydrogenated contamination on the target surfaces.

The charge-to-mass ratio and energy of ions emitted from the target are measured using a high-resolution Thomson spectrometer incorporating a 0.6 T, 50 mm long magnetic field, and an electric field which varies in strength from 3.0 to 0.3 kV/mm over a distance of 200 mm. The solid angle is varied between 5×10^{-9} and 2×10^{-7} sr, depending on the ion flux. Ions (and fast neutral atoms) are detected using CR-39 plastic track detectors positioned in the dispersion plane of the spectrometer. CR-39 is sensitive to ions, but insensitive to electrons and electromagnetic radiation. Each ion entering the CR-39 damages the plastic and a corresponding "pit" (between 5 and 20 μm diameter) is produced after etching in NaOH solution. The spatial distribution of the pits is mapped out using an automated scanning microscope with pit recognition and analysis software [20]. Ions of a given

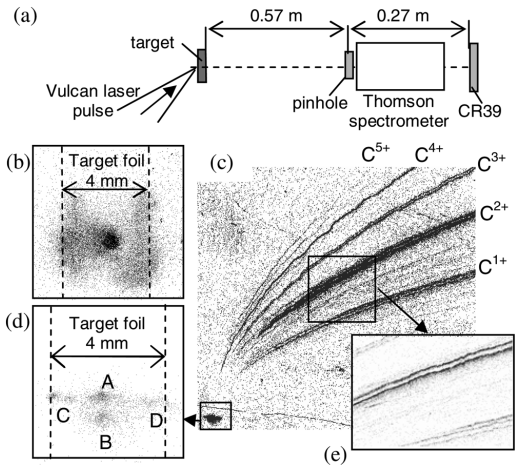

FIG. 1. (a) Schematic of the experiment arrangement in which a Thomson spectrometer is used as an ion pinhole camera. (b) Optical scanned image of pits in CR-39 produced by fast uncharged atoms (recombined ions). Ions are accelerated from a central spot and from linear regions corresponding to the target edge. (c) Spatial mapping of pit distributions on a CR-39 detector in the dispersion plane of a Thomson spectrometer, produced using an automated scanning microscope with pit recognition software [20]. Mainly carbon ions are detected in distinct ion traces. (d) Enlarged region corresponding to fast neutral atoms undeflected in the spectrometer fields. Source regions are observed at the center of the target foil, A, at the edge of a 50 μm hole, B, and at the edges of the foil, C and D. (e) Enlarged region showing multiple carbon ion tracks. Each track results from one of the four source regions in (d).

charge-to-mass ratio originating from a point source produce a single signature parabolic track of pits in the CR-39. The coordinates of every pit in a given track are extracted to determine the ion energy spectrum.

In good agreement with previous results we find that protons are the dominant ions emitted in laser interactions with unheated targets, and that carbon ions are efficiently accelerated when target foils are heated [17,21]. However, unexpectedly we observe ions from more than one source region on the target foil. In particular, we find that, regardless of whether we irradiate Al or Au foils, heated or unheated, we observe ion emission from the edges of the target foils, 2 mm on either side of the laser focal spot.

To illustrate the observation Fig. 1(b) shows part of an optically scanned image of pits produced in a CR-39 sample. The Thomson spectrometer in this example was positioned along target normal and at the rear of a 10 μm thick unheated Al target irradiated by a 200 J, 1 ps, 3×10^{20} W/cm^2 laser pulse. The image is produced by fast neutral atoms, which are observed on every shot and result from fast ions undergoing recombination before entering the spectrometer. The pits produced by these recombined ions mark the zero-deflection axis of the spectrometer onto the CR-39 detector. The 300 μm diameter aperture at the entrance to the spectrometer in combination with the spatially resolving detection facilitated by the CR-39 effectively works as a demagnifying pinhole camera of fast-ion emission from the target. Figure 1(b) is therefore a 2D spatially resolved measurement of ion emission. The magnification factor is 0.47 and the spatial resolution, which is a function of the aperture size, is 930 μm for the measurement in Fig. 1(b). Most ions are emitted from a central spot on the target, opposite to the laser focal spot on the front surface. Linear regions of ion emission on either side of the central spot are clearly observed, and the demagnification factor confirms that these ions are emitted from the edges of the target, 2 mm on either side of the focal spot.

Next we investigate the ion species accelerated from each of the source regions by increasing the spatial resolution of the spectrometer to 155 μm and looking for multiple sets of ion tracks on the CR-39 detector. Figure 1(c) shows a spatial mapping, at the higher resolution, of pits distributed in a full CR-39 detector. This particular measurement was obtained with a 340 J energy laser pulse focused to a spot size of 40 μm (FWHM), corresponding to an intensity of 1×10^{19} W/cm^2, onto a heated Au foil target. The main tracks are produced by C ions from hydrocarbon contamination layers. Two main features of interest in the figure are enlarged. The first is the signal produced by the recombined ions, Fig. 1(d). As before, we observe ion emission from the edges of the target (C and D). The signal is considerably reduced compared to the result shown in Fig. 1(b) due to a factor of 36 reduction in the solid angle sampled by the spectrometer and a factor 30 reduction in laser intensity. Another ion source (B), vertically offset from the main source (A), corresponds to emission from the edge of a 50 μm diameter witness hole positioned 500 μm from the focal spot. The total recombined ion signal from the four sources is $\sim$3% of the total ion signal detected on the CR-39, in good agreement with previous estimates for experiments of this type [17]. Importantly, with the higher spatial resolution we observe multiple ion tracks for many of the charge states of carbon, as shown in Fig. 1(e). Each track has been identified as resulting from one of the four ion sources shown in Fig. 1(d), revealing that, in addition to the main source (A) carbon ions are also emitted from the edges of the irradiated target foil and the hole, as listed in Table I.

We use carbon ion emission to diagnose *E*-field generation using the method described by Hegelich *et al.* [17] and used by Schreiber *et al.* [18]. The charge states observed provide a measure of the peak *E*-field strength and the ion energy spectra provides information on the temporal and spatial extent of the field. Because of the stopping range of multi-MeV C ions in Au, we assume that the energetic C ions detected originate on the rear surface of the target. We rule out ionization at the rear of the target as arising due to

PRL 98, 145001 (2007) PHYSICAL REVIEW LETTERS week ending 6 APRIL 2007

TABLE I. C^{q+} ions observed from each of the four sources (A–D) in Fig. 1 and calculated field parameters. E_q^{thresh} is the lower threshold E field required to produce a carbon ion of charge q. $E_q^{\max}$ is the maximum E field and is used to calculate $\tau_q^{\min}$ and $l_q^{\min}$, the minimum field duration and acceleration length, respectively, to accelerate the ionic charge state to the detected maximum energy $W_q^{\max}$.

	q	$W_q^{\max}$ (MeV)	E_q^{thresh} (TV/m)	$E_q^{\max}$ (TV/m)	$\tau_q^{\min}$ (ps)	$l_q^{\min}$ (μm)
A	1	3.4	0.022	0.052	18	67
	2	5.4	0.052	0.13	4.4	21
	3	11	0.13	0.18	3.1	21
	4	25	0.18	5.3	0.12	1.2
	5	38	5.3	7.0	0.09	1.1
B	1	4.7	0.022	0.052	21	92
	2	5.9	0.052	0.13	4.6	22
	3	19	0.13	0.18	4.0	35
C	1	1.5	0.022	0.052	12	30
	2	4.4	0.052	0.13	4.0	17
D	2	⋯	0.052	0.13	⋯	⋯

the laser pulse, as it is absorbed in the preplasma, or due to a shock wave driven by the ASE, due to the thickness and density of the target foil. Similar to Hegelich *et al.* [17] we calculate the collisional ionization rate due to the hot electrons and the cold electron return current and find it to be lower than the ionization rate due to field ionization by barrier suppression (FIBS) for C^{q+}: $q = 1$–4, and thereby assume FIBS to be the dominant ionization mechanism at the rear of the target. The threshold field E_q^{thresh} for the production of each ion of charge q is calculated using

$$E_q^{\text{thresh}} = U_{q-1}^2 \varepsilon_0 \pi / qe, \tag{1}$$

where U_q is the ionization potential in eV. A lower limit for the acceleration time τ and the acceleration length l (minimum longitudinal spatial extent of the field) required to produce the measured maximum energy of each ion species from each source is calculated assuming that a given ion of charge q will experience a maximum electric-field strength given by $E_q^{\max} = E_{q+1}^{\text{thresh}}$, the threshold for further ionization. The calculated parameters for each of the four sources are presented in Table I.

We find that the highest field strength, >5.3 TV/m, is produced in the region of the target rear surface opposite to the laser focal spot. A field of between 0.13 and 0.18 TV/m is generated on the edge of the hole 0.5 mm from the focal spot and fields of between 0.05 and 0.13 TV/m are generated at the target edges. E fields of this order 2 mm away from the focal spot indicate that the lateral transport of energetic electrons in the foil continues long after the laser pulse. This is consistent with time resolved measurements of $K\alpha$ x-ray production for thin, isolated targets [22].

To demonstrate that this picture of the expanding charge cloud is realistic we perform 2D cylindrical simulations of the charge cloud dynamics with the LSP computer model [19] using a kinetic (PIC) description of the energetic electrons and a fluid description of the bulk of the target. The simulation grid covers 600 μm × 600 μm with 2400 × 2400 cells. The cell size of 0.25 μm is just adequate to resolve the distribution of electrons in the bulk of the 10 μm thick target foils, but does not enable investigation of ion dynamics. Electrons are created to correspond to the distribution of accelerated electrons from the laser. A laser-to-electron energy conversion efficiency of 30% is assumed and the mean electron energy is 1 MeV, equal to the ponderomotive potential, for a laser intensity of 10^{19} W/cm^2.

For a laser pulse of duration T the electron temperature is increased over $0.1T$, held constant for $0.8T$, and decreased over $0.1T$. The axial distribution corresponds to half of a relativistic thermal distribution (in the laser direction) and the angular spread is around 30° half-angle. Most of the electrons pass through the target and are reflected in the expanding Debye sheath on the rear surface. The motion of the Debye sheath results in a reduction of the axial component of electron velocity while the transverse velocity is largely unaltered. As the electrons reflux [23] within the foil many times the charge cloud expands out laterally forming a disk. The radial expansion requires a return current to flow via the "cold" electrons of the target foil, and the resistivity of the target gives rise to an E field which hinders the expansion. Because of the fall off in current density as the cloud expands radially, the effect of this E field rapidly diminishes with radius.

Our LSP simulations show a very strong enhancement of the electron density and E field when the charge cloud reaches the edge of the target disk, as illustrated in Fig. 2, where (a) and (b) show the hot electron density and magnitude of the resulting E field, respectively, after 0.25 ps; Figs. 1(c) and 1(d) show the corresponding results after 2.5 ps. At the edge of the target the return current is no longer supported and the expansion is halted by the radial component of the electrostatic field caused by the buildup of net negative charge. The electrons "pile up" at the target edge and are eventually reflected after a time of the order of the plasma period (350 fs for an electron density of 10^{17} cm^{-3}). The E fields at the target edge in the simulation (400 μm radius) are about 0.2 TV/m and fields greater than 0.02 TV/m extend out to a distance of about 15 μm from the target.

Figure 2(e) shows how the temporal evolution of the E field (potential drop over a distance of 25 μm from the surface of the target in the direction normal to the surface) varies as a function of time for selected distances from the laser focal spot. As the simulation grid is smaller than the

PRL 98, 145001 (2007) PHYSICAL REVIEW LETTERS week ending 6 APRIL 2007

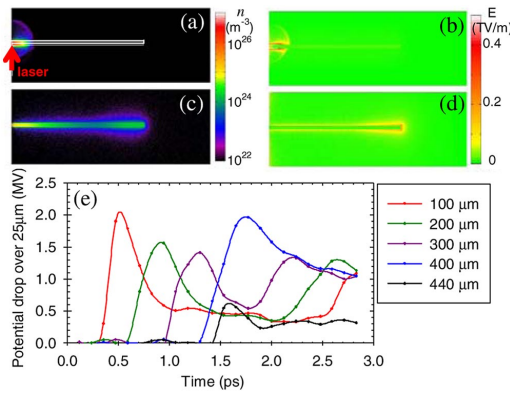

FIG. 2 (color online). (a) Electron density n 0.25 ps after the start of the laser pulse. The target profile (400 μm radius and 10 μm thickness) is illustrated by the white line. The simulation space is cylindrically symmetric about the laser axis, marked by the (red) arrow. (b) Resultant E-field strength after 0.25 ps. (c),(d) Corresponding results 2.5 ps after the start of the laser pulse. (e) Temporal evolution of the potential drop over 25 μm from the surface of the target at given radii from the laser focal spot. The field becomes higher and remains high at the edge of the target (400 μm) for much longer than at smaller radii. A second later peak in the transient field at the smaller radii is produced by electrons which are reflected from the target edge and transverse the target again, in the opposite direction.

size of the target (the radius of the target in the simulation is 400 μm and in the experiment is 2 mm) the pulse duration in the simulation is 200 fs—scaled down to the transit time for the expanding charge cloud to reach the target edge. It is observed that the charge wave moves laterally at approximately $0.75c$ (where c is the speed of light in vacuum). The magnitude of the field at the edge remains large over a much longer duration than the transient field at other radii within the target. Although we see some ion emission across the target in our experiment, we predominantly observe ions from the laser focal spot and the target edges, indicating that ion emission as a diagnostic of E-field generation is more sensitive to the longer duration field at the edges. In this respect ion emission provides a unique probe of transient E-field strength in intense laser-foil interactions.

We have shown that there is significant lateral expansion of the electron cloud in thin foils irradiated by ultraintense laser pulses and that the electron motion is inhibited at target-vacuum interfaces, leading to the formation of strong electric fields and resulting in ionization and ion acceleration. Using ion emission to quantify the E field at varying distances from the laser focus, we have also shown that hot electron transport occurs long after the time of the laser pulse driver.

Two-dimensional spatial mapping of ion emission complements other methods of E-field measurement such as proton probing [24], which provide an integrated measurement across the target surface, and opens the possibility to access new physics on transient E-field detection.

The authors would like to acknowledge the scientific and technical expertise of the personnel at the Vulcan Laser Facility. O. L. and F. L. acknowledge support from the COST program. M. Z. received support from the Royal Society.

*Author to whom correspondence should be addressed.
Email address: p.mckenna@phys.strath.ac.uk
†Also at AWE plc, Aldermaston, Reading, RG7 4PR, UK.

[1] M. Tabak *et al.*, Phys. Plasmas **1**, 1626 (1994).
[2] S. C. Wilks *et al.*, Phys. Plasmas **8**, 542 (2001).
[3] M. Roth *et al.*, Phys. Rev. ST Accel. Beams **5**, 061301 (2002).
[4] P. Gibbon, Phys. Rev. E **72**, 026411 (2005).
[5] L. Robson *et al.*, Nature Phys. **3**, 58 (2007).
[6] C. Reich *et al.*, Phys. Rev. Lett. **84**, 4846 (2000).
[7] K. Eidmann *et al.*, Appl. Phys. Lett. **43**, 440 (1983).
[8] D. W. Forslund and J. U. Brackbill, Phys. Rev. Lett. **48**, 1614 (1982).
[9] F. Amiranoff *et al.*, J. Phys. D **15**, 2463 (1982).
[10] T. Nakamura *et al.*, Phys. Rev. Lett. **93**, 265002 (2004).
[11] Y. T. Li *et al.*, Phys. Rev. Lett. **96**, 165003 (2006).
[12] H. Habara *et al.*, Phys. Rev. Lett. **97**, 095004 (2006).
[13] Y. Sentoku *et al.*, Phys. Plasmas **11**, 3083 (2004).
[14] S. D. Baton *et al.*, Plasma Phys. Controlled Fusion **47**, B777 (2005).
[15] P. K. Patel *et al.*, Plasma Phys. Controlled Fusion **47**, B833 (2005).
[16] G. D. Tsakiris *et al.*, Phys. Rev. Lett. **46**, 1202 (1981).
[17] M. Hegelich *et al.*, Phys. Rev. Lett. **89**, 085002 (2002).
[18] J. Schreiber *et al.*, Appl. Phys. B **79**, 1041 (2004).
[19] D. R. Welch *et al.*, Nucl. Instrum. Methods Phys. Res., Sect. A **464**, 134 (2001).
[20] TASL-IMAGE, Track Analysis Systems Limited. Details online at www.tasl.co.uk.
[21] P. McKenna *et al.*, Phys. Rev. E **70**, 036405 (2004).
[22] J. C. Kieffer *et al.*, J. Opt. Soc. Am. B **13**, 132 (1996).
[23] Y. Sentoku *et al.*, Phys. Plasmas **10**, 2009 (2003).
[24] M. Borghesi *et al.*, Phys. Plasmas **9**, 2214 (2002).

Paper XI

Laser-wakefield acceleration of monoenergetic electron beams in the first plasma-wave period

S. P. D. Mangles, A. G. R. Thomas, M. C. Kaluza, O. Lundh, F. Lindau, F. S. Tsung, Z. Najmudin, W. B. Mori, C.-G. Wahlström and K. Krushelnick.

Physical Review Letters **96**, 215001 (2006).

PRL 96, 215001 (2006) PHYSICAL REVIEW LETTERS week ending 2 JUNE 2006

Laser-Wakefield Acceleration of Monoenergetic Electron Beams in the First Plasma-Wave Period

S. P. D. Mangles,[1] A. G. R. Thomas,[1] M. C. Kaluza,[1] O. Lundh,[2] F. Lindau,[2] A. Persson,[2] F. S. Tsung,[3] Z. Najmudin,[1] W. B. Mori,[3] C.-G. Wahlström,[2] and K. Krushelnick[1]

[1]*Blackett Laboratory, Imperial College London, London SW7 2BZ, United Kingdom*
[2]*Department of Physics, Lund Institute of Technology, P.O. Box 118, S-22100 Lund, Sweden*
[3]*Department of Physics and Astronomy, UCLA, Los Angeles, California 90095, USA*

(Received 8 March 2006; published 30 May 2006)

Beam profile measurements of laser-wakefield accelerated electron bunches reveal that in the monoenergetic regime the electrons are injected and accelerated at the back of the first period of the plasma wave. With pulse durations $c\tau \geq \lambda_p$, we observe an elliptical beam profile with the axis of the ellipse parallel to the axis of the laser polarization. This increase in divergence in the laser polarization direction indicates that the electrons are accelerated within the laser pulse. Reducing the plasma density (decreasing $c\tau/\lambda_p$) leads to a beam profile with less ellipticity, implying that the self-injection occurs at the rear of the first period of the plasma wave. This also demonstrates that the electron bunches are less than a plasma wavelength long, i.e., have a duration <25 fs. This interpretation is supported by 3D particle-in-cell simulations.

DOI: 10.1103/PhysRevLett.96.215001 PACS numbers: 52.38.Kd, 52.59.−f

Laser-wakefield acceleration (LWFA) has been brought closer to practical reality with recent experimental results [1–3] which demonstrated the production of narrow energy spread $\Delta E/E \simeq 3\%$ electron beams from compact, high gradient laser-plasma accelerators. LWFA works through the interaction of a short ultraintense laser pulse with a low density plasma. The ponderomotive force of the laser pulse pushes electrons away from regions of high intensity. Space charge forces due to the stationary ion background lead to the formation of a plasma wave in the wake of the laser pulse. The plasma-wave phase velocity matches the group velocity of the laser in the plasma, which, in low density plasmas, is close to (but slightly less than) the speed of light in vacuum. Because the plasma wave consists of regions of high and low electron density there is an associated longitudinal electric field with a phase velocity close to c—ideal for the acceleration of electrons. The acceleration gradients are typically orders of magnitude higher than those possible in conventional accelerators, allowing electrons with hundreds of MeV to be produced over distances on the order of a few millimeters. Such compact accelerators offer the opportunity of university scale (as opposed to national laboratory scale) radiation sources including electrons, x rays [4], and THz radiation [5].

By driving the plasma wave to large amplitude, which is generally achieved through self-focusing and pulse compression of the driving laser pulse in the wake itself in a positive feedback process, it is possible to inject background electrons into the plasma wave to be accelerated, removing the need for external injection mechanisms. Prior to the experimental results reported in [1–3] and the simulations presented in [6], the electron energy distribution measured in self-injected wakefield acceleration experiments were always ''quasi-Maxwellian,'' having an exponential reduction in number towards high energies.

With a sufficiently short high-intensity pulse, or with sufficient self-modulation and compression, it is possible to enter the ''bubble'' regime [6,7] (similar to the ''blow-out'' regime in particle driven wakefield accelerators [8]). Here a short pulse is defined to be one where the pulse length is comparable to the wavelength of the plasma wave it generates, i.e., when $c\tau \simeq \lambda_p$ [τ is the FWHM duration of the laser pulse and λ_p is the wavelength of a relativistic plasma wave; $\lambda_p = 2\pi c/\omega_p$; ω_p is the plasma frequency $\omega_p = (n_e e^2/m_e \epsilon_0)^{1/2}$]. In the bubble regime the electrons are pushed away so strongly by the laser pulse that a plasma cavity (i.e., a region devoid of electrons) forms behind the laser. Because the heavy plasma ions are much less affected by the ponderomotive force the cavity has a strong electric field which has ideal accelerating properties including linear accelerating and focusing fields.

Simulations of recent experiments which produced monoenergetic electron beams have shown that the electrons are trapped within the first period of the plasma wave. This has been difficult to test experimentally because the physical size and duration of the injected bunch are small and the electron bunch is within the plasma bubble, making probing (with, for example, laser or particle sources) difficult.

In this Letter, we report a measurement that demonstrates that the high-energy electrons are indeed injected into the rear of the first plasma-wave period. Measurements of the transverse profile of the electron beam in a LWFA experiment reveal that, when the laser pulse length is comparable to the plasma wavelength, the electron beam profile is elliptical. This is due to an increase in the beam emittance in the plane of polarization of the laser caused by

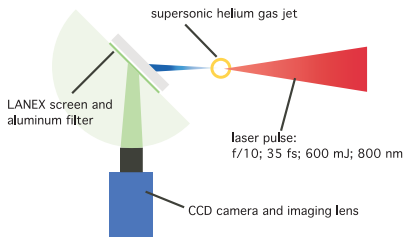

FIG. 1 (color online). Schematic of the experimental setup shown from above.

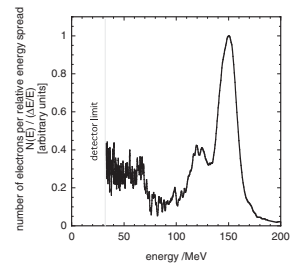

FIG. 2. Example electron spectrum taken at a plasma density of $n_e = 2 \times 10^{19}$ cm^{-3} with laser parameters of $\tau = 35$ fs, $E = 600$ mJ.

the interaction of the electrons with the laser electric field. When the pulse length is made shorter than the plasma wavelength the degree of ellipticity decreases, confirming that this effect is indeed due the interaction with the laser pulse.

The experiments were performed with the 10 Hz multi-THz femtosecond laser at the Lund Laser Centre, a Ti:sapphire system delivering 35 fs pulses of up to 35 TW at a central wavelength of 800 nm. The laser pulses are focused onto the edge of a supersonic gas jet using an $f/10$ off-axis parabolic mirror. The experimental setup is shown in Fig. 1. The gas jet is capable of producing electron densities in the range $(0.5–5) \times 10^{10}$ cm^{-3}. Measurements of the electron energy distribution were performed using a magnetic spectrometer with a scintillating screen (Kodak Lanex) and CCD imaging system as the detector. These show the production of narrow energy spread electron beams over a range of densities with energies up to 200 MeV and energy spreads of a few percent. An example electron spectrum is shown in Fig. 2 taken at a plasma density of $n_e = 2 \times 10^{19}$ cm^{-3}.

A separate Lanex screen could be inserted into the path of the electron beam to allow the electron beam profile to be measured. The screen was 320 ± 10 mm from the laser focus. A 12 mm layer of aluminum is placed in front of this screen so that the beam profile was due to electrons with energies above ≈ 7 MeV. Scattering through the aluminum plate for the high-energy electron beam contributes to less than 5% of the beam size for electron energies greater than 70 MeV (corresponding to the majority of the electron signal above 7 MeV). The scintillator screen emits light through 2π sr and can therefore be viewed from a range of angles. By placing the screen at 45° to the beam propagation direction and imaging the screen from a viewing angle of 90° we could observe the electron beam profile without any projection error and without the need to place mirrors or detectors into the electron beam path behind the screen.

A zero order mica $\lambda/2$ plate was placed in the unfocused laser beam to allow the plane of polarization to be continuously rotated, allowing any effects of the laser polarization on the beam profile to be investigated. The plasma density in the gas jet was obtained from forward Raman scattering measurements. These were performed by detuning the grating compressor resulting in a significantly longer laser pulse ($c\tau \gg \lambda_p$) than that used in the electron acceleration experiments as the growth rate of forward Raman scattering is too small in the regime where $c\tau \simeq \lambda_p$ [9].

The first set of results presented were obtained with a pulse duration of 68 fs and a plasma density of 2.2×10^{19} cm^{-3}, i.e., with $c\tau \simeq 3\lambda_p$. The beam profile of the electron beam ($E > 7$ MeV) was measured as described above for various polarization angles. Figure 3 shows some typical beam profiles. The profiles are clearly elliptical and the axis of the ellipse is directly correlated with the polarization of the laser.

To quantify the electron beam ellipticity an ellipse is fitted to the half-maximum contour of the profile, hence the eccentricity of the ellipse $\epsilon = \sqrt{(1 - b^2/a^2)}$, where a and b are the major and minor axes of the ellipse, can be calculated for each profile. Figure 4 shows how the tilt angle of the ellipse varied with the laser polarization. A direct correlation is revealed by a least-square fit to the data, indicating a gradient close to unity of 1.09 ± 0.06 and a correlation coefficient of $R^2 = 0.77$. The error bars represent our estimate of a systematic error in the laser polarization angle after insertion of the wave plate. The fluctuations in the beam profile tilt are probably due to shot-to-shot fluctuations in the experimental parameters, the main sources of fluctuation include the laser energy, pulse duration, focal spot, and plasma profile. The fact that the

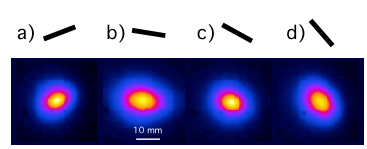

FIG. 3 (color online). Representative data showing the variation of electron beam profile with laser polarization at $n_e = 2.2 \times 10^{19}$ cm^{-3} with a pulse duration of 68 fs. The black line indicates the laser polarization angle ±5°. (a) −20°, (b) 10°, (c) 30°, and (d) 50°.

PRL **96,** 215001 (2006) PHYSICAL REVIEW LETTERS week ending 2 JUNE 2006

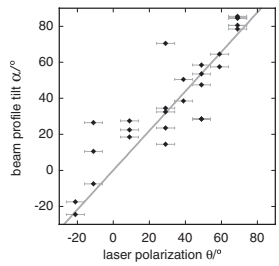

FIG. 4. Variation of electron beam profile tilt with respect to laser polarization. Black squares: experimental data. Gray line: least-squares linear fit, gradient 1.09 ± 0.07.

elliptical profile varies with the laser polarization indicates that it is not caused by an asymmetry in the focal spot. The effect on the focal spot after insertion of the wave plate has been tested and shown to be negligible. Measurements of the electron beam profile farther downstream show a larger eccentricity indicating that the ellipticity is a signature of an asymmetry in the transverse emittance rather than simply an asymmetric beam divergence.

With a shorter laser pulse duration of 35 fs we were able to observe the variation of the electron beam profile shape over a range of plasma densities. This part of the experiment was performed with the $\lambda/2$ plate removed from the setup.

Figure 5 shows four typical electron beam profiles at various plasma densities. The beam is highly collimated with a divergence angle of less than 25 mrad over the range of densities studied. The analyzed data from a number of beam profiles is shown in Fig. 6. At the lowest density the electron beam has the lowest ellipticity ($\epsilon = 0.63 \pm 0.08$ at $n_e = 2.1 \times 10^{19}$ cm^{-3}) and the beam becomes more elliptical as the plasma density is increased. The peak ellipticity observed was at $n_e = 2.7 \times 10^{19}$ cm^{-3} with $\epsilon = 0.77 \pm 0.03$. When the density was increased further the beam divergence at 90° to the laser polarization increased, leading to a more divergent but more circular beam.

The fact that the electron beam ellipticity reduces as the ratio $c\tau/\lambda_p$ reduces implies that the electrons spatially overlap the laser pulse and in fact stem from the back of the first wave period. Extrapolation of the eccentricity data

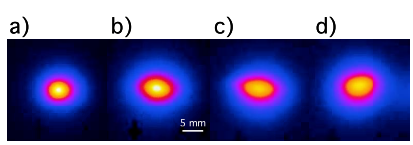

FIG. 5 (color online). Four typical electron beam profile measurements at various plasma densities. (a) $n_e = 2.1 \times 10^{19}$ cm^{-3}, (b) $n_e = 2.4 \times 10^{19}$ cm^{-3}, (c) 2.7×10^{19} cm^{-3}, and (d) 3.0×10^{19} cm^{-3}. The laser polarization is horizontal.

(from the lowest three densities measured) to still lower densities reveals that the beam profile is expected to be circular (i.e., $\epsilon = 0$) at a plasma density corresponding to $c\tau \approx \lambda_p/2$ as shown in the inset of Fig. 6(a). Extrapolation of the beam size data is also not inconsistent with a circular beam close to $c\tau = \lambda_p/2$. This is because the bubble is approximately λ_p long and the electrons only extend into the bubble by half a plasma wavelength, as this is the dephasing point. This implies that the electron bunches in this experiments are less than a plasma wavelength long and therefore have a duration of less than 25 fs at a plasma density of $n_e = 2.1 \times 10^{19}$ cm^{-3}.

At lower density, λ_p is longer and the laser pulse occupies a smaller fraction at the front of the plasma wave. In the regime where $c\tau < 2\lambda_p$ the intensity of laser light at the back of the first wave period is reduced for longer plasma wavelengths, i.e., lower electron densities. Hence, if the electrons are generated at the back of the first wave period, then at low densities the effect of the laser field on the electron motion will be reduced, as observed experimentally. The observed increase in the divergence at 90° to the laser polarization at high density is probably because the effects of the transverse plasma fields are greater than the effect of the interaction with the laser field. This is due to the increase in the plasma-wave electric field and the decrease of the transverse size of the plasma wave with increasing density. This is probably why these effects have not been observed in earlier self-modulated wakefield experiments.

Earlier theoretical work on multidimensional wave breaking suggested that transverse wave breaking occurs more easily farther behind the laser pulse [10] due to an increase in the curvature of the wakefield, and hence we might have expected the electron injection to occur in trailing wave periods. The fact that the electrons in our

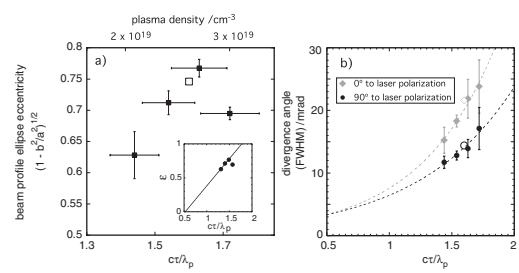

FIG. 6. (a) Variation of electron beam profile ellipticity with plasma density (top axis) and ratio of pulse duration to plasma wavelength, $c\tau/\lambda_p$ (bottom axis). Inset shows the same data with an extrapolation to $\epsilon = 0$. (b) Variation of the electron beam divergence with the ratio $c\tau/\lambda_p$. Diamonds: beam divergence in the plane of polarization of the laser. Circles: beam divergence 90° to the plane of laser polarization. Open symbols are data from the 3D particle-in-cell simulation described in the text.

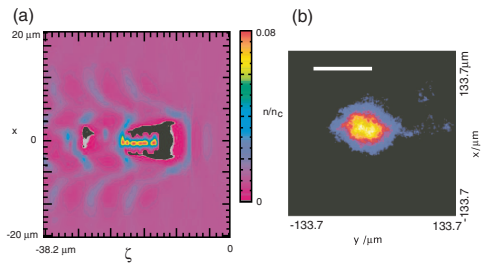

FIG. 7 (color online). (a) Electron density in x-ξ plane from a 3D simulation (described in the text) showing injection of electrons at the rear of the first plasma-wave period. (b) Projection of the electron beam profile 2.3 mm from focus; the white line indicates the laser polarization.

experiments come from the first wave period is strong evidence that the wakefield structure is more like the bubble regime first described in [6], although it is likely that some evolution of the laser pulse (i.e., self-focusing and pulse compression in the wakefield) must occur before the bubble regime is reached. Simulations of similar experimental parameters have already been reported [1–3,11–14].

Results from a 3D simulation performed at a density where $c\tau = 1.6\lambda_p$ are presented in Fig. 7. The pulse parameters correspond to a peak vacuum intensity of 5×10^{18} W cm^{-2} in a focal waist of $w_0 = 12.5$ μm. The pulse duration (FWHM) $\tau = 40$ fs and $n_e = 2 \times 10^{19}$ cm^{-3}. The simulation window moves along the laser propagation direction at the speed of light ($\xi = z - ct$ is the direction of laser propagation, and x and y are the transverse coordinates). The resolution of the simulation was carefully chosen to minimize numerical dispersion effects, with 40 cells/λ_0 in the laser propagation direction and 27 cells/λ_p in the transverse dimensions. This resolution was chosen as the result of a series of 2D simulations as discussed in [15].

Figure 7(a) shows a cross section (at $y = 0$) of the electron density in the simulation. The high density "stem" of electrons emanating from the back of the bubble are the self-injected electrons. At this density the electrons interact with the laser field, resulting in a larger transverse emittance in the plane of laser polarization. It is this motion in the laser field which gives rise to the elliptical beam profile shape observed in the experiment. The projected x-y profile of the electron beam ($E > 10$ MeV) from the 3D simulation is shown in Fig. 7(b). This profile is calculated from the trajectories of electrons at the end of the simulation and is projected 0.3 mm from the end of the plasma (2.3 mm from the laser focus). There is a clear ellipticity to the beam profile, with the divergence angle for electrons with $E > 10$ MeV (FWHM) being 22 mrad in the plane of laser polarization and 14 mrad at 90° to the laser polarization. The eccentricity of this profile, calculated using the same method as the experimental profiles, is $\epsilon = 0.75$. The electron beam eccentricity and divergence from the simulation are shown as open symbols in Fig. 6 and are in good agreement with the experimentally observed values.

The agreement between 3D particle-in-cell simulations and laser-plasma acceleration experiments can be excellent in terms of the principal output (e.g., the electron spectra in [3]). However, it is more difficult to ensure that the physical processes, such as electron injection, are accurately described by the numerical modeling. The results described here help to improve our confidence in the numerical modeling techniques employed.

These results also show experimentally that the best quality electron bunches, especially in terms of transverse emittance, will be produced when the ratio of pulse duration to plasma wavelength is small, as was discussed in [16]. It may also be possible to reduce the emittance even in the case of $c\tau \simeq \lambda_p$ with the use of circularly polarized laser pulses; however, this is a subject for further investigation.

We acknowledge support from the Swedish Research Council, the Knut and Alice Wallenberg foundation, the EU Access to Research Infrastructures Programme (RII3-CT-2003-506350 Laserlab Europe) and Research Councils U.K.

[1] S. P. D. Mangles *et al.*, Nature (London) **431**, 535 (2004).
[2] C. G. R. Geddes *et al.*, Nature (London) **431**, 538 (2004).
[3] J. Faure *et al.*, Nature (London) **431**, 541 (2004).
[4] A. Rousse *et al.*, Phys. Rev. Lett. **93**, 135005 (2004).
[5] W. P. Leemans *et al.*, Phys. Rev. Lett. **91**, 074802 (2003).
[6] A. Pukhov and J. Meyer-ter Vehn, Appl. Phys. B **74**, 355 (2002).
[7] I. Kostyukov, A. Pukhov, and S. Kiselev, Phys. Plasmas **11**, 5256 (2004).
[8] J. B. Rosenzweig *et al.*, Phys. Rev. A **44**, R6189 (1991).
[9] W. B. Mori, IEEE J. Quantum Electron. **33**, 1942 (1997).
[10] S. V. Bulanov *et al.*, Phys. Rev. Lett. **78**, 4205 (1997).
[11] F. S. Tsung *et al.*, Phys. Rev. Lett. **93**, 185002 (2004).
[12] K. Krushelnick *et al.*, Phys. Plasmas **12**, 056711 (2005).
[13] C. G. R. Geddes *et al.*, Phys. Plasmas **12**, 056709 (2005).
[14] V. Malka *et al.*, Phys. Plasmas **12**, 056702 (2005).
[15] F. S. Tsung *et al.*, Phys. Plasmas (to be published).
[16] V. Malka *et al.*, Science **298**, 1596 (2002).

Paper XII

On the stability of laser wakefield electron accelerators in the monoenergetic regime

S. P. D. Mangles, A. G. R. Thomas, O. Lundh, F. Lindau, M. C. Kaluza, A. Persson, C.-G. Wahlström, K. Krushelnick and Z. Najmudin.

Physics of Plasmas **14**, 056702 (2007).

PHYSICS OF PLASMAS **14**, 056702 (2007)

On the stability of laser wakefield electron accelerators in the monoenergetic regime[a)]

S. P. D. Mangles[b)] and A. G. R. Thomas
Blackett Laboratory, Imperial College, London SW7 2BZ, United Kingdom

O. Lundh and F. Lindau
Department of Physics, Lund University, PO Box 118, S-22100 Lund, Sweden

M. C. Kaluza[c)]
Blackett Laboratory, Imperial College, London SW7 2BZ, United Kingdom

A. Persson and C.-G. Wahlström
Department of Physics, Lund University, PO Box 118, S-22100 Lund, Sweden

K. Krushelnick[d)] and Z. Najmudin
Blackett Laboratory, Imperial College, London SW7 2BZ, United Kingdom

(Received 3 November 2006; accepted 12 December 2006; published online 21 March 2007)

The effects of plasma density and laser energy on the stability of laser produced monoenergetic electron beams are investigated. Fluctuations in the principal beam parameters, namely, electron energy, energy-spread, charge, and pointing, are demonstrated to be minimized at low densities. This improvement in stability is attributed to the reduced time for pulse evolution required before self-injection occurs; i.e., that the pulse is closest to the matched conditions for these densities. It is also observed that electrons are only consistently produced above a density-dependent energy threshold. These observations are consistent with there being a threshold intensity ($a_0 \gtrsim 3$) required for the occurrence of self-injection after accounting for pulse compression. © *2007 American Institute of Physics*. [DOI: 10.1063/1.2436481]

I. INTRODUCTION

The production of high-energy electrons from university laboratory scale high-power lasers is currently a very active field of research. By using short, intense laser pulses to drive relativistic plasma waves, it is possible to produce electron beams with high energy, low energy-spread, and low divergence. Such electron beams may have energies at the GeV level, energy-spreads of a few percent, normalized transverse emittance below π mm mrad, and bunch durations below 25 fs.[1–6]

When an intense laser pulse travels through an underdense plasma, it can excite a relativistic plasma wave. The plasma wave is generated by the ponderomotive force of the laser pulse, which expels the mobile electrons from regions of high laser intensity while the heavier ions remain stationary. The resulting space charge distribution is an electron plasma wave traveling with a phase velocity set by the group velocity of the laser pulse. In a sufficiently underdense plasma this velocity is close to the speed of light. The strong electric fields set up by the charge separation are ideal for accelerating electrons. Wakefield generation is most efficient when the pulse dimensions (i.e., waist and pulse length) are on the order of the wavelength of the plasma wave $\lambda_p = 2\pi c/\omega_p$, where ω_p is the plasma frequency.

Electrons are produced from these interactions when some of the electrons in the plasma are injected into and trapped by the wave. This can happen if the wakefield amplitude is sufficiently high, i.e., for electric field strengths $E \gtrsim E_0 = m_e c \omega_p / e$. In a one-dimensional (1D) plasma wave, the electrons have longitudinal velocity associated with their wave motion. Hence, to accelerate an electron that is part of the wave motion, it is necessary to turn around an electron moving backwards at $-v_p$, so that it is going forwards at $+v_p$. In 1D, the relativistically correct electric field strength associated with the plasma wave for this to happen is given by $E_{\mathrm{WB}} = \sqrt{2(\gamma_p - 1)} \cdot E_0$, where γ_p is the Lorentz factor associated with the phase velocity of the wave v_p.[7] If too many electrons are dephased from the wave motion, the wave structure can no longer be sustained; i.e., the wave breaks. In a multidimensional plasma wave, the transverse motion of electrons means that it is possible to have electrons that are part of the wave motion, but that also have only a sufficiently small longitudinal velocity at the correct phase of the plasma wave for them to be picked up and accelerated at reduced values of the electric field strength compared to the 1D cold wavebreaking limit.

When the wakefield structure becomes spherical (i.e., a λ_p^3 "bubble") electrons at the back of the bubble have zero forward momentum in the wave frame $\xi = z - v_p t$, and thus can be injected into the accelerating fields of the bubble. If this process is controlled so that it takes place sufficiently slowly, the wave structure remains intact. Because the injection occurs in a spatially localized position and the electrons

[a)] Paper UI2 4, Bull. Am. Phys. Soc. **51**, 259 (2006).
[b)] Invited speaker.
[c)] Current address: Institut für Optik und Quantenelektronik, Friedrich-Schiller-Universität, Max-Wien-Platz 1, 07743 Jena, Germany.
[d)] Current address: Center for Ultrafast Optical Science and Department of Nuclear Engineering, 6103 ERB-1, 2200 Bonisteel Blvd., University of Michigan, Ann Arbor, Michigan.

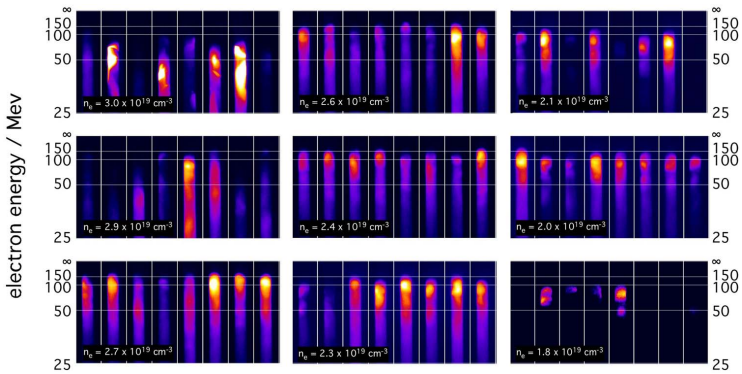

FIG. 1. (Color online) Shot-to-shot variation in electron energy spectrum at various plasma densities. Laser parameters $\mathcal{E}_L \approx 0.7$ J, $\tau_{\mathrm{FWHM}}=35$ fs. The spectrometer axis is at the top of each image (marked by ∞), electrons are deflected downwards according to their energy. The shots were taken with collimation angle $\approx 0.5°$, giving energy resolution $\approx 10\%$ at 100 MeV and $\approx 2\%$ at 25 MeV. The brightness of the image is proportional to the charge incident on the screen (false color). The color scale for each density is normalized to the peak signal for that density.

are injected with similar energies, after acceleration a narrow-energy-spread electron beam can be produced. Electrons may continue to be injected until the space charge field of the injected bunch becomes comparable to the wakefield strength. At this point beam loading can stop further injection. If the period of injection is significant compared to the dephasing time, then the electrons injected at the beginning of the injection phase will have different energy to those injected later. Even in this case the narrow-energy-spread beams may be produced by phase rotation as the beam overtakes (dephases from) the plasma wave. Though in this case, the monoenergetic peaks are likely to sit on top of a spectrum with greater energy-spread.[8] For wakefields with an amplitude E_0, the length over which dephasing occurs is $L_{\mathrm{dp}}=\lambda_p n_c/n_e$. Dephasing also limits the maximum energy gain to $w_{\max}=2m_e c^2 n_c/n_e$. Here, n_e is the electron density and n_c is the critical density for propagation of the laser (i.e., when $\omega_0=\omega_p$).

A narrow energy-spread is vital for many applications of these electron beams, such as their use in the generation of short wavelength coherent radiation from free-electron lasers. An equally important property required for applications of these electron beams is stability. It is inconceivable that quality research can be done using laser produced electrons, or radiation generated by them, if the electron beam parameters suffer from large shot-to-shot fluctuations. This paper demonstrates the degree of stability achievable with current laser systems, and discusses how these fluctuations can be reduced. By studying the stability we are able to deduce that pulse evolution is one of the major sources of instability, implying that using matched pulses sufficiently intense to inject electrons will result in further improvements in stability.

II. SHOT-TO-SHOT STABILITY OF LASER-PRODUCED ELECTRON BEAMS

The experiments were performed with the 10 Hz multiterawatt femtosecond laser at the Lund Laser Centre, a Ti:sapphire system delivering 35-fs pulses of up to 35 TW at a central wavelength of 800 nm. The laser pulses are focused onto the edge of a supersonic gas jet using an $f/10$ off-axis parabolic mirror. The diffraction limited spot size ($1/e^2$ intensity radius) for a Gaussian beam in this geometry is $w_0=5$ μm, with a Rayleigh range of $2Z_{\mathrm{R}}=2\pi w_0^2/\lambda=196$ μm. For a top-hat profile, the full width at half-maximum $w_{\mathrm{FWHM}}=8.3$ μm, $w_{1/e^2}=5.4$ μm, with a Rayleigh range of $2Z_{\mathrm{R}}=215$ μm. Cryogenic cooling of the Ti:sapphire crystal in the final amplifier ensures close to diffraction limited performance. During this experiment, the laser was capable of producing on-target energies up to 0.7 J, corresponding to a peak intensity of $I_0 \simeq 4\times 10^{18}$ W cm^{-2}, or normalized vector potential of $a_0 \simeq 1.4$.

The helium gas jet is capable of producing electron densities in the range $n_e=(0.5-5)\times 10^{19}$ cm^{-3} (measured offline using an interferometric technique). The supersonic nozzle produces a 2 mm top-hat radial profile with an approximately 300 μm linear ramp at the edges.

Measurements of the electron energy distribution were performed using a magnetic spectrometer with a scintillating screen (Kodak Lanex) and CCD imaging system as the detector. The magnet in the spectrometer consists of 38 mm diameter circular pole pieces and can produce field strengths up to 0.8 T. For 0.8 T, the spectrometer can measure electron energies $W<300$ MeV with a few percent resolution when used in conjunction with a steel collimator. Separate measurements of the electron beam profile were made with a second scintillating screen placed between the electron spectrometer and the gas jet. A 12 mm thick aluminum sheet was placed in front of the beam profile monitor to prevent electrons below ≈ 7 MeV reaching the detector. The beam profile monitor was placed at 45° to the laser beam axis to allow imaging at 90° without projection errors.

Figure 1 shows a series of measured electron energy spectra for a range of different plasma densities. The highest density presented ($n_e=3\times 10^{19}$ cm^{-3}) shows a highly unstable spectrum, containing some narrow-energy-spread features. However, these narrow-energy-spread features are superimposed on top of a broad-energy-spread "dark current." There is also structure in the transverse direction.

As the density is reduced the electron beam becomes more monoenergetic, with the energy spread of the electron bunch becoming narrower. The stability of the electron beam

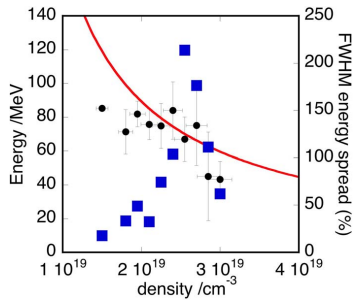

FIG. 2. (Color online) Variation in electron beam energy (circles, left axis) and percent FWHM energy-spread (squares, right axis) with plasma density. The curves shows the linear estimate for maximum energy $w_{\max}=2m_ec^2(n_c/n_e)$. The error bars on the beam energy represent the standard deviation from the mean value over a series of shots.

is noticeably improved. The ratio of the charge in the monoenergetic peak to the charge in the dark current, also increases as the density decreases. Finally, it is noted that the energy of the electron beam also increases as the density is decreased.

The data clearly show a density threshold for the appearance of monoenergetic beams. Above $n_e=2\times10^{19}$ cm^{-3}, monoenergetic electrons beams are consistently observed (close to 90% of shots). When the density is reduced below $n_e=2\times10^{19}$ cm^{-3}, the monoenergetic electron beam appears more sporadically ($\lesssim$50% of the time) and the dark current is also dramatically reduced.

Figure 2 summarizes the data presented in Fig. 1. It shows the variation of the electron beam energy with plasma density and the variation of the relative energy-spread of the electron beam. The curve is the linear (nonrelativistic) estimate for the maximum energy gain $W_{\max}$ from the plasma wave due to dephasing.

At high electron number density ($n_e=3\times10^{19}$ cm^{-3}) the monoenergetic beam energy is below $w_{\max}$, while for number densities in the range $n_e=(2-2.7)\times10^{19}$ cm^{-3}, the beam energy is approximately $W_{\max}$. Below $n_e=2\times10^{19}$ cm^{-3}, the beam energy is again lower than $W_{\max}$. At these lower densities, it is likely that the electrons have not reached the dephasing length; i.e., the interaction length was too short to reach the maximum energy $W_{\max}$. The (linear) dephasing length $L_{\rm dp}$ for $n_e=1\times10^{19}$ cm^{-3} is 1.85 mm, close to the entire length of the gas jet. Since there must be some evolution of the pulse (i.e., self-focusing and compression) before the wakefield reaches the point of self-injection, there is unlikely to be sufficient length in the 2 mm gas jet after injection, for the electron beam to reach the dephasing energy, $W_{\max}$.

The standard picture of self-injection in multidimensional nonlinear plasma waves is as follows: after the ponderomotive force of the laser pulse expels electrons at the front of the plasma wave bubble, electrons return laterally at the back of the bubble in response to the charge imbalance. In the wave frame, electrons that have low longitudinal velocity are injected at the rear of the bubble. Those electrons that are injected first are accelerated ahead of those injected last until they reach the front of the plasma wave and are dephased. At this point, the tail of the bunch approaches the same energy as the head of the bunch. In this simple model, one would expect the energy-spread to be minimized when the electron beam energy is close to the dephasing energy. For this simple model to remain valid requires that the plasma wave electric field strength is constant over the duration of injection. The plasma wave amplitude can be affected by beam loading and laser pulse evolution. Simulations and experimental evidence[6] show that the electron bunch is less than a plasma wavelength in length ($<$25 fs), and simulations show that significant pulse evolution occurs over many $1/\omega_p$. It is therefore unlikely that the change in the wakefield amplitude due to pulse evolution is the cause for the observed increase in the beam energy spread as the beam energy approaches $W_{\max}$.

Beam loading, i.e., the flattening of the laser wake due to the space charge of the electron bunch, will be more significant at higher densities, since the accelerated bunch has more charge, but beam loading is also unlikely to lead to increased energy spread. Once the plasma wakefield reaches the threshold for self-injection, electrons are continuously injected into the wave. The major effect of beam loading is to lower the electric field at the back of the bubble. If there is any significant lowering of the electric field then trapping can no longer occur. The cessation of trapping leads to narrow-energy-spread, short duration electron bunches. The flattening of the wake electric field due to beam loading results in the maximum energy of electrons injected later being lower than the maximum energy of those injected earlier, This may result in some increase in the energy spread but is unlikely to lead to the very large energy spreads observed when the beam energy approaches $W_{\max}$. This suggests an additional mechanism is causing longitudinal energy spread in the accelerated electron bunch.

It has been shown experimentally and in simulations that the interaction of the injected electrons and the laser field leads to an increase in the transverse emittance of the electron bunch.[6] This effect is greater at high densities due to the increased overlap between the electron bunch and laser field. An alternative explanation for the increased energy spread observed in these experiments when $W\approx W_{\max}$ is that the interaction with the laser field increases the longitudinal emittance. The increase in transverse emittance is simply due to the extra transverse momentum electrons gain from the laser electric field. To explain an increase in longitudinal emittance due to the overlap between the electron bunch and the laser pulse requires that there is some direct laser acceleration occurring. At high densities the overlap between the laser pulse and the electron bunch at the back of the first plasma wave period is greater than at lower densities because at high density the laser occupies more of the first plasma wave period. The requirements for a direct laser acceleration (DLA) mechanism, such as that described in Ref. 9, are that there is an electron bunch, a transverse focusing force, and an intense laser field. These are clearly present in the situation described and an overlap between the electron bunch and the laser field (i.e., at high density) should result in some

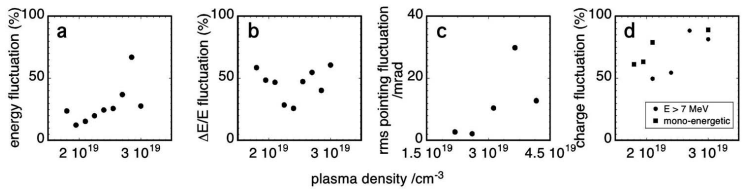

FIG. 3. Fluctuation of electron beam parameters as a function of plasma densities. (a) Standard deviation of electron beam peak energy ($\sigma_W/\bar{W}$). (b) Standard deviation of relative energy-spread [$\sigma_{\Delta W/W}/(\overline{\Delta W/W})$]. (c) Root mean square pointing fluctuation [$\sqrt{(\theta-\bar{\theta})^2}$]. (d) Standard deviation of electron charge as measured in the monoenergetic peak on the electron spectrometer (black squares) and as measured with a beam profile monitor for $W>7$ MeV (gray circles) ($\sigma_C/\bar{C}$).

DLA. The acceleration of the bunch will still be dominated by the plasma wave electric field, but the DLA mechanism should act to increase the longitudinal emittance (i.e., energy spread) of the bunch.

Figure 3 shows the variation with density of the fluctuations in the principal beam parameters, specifically the energy, relative energy-spread, pointing, and charge. Each point on these graphs represents the standard deviation in the beam parameter from at least five measured electron spectra. There are some clear trends with density. The electron beam energy is significantly more stable at low densities exhibiting a standard deviation of 12% from its mean value [Fig. 3(a)]. However the shot-to-shot variation in energy-spread of the electron beam $\Delta W/W$ shows no obvious trend with density [Fig. 3(b)]. The relative energy-spread fluctuates by approximately 50% for all the densities investigated.

The beam pointing fluctuation, expressed as the root mean squared angular deviation from the mean position of the beam, shows a strong trend with density, with the stability increasing at lower densities [Fig. 3(c)]. The most stable beams showed fluctuations in pointing of 6 mrad. The beam charge also shows a trend of increasing stability with decreasing density. Figure 3(d) shows two sets of data recorded on different data runs. One set shows the fluctuation in the total charge of the beam as measured using the integrated signal on a beam profile monitor (for electrons with $W>7$ MeV). The second set of data shows the fluctuations in the charge contained in the monoenergetic peak in the electron spectrometer, which shows that there is an appreciable variation in the charge in the accelerated beam, even in the best case (>50%). Because the pointing stability and beam divergence are on the same order as the acceptance angle of the electron spectrometer, there is a coupling between pointing and charge stability. This explains why the fluctuations in the charge in the monoenergetic beam on the spectrometer are greater than the fluctuations of the whole beam profile.

The experimental data clearly show that the most stable beams were achieved at the lower densities close to $n_e=2\times10^{19}$ cm^{-3}. At this density, the plasma wavelength is 7.6 μm. It has been demonstrated experimentally and in simulations[10] that self-focusing of an ultrashort pulse occurs until the pulse beam diameter (FWHM) reaches a stable value. In this regime ($a_0\sim1$), the stable value is on the order of the plasma wavelength λ_p. Since the (diffraction limited) vacuum focal spot is approximately 8 μm, it is clear that the lowest density corresponds to the closest to a matched spot. At higher densities, where the matched spot size is smaller, a greater degree of self-focusing must occur before the matched spot size is reached and this will lead to a greater degree of instability. The same is true when considering pulse compression and self-modulation of the pulse. At the highest density ($n_e=3\times10^{19}$ cm^{-3}), the ratio of pulse length to plasma wavelength ($c\tau/\lambda_p$) is 1.7. At $n_e=2\times10^{19}$ cm^{-3}, $c\tau/\lambda_p$ is closer to unity. Since pulse evolution also occurs in a plasma wave until $c\tau/\lambda_p<1$ due to a combination of photon acceleration (and deceleration) and group velocity dispersion, the less the initial pulse length, the less evolution will be required. These data suggest that the instabilities in the electron beam parameters result from the period of pulse evolution occurring before injection. Hence, using a matched pulse with sufficient intensity to inject electrons immediately upon entry into the plasma would mitigate some of the sources of instability present in the current generation of self-injecting laser wakefield accelerators.

III. THRESHOLD FOR GENERATION OF MONOENERGETIC ELECTRON BEAMS

A characteristic of these experiments is a density threshold for the production of monoenergetic electron beams. Above this threshold, monoenergetic electron beams are produced consistently. At a plasma density of $n_e=2.0\times10^{19}$ cm^{-3}, 89% of 27 shots showed monoenergetic electron beams. Just below this density, at $n_e=1.8\times10^{19}$ cm^{-3} only 50% of eight shots showed monoenergetic electrons beams. When the density was decreased further to at $n_e=1.5\times10^{19}$ cm^{-3}, no energetic electrons were detected (0% of 10 shots).

This threshold is due to the fact that below a certain density the laser energy is too low to drive the wakefield to the point where injection of electrons occurs, even after pulse compression. The laser pulses used in these experiments are not sufficiently intense to drive the plasma wave to the point of injection immediately upon entry into the plasma. Instead, the production of electron beams relies on pulse evolution, i.e., self-focusing and compression, which occurs due to the refractive index gradients in the plasma wave. As the pulse becomes more intense, it is capable of driving a higher-amplitude plasma wave, which has steeper refractive index gradients and thus leads to further pulse focusing and com-

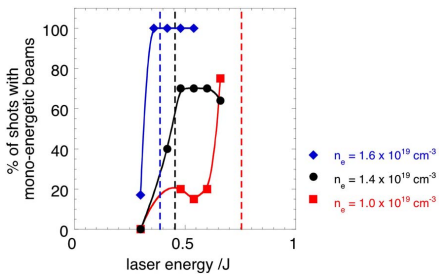

FIG. 4. (Color online) Percentage of shots showing monoenergetic spectra as a function of laser energy for three plasma densities. Diamonds: $n_e = 1.0\times 10^{19}$ cm^{-3}; circles: $n_e = 1.4\times 10^{19}$ cm^{-3}; squares: $n_e = 1.0\times 10^{19}$ cm^{-3}. Dotted lines represent $\mathcal{E}_{\text{threshold}}$ for a threshold vector potential of $a_{\text{threshold}} = 3.2$.

pression. This positive feedback process continues until saturation, which occurs when the pulse has dimensions on the order of $w_{\text{FWHM}} = \lambda_p$ (see Ref. 10) and $c\tau_{\text{FWHM}} = \lambda_p/2$.[11] The density threshold for electron production with a given initial laser energy therefore occurs because there will be some density below which the intensity of the matched pulse will be insufficient to drive the wakefield to the point where injection occurs.

To investigate the effect of this phenomenon on the observed density threshold, the laser energy was varied for a number of fixed densities. In this experiment the plasma density was calculated from the frequency of Raman satellites present in the transmitted laser spectrum when a deliberately lengthened pulse was incident on the gas jet just prior to each set of data. This *in situ* measurement system was developed to monitor degradation in the jet density profile due to wear in the gas jet solenoid. In Fig. 4, the percentage of shots that show monoenergetic spectra as a function of laser energy is plotted for three different densities. Each curve in Fig. 4 shows behavior consistent with the threshold argument described above. At the highest density of $n_e = 1.6\times 10^{19}$ cm^{-3}, the threshold is the most pronounced and occurs at the lowest laser energy, in the range $0.30 < \mathcal{E}_{\text{threshold}}/\text{J} < 0.36$. At this density, the monoenergetic electron beams were seen on 100% of five shots. Evidently, at this density, the laser is compressed to the smallest volume and therefore will achieve the highest intensity once it reaches the matched pulse width and duration. At $n_e = 1.4\times 10^{19}$ cm^{-3}, the threshold behavior is still present, with 70% of 10 shots showing a monoenergetic spectrum. At this density, the threshold occurs in the range $0.30 < \mathcal{E}_{\text{threshold}}/\text{J} < 0.5$. At the lowest density ($n_e = 1.0\times 10^{19}$ cm^{-3}), the stability increases with increasing laser energy, although a stable plateau has not been reached by $\mathcal{E}_{\text{laser}} = 0.68$ J.

We note that the observed thresholds in this data set occur at slightly lower densities than in the initial data set presented in Fig. 1. This is likely due to a better optimized gas flow from the gas jet in the second set of data. The electron beam energies in this data set were also higher, close to $W = 140$ MeV [$W_{\text{max}} \approx 180-110$ MeV in the range $n_e = (1.0-1.8)\times 10^{19}$ cm^{-3}] consistent with this data set being at a lower plasma density than the data in Fig. 1. An improved optimization of the neutral gas probably results in a shorter density scale length at the edges of the gas flow which may promote injection at lower densities. The interaction of the laser pulse with the 100 s μm scale density ramp complicates the pulse evolution stage of the interaction and may effect, for example, pump depletion or the amount of laser energy trapped in the self-focused filament. This demonstrates that the exact gas profile is important in determining the parameters (or threshold) for self-injection and indicates that control of the density profile may be a useful method of controlling the self-injection process.

Using a simple model we can estimate the threshold vector potential required for electron injection. The laser power is related to the spot size and plasma wavelength by

$$\frac{P_L}{P_c} \simeq \frac{\pi^2}{8} a_0^2 \frac{w_0^2}{\lambda_p^2}, \tag{1}$$

where $P_c = 17.3 n_c/n_e$ GW is the critical power for self-focusing, w_0 is the beam waist, and a_0 is the peak normalized vector potential of the laser field. For a Gaussian temporal profile, the pulse duration τ [fs] is related to the peak power by $P_L \simeq 0.92\mathcal{E}_L/\tau_{\text{FWHM}}$ [GW]. If we assume that the compressed pulse waist tends towards λ_p, and the pulse duration towards $\tau_{\text{FWHM}} = \lambda_p/2$ and that all of the initial laser energy is compressed, an expression can be obtained for the threshold laser energy for self-injection:

$$\mathcal{E}_{\text{threshold}} = 23.3 \times 10^9 \left(\frac{n_c}{n_e}\right) a_{\text{threshold}}^2 \tau_{\text{FWHM}}\ [\text{J}]. \tag{2}$$

Treating the vector potential threshold $a_{\text{threshold}}$ as a free parameter, the observed energy thresholds can be fitted to the model using a least-squares method. The predicted values are shown as dotted lines in Fig. 4. Assuming 100% of the initial laser energy is compressed leads to a best fit for $a_{\text{threshold}} = 3.2$. These values are consistent with the observed trends in two-dimensional (2D) and three-dimensional (3D) particle-in-cell (PIC) simulations.[12] This simplified model does not include the following factors: frequency shifts can strongly affect the vector potential; similarly, the fraction of energy trapped and compressed is not likely to be constant over a wide range of densities. In particular, at higher densities, it is unlikely that all of the laser energy will be trapped in a single filament.[10] Nevertheless, the model does provide direct experimental evidence that normalized vector potentials $a_0 \gtrsim 3$ are required in a matched pulse for self-injection to occur. For a multidimensional treatment of nonlinear plasma waves, the matched pulse waist is given by $w_0 = \sqrt{2} a_0 c/\omega_p$.[13] Assuming a Gaussian profile with $a_{\text{threshold}} \simeq 3.2$, this expression becomes $w_{\text{FWHM}} \simeq 5.3 c/\omega_p$, similar to the observed matched spot size.[10]

IV. DISCUSSION

This paper reports a study into the stability of single beam self-injection laser wakefield accelerators. The stability achieved on the Lund multi-terawatt laser system is, in terms of the principal electron beam parameters of energy, energy-

spread, pointing, and charge, an order of magnitude better than achieved in the first proof-of-principle experiments on the Astra laser.[2]

These beams are now of suitable reproducibility for detailed investigations of beam characteristics. For example, it has been possible to effectively cross-correlate the laser field with the electron bunch. In so doing, the injection dynamics have been verified and the ultrashort duration of the electron bunch demonstrated.[6]

It is noted that the laser energy was approximately the same in the two experiments. The major differences between the present experiments and the first experiments are a shorter pulse duration (35 fs compared with 45 fs) and tighter focusing ($f/10$ compared with $f/16$). Both factors result in the laser pulse being initially closer to the matched parameters in the present study, especially the spot size. This is emphasized by the experimentally determined density dependence, which demonstrates an enhanced stability at lower plasma densities, for which the pulse is most closely matched to the ideal dimensions.

Another important factor is the contrast ratio. For the present investigations, the contrast ratio $I_0/I_{\mathrm{ASE}}=10^8$ as compared with 10^6 previously. This has also been demonstrated to improve the observed stability.[14]

The experimental results are also consistent with a threshold intensity required for self-injection, corresponding to a normalized vector potential in the matched pulse of $a_0 \simeq 3$. This is consistent with theoretical calculations for the intensity threshold for transverse self-injection into a 3D plasma wave.[13]

Many of these results are of important consequence for future laser plasma acceleration experiments. For the next generation of ultrashort petawatt class lasers, it should be possible to introduce the pulse into the plasma with a matched pulse width of sufficient intensity to initiate self-injection immediately. For example the Astra Gemini laser, currently under development at the Rutherford-Appleton Laboratory, which will have a pulse energy of $\mathcal{E}_L=15$ J and pulse duration of $\tau=30$ fs. One of the experimental configurations available will be $f/20$ focusing. The focal spot in this configuration will be $w_0 \approx 20$ μm, which will be close to matched at a plasma density $n_e=2\times10^{18}$ cm^{-3}. The linear dephasing energy and length at this density are $W_{\max}=0.85$ GeV and $L_{\mathrm{dp}}=19$ mm. Since the matched pulse is stable to diffraction and focusing it is reasonable to expect that self-guiding over this range will be achievable. To investigate this we have performed a centimeter scale simulation of the long focal length configuration, close to the matched density. The simulation presented was on a grid 204×204 μm with a resolution of 30 cells per laser wavelength in $x-ct$, the propagation direction, and 7.9 cells per laser wavelength in the transverse direction y. The laser was polarized in the slab. Figure 5(a) shows the electron density profile after the laser has propagated for 9 mm. There is a clear plasma wave bubble and electrons have been injected into the first plasma wave period. The laser spot was close to matched, oscillating slightly about the matched spot size. This is shown in Fig. 5(b) as a time history of the integrated transverse laser intensity profile. The oscillation period is

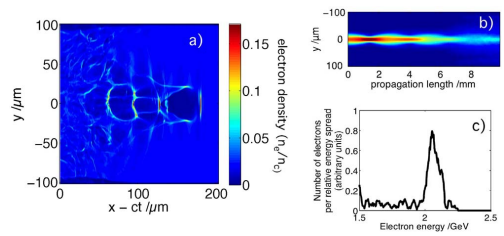

FIG. 5. (Color online) Results from a 2D PIC simulation with OSIRIS for the Astra Gemini system. $\mathcal{E}_L=10$ J, $\tau=30$ fs, $w_0=20$ μm, $a_0=4.8$, $n_e=2\times10^{18}$ cm^{-3}, (a) Electron density profile after the laser has propagated 9 mm. (b) Laser transverse intensity profile (integrated along $x-ct$) as a function of propagation distance. (c) Electron energy spectrum after 9 mm propagation.

close to 2 mm, on the same order as the Rayleigh range $Z_{\mathrm{R}}=1.57$ mm. After propagating 9 mm, the laser has undergone significant pump depletion and pulse etching. The electron energy spectrum at this point is shown in Fig. 5(c). In this 2D simulation the beam has reached 2 GeV with an energy spread of a few percent. This is close to, but significantly higher than, the basic linear prediction of 0.85 GeV, indicating that the simple scaling law needs to be modified for high initial laser intensities.

In summary, we have observed the production of quasimonoenergetic electron beams from a 20 TW laser system. We find that the stability of the electron beam is significantly improved for plasma densities that correspond to the laser pulse being matched to the wakefield dimensions. It was the improved electron beam stability that led directly to the ability to perform experiments into the electron trapping dynamics as reported in Ref. 6. We have observed an energy-density threshold for the stable production of monoenergetic electron beams. This threshold is consistent with the model that the laser is compressed in time and space to dimensions on the order of λ_p, and that injection occurs when there is an intensity corresponding to $a_0 \gtrsim 3$ in this matched spot. Matching reduces the amount of evolution required before injection occurs and indicates that stability may be improved further if the laser is sufficiently intense to inject electrons into the wake without evolution.

ACKNOWLEDGMENTS

We acknowledge support from the Swedish Research Council, the Knut and Alice Wallenberg foundation, the EU Access to Research Infrastructures Programme (RII3-CT-2003-506350 Laserlab Europe) and Research Councils UK.

[1] W. P. Leemans, B. Nagler, A. J. Gonsalves *et al.*, Nature (London) **2**, 696 (2006).
[2] S. P. D. Mangles, C. D. Murphy, Z. Najmudin *et al.*, Nature (London) **431**, 535 (2004).
[3] C. G. R. Geddes, C. Toth, J. v. Tilborg *et al.*, Nature (London) **431**, 538 (2004).
[4] J. Faure, Y. Glinec, A. Pukhov *et al.*, Nature (London) **431**, 541 (2004).
[5] S. Fritzler, E. Lefebvre, V. Malka *et al.*, Phys. Rev. Lett. **92**, 165006 (2004).

[6]S. P. D. Mangles, A. G. R. Thomas, M. C. Kaluza *et al.*, Phys. Rev. Lett. **96**, 215001 (2006).
[7]A. I. Akhiezer and R. V. Polovin, Zh. Eksp. Teor. Fiz. **30**, 915 (1956).
[8]A. Pukhov and J. Meyer-ter Vehn, Appl. Phys. B: Lasers Opt. **74**, 355 (2002).
[9]A. Pukhov, Z. M. Sheng, and J. Meyer-ter Vehn, Phys. Plasmas **6**, 2847 (1999).
[10]A. G. R. Thomas, Z. Najmudin, S. P. D. Mangles *et al.*, Phys. Rev. Lett. **98**, 095004 (2007).
[11]J. Faure, Y. Glinec, J. J. Santos *et al.*, Phys. Rev. Lett. **95**, 205003 (2005).
[12]F. S. Tsung, W. Lu, M. Tzoufras *et al.*, Phys. Plasmas **13**, 056708 (2006).
[13]W. Lu, C. Huang, M. Zhou *et al.*, Phys. Rev. Lett. **96**, 165002 (2006).
[14]S. P. D. Mangles, A. G. R. Thomas, M. C. Kaluza *et al.*, Plasma Phys. Controlled Fusion **48**, B83 (2006).

Paper XIII

Effect of laser contrast ratio on electron beam stability in laser wakefield acceleration experiments

S. P. D. Mangles, A. G. R. Thomas, M. C. Kaluza, O. Lundh, F. Lindau, A. Persson, Z. Najmudin, C.-G. Wahlström, C. D. Murphy, C. Kamperidis, K. L. Lancaster, E. Divall and K. Krushelnick.

Plasma Physics and Controlled Fusion **48**, B83 (2006).

INSTITUTE OF PHYSICS PUBLISHING PLASMA PHYSICS AND CONTROLLED FUSION

Plasma Phys. Control. Fusion **48** (2006) B83–B90 doi:10.1088/0741-3335/48/12B/S08

Effect of laser contrast ratio on electron beam stability in laser wakefield acceleration experiments

S P D Mangles[1], A G R Thomas[1], M C Kaluza[1,4], O Lundh[2], F Lindau[2], A Persson[2], Z Najmudin[1], C-G Wahlström[2], C D Murphy[1,3], C Kamperidis[1], K L Lancaster[3], E Divall[3] and K Krushelnick[1]

[1] Blackett Laboratory, Imperial College, London, SW7 2BZ, UK
[2] Department of Physics, Lund Institute of Technology, PO Box 118, S-22100, Lund, Sweden
[3] Central Laser Facility, CCLRC Rutherford Appleton Laboratory, Oxfordshire, OX11 0QX, UK

E-mail: stuart.mangles@imperial.ac.uk

Received 23 June 2006
Published 8 November 2006
Online at stacks.iop.org/PPCF/48/B83

Abstract

Laser wakefield accelerators offer the possibility of compact electron acceleration. However one of the key outstanding issues with the results reported to date is the electron beam stability. Experiments on two laser systems reveal that the contrast ratio between the ASE pedestal and main pulse is an important factor in determining the quality of the electron beam. With a high contrast ratio (10^8) the electron beam profile is a well collimated single beam having a low pointing instability (<10 mrad rms). With a lower contrast (10^6) the beam profile contains multiple beamlets which exhibit a large pointing instability ($\simeq$50 mrad rms). A high contrast ratio not only improves the beam pointing stability ($\simeq$6 mrad) but also stabilizes the electron beam energy reproducibility (5%).

(Some figures in this article are in colour only in the electronic version)

1. Introduction

The practical reality of a compact laser driven electron accelerator has been brought closer with recent experimental results [1–3]. The generation of well-collimated, narrow energy spread electron beams with energies on the order of 100 MeV has now been demonstrated on a number of laser systems [4–8].

These experiments have used laser produced relativistic plasma waves, or wakefields, to accelerate electrons. Wakefields are electric field structures with a relativistic phase velocity and accelerating and focusing forces, which are set up in the wake of an intense laser pulse

[4] Current address: Institut für Optik und Quantenelektronik, Friedrich-Schiller-Universitt, Max-Wien-Platz 1, 07743 Jena, Germany.

0741-3335/06/SB0083+08$30.00

Table 1. Laser parameters for the three experiments.

Experiment	Pulse duration (fs)	Pulse energy (mJ)	Focusing geometry	Contrast ratio
Astra 2005	45	400	$f/16$	10^6
Lund 2005	35	700	$f/10$	10^6–10^8
Astra 2006	45	600	$f/12$	10^8

travelling through a plasma by the laser's ponderomotive force. This pushes out electrons but not the heavier ions. The resulting space charge forces pull the electrons back into the ion channel and a periodic structure is formed. The frequency of the oscillations is the electron plasma frequency $\omega_p = \sqrt{n_e e^2/(m_e \epsilon_0)}$ (here n_e is the plasma electron density, e is the electron charge, m_e is the electron mass and ϵ_0 is the permittivity of free space). The phase velocity of the wake is set by the group velocity of the laser pulse, so that in underdense plasmas (i.e. $\omega_p < \omega_0$ where ω_0 is the laser frequency) the plasma wavelength is given by $\lambda_p \simeq 2\pi c/\omega_p$ (where c is the speed of light in vacuum).

Wakefield acceleration is most efficient when the laser pulse length is less than a plasma wavelength ($c\tau < \lambda_p$) [9] and when it is focused to a spot size on the order of a plasma wavelength ($w_0 \sim \lambda_p$) [10]. The most impressive results from laser wakefield accelerators have to date used a self-injection mechanism which relies on the plasma wave amplitude being sufficiently high to trap and accelerate electrons rapidly to relativistic energies [1–3]. However this regime can, at present, only be reached after the laser pulse undergoes some self-focusing and self-compression in the plasma wave it creates.

Since the discovery that self-injection can lead to high quality electron beams (i.e. narrow energy spread and low emittance), one of the major remaining barriers to the development of a usable laser-wakefield accelerator has been significant shot-to-shot fluctuations. These fluctuations occur in the measured beam energy, energy spread, charge and beam profile. In this paper we report on measurements of the shot-to-shot fluctuations in the electron beam profile and discuss how this affects the measured energy spectrum on most experiments. We also identify that one of the major sources of electron beam pointing fluctuations is the laser contrast ratio between the ASE pedestal and the main pulse intensity. The contrast of most multi-TW laser systems is in the range $r = 10^5$–10^8.

2. Description of experiments

This paper reports on data collected from three separate experiments. The experiments were performed on two laser systems, Astra at the Rutherford Appleton Laboratory in the UK and the 10 Hz multi-TW laser at the Lund Laser Centre in Sweden. The experimental parameters for the three experiments discussed in this paper are outlined in table 1. Results from two experiments on Astra are reported (from 2005 and 2006), the principal difference in the Astra laser between these two experiments was an improvement in the contrast ratio from $r = 10^6$ to $r = 10^8$. The Lund laser system has a contrast ratio that can be varied and this was used to systematically investigate the effect of contrast ratio on the electron beam profile.

The set up of the three experiments is similar, with the laser pulse focused onto the edge of a supersonic gas jet by an off-axis parabolic mirror. The plasma is produced by the interaction of the intense laser pulse with the gas jet which can provide plasma densities up to $n = 5 \times 10^{19}$ cm^{-3}. The electron beam which is emitted from the gas jet can be analysed either in terms of its profile or its energy spectrum. To measure the beam profile a scintillating screen

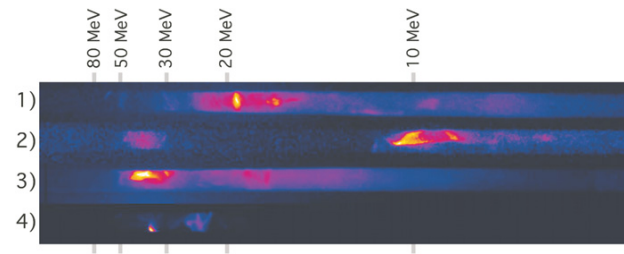

Figure 1. Variation in the observed electron energy spectrum on Astra laser in 2005 experiment. The four shots shown were taken consecutively at $n_e = 1 \times 10^{19}$ cm^{-3}. Laser parameters: $\tau = 45$ fs $E = 350$ mJ, $f/16$ focusing. Colour scale is proportional to the number of electrons.

(Kodak Lanex regular) is placed in the beam path and the scintillation pattern is recorded by an imaging lens and CCD camera system. Metallic filters can be placed in front of the scintillator to prevent low energy electrons from reaching the screen.

To measure the electron beam energy spectrum a magnetic spectrometer is used. This consists of a simple bending magnet which deflects electrons onto a position sensitive electron detector. We use either an image plate (Fuji BAS-MS) or a scintillating screen (Kodak Lanex regular) as the detector. At the entrance to the spectrometer an aluminium collimator is used, this limits the acceptance angle of the spectrometer and hence sets the energy resolution (approximately 1% over the range of electron energies observed).

3. Results

All three experiments produced electron beams with narrow energy spread features, however each experiment exhibited different degrees of electron beam stability. First of all we discuss the measured energy spectrum from the Astra 2005 experiment. At a plasma density of $n_e = 1 \times 10^{19}$ cm^{-3}, the spectrum typically exhibited narrow energy features. However in this experiment there was considerable shot-to-shot variation in the measured spectrum. The electron energy spectrum from four consecutive shots with the same experimental parameters are shown in figure 1.

Measurements of the electron beam profile reveal one of the principal reasons for this observed shot-to-shot fluctuations—namely that there was not a single well-collimated electron beam in this experiment but that the electron beam consisted of multiple beamlets which moved around from shot-to-shot.

Figure 2(*a*) shows the beam profile of the electron beam at a density of $n_e = 1 \times 10^{19}$ cm^{-3} over a typical series of shots clearly showing the fluctuations in profile shape and position.

If each beamlet is the result of a separate instance of self-injection (either in trailing wave periods or multiple instances in the first wave period) then it is likely that each beamlet will have a different energy spectrum. The measured beam profile then suggests that the electron spectrum will change from shot-to-shot depending on the relative alignment of the electron spectrometer collimator and the electron beam itself. Variations in both spectrum and charge would be observed. It is possible that some of these fluctuations could be reduced through the use of electron optics to ensure the whole beam is collected and measured by the spectrometer (as opposed to only the section of the beam which passes through the collimator). However the beam profile in this experiment is clearly unstable and of insufficient quality for applications.

A subsequent experiment, this time performed at the Lund Laser Centre with 35 fs, 680 mJ pulses and $f/10$ focusing showed a marked improvement in the stability of the electron beam.

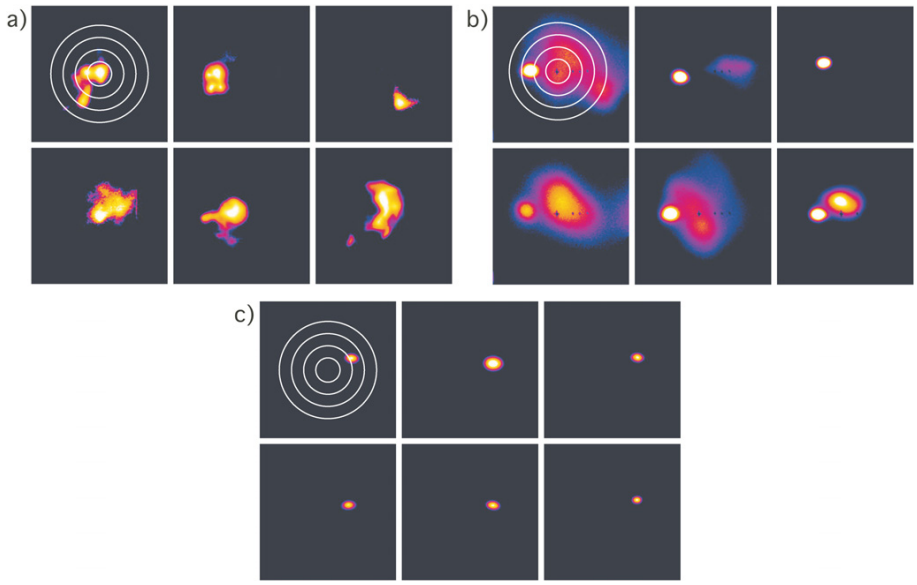

Figure 2. Electron beam profile measurements for (*a*) Astra 2005 ($r = 10^6$), (*b*) Lund ($r = 10^6$) and (*c*) Lund ($r = 3 \times 10^7$). Contours are shown at 50, 100, 150 and 200 mrad, centred on the laser axis. All shots at a plasma density of $n_e = 1 \times 10^{19}$ cm^{-3}. Astra data is for electrons with energy $E > 10$ MeV, Lund data is for electrons with $E > 7$ MeV.

The best contrast ratio of the Lund laser system is $r = 10^8$, during this experiment the highest was $r = 3 \times 10^7$. The Lund laser also employs a fast Pockels cell which limits the duration of the ASE pedestal to less than 1 ns. The contrast ratio was measured using a third-order-autocorrelator (Amplitude Technologies Sequoia) and the contrast was controlled by varying the RF power to the acousto-optic programmable dispersive filter (Fastlite Dazzler) used to optimize pulse compression over the range $r = 3 \times 10^7 - 10^6$.

Figures 2(*b*) and 2(*c*) show a number of electron beam profiles, taken on consecutive shots at two different pre-pulse levels. The best contrast ratio obtained produced the most stable electron beam (figure 2(*c*)), with the profile consisting of a single well collimated (less than 20 mrad) electron beam. At a lower contrast ratio ($r = 10^6$), the electron beam profile exhibits multiple beamlets which have a larger pointing instability. The beamlets are, on average, less well collimated than with a high contrast ratio. With the Lund laser there is however a principal beamlet which contains more charge than the secondary beamlets. The collimation and pointing stability of this principal beamlet are closer to the collimation and stability of the single beam observed with a high contrast ratio. It should be noted that regardless of the contrast ratio, the principal electron beam was not on the laser axis (as measured in vacuum). However the position of the principal beamlet relative to the vacuum laser axis does move with contrast ratio, and for a fixed contrast ratio the position of the principal beamlet is stable from shot-to-shot.

Measurements of the electron spectrum at the highest contrast ratio show a marked improvement in the stability of the electron beam in terms of energy and charge compared with previous experiments on Astra. A set of eight consecutive shots are shown in figure 3 for a plasma density of $n_e \simeq 3 \times 10^{19}$ cm^{-3} showing a quasi-monoenergetic distribution (instrument limited) peaked at $E \simeq 45$ MeV. Over the eight shots the energy of the peak in the

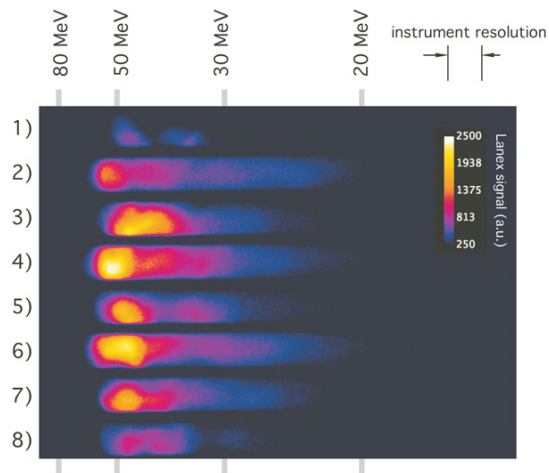

Figure 3. Eight consecutive measurements of the electron energy spectra on the Lund laser system at a plasma density of $n_e \simeq 3 \times 10^{19}\text{cm}^{-3}$. Laser parameters: $\tau = 35\,\text{fs}$ $E = 600\,\text{mJ}$, $f/10$ focusing.

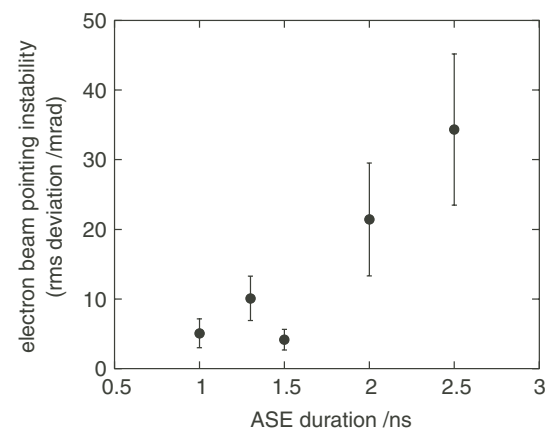

Figure 4. Variation of electron beam pointing stability with ASE duration on the Lund laser system at a plasma density of $n_e \simeq 1 \times 10^{19}\text{cm}^{-3}$ and a contrast ratio of $r = 3 \times 10^7$.

distribution varies by less than 5%. This represents a significant improvement in the electron beam stability compared with other reported experiments.

We have also investigated the effect of the ASE pedestal duration on the pointing stability. The ASE pedestal duration can be controlled by varying the timing of the fast Pockels cell. Using this technique we could vary the pedestal duration from 1 ns to 4.5 ns. Figure 4 shows the effect this has on the electron beam pointing stability at a contrast ratio of $r = 3 \times 10^7$. The data clearly shows that the longer the ASE pedestal the worse the electron beam pointing stability. Even at this high contrast ratio, a few nanoseconds of ASE pedestal is sufficient to seriously degrade the electron beam properties.

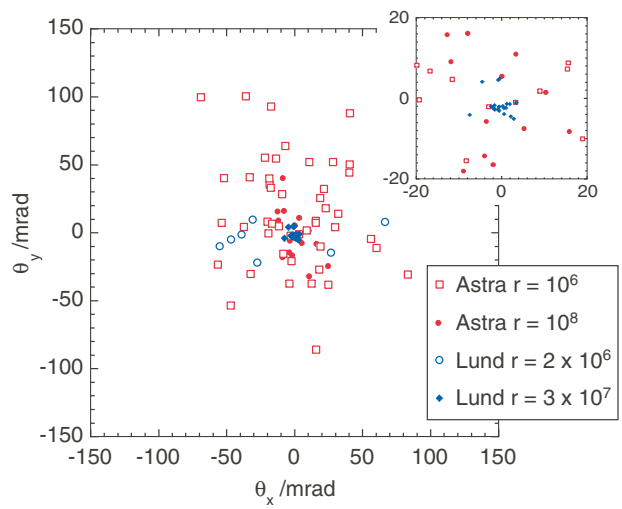

Figure 5. Comparison of the beam pointing from Astra and Lund experiments. Each point represents the position of an observed electron beam or beamlet. Red open squares: Astra 2005 ($r = 10^6$). Red solid circles: Astra 2006 ($r = 10^8$). Blue open circles: Lund low contrast ($r = 2 \times 10^6$). Blue solid diamonds: Lund high contrast ($r = 3 \times 10^7$). Inset—enlarged central region.

Recently improvements have been made to the Astra laser, resulting in a better contrast ratio ($r = 10^8$). A recent experiment with $f/12$ focusing of the 45 fs, 600 mJ pulses has shown an improvement of the electron beam profile stability.

To illustrate the improvement in pointing stability we plot the centre of each electron beamlet from a series of shots for the two Astra experiments and from the Lund experiment (figure 5). There is a marked improvement between the two Astra experiments, indicating the importance of the ASE contrast level. The data from the Lund experiment clearly shows a much smaller scatter when the contrast level is high (3×10^7 as compared with 10^6). The contrast ratio was varied over a range of values on the Lund laser system and the *rms* deviation of the electron beam pointing is plotted against the contrast ratio in figure 6. On the Lund laser system, the most stable pointing (6 mrad rms) was obtained at the highest contrast ($r = 3 \times 10^7$), however the Astra 2006 experiment has a slightly better contrast ratio ($r = 1 \times 10^8$) and the observed pointing stability is 20 mrad rms. This represents more than a factor of two improvement compared with the Astra 2005 experiment.

4. Discussion

This paper has presented data demonstrating a significant (order of magnitude) improvement in the pointing stability (now better than 6 mrad rms) and energy stability (now at 6% rms variation) of the electron beams produced in a single beam, self-injecting laser wakefield accelerator by controlling the pre-pulse level so that there is no nanosecond timescale pre-plasma formation.

Previous work, outside the monoenergetic regime, indicated that hydrodynamic shock formation by the ASE pedestal can significantly alter electron injection [11], however that experiment was in a significantly different regime (∼4 TW) where injection could only occur when the pulse crossed a density transition. More recent results from the same group [6]

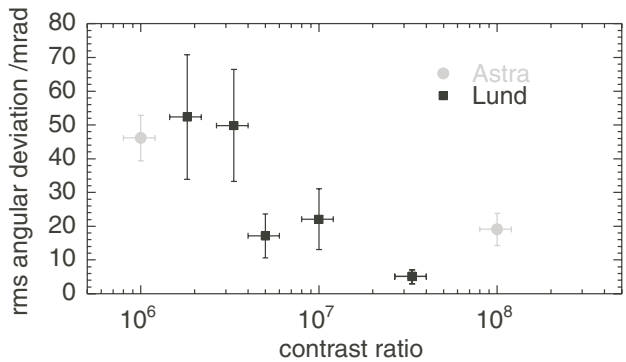

Figure 6. Variation of electron beam pointing instability with contrast ratio. Black squares: data from Lund Laser Centre. Grey circles: data from the Astra laser.

showed a strong correlation of monoenergetic electron production and guiding in a pre-pulse formed plasma cavity, however the experimental parameters varied significantly from those reported here. Their peak laser intensity was an order of magnitude higher and the range of contrast ratios studied was also significantly different ($I_{\mathrm{ASE}} = 10^{12}$–$10^{13}\,\mathrm{W\,cm^{-2}}$ compared with $I_{\mathrm{ASE}} = 10^{10}$–$10^{12}\,\mathrm{W\,cm^{-2}}$ in the experiments reported here) such that in the work of Hosokai *et al* there is significant pre-plasma formation and hydrodynamic evolution before the main pulse arrives. Shadowgraphic measurements performed on Astra with $f/16$ focusing and a contrast ratio of $r = 10^6$ show no evidence of plasma cavity or shock formation at these plasma densities and pre-pulse intensities.

At a plasma density of $n_{\mathrm{e}} = 1 \times 10^{19}\,\mathrm{cm^{-3}}$ the pre-pulse intensities in our experiment cross the optical breakdown threshold and as such we believe that the observed instability in the electron beam pointing is driven or seeded by an ionization instability which affects the laser propagation such as that described by Antonsen and Bian [12].

The data presented in this paper demonstrates the importance of laser contrast level in self-injected laser wakefield experiments, however it is also clear that this is not the only factor; other factors including pulse duration and pulse energy may also be important as self-injection currently relies on self-focusing and self-compression of the laser pulse in the plasma wave. This pulse evolution is likely to be one of the principal remaining causes of electron beam stability. Due to the different pulse durations of the Astra (45 fs) and Lund (35 fs) laser systems this could explain the greater degree of beam instability observed on Astra with $r = 10^8$ compared with $r = 3 \times 10^7$ on the Lund laser.

Electron beam stability is one of the most important issues that remain to be solved for self-injected laser wakefield accelerators to become truly high quality, usable electron sources. The experiments described in this paper have demonstrated that one of the critical parameters for the stability of the electron beam is the laser contrast ratio, a point which is worth considering with the current surge in development of 100 TW–1 PW short pulse laser systems around the world.

Acknowledgments

The experiment in Lund was supported by the Access to Research Infrastructures activity in the Sixth Framework Programme of the EU (contract RII3-CT-2003-506350, Laserlab Europe). This work was supported in part by EPSRC and RCUK.

References

[1] Mangles S P D *et al* 2004 *Nature* **431** 535–8
[2] Geddes C G R *et al* 2004 *Nature* **431** 538–41
[3] Faure J *et al* 2004 *Nature* **431** 541–4
[4] Mangles S P D *et al* 2006 *Phys. Rev. Lett.* **96** 215001
[5] Hsieh C T *et al* 2006 *Phys. Rev. Lett.* **96** 095001
[6] Hosokai T *et al* 2006 *Phys. Rev.* E **73** 036407
[7] Miura E *et al* 2005 *Appl. Phys. Lett.* **86** 251501
[8] Yamazaki A *et al* 2005 *Phys. Plasma.* **12** 093101
[9] Tajima T and Dawson J 1979 *Phys. Rev. Lett.* **43** 267
[10] Thomas A G R *et al* 2006 *Phys. Rev. Lett.* submitted
[11] Hosokai T *et al* 2003 *Phys. Rev.* E **67** 036407
[12] Antonsen T M and Bian Z 1999 *Phys. Rev. Lett.* **82** 3617

Paper XIV

Optimization toward a high-average-brightness soft-x-ray laser pumped at grazing incidence

K. Cassou, S. Kazamias, D. Ros, F. Plé, G. Jamelot, A. Klisnick, O. Lundh, F. Lindau, A. Persson, C.-G. Wahlström, S. de Rossi, D. Joyeux, B. Zielbauer, D. Ursescu and T. Kühl.

Optics Letters **32**, 139 (2007).

January 15, 2007 / Vol. 32, No. 2 / OPTICS LETTERS 139

Optimization toward a high-average-brightness soft-x-ray laser pumped at grazing incidence

K. Cassou, S. Kazamias, D. Ros, F. Plé, G. Jamelot, and A. Klisnick
LIXAM, UMR 8624, Université Paris Sud, F-91405 Orsay Cedex, France

O. Lundh, F. Lindau, A. Persson, and C.-G. Wahlström
Department of Physics, Lund University, S-22100 Lund, Sweden

S. de Rossi and D. Joyeux
Laboratoire Charles Fabry de l'institut d'Optique, Campus de Polytechnique-RD128, F-91127 Palaiseau, France

B. Zielbauer, D. Ursescu, and T. Kühl
Gesellschaft für Schwerionenforschung (GSI), D-64291 Darmstadt, Germany

Received August 21, 2006; revised October 10, 2006; accepted October 11, 2006;
posted October 16, 2006 (Doc. ID 74292); published December 23, 2006

We report the near-field imaging characterization of a 10 Hz Ni-like 18.9 nm molybdenum soft-x-ray laser pumped in a grazing incidence pumping (GRIP) geometry with a table-top laser driver. We investigate the effect of varying the GRIP angle on the spatial behavior of the soft-x-ray laser source. After multiparameter optimization, we were able to find conditions to generate routinely a high-repetition-rate soft-x-ray laser with an energy level of up to 3 μJ/pulse and to 6×10^{17} photons/s/mm^2/mrad^2/(0.1% bandwidth) average brightness and 1×10^{28} photons/s/mm^2/mrad^2/(0.1% bandwidth) peak brightness. © 2006 Optical Society of America

OCIS codes: 140.7240, 340.7440.

In the development of coherent soft-x-ray sources, as a tool for chemistry, biology, and solid-state physics, plasma-based soft-x-ray lasers (SXRLs) are receiving an increased interest. A major advance has been made recently in significantly enhancing the pump efficiency and repetition rate of transient collisionally pumped SXRLs through the use of grazing incidence pumping (GRIP).[1] Saturated SXRLs have been demonstrated down to 13 nm with subjoule laser pump energies[2,3] at 5–10 Hz repetition rates,[4,5] while the shortest soft-x-ray laser wavelength driven into saturation is 5.9 nm when a low-repetition-rate, subkilojoules laser system is used.[6] This progress allows the construction of compact SXRL beamlines at university-scale laboratories that can become alternatives to larger-scale facilities such as synchrotrons or free-electron lasers for some specific applications. The GRIP concept is a variation of the transient collisional pumping scheme in which a preformed plasma column is heated at near-normal incidence by a short laser pulse. In the GRIP scheme the short pulse beam is incident at grazing angle and refracted in the plasma [Fig. 1(a)]. The increased path length in the heated region leads to better energy deposition, hence better pumping efficiency. Further, the electron density at which the energy is absorbed can be controlled to the optimum pumping density by adjusting the GRIP angle, Φ, following $n_{e,\mathrm{abs}}=n_c \sin^2\Phi$, where n_c is the critical density.[7] Most of the work until now has focused on the optimization of the SXRL beam intensity detected by an XUV spectrometer. Very little work has been done yet to investigate the effect of GRIP angle on the plasma itself and to characterize the SXRL source in terms of size and position. Such information is needed to provide benchmarks for numerical simulations and to improve the physical understanding of GRIP systems. Moreover, the control of the spatial characteristics of the source is crucial for applications, as it directly influences the main features of the SXRL beam.[8]

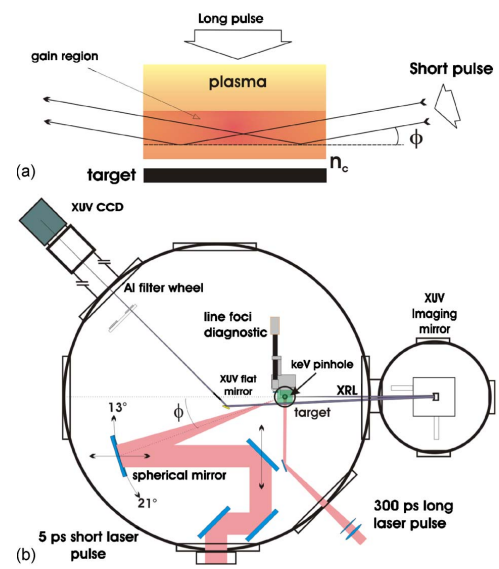

Fig. 1. (Color online) (a) Schematic view of the GRIP scheme. (b) Experimental setup showing the pump laser beamlines and SXRL diagnostics.

140 OPTICS LETTERS / Vol. 32, No. 2 / January 15, 2007

In this Letter we report on a detailed characterization of a nickel-like molybdenum ($4d^1S_0$–$4p^1P_1$) transient SXRL pumped in GRIP geometry, using a two-dimensional (2-D) high-spatial-resolution diagnostics imaging the SXRL at the output of the plasma rod. The position and energy distribution of the SXRL source were measured while optimizing the SXRL energy with respect to a set of parameters. At the optimum GRIP angle, found to be 19°, the gain region is the closest to the target surface. A maximum integrated output energy of 3 μJ/pulse was routinely obtained at 10 Hz, corresponding to an average power of 30 μW. In addition, we found that the SXRL source size and shape can be controlled and optimized by adjusting the delay and level of a low-energy prepulse. In this way, we were able to decrease the source diameter to $\sim$10 μm FWHM, yielding a nearly complete spatially coherent SXRL source with an output fluence of 1 J cm^{-2}.

The experiment was performed at the Lund Laser Centre, Sweden, using a chirped-pulse amplification Ti:sapphire laser operating at 10 Hz. The 1.4 J, 300 ps chirped-pulse beam available after the final amplification stage was split into an uncompressed long pulse (LP), which created a plasma, and a short pulse (SP), partly compressed to 5 ps, which heated the plasma and generates the SXRL emission. The splitting ratio between the LP and the SP was variable and was adjusted for optimum x-ray output. In the rest of the study, the LP delivered 480 mJ and the SP delivered 500 mJ on target. A prepulse (PP) generator was inserted in the LP beamline to provide an additional low-energy PP. For most of the experiment, the PP preceded the LP by 1.3 ns and contained 7% of its energy. All three pulses irradiated a 4 mm long Mo slab target, as shown in Fig. 1(b). The 300 ps LP and PP beams were focused into a 70 μm $\times$5 mm FWHM line focus with a combination of a spherical lens (f=1 m) and a cylindrical lens (f=−4 m), yielding irradiances of 3.8×10^{11} W cm^{-2} and $\sim5\times10^{10}$ W cm^{-2}, respectively. The SP beam was focused into a line of 40 μm FWHM in width, with a f=650 mm spherical mirror onto the target at a grazing angle, adjustable under vacuum from 13° to 21° [Fig. 1(a)]. The length of the line focus, which depends on the beam diameter and grazing angle, varied from 5 mm for 13° to 9 mm for 21°. This focusing configuration induced an intrinsic traveling wave with a velocity close to the speed of light (within less than 5% deviation). The superposition of the LP and SP at the target plane was controlled with an imaging microscope device, with a resolution of about 3 μm. In contrast with previous work,[2] we vary the GRIP angle Φ by tilting and translating the SP beam mirrors, instead of the target. This condition was found to be important to get a constant line focus quality and to allow the implementation of high-spatial-resolution diagnostics of the SXRL plasma. The diagnostics, shown in Fig. 1(b), consisted of a 2-D XUV near-field imaging system. This diagnostic consisted of a 1 m radius-of-curvature spherical multilayer mirror used at 0.7° from normal incidence. After redirection by a flat multilayer mirror, the image was detected on a 16-bit back thinned XUV charge-coupled device camera placed 4.28 m from the imaging mirror, yielding a magnification of 7.6. The resolution was 1.7 μm, limited by the 13 μm pixel size. A set of 1 to 6 μm thick aluminum filters was used to adjust the signal level. Figure 2 shows the effect of varying the GRIP angle. At 19° the mean fluence in the SXRL source aperture exhibits a clear optimum of 0.33 J cm^{-2}, corresponding to an integrated energy of 3 μJ. We assume for the estimation of SXRL energy that Al foil absorption is given by Henke tables,[9] and we consider a 7.5 nm thick oxide layer on each side of the Al filter foil. Also plotted in Fig. 2 is the position of the SXRL source relative to the target surface. The position of the SXRL source moves toward the target surface when the GRIP angle is increased from 15° (60 μm) to 19° (35 μm). This trend is expected as the pump laser beam penetrates deeper into the plasma and is absorbed at a higher electron density for increasing GRIP angle. Above that angle, the SXRL source aperture is shifted to larger distances. This can be interpreted as a result of steeper density gradient in the absorption region, leading to enhanced refraction of the SXRL beam. From Fig. 2, Φ=19°, the GRIP angle clearly corresponds to the optimum angle with regard to SXRL output and gives the smallest distance between source and target surface. At the optimum angle the electron density corresponding to the perigee point is $n_e\approx1.8\times10^{20}$ cm^{-3}. Accordingly, optimization of the SXRL output with regard to grazing angle appears to be a balance between absorption at high-electron-density and low-electron-density gradients.

Figure 3 shows the behavior of the SXRL source at the optimum GRIP angle of 19° as a function of the LP–SP delay (peak to peak). While the horizontal (target normal) width does not vary significantly, the vertical width is observed to strongly increase with the LP–SP delay up to 400 ps, where it reaches the line focus width of the SP, and remains approxi-

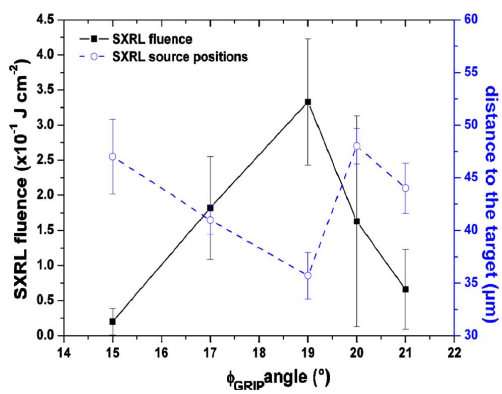

Fig. 2. (Color online) Mean SXRL fluence (solid curve), distance to the target surface of the emission peak of the SXRL (dashed curve). Each data point is an average over 10 to 20 shots.

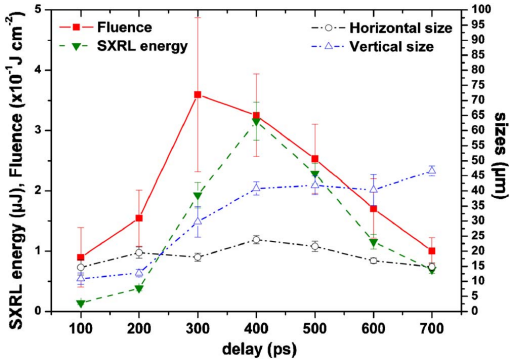

Fig. 3. (Color online) LP–SP delay effect at $\Phi = 19°$. Left scale, integrated energy and mean fluence, right scale, SXRL FWHM vertical and horizontal widths.

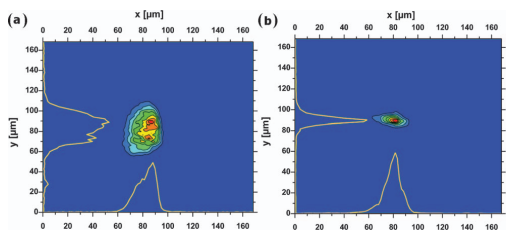

Fig. 4. Near field images, $\Phi = 19°$: (a) PP–LP delay, 1.3 ns; (b) doubled energy in the PP and PP–LP delay, 2.4 ns.

mately constant for longer delays. As a result, the SXRL integrated energy peaks at 400 ps, while the mean fluence is maximum for a shorter delay of 300 ps. The behavior of the vertical width can be attributed to the lateral expansion of the plasma in the region where the short pulse is absorbed. At optimal conditions, we find that the SXRL is operated in the onset of saturation regime, with a measured gain coefficient of $g \sim 45$ cm^{-1}. Finally, Fig. 4 illustrates the influence of the low energy prepulse on the size and shape of the SXRL source. The reference case is shown in Fig. 4(a) and corresponds to the maximum output energy of 3 μJ at 19° GRIP angle. The energy distribution in the SXRL near field is relatively smooth with a 21 μm $\times$ 42 μm FWHM size. Figure 4(b) shows the dramatic effect of varying the PP–LP delay from 1.3 to 2.4 ns and doubling the PP energy level. This leads to a very small, nearly circular, source of $\sim$10 μm FWHM in diameter, containing 1 μJ and reaching a mean fluence close to 1 J cm^{-2}. The maximum theoretical transverse coherence length at the exit aperture[8] is estimated to 8 μm, considering the amplifier geometry. It leads to a transverse coherence length similar to the size of the SXRL source. This result, which needs further investigation, was obtained in a reproducible way with a similar source size over a wide LP–SP delay range. Figure 4 hence demonstrates the relevance of the near-field imaging diagnostic to performing SXRL optimization.

In conclusion, we present an extensive multiparameter optimization of a transient Ni-like Mo soft-x-ray laser at 18.9 nm, pumped under grazing incidence. By imaging the SXRL at the output of the plasma rod, we obtain, for the first time to our knowledge, a detailed insight into the effect of varying the GRIP angle among other parameters. At optimal conditions we demonstrate 10 Hz operation with a maximum mean energy of 3 μJ per pulse, corresponding to both high pumping efficiency (3×10^{-6}) and average power of 30 μW. By adjusting the low-energy prepulse, we obtain the smallest source with nearly complete spatial coherence and high mean fluence of 1 J cm^{-2}. Assuming a reasonable value for the pulse duration ($\approx$5 ps),[8] we estimate the average brightness to be 6×10^{17} photons/s/mm^2/mrad^2/(0.1% bandwidth) and the peak brightness to be 1×10^{28} photons/s/mm^2/mrad^2/(0.1% bandwidth), which compares well with third-generation synchrotron sources and, if we take in account the spectral bandwidth ($\sim 10^{-5}$), also to free-electron laser sources.

This work was supported by the Swedish Research Council, the Knut and Alice Wallenberg Foundation, and EU Access to Research Infrastructures activity (contract RII3-CT-2003-506350, Laserlab Europe). K. Cassou's e-mail address is kevin.cassou@lixam.u-psud.fr.

References

1. R. Keenan, J. Dunn, P. K. Patel, D. F. Price, R. F. Smith, and V. N. Shlyaptsev, Phys. Rev. Lett. **94**, 103901 (2005).
2. B. M. Luther, Y. Wang, M. A. Larotonda, D. Alessi, M. Berrill, M. C. Marconi, and J. J. Rocca, Opt. Lett. **30**, 165 (2005).
3. Y. Wang, M. A. Larotonda, B. M. Luther, D. Alessi, M. Berril, V. N. Shlyaptsev, and J. J. Rocca, Phys. Rev. A **72**, 053807 (2005).
4. A. Weith, M. A. Larotonda, Y. Wang, B. M. Luther, D. Alessi, M. C. Marconi, and J. J. Rocca, Opt. Lett. **31**, 1994 (2006).
5. J. Tümmler, K. A. Janulewicz, G. Priebe, and P. V. Nickles, Phys. Rev. E **72**, 037401 (2005).
6. R. Smith, G. J. Tallents, J. Zhang, G. Eker, S. McCabe, G. J. Pert, and E. Wolfrum, Phys. Rev. A **59**, R47 (1999).
7. G. J. Pert, Phys. Rev. A **73**, 033809 (2006).
8. O. Guilbaud, A. Klisnick, K. Cassou, S. Kazamias, D. Ros, G. Jamelot, D. Joyeux, and D. Phalippou, Europhys. Lett. **74**, 823 (2006).
9. B. L. Henke, E. M. Gullikson, and J. C. Davis, At. Data Nucl. Data Tables **54**, 181 (1993).

Paper XV

Characterization of a transient collisional Ni-like molybdenum soft x-ray laser pumped in grazing incidence

S. Kazamias, K. Cassou, D. Ros, F. Plé, G. Jamelot, A. Klisnick, O. Lundh, F. Lindau, A. Persson, C.-G. Wahlström, S. de Rossi, D. Joyeux, B. Zielbauer, D. Ursescu and T. Kühl.

Physical Review A **77**, 033812 (2008).

PHYSICAL REVIEW A **77**, 033812 (2008)

Characterization of a transient collisional Ni-like molybdenum soft-x-ray laser pumped in grazing incidence

S. Kazamias,* K. Cassou, D. Ros, F. Plé, G. Jamelot, and A. Klisnick
LIXAM, UMR 8624, Université Paris Sud, F-91405 Orsay Cedex, France

O. Lundh, F. Lindau, A. Persson, and C.-G. Wahlström
Department of Physics, Lund University, S-22100 Lund, Sweden

S. de Rossi and D. Joyeux
Laboratoire Charles Fabry de l'Institut d'Optique, Campus Polytechnique, RD 128, F-91127 Palaiseau, France

B. Zielbauer, D. Ursescu, and T. Kühl
Gesellschaft für Schwerionenforschung (GSI), D-64291 Darmstadt, Germany
(Received 27 July 2007; published 6 March 2008)

We present experimental results from an extensive investigation of a Ni-like Mo x-ray laser pumped in the transient regime and GRIP configuration (GRazing Incidence Pumping). The pump laser is a 10 Hz, 1 J, Ti:sapphire laser system. The main diagnostic is a monochromatic near-field imaging system with a 1.7 micron spatial resolution that shows the soft-x-ray laser source size and position relative to the target surface. Changes of those characteristics are observed for different GRIP angles, varied between 15° and 21°, while keeping all other parameters constant. Intense lasing is observed routinely at 18.9 nm with up to 3 microjoule output energy and stable operation is demonstrated at 10 Hz. We have investigated the role of several pumping parameters, in particular, the relative energy and delay between the long and short pulse. We show that this multiparameter scan leads to a well-defined optimal regime of operation and better understanding of the GRIP configuration. Finally, as the GRIP scheme requires careful tailoring of the plasma conditions to the specific soft-x-ray laser under investigation, we add a prepulse before the plasma producing long pulse to generate large-scale preplasmas. This increases the brightness of the soft-x-ray beam and leads to an almost Gaussian near-field spatial profile.

DOI: 10.1103/PhysRevA.77.033812 PACS number(s): 42.55.Vc, 32.30.Rj, 42.60.Da, 52.50.Jm

I. INTRODUCTION

Since the mid-1990s, intense and successful efforts, both experimental and theoretical, have been done in soft-x-ray laser research to establish the viability of tabletop pumped devices that would enable the use of this exceptionally bright source in the soft-x-ray spectral domain for applications at the university scale.

The soft-x-ray laser research field is currently experiencing a rapid development since the first demonstration of high repetition rate transient soft-x-ray laser from solid target by Keenan *et al.* [1] who used a Ti:sapphire laser as the pump laser. They also showed the advantage of the so-called GRazing Incidence Pumping (GRIP) configuration for which the plasma is pumped at grazing incidence and the pump laser is refracted in the plasma. This first demonstration was followed by the work of other groups [2–5] who obtained the saturation of different kinds of soft-x-ray lasers at various wavelengths down to 11 nm.

The GRIP configuration has many advantages over the normal incidence pumping [6]: in particular, the grazing angle is a new parameter that can be adjusted to match the energy deposition and plasma heating to the optimum zone for gain. As the density in the plasma where the energy is absorbed becomes smaller when the grazing angle is reduced, there should also be less density gradient in this region. This should improve the propagation of the soft-x-ray laser beam in the amplifying medium. It is therefore of great importance to precisely investigate the effect of GRIP angle on the plasma and soft-x-ray laser characteristics and to make possible comparisons with detailed quantitative simulations. This will increase the physical understanding of GRIP systems, which is crucial for their optimization and their use as an amplifier medium for coherent radiation such as high order harmonics [7,8] or as a direct source for applications.

During an experimental campaign on the 10 Hz, 35 TW Ti:sapphire laser system at the Lund Laser Center in Sweden, we used the GRIP configuration to produce a saturated soft-x-ray laser at 18.9 nm from a Ni-like molybdenum plasma generated on a 4 mm solid target [9]. By high resolution near-field imaging of the soft-x-ray laser source, we investigated in detail the effect of the GRIP angle on the soft-x-ray laser output characteristics such as integrated energy, vertical and horizontal size, and emission distance from target surface. This was done for a large set of parameters such as the delay between the long and short pulse and their relative energy but also the presence of a small prepulse, before the long pulse that creates the plasma, was investigated.

After a detailed description of the experimental setup in Sec. II, the rest of the paper will be dedicated to the study of

*sophie.kazamias@u-psud.fr

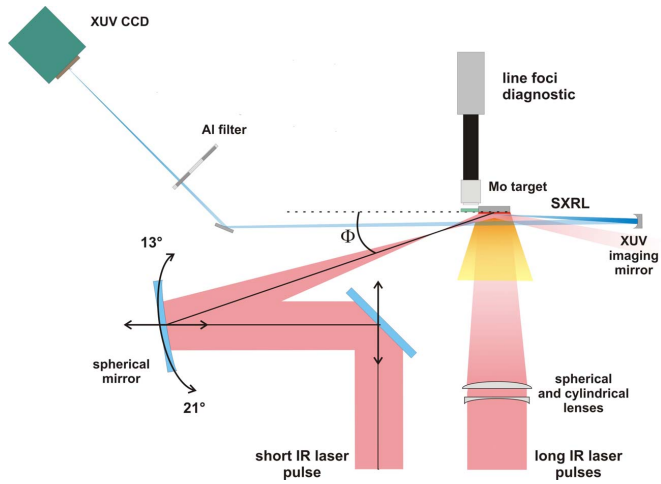

FIG. 1. (Color online) Schematic top view of the experimental setup.

first the influence of grazing angle (Sec. III), then the influence of the delay between the two main laser pulses (Sec. IV) and the effect of a small prepulse before the long pulse (Sec. V). We will conclude on the best characteristics obtained for this source in terms of energy in the soft-x-ray laser pulse, size, position, etc. (Sec. VI).

II. EXPERIMENTAL PRINCIPLE AND CONFIGURATION

The pump laser for the following study of soft-x-ray laser generated in GRIP configuration is the 30 TW laser system of the Lund Laser Center in Sweden. It is a chirped pulse amplification (CPA) Ti:sapphire laser system that usually delivers 1 J in 35 femtosecond (fs) pulses at 10 Hz repetition rate and 800 nm central wavelength. For the soft-x-ray laser generation, the 1.4 J of uncompressed energy is split after the last amplifier stage into two beams with adjustable energy ratio. One of the beams, the so-called long pulse (LP), remains uncompressed, with 300 ps duration and is used to create the plasma. The other one, the so-called short pulse (SP), enters the compressor and is compressed down to 5 ps to heat the plasma and pump the soft-x-ray laser transition. We found that the best condition corresponds to the same energy level for the long and short pulse: approximately 500 mJ on target in each arm.

A low energy prepulse generator was installed in the long pulse beam path to allow additional control of the preplasma conditions. The device is composed of a combination of a half-wave plate and a cube polarizer and is designed to vary continuously the energy balance between the prepulse and the long pulse, from 0 to 100%. However, the smallest prepulse energy level that is practically obtained was 7% due to the polarizer quality. At this low level, the noise on the photodiode is rather large and the energy evaluation is given with large fluctuations. The maximum delay between the pulses is given by the size of the delay line and reaches 2.4 ns. For most of the experiment, the prepulse preceded the long pulse by 1.3 ns and contained 7% of its energy but results obtained in significantly different conditions will also be discussed in this paper. All of these beams were focused in line on a 4-mm-long molybdenum slab target.

The focusing system for the long pulse(s) with a 17 mm beam diameter consisted of a combination of a cylindrical ($f=-4$ m) and a spherical ($f=1$ m) lens. The position of the latter was adjusted to vary the width of the focal line. The length of the line focus was 6 mm and led to irradiance on targets of 2.9×10^{10} W cm^{-2} and 3.8×10^{11} W cm^{-2} for the 7% prepulse and the long pulse, respectively. The focusing system for the short pulse with a 50 mm beam diameter and incident on target at grazing incidence, was composed of a spherical mirror ($f=650$ mm) whose incidence angle was adjustable under vacuum between 7.5° and 10.5° to lead to GRIP angle Φ, on target between 15° and 21°. The focal line length, which only depends on beam diameter and grazing angle, was between 5 and 9 mm, whereas its width was approximately 40 μm. An important point is that the spherical mirror position, together with the 45° mirror before it (see Fig. 1), were adjustable under vacuum to maintain the target position and direction constant while changing the GRIP angle. The superposition and shape of the focused beams were controlled with an imaging microscope with a resolution reaching 3 μm. The delay between the pulses was adjustable under vacuum, from 100 to 800 ps with 100 ps time resolution, using a delay line placed in the long pulse beam path. This setup design is different from the one presented, for example, in Ref. [3] where the GRIP angle was varied by rotating the target. This technical solution leads to better quality focusing and superposition of the focal lines. It is also required when using high resolution diagnostics of the plasma and soft-x-ray laser.

The main diagnostic shown in Fig. 1 is a two-dimensional (2D) soft-x-ray near-field imaging system composed of a f

=500 mm multilayer spherical mirror coated for spectral selection at the soft-x-ray laser wavelength (Institut d'Optique design and manufacturing). To get a very high resolution with low astigmatism, the mirror is used at the minimum available incidence angle (0.7°) to allow the beam redirection by a flat mirror placed at the center of the vacuum chamber. After more than 4 m propagation, the magnified image of the soft-x-ray laser source, at the exit plane of the plasma, is detected on a calibrated 16-bit back thinned soft-x-ray charge coupled device (CCD) camera. The resolution given by the system is 1.7 μm and corresponds to a magnification factor of 7.6. A set of aluminum filters with thicknesses between 1 and 6 μm was placed in the soft-x-ray laser beam to adjust the intensity level. The 6 μm filter was used in most of the experimental configurations, indicating in itself a high signal level for the soft-x-ray laser output.

The high repetition rate operation of this soft-x-ray laser allows one to perform a complete series of multidimensional parameter optimization. The recorded images were carefully analyzed to extract physical quantities such as the integrated energy, the horizontal and vertical widths of the source, and its distance from the target surface. The mean fluence of the source could then be derived from the measured data, as well as the mean peak intensity when assuming a pulse duration of 5 ps, as measured in a similar experiment [10]. All the measurements presented below are the result of an average over at least five shots recorded in the same experimental conditions. A recent paper [11] presents in detail the 10 Hz operation of this type of soft-x-ray laser as a source for applications: it shows that soft-x-ray laser output characteristics depend on the target operation, static or moving, and target preparation through the level of oxidation and surface roughness. The soft-x-ray laser output stability is also directly dependent on the pump laser stability in terms of energy and beam pointing.

III. INFLUENCE OF THE GRIP ANGLE

The behavior of the soft-x-ray laser output as a function of the short laser pulse grazing angle is presented in Fig. 2. The delay between the long and short pulses is fixed to Δt_{LP-SP}=400 ps, which corresponds to the optimum measured delay for most of the angles Φ between 15° and 21° as will be shown in the next section. Note that working at a fixed delay Δt_{LP-SP}, allows one to study the interaction of the short pulse with the same preplasma conditions whatever the GRIP angle. As was briefly presented in a recent letter [9], the mean output fluence shows a clear optimum for a 19° GRIP angle and reaches 0.33 J/cm^2, which corresponds to an integrated soft-x-ray laser energy up to 3 μJ.

The distance of the source from the target surface also varies significantly with the GRIP angle: it first decreases from 60 to 35 μm for angles between 15° and 19°, then increases to around 50 μm for larger ones until 21°. Such a trend was expected since the pump laser beam penetrates deeper in the plasma and is absorbed at higher electron density when the GRIP angle is increased, following the well-known mirage formula $n_e=n_c \sin^2 \Phi$, where n_e is the electron density of the plasma and n_c is the critical density for

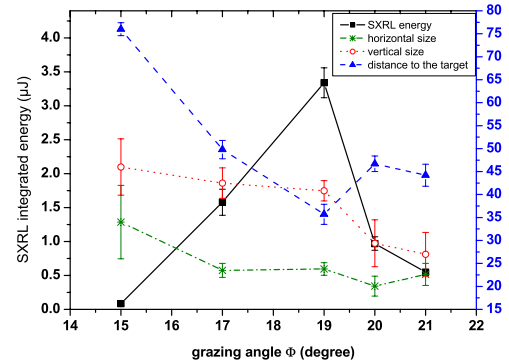

FIG. 2. (Color online) Grazing angle effect on the soft-x-ray laser integrated energy, position relative to the target surface, (FWHM) horizontal and vertical widths.

the laser wavelength [6]. In our case, n_e is just below 1.8 $\times 10^{20}$ cm^{-3} for a 19° GRIP angle. Above the optimum grazing angle, the soft-x-ray laser source aperture is shifted to larger distances. This can be interpreted as due to a stronger refraction of the IR laser beam followed by a spatial reshaping of the gain zone, since absorption occurs at a higher density where the density gradient is steeper. As additional information on the grazing angle effect, both horizontal and vertical sizes of soft-x-ray laser pupil are reduced when increasing the grazing angle. Pumping in a denser plasma region should indeed correspond to a decrease of the plasma scale length ($L=n_e/\nabla n_e$). Numerical simulations performed for similar pumping conditions but for a different lasing element tend to indicate that the 19° GRIP angle corresponds to an electronic density for which the density profile experiences a steeper increase along the horizontal axis [6], leading to a more dramatic increase of the density gradient. The fine study and understanding of the influence of electronic density gradients on the gain zone creation would require more detailed simulations.

The optimum GRIP angle is thus a compromise between absorption at high electron density and low electron density gradient together with a high abundance of Ni-like ions. An important experimental result is that the optimum angle is observed at the same value for a wide range of other experimental parameters such as delay between the short and long pulse, energy balance between them, and focusing geometry.

IV. INFLUENCE OF THE HEATING DELAY

We discuss in this section the influence of the peak-to-peak delay between the long and short pump pulses, on the shape and energy of the soft-x-ray laser source. For increasing delays, plasma expands and the dense area of interest ($5\times 10^{19} \leq n_e \leq 1\times 10^{21}$ cm^{-3}) cools down. As a result, the electron density gradient decreases in time, mainly along the horizontal axis normal to the target surface.

Figure 3 shows the integrated soft-x-ray laser energy as a function of the delay, from 50 to 850 ps for five GRIP angles

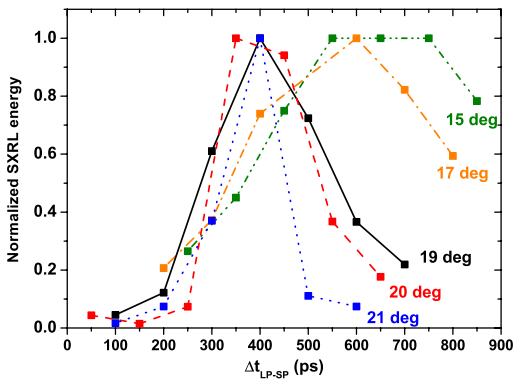

FIG. 3. (Color online) Normalized soft-x-ray laser energy, for a grazing angle from 15° to 21°, as a function of the delay between long pulse and short pulse.

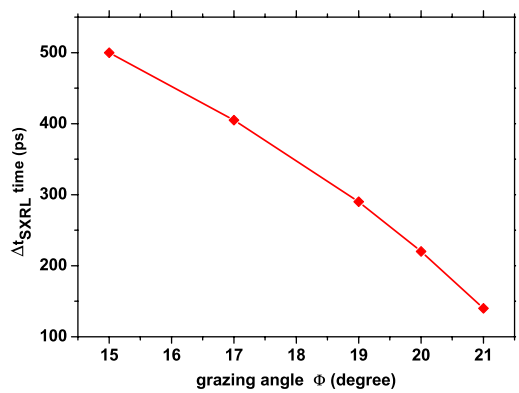

FIG. 4. (Color online) Full width at half maximum duration of the soft-x-ray laser delay window over which efficient lasing is observed.

between 15° and 21°. In order to make the comparison between different GRIP angles easier, the values shown in Fig. 3 are normalized to the maximum for each series corresponding to a given angle. Each point on this figure corresponds to the average over several shots, typically 5–10, with fluctuations of the order of 10–30 % depending on the signal level as explained in detail in Ref. [11]. It can be seen that for the smallest angles the optimum delay is around 600 ps ($\Phi = 15° \rightarrow \Delta t_{LP-SP} = 700$ ps, $\Phi = 17° \rightarrow \Delta t_{LP-SP} = 600$ ps), while it is around 400 ps for the grazing angle 19° and above. Note that, at optimum delay, the short pulse is always largely after the end of the long pulse whose duration is 300 ps: in other words, the soft-x-ray laser is really pumped sequentially by separated pulses playing distinct roles. Another interesting feature exhibited in Fig. 3 is that the delay interval during which lasing is obtained, is much larger for small angles than for larger ones. Actually this delay interval constantly decreases when increasing the GRIP angle, as shown in Fig. 4.

The falloff of the soft-x-ray laser energy at the shortest delays can be explained by steep density gradients in a plasma which has not had enough time to expand and thus allows the efficient propagation of both the pumping laser pulse and the soft-x-ray laser beam. It can be seen in Fig. 3, that this effect is more crucial for larger GRIP angles such as $\Phi = 20$ and 21° that exhibit almost no signal for delays shorter than 250 ps whereas for $\Phi = 15$ and 17° the signal for 200 ps is still not negligible as compared to the maximum value (20%).

On the other hand, the falloff of the soft-x-ray laser energy toward longer delays is controlled by plasma cooling and recombination. In those cases, the short pulse is indeed incident in a plasma where the temperature and the average ionization have decreased, resulting in a lower density of lasing ions and, hence lower gain. This effect is more pronounced at higher electron density (recombination rates are higher), i.e., when the GRIP angle is larger. This explains why the delay interval for lasing is reduced for larger GRIP angles, as represented in Fig. 4.

The fact that refraction is the main mechanism which prevents lasing for the shortest delays is also confirmed by the near-field images shown in Fig. 5. For the shortest delay, 200 ps, the soft-x-ray laser source has a vertical double structure which is likely to be induced by refraction in the vertical direction of the IR pump beam. Such double structures were reproducibly observed for delays below 250 ps, but disappeared for larger delays, as shown in Fig. 5.

In conclusion, varying both delay Δt_{LP-SP} and GRIP angle, gives rise to a complex behavior of preplasma as it interacts with the short laser pumping pulse. The optimum delay for soft-x-ray laser emission is governed by a compromise between refraction for short delays and dense plasma cooling for longer ones. The sensitivity of amplification to the delay increases with the GRIP angle.

V. INFLUENCE OF PREPLASMA CONDITIONING AND PREPULSE EFFECTS

The importance of adding a low-energy prepulse a few nanoseconds before the main long pulse, which creates the plasma, is well known since the first experimental demonstrations of soft-x-ray laser pumped in the quasi-steady-state regime in the mid-1990s [12–14]. Simulations performed for the transient collisional scheme for normal [15] or longitudinal incidence [16] also confirm the relevance of this tech-

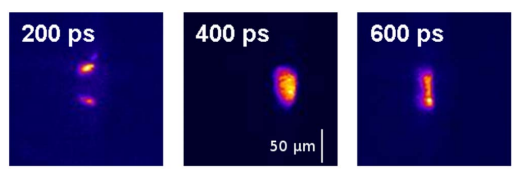

FIG. 5. (Color online) Near-field images for different delay between the long and short laser pulses. Experimental conditions were $\Phi = 19°$, and the IR energy balance was 500 mJ on each arm.

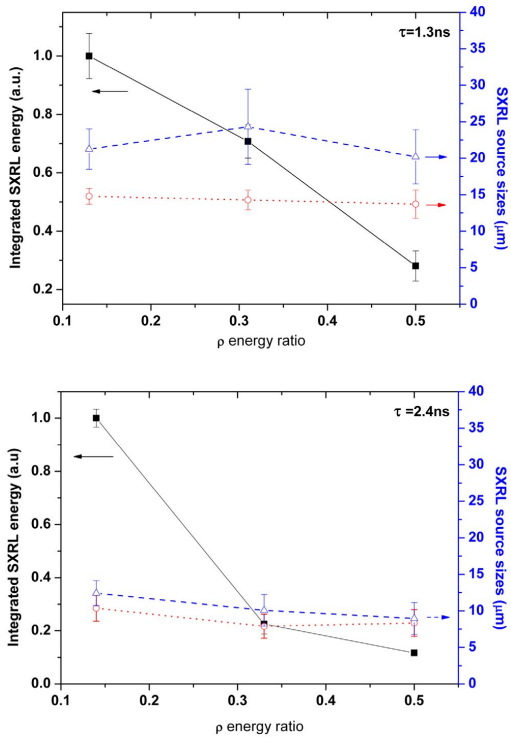

FIG. 6. (Color online) Soft-x-ray laser source characteristics (solid square: normalized integrated energy; open triangle: vertical size; open circle: horizontal size) for optimized conditions $\Delta t_{LP-SP}=400$ ps with prepulse delays $\tau=1.3$ ns (a) and $\tau=2.4$ ns (b) at variable energy ratio ρ, between prepulse and long pulse.

nique to shape an ideal preplasma for soft-x-ray laser generation. By adding a prepulse, the plasma interaction volume increases by hydrodynamic expansion. This leads to a reduction of the density gradient and an increase of the absorption of the main pulse. When working in the GRIP geometry, the use of a low-energy prepulse hence allows one to efficiently heat the plasma at the optimum density where the lasing ions are abundant, together with a reduced density gradient.

The prepulse generator, as described in Sec. II, allows the delay τ between the prepulse and the long pulse, and the energy ratio ρ between them ($\rho=E_{prepulse}/E_{long\ pulse}$) to be varied. The total energy $E_{prepulse}+E_{long\ pulse}$ and the GRIP angle $\Phi=19°$ were kept constant for the following study. Note that $\rho=10\%$ corresponds to an irradiation level on a target of 4×10^{10} W/cm^2.

From the optimized conditions described in previous sections, we first varied the so-called contrast from 7% to 50% at a fixed delay between prepulse and long pulse ($\tau=1.3$ ns) and fixed total pump energy. The results are shown in Fig. 6(a): no significant change as a function of ρ was observed on the soft-x-ray laser source size, neither vertical nor horizontal. We rather noted an increase of the source

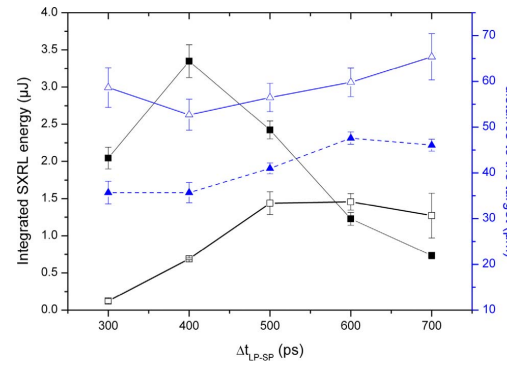

FIG. 7. (Color online) Comparison of the soft-x-ray laser source characteristics for optimized conditions with a prepulse delay $\tau=2.4$ ns [open symbol, case of Fig. 6(b)] and $\rho=14\%$ and $\tau=1.3$ ns [solid symbol, case of Fig. 6(a)] and $\rho=7\%$ at variable delay between long pulse and short pulse. The squares show integrated energy and the triangles show distances to the target surface.

instability and even an energy reduction for large ρ values. The latter might be attributed to the fact that the total energy between prepulse and long pulse is kept constant and thus that increasing ρ means consequently decreasing the long pulse irradiation level on target, reaching a real multipulse irradiation scheme. Figure 6(b) shows the same phenomenon at a larger delay ($\tau=2.4$ ns) and confirms that only changing the prepulse energy ratio, without changing the delay, has no real impact on the geometrical soft-x-ray laser characteristics.

The importance of preplasma conditioning through the increase in delay between prepulse and long pulse can be understood thanks to the two following experimental facts: first, as shown in Fig. 7, the source position is strongly influenced by τ: changing τ from 1.3 to 2.4 ns, the distance to the target increases from 35 to 55 μm. Second, when varying the second delay Δt_{LP-SP} between the long and short pumping pulse for $\tau=1.3$ and 2.4 ns, the soft-x-ray laser energy reduction at large delays attributed in Sec. IV to dense plasma cooling, is more important for small τ. These observations confirm that the preplasma effect is governed by plasma hydrodynamic expansion and that increasing τ leads to the shift of the gain region toward low density regions of the plasma together with low gradients.

Finally, the main interesting feature shown by comparing Figs. 6(a) and 6(b), and already reported in [9], is that the soft-x-ray laser source dimension in both directions is significantly reduced when the prepulse to long pulse delay goes from 1.3 to 2.4 ns. This source size reduction is also accompanied by an energy reduction: a factor of 2 in our case. We observed experimentally that the source size is more critical on the fluence than purely the source energy (quadratical variation for the geometrical aspect). Although this behavior is not yet fully understood, it yields a very interesting level of source fluence up to 1.2 J/cm^2 as compared to approximately 0.3 J/cm^2 in the usual energy-

optimized case. For some applications such as irradiation experiments, where the relevant parameter is more the source fluence than the integrated energy [17], such a result is hence of high interest.

As a preliminary conclusion, the addition of a small prepulse before the long pulse with the appropriate delay may increase significantly the source fluence and quality. We observed that the delay has more effect on the source geometry than simply changing the prepulse energy level. Detailed multiscan experimental optimization of this prepulse effect should be further explored.

VI. CONCLUSIONS

In conclusion, we have performed experiment and here reported on an extensive multiparameter optimization of a transient Ni-like Mo soft-x-ray laser at 18.9 nm, pumped under grazing incidence. By imaging the soft-x-ray laser at the output of the plasma rod, we obtain, for the first time, detailed insight on the effect of varying the GRIP angle among other parameters. We demonstrate that varying the GRIP angle strongly influences the pump laser coupling into the plasma: the soft-x-ray laser output energy is indeed reduced by more than one order of magnitude when changing the GRIP angle by only a few degrees around the best position, found to be close to 19°.

Moreover, we show that the soft-x-ray laser source shifts closer to the target when increasing the grazing angle, which directly demonstrates the concept of GRIP: the density at which the soft-x-ray laser is generated can be varied with the GRIP angle. For angles larger than optimum value, refraction of both the pump and soft-x-ray laser beams seems to play an important role. The optimization versus the delay between the long and short pulses led to a clear optimum at 400 ps in almost any experimental configuration, including, in particular, different GRIP angle values. An interesting result is that the range of delays over which an important soft-x-ray laser emission is observed decreases with the GRIP angle: increasing this parameter thus makes the delay optimization more critical.

Finally, our preliminary results on the effect of a weak prepulse to shape the preplasma indicate that the delay between prepulse and long laser pulse is a more critical parameter to control than only the energy level. For long prepulse delay (τ) condition and increased prepulse energy of $\approx 10\%$ corresponding to an intensity of $\approx 4 \times 10^{10}$ W/cm^2. As also mentioned in Ref. [9] we observe soft-x-ray laser sources with an exceptionally high brightness level.

This detailed study of the physics of the soft-x-ray laser, pumped in grazing incidence, should give useful benchmarks for numerical studies to further optimize and understand this type of source that is nowadays the best candidate for simple seeding experiments of high order harmonics in soft-x-ray laser lasers from solid targets [8]. Our work provides a quantitative and accurate characterization of physical quantities which play a crucial role in the optimization of seeding with high order harmonics: the position and size of the active region in the plasma amplifier, as well as the output mean fluence.

ACKNOWLEDGMENTS

This work was supported by the Swedish Research Council, the Knut and Alice Wallenberg Foundation, and through the EU Access to Research Infrastructures activity (Contract No. RII3-CT-2003-506350, Laserlab Europe). Mechanical drawing has been achieved by Jean-Claude Lagron.

[1] R. Keenan, J. Dunn, P. K. Patel, D. F. Price, R. F. Smith, and V. N. Shlyaptsev, Phys. Rev. Lett. **94**, 103901 (2005).
[2] B. M. Luther, Y. Wang, M. A. Larotonda, D. Alessi, M. Berrill, M. C. Marconi, and J. J. Rocca, Opt. Lett. **30**, 165 (2005).
[3] Y. Wang, M. A. Larotonda, B. M. Luther, D. Alessi, M. Berrill, V. N. Shlyaptsev, and J. J. Rocca, Phys. Rev. A **72**, 053807 (2005).
[4] A. Weith, M. A. Larotonda, Y. Wang, B. M. Luther, D. Alessi, M. C. Marconi, and J. J. Rocca, Opt. Lett. **31**, 1994 (2006).
[5] J. Tümmler, K. A. Janulewicz, G. Priebe, and P. V. Nickles, Phys. Rev. E **72**, 037401 (2005).
[6] G. J. Pert, Phys. Rev. A **73**, 033809 (2006).
[7] Ph. Zeitoun, G. Faivre, S. Sebban, T. Mocek, A. Hallou, M. Fajardo, D. Aubert, Ph. Balcou, F. Burgy, D. Douillet, S. Kazamias, G. de Lacheze-Murel, Th. Lefrou, S. Le Pape, P. Mercere, H. Merdji, A. S. Morlens, J. P. Rousseau, and C. Valentin, Nature (London) **431**, 426 (2004).
[8] Y. Wang, E. Granados, M. A. Larotonda, M. Berrill, B. M. Luther, D. Patel, C. S. Menoni, and J. J. Rocca, Phys. Rev. Lett. **97**, 123901 (2006).
[9] K. Cassou, S. Kazamias, D. Ros, F. Plé, G. Jamelot, A. Klisnick, O. Lund, F. Lindau, A. Persson, C.-G. Wahlstrom, S. de Rossi, D. Joyeux, B. Zielbauer, D. Ursescu, and T. Kühl, Opt. Lett. **32**, 139 (2007).
[10] M. A. Larotonda, Y. Wang, M. Berril, B. M. Luther, J. J. Rocca, M. M. Shakya, S. Gilbertson, and Z. Chang, Opt. Lett. **31**, 3043 (2006).
[11] F. Lindau, O. Lundh, A. Persson, K. Cassou, S. Kazamias, D. Ros, F. Plé, G. Jamelot, A. Klisnick, S. de Rossi, D. Joyeux, B. Zielbauer, D. Ursescu, T. Kühl, and C.-G. Wahlstrom, Opt. Express **15**, 9486 (2007).
[12] O. Guilbaud, A. Klisnick, K. Cassou, S. Kazamias, D. Ros, G. Jamelot, D. Joyeux, and D. Phalippou, Europhys. Lett. **74**, 823 (2006).
[13] R. Keenan, C. L. S. Lewis, J. S. Wark, and E. Wolfrum, J. Phys. B **35**, L447 (2002).
[14] B. Rus, Ph. Zeitoun, Th. Mocek, S. Sebban, M. Kalal, A. Demir, G. Jamelot, A. Klisnick, B. Kralikova, J. Skala, and G. J. Tallents, Phys. Rev. A **56**, 4229 (1997).
[15] X. Lu, Y. J. Li, Y. Cang, K. Li, and J. Zhang, Phys. Rev. A **67**, 013810 (2003).
[16] T. Osaki, H. Nakano, and H. Kuroda, J. Opt. Soc. Am. B **19**, 1335 (2002).
[17] S. Kazamias, K. Cassou, O. Guilbaud, A. Klisnick, D. Ros, F. Plé, G. Jamelot, B. Rus, M. Koslova, M. Stupka, Th. Mocek, D. Douillet, Ph. Zeitoun, D. Joyeux, and D. Phalippou, Opt. Commun. **263**, 98 (2006).

Paper XVI

Quantitative study of 10 Hz operation of a soft x-ray laser – energy stability and target considerations

F. Lindau, O. Lundh, A. Persson, K. Cassou, S. Kazamias, D. Ros, F. Plé, G. Jamelot, A. Klisnick, S. de Rossi, D. Joyeux, B. Zielbauer, D. Ursescu, T. Kühl and C.-G. Wahlström.

Optics Express **15**, 9486 (2007).

Quantitative study of 10 Hz operation of a soft x-ray laser — energy stability and target considerations

F. Lindau,[1] O. Lundh,[1] A. Persson,[1] K. Cassou,[2] S. Kazamias,[2] D. Ros,[2] F. Plé,[2] G. Jamelot,[2] A. Klisnick,[2] S. de Rossi,[3] D. Joyeux,[3] B. Zielbauer,[4] D. Ursescu,[4] T. Kühl [4] and C.-G. Wahlström[1]

[1]*Department of Physics, Lund University, P.O. Box 118, S-22100 Lund, Sweden*

[2]*LIXAM, UMR 8624, Université Paris Sud, F-91405 Orsay Cedex, France*

[3]*Laboratoire Charles Fabry (IOTA), CNRS, Université Paris Sud Campus Polytechnique, RD 128, 91127 Palaiseau, France*

[4]*Gesellschaft für Schwerionenforschung (GSI), D-64291 Darmstadt, Germany*

filip.lindau@fysik.lth.se

Abstract: A soft x-ray laser from Ni-like Mo, pumped in grazing incidence (GRIP), is analyzed with regard to high repetition rate operation. Reliable lasing is obtained, but with significant energy fluctuations attributed mainly to beam pointing jitter from the pump laser. Two modes of operation are compared: continuously moving target and stationary target. With a moving target the soft X-ray output is constant on average, whereas the repeated use of the same target position leads to a pulse energy which increases for several tens of shots. This effect might be caused by improved guiding of the pump laser in the formed groove and the removal, through laser ablation, of the oxide layer on the target surface.

OCIS codes: (140.7240) UV, XUV, and X-ray lasers; (340.7440) X-ray imaging.

References and links

1. D. T. Attwood, K. Halbach and K. J. Kim, "Tunable coherent X-rays," Science **228**, 1264 (1985).
2. A. Rundquist, C. G. Durfee, Z. H. Chang, C. Herne, S. Backus, M. M. Murnane and H. C. Kapteyn, "Phase-matched generation of coherent soft X-rays," Science **280**, 1412 (1998).
3. O. Guilbaud, A. Klisnick, D. Joyeux, D. Benredjem, K. Cassou, S. Kazamias, D. Ros, D. Phalippou, G. Jamelot and C. Moller, "Longitudinal coherence and spectral profile of a nickel-like silver transient soft X-ray laser," Euro. Phys. J. D **40**, 125 (2006).
4. A. Klisnick, J. Kuba, D. Ros, R. Smith, G. Jamelot, C. Chenais-Popovics, R. Keenan, S. J. Topping, C. L. S. Lewis, F. Strati, G. J. Tallents, D. Neely, R. Clarke, J. Collier, A. G. MacPhee, F. Bortolotto, P. V. Nickles and K. A. Janulewicz, "Demonstration of a 2-ps transient X-ray laser," Phys. Rev. A **65**, 033810 (2002).
5. D. L. Matthews, P. L. Hagelstein, M. D. Rosen, M. J. Eckart, N. M. Ceglio, A. U. Hazi, H. Medecki, B. J. MacGowan, J. E. Trebes, B. L. Whitten, E. M. Campbell, C. W. Hatcher, A. M. Hawryluk, R. L. Kauffman, L. D. Pleasance, G. Rambach, J. H. Scofield, G. Stone and T. A. Weaver, "Demonstration of a soft-x-ray amplifier," Phys. Rev. Lett. **54**, 110 (1985).
6. P. V. Nickles, V. N. Shlyaptsev, M. Kalachnikov, M. Schnrer, I. Will and W. Sandner, "Short pulse X-ray laser 32.6 nm based on transient gain in Ne-like titanium," Phys. Rev. Lett. **78**, 2748 (1997).
7. R. Keenan, J. Dunn, P. K. Patel, D. F. Price, R. F. Smith and V. N. Shlyaptsev, "High-repetition-rate grazing-incidence pumped X-ray laser operating at 18.9 nm," Phys. Rev. Lett. **94**, 103901 (2005).

8. J. J. Rocca, Y. Wang, M. A. Larotonda, B. M. Luther, M. Berrill and D. Alessi, "Saturated 13.2 nm high-repetition-rate laser in nickellike cadmium," Opt. Lett. **30**, 2581 (2005).
9. A. Weith, M. A. Larotonda, Y. Wang, B. M. Luther, D. Alessi, M. C. Marconi, J. J. Rocca and J. Dunn, "Continuous high-repetition-rate operation of collisional soft-x-ray lasers with solid targets," Opt. Lett. **31**, 1994 (2006).
10. K. Cassou, S. Kazamias, D. Ros, F. Plé, G. Jamelot, A. Klisnick, O. Lundh, F. Lindau, A. Persson, C.-G. Wahström, S. de Rossi, D. Joyeux, B. Zielbauer, D. Ursescu and T. Kühl, "Optimization toward a high-average-brightness soft-x-ray laser pumped at grazing incidence," Opt. Lett., **32**, 139 (2007)
11. Y. Li, J. Dunn, J. Nilsen, T. W. Barbee, A. L. Osterheld and V. N. Shlyaptsev, "Saturated tabletop x-ray laser system at 19 nm," J. Opt. Soc. Am. B, **17**, 1098 (2000).
12. D. Strickland and G. Mourou, "Compression of amplified chirped optical pulses," Opt. Commun. **56**, 219 (1985).
13. K. Cassou, P. Zeitoun, P. Velarde, F. Roy, F. Ogando, M. Fajardo, G. Faivre and D. Ros, "Transverse spatial improvement of a transiently pumped soft-x-ray amplifier," Phys. Rev. A **74**, 045802 (2006).
14. R. Tommasini, F. Löwenthal, and J. E. Balmer, "Saturation in a Ni-like Pd soft-x-ray laser at 14.7 nm," Phys. Rev. A **59**, 1577 (1999).
15. J. G. Lunney, "Wave-guiding in soft-x-ray laser experiments," Appl. Phys. Lett. **48**, 891 (1986).
16. J. Filevich, J. J. Rocca, M. C. Marconi, R. F. Smith, J. Dunn, R. Keenan, J. R. Hunter, S. J. Moon, J. Nilsen, A. Ng and V. N. Shlyaptsev, "Picosecond-resolution soft-x-ray laser plasma interferometry," Appl. Opt. **43**, 3938 (2004).
17. D. L. Douglass, *Oxidation of Metals and Alloys*, (American Society of Metals, USA, 1970).
18. O. Kubaschewki and B. E. Hopkins *Oxidation of Metals and Alloys*, (Butterworths, UK,1967).

1. Introduction

Among the many applications for light in the soft X-ray region (wavelengths up to a few tens of nm) are holography, interferometry, lithography and materials processing. Currently, this type of radiation is generated by e.g. synchrotrons [1] or by upconverting a longer wavelength laser using high order harmonic generation (HHG) [2]. These methods have their specific advantages and drawbacks. Synchrotron radiation has tunable wavelength, high average power and brightness, and very high repetition rate ($\sim 100\,\mathrm{MHz}$), but has low coherence and requires large, costly facilities. HHG from visible and near infrared (IR) lasers have excellent coherence and can be generated with, in this context, low-cost table-top laser systems operating typically at 10 Hz or 1 kHz. However, they suffer from relatively low pulse energies.

Soft X-ray lasers (SXRL) present an interesting alternative to synchrotrons and harmonic generation. They offer the possibility of high pulse energy and peak brightness, together with good temporal coherence [3]. The pulse duration is typically a few picoseconds [4], i.e. in a range between HHG (few tens of femtoseconds or even attoseconds) and synchrotrons ($\sim 100\,\mathrm{ps}$). The SXRL generating process is based on population inversion of an electronic transition in the selected ion species, that consequently completely determines the wavelength of the laser. Ever since the first SXRL was demonstrated about 20 years ago [5], they have been associated with high energy pump lasers. Inherent to such systems are very low repetition rate and large cost. But, the amount of pump energy needed for a saturated X-ray laser has decreased gradually over the years. Notable advances are the introduction of transient collisional pumping [6], and more recently grazing incidence pumping (or GRIP) [7]. Now, a saturated soft X-ray laser can be produced with less than one joule of pump energy, making high repetition rate operation (see e.g. [8, 9]) possible at relatively low-cost, university scale facilities. This development makes the SXRL a promising tool for a wide range of applications, and the field of XRL studies has therefore received increased interest world-wide.

The GRIP technique is a version of the transient collisional pumping scheme, where the plasma formation and the actual pumping of the laser transition is separated into two pulses. First, a long (hundreds of ps) IR laser pulse hits the target and creates a plasma which is allowed to expand and form a smooth density gradient. After a given time delay, the second, short (a few ps), pump pulse is incident on the plasma at a grazing angle, φ, and heats free electrons through inverse bremsstrahlung absorption. As opposed to the normal incidence pumping in the original transient collisional method, the pump is refracted by the plasma density gradient and changes

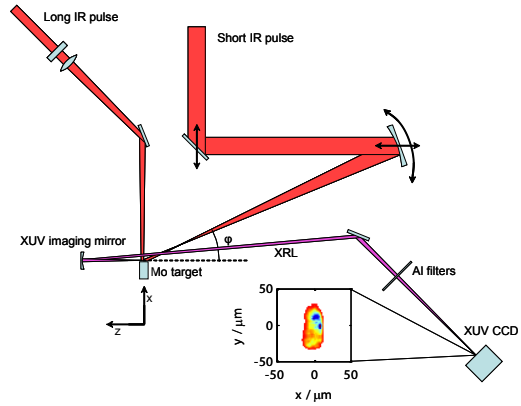

Fig. 1. Overview of the experiment setup. The XRL near field imaging diagnostic is indicated. Inset is an image of a typical near field SXRL intensity distribution.

direction at a plasma density that depends on the angle of incidence. In the turning point region, laser energy is efficiently transferred to the plasma. Advantages of the GRIP scheme, compared to normal incidence, are less refraction of the SXRL beam due to the smooth plasma density gradient, pump energy deposition localized to the gain region and increased path length of the pump laser in the gain medium.

In a recent study, we have investigated various aspects of optimizing grazing incidence pumping, such as grazing angle φ, delay and energy ratio between the long and short pulses [10]. Single shot soft X-ray energies of up to $3\,\mu$J were measured. This is comparable to the $2.3\,\mu$J per shot obtained by Li *et al.* [11] for a saturated Ni-like molybdenum X-ray laser using a much larger 10 J driving laser. We report here findings related to 10 Hz operation during the experiment described in [10] and in particular on energy stability and target considerations.

2. Experimental

The driving laser is the 10 Hz multi-TW laser at the Lund Laser Centre. It is a Ti:sapphire CPA [12] system, with 800 nm central wavelength, delivering pulses with up to 1.6 J before compression. When fully recompressed, the pulse length is 35 fs FWHM. However, the GRIP technique requires a longer, ~ 1 ps, duration for the grazing incidence pump pulse. This was accomplished by moving a grating in the compressor. Part of the uncompressed (~ 300 ps) beam was split off after the last amplifier and used to preform the plasma medium. A spherical / cylindrical lens package was used to focus the long pulse beam to a line, $70\,\mu$m $\times$ 5 mm FWHM. Refractive optics is not an option for the short pump pulse, due to non-linear effects induced at high intensity. Instead, a spherical mirror was used off-axis to produce an astigmatic focal line. The grazing angle on target, which is twice the angle on the spherical mirror, varied between 15° to 21°. The line focus was about $40\,\mu$m wide and 6 to 8 mm long depending on the angle. The target was a 5 cm long and 4 mm wide slab of molybdenum, polished with standard mechanical grinding. The selected lasing transition was $4d\,^1S_0 - 4p\,^1P_1$ in the Ni-like ion Mo^{14+} at 18.9 nm. For this study, the energy content in the driving laser pulses were 0.5 J in the long pulse and 0.5 J in the 5 ps short pulse. The delay between them was set to 500 ps. The optimum GRIP angle was found to be 19°. An additional prepulse, containing 14% of the total long pulse energy, preceeded the main pulse by 2.3 ns to improve the plasma conditions.

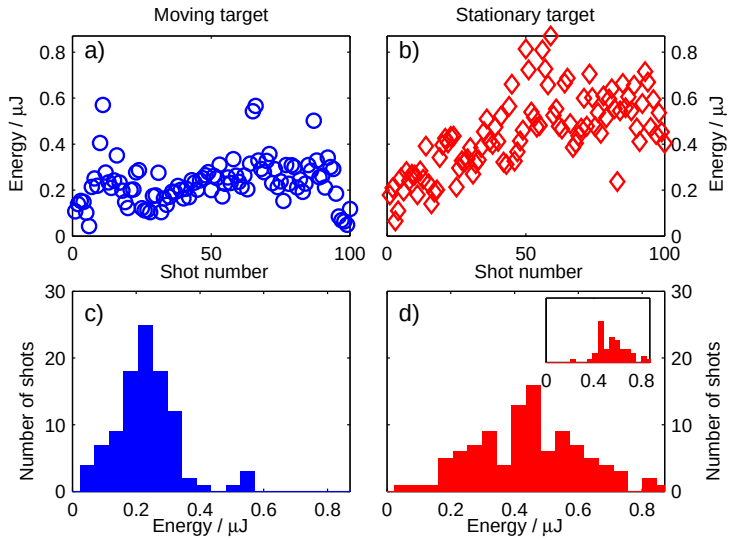

Fig. 2. X-ray laser output energy time series and histogram for moving target (parts a and c) and stationary target (parts b and d). Inset in d) is the histogram for the last half of the shot sequence. Mean energy is 0.22 μJ and 0.42 μJ for moving and stationary targets respectively.

The main diagnostic instrument was a high-resolution near field imaging device. It imaged the soft X-ray laser energy distribution at the exit of the gain region, by means of a curved X-ray mirror, onto a CCD chip. The pixel resolution was 1.7 μm at the object plane, corresponding to a magnification factor of about 7. Figure 1 shows a schematic of the setup. Aluminium filters of different thicknesses were used to attenuate the SXRL beam and to reduce the plasma background emission. To achieve 10 Hz frame rate, the camera was set to capture only a 46 $\times$ 41 pixel region of interest. The small area combined with the moving source position for a stationary target limited the number of shots to about 100 in a single run.

3. Results

10 Hz operation of the X-ray laser is tested in two different ways. First the target is moved at a constant rate of 0.4 mm/s, corresponding to the width of the focal spot between shots, to supply a fresh target surface for every shot. Then the target is stopped, allowing the pump laser to dig into the bulk of the target. This is done in immediate connection in time during a total of 20 s (200 shots), to minimize any effect of laser drift. Time series of the integrated energy in every shot are shown in Fig. 2. The moving target has a stable output level (there are no missed shots) with an average SXRL pulse energy of 0.22 μJ and a standard deviation of 0.09 μJ, i.e. 41% of the mean. When the target is stopped, the pulse energy ramps up during approximately 50 shots, leveling off at mean energy of 0.53 μJ and a slightly higher standard deviation 0.11 μJ. The relative standard deviation is thus lower, at 21% of the mean. Additional tests indicate that the higher output level for a stationary target can be sustained for several hundred shots.

The RMS size of the near field emission region is roughly 7 μm in both vertical and horizontal directions, see Fig. 3. The shot-to-shot fluctuations are much larger in the vertical direction than in the horizontal. There is, however, no significant change in source size for the two cases

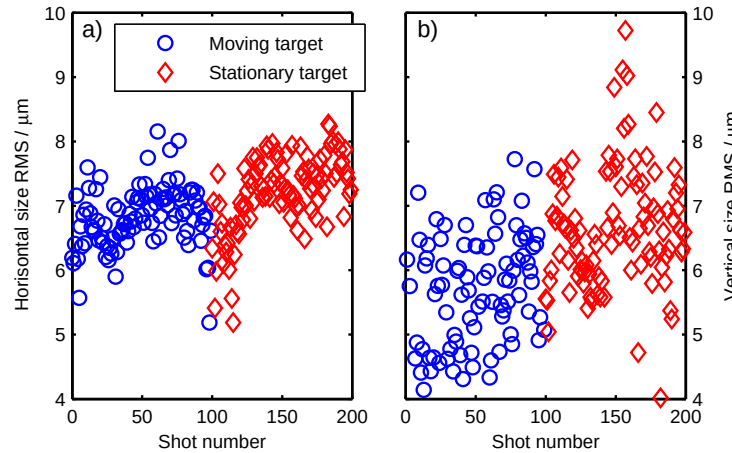

Fig. 3. Size of the near field distribution of the soft X-ray laser for both moving and stationary targets. In a), the horizontal size (perpendicular to the target surface) is plotted and b) shows the vertical size (tangential to the target surface).

of moving or stationary target.

Figure 4 shows the distribution of the distance of the X-ray laser near field centroid positions to the target surface for the two shot series. The SXRL emission centroids with a moving target are clustered in a region roughly $10 \times 15\,\mu$m in size, corresponding to the beam pointing of the driving laser. When the target is stopped, the centroid position starts moving steadily in toward the original target surface, at a rate of $\sim 0.22\,\mu$m/shot.

4. Discussion

The shot-to-shot fluctuations in output energy can partly be attributed to fluctuations in the driving laser itself, in terms of both energy per pulse and beam pointing. The IR laser has shot-to-shot energy fluctuations of the order of 10%. A graph showing SXRL output energy as a function of short pulse pump energy is plotted in Fig. 5(a). The laser parameters used to obtain this graph were slightly different from the ones in the rest of the paper, but the general shape of the curve is independent of these differences. Clearly, at the 500 mJ pump energy used in the present experiment, a 10% variation in laser energy results in $\sim$ 10% variation in the SXRL pulse energy.

Another likely cause of energy fluctuations is beam pointing jitter of the pump lasers. The two line foci, $40\,\mu$m and $70\,\mu$m wide respectively, must overlap perfectly to ensure optimal X-ray lasing. A scan where the long pulse line focus was moved relative to the short one is found in Fig. 5(b). The width of the SXRL peak is only $\sim$ 30% of the long pulse focal line. This is because the lasing ions are produced only in the central, high-intensity, part of the focus, due to the gaussian intensity profile of the pump laser [13]. With an estimated $15\,\mu$m shot-to-shot fluctuation, due to mechanical vibrations, of the relative positions of the focal spots, Fig. 5(b) indicates that there will be significant variations in output energy, consistent with our observations.

The target surface conditions are also believed to have a significant effect on the observed behavior for both stationary and moving target operation. After the experiment, the target slab

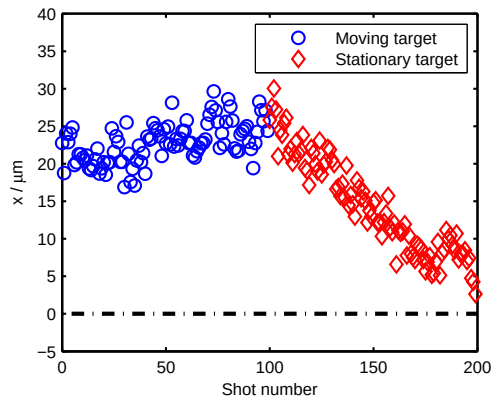

Fig. 4. Distance between the centroid of the X-ray laser near field and the target surface for both moving and stationary target. The original target surface is indicated with a dash-dotted line. With a moving target, the gain region is hovering 23 μm from the target (a situation corresponding to single shot operation). When the target is stopped, the pump laser ablates the target, causing the gain region to move inward at a constant rate.

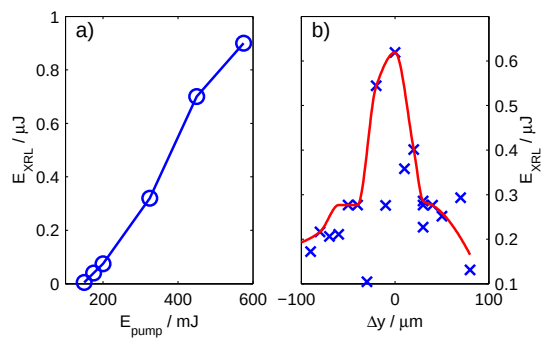

Fig. 5. The output X-ray laser energy versus short-pulse pump energy is plotted in a). This particular data set is for $\varphi = 17^\circ$ and 600 ps delay between long and short pulse. In b), the sensitivity of the X-ray output to the overlap between the two line foci is shown. The red line outlines the envelope of the shots. FWHM of the peak is approximately 30 μm.

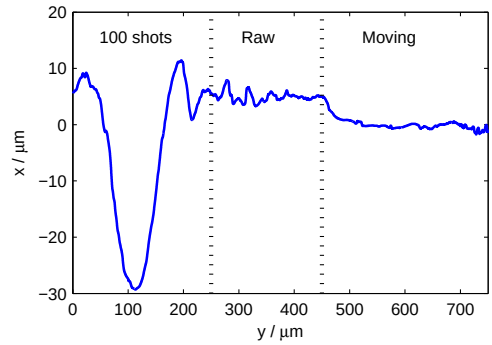

Fig. 6. Target profile in the plane normal to the SXRL axis, as measured with a surface profilometer. Three regions are highlighted: irradiated stationary target, raw target and irradiated moving target. The reduced roughness of the target surface after a single laser exposure is clearly seen in the moving target region. Firing 100 shots on the same target position produces a deep crater with material thrown up to the sides.

has been analyzed with a surface profilometer. The results are shown in Fig. 6. The unexposed raw surface roughness is initially $1\,\mu$m, and after one shot it is smoothed to $\sim 0.5\,\mu$m (such as in the moving target case). This could account for the larger shot-to-shot variations for a moving target, since it has been shown that the laser–plasma interaction is strongly dependent on the surface quality on a microscopic scale [14].

The higher output energy for the stationary target could also to some extent be explained by the reduced surface roughness. A smoother target surface leads to the creation of a more homogeneous plasma and a better interaction with the pump laser. However, this smoothing should only occur during the first few shots, and not provide additional improvement for the next several tens of shots. The groove produced during the tests with a stationary target improves the coupling between the plasma and the pump laser [15, 16], and can thus lead to the gradual increase in SXRL energy over the first 50 shots. The depth of the groove is $30\,\mu$m, i.e. the IR laser is eating into the target bulk at rate of $0.3\,\mu$m/shot. This is in fair agreement with the observed movement of the source position. As evident from Fig. 6, the material is to a large extent thrown up to the sides, forming walls on either side of the groove, providing additional guiding of the pump laser.

The presence of an oxide layer (MoO_2) [17] on the target surface is an additional reason for the lower output level observed with the moving target, since the oxide leads to a lower density of lasing ions and hence a lower gain. The oxide layer is very thin [18], and should be removed by the first few laser shots. This has been confirmed with a spectrometer, where O^{5+} from plasma emission and SXRL lines were simultaneously recorded. After five shots, the O^{5+} line almost disappears, whereas the SXRL intensity still increases.

5. Conclusions

High repetition rate operation of a soft X-ray laser has been characterized with quantitative precision by means of real time acquisition of near-field images from the exit aperture of a soft X-ray laser pumped in GRIP configuration. This diagnostic allows for energy and 2D-spatial characterization of the X-ray emission as a function of shot number over series of a few hundreds shots. We confirm the results obtained by Weith *et al.* [9], concerning the level of

energy fluctuations for a Ni-like molybdenum X-ray laser ($\sim$ 20–40%).

Moreover, we compared two different types of operation, moving or stationary target, which exhibit distinct behaviors. With the moving target, the pump laser is always incident on a fresh target and we observe a significant reduction of the output energy and an increase of the fluctuations. This is partly attributed to the existence of a thin layer of molybdenum oxide, which is supported by spectroscopic observations. The roughness of the target also plays an important role by degradating the plasma homogeneity. Both these effects could be removed in the near future by irradiating the target with a low intensity laser before an X-ray laser shot.

With the stationary target, we observe a progressive and significant increase of the output energy over the first 50 shots, accompanied by a constant drift of the source position toward the target direction at a rate of $0.3\,\mu$m per shot. This behavior is attributed to the formation of a groove that could affect laser absorption and/or plasma expansion. It seems thus more advantageous to operate the Mo X-ray laser with a stationary target, since the improved target surface conditions leads to an increased output energy. However in application experiments, the constant drift of the source towards the target by a few $10\,\mu$m, which is not a severe problem if the source is used in free propagation, could become problematic if the source is used in imagery.

Finally we show that the fluctuations of the pump laser, in terms of energy and beam pointing, contribute to the shot-to-shot variations in the SXRL energy. Possible solutions to improve the stability of the SXRL include: increasing the pump energy to reach saturated amplification where the sensitivity to pump energy fluctuations is reduced, increasing the width of the plasma to reduce sensitivity to pointing variations, and installing vibration decoupling in the pump laser to improve the pointing stability. In conclusion, thanks to the above study and with simple and realistic improvements, the 10 Hz operation of soft X-ray laser becomes possible for applications in imagery and irradiation having the same stability requirements than for any usual infrared laser facility.

Acknowledgments

This work was supported by the Swedish Research Council, the Knut and Alice Wallenberg Foundation, and the EU Access to Large-Scale Facility Programme (RII3-CT-2003-506350 Laserlab Europe). We acknowledge the help from A. Jérome, M. F. Ravet, F. Delmotte for the profilometer measurements, J. Gauthier for information on Mo oxidation, and J.-C. Lagron for mechanical drawings.